The Origin and Evolution of Dust

Haley Louise Morgan

A thesis submitted to the
University of Wales,
Cardiff,
for the degree of

Doctor of Philosophy

September 2004

ProQuest LLC
789 East Eisenhower Parkway
P.O. Box 1346
Ann Arbor, MI 48106-1346

Acknowledgements

There are many people who have contributed to this research, both academically and socially. In my academic life, I would like to thank Jon Davies for allowing me onto this degree course in the first place; John Inglesfield for being a great Postgraduate tutor, and for listening when no-one else would; and Steve Eales for his humour, wisdom, wonderful abundance of ideas, for writing great references, and for giving me the opportunity to work on one of the most exciting, important areas of our field (I'm sorry for making you read all those drafts!). Thanks also to Jacco van Loon for smiling so much; Rob Ivison for helping with the papers and Eli Dwek for making things interesting. Finally, I'd like to express my gratitude to Prof. Mike Edmunds who took me on as a PhD student and taught me to fly. Thanks for never pushing me in one direction and allowing me to follow my own research ideas.

Other people from work who really should be thanked are the computing staff, especially Paul Jones. You have helped this thesis to grow by solving all my computing issues so quickly.

From the terminal room in which I spent every working day for two years (but have now vacated for my own computer!), I would like to thank Dave Nutter and Hannah Loebl for knowing absolutely everything in the world that anyone could ever need to know. You guys are extremely patient with us mere mortals and I really appreciate it! I would like to thank Kris Wojciechowski for web-based distractions, Sarah Roberts and Melanie Bowden for being great back up for fights against the boys and Dean Trolley for the hugs. David Hubber, Diego Garcia, Catherine Vlahakis, Ian Bacchus, Iain Brown, Robbie Auld, and Erwin de Blok (he of the immortal "dark matter haleys" quote!) also deserve a mention for brightening up the working day. Extra thanks to Tim Waskett, who not only reduced some of the X-ray images used in this thesis, but has also helped me in my general understanding of astronomy by being patient and extremely clever (he won't deny this either!). You are great and I appreciate all of your help. It is because of you guys that I actually look forward to coming to work. That means I owe a lot of this PhD credit to you!

Lastly from my work life, I'd like to thank Loretta Dunne. She has been a fantastic inspiration both academically and as a friend. There are a lot of things I would not have experienced in this life if it wasn't for her pushing me forward. She has made me a braver person. I would also like to thank Stuart Peters who was with me on this journey for the first 6 years, he was the first to make me believe I could do this.

Thanks also to my family: my parents Gaynor and Lawrence and sister Gemma, as well as my newly found family: Jane, Sean and Olivia Gomez. Thanks for putting up with me and accepting me, even though I've been a student for so long! I apologise for all the times where I have been stressed about work but this is the reason why! And at last I have a real job! I thank you all for your unconditional love, support and strength, this thesis is about me wanting to make you proud.

Lastly, I would like to thank my fiancé Edward Gomez. He is the most important person in my life and because of him, I have begun to grasp the bigger picture and yearn to understand it. He has faced adversity with such courage and is a wonderful example to any of us trying to make it in astronomy. He has also had to put up with me talking about my research day and night and helping me obtain a clearer point of view! I thank him from my heart for many things, but mainly for making me want to believe in a better world, introducing me to such a wonderful set of people whom I now name amongst my dearest friends, and for all the coffee, without which time would have passed far too quickly. I love you.

This thesis has made use of the Canadian Astronomy Data Centre, which is operated by the Dominion Astrophysical Observatory for the National Research Council of Canada's Herzberg Institute of Astrophysics and NASA's Astrophysics Data System. I acknowledge the support of the staff at the JCMT, which is operated by the Joint Astronomy Centre on behalf of PPARC of the UK, the Netherlands OSR, and NRC Canada.

I would also like to pay tribute to a wonderful person who I had the pleasure of knowing for 7 years, Richard (Dicky) Taylor. Whilst I was writing these acknowledgements, Richard died at 23, from a skating accident. As well as being British No 1 for the second year in a row, he had recently won the British Freestyle Skiing championships. He was a true star and an inspiration for the rest of us to shoot for the moon.

Abstract

Interstellar dust affects our view of the Universe, with half of the starlight emitted since the Big Bang being absorbed by dust grains and re-radiated in the Infra-Red. This thesis is concerned with understanding the origin of interstellar dust and determining the relative importance of different dust formation sites in the Universe.

The sources and maximum amount of dust in early galaxies are investigated using published extended atmosphere models, stellar evolution tracks and nucleation conditions. A chemical evolution model is modified to include the estimated condensation efficiencies. The implications are investigated and we show that a supernovae source is required to produce large amounts of dust in galaxies. The atmospheres of AGB stars evolve too slowly to be responsible for high redshift dust. If SNe are not responsible for dust, then significant dust masses can only be generated at $z > 5$ by galaxies with very efficient star formation and no dust destruction.

The first sub-millimetre analysis of the galactic remnant Kepler is presented with $0.3 - 3$ $M_{\odot}$ of dust, depending on the absorption properties. This a *1000* times more than previous Infra-red observations found. The sub-mm emission anti-correlates with the other wavelengths, including the warm dust and the most likely origin is from freshly synthesised dust in the supernova and dust formed from the interaction of the supernova shock with the ambient medium. Iron needles as a possible origin of the sub-mm emission are investigated.

Finally, the sub-mm observations of the massive LBV star, η Carinae are presented to show that the winds of massive stars may also be important contributors to the dust budget. We conclude that supernovae, or their massive star progenitors, are a dominant contributor to interstellar dust and make suggestions for future work.

Publications

Morgan, H.L., Dunne, L., Waskett, T., Eales, S., Ivison, R., Edmunds, M.G., *Evidence for Dust Formation in Supernovae*, submitted, MNRAS, 2004

Dunne, L., **Morgan, H.**, Eales, S., Ivison, R., Edmunds, M.G., 2003, *The Origin of Cosmic Dust*, New Astron. Revs, 48, 611

Morgan, H.L., Dunne, L., Eales, S., Ivison, R., Edmunds, M.G., 2003, *Cold Dust in Kepler's Supernova Remnant*, ApJL, 597, 33

Dunne, L., Eales, S., Ivison, R., **Morgan, H.L.**, Edmunds, M.G., 2003, *The Origin of Cosmic Dust*, Nature, 424, 285

Morgan, H.L. & Edmunds, M.G., 2003, *Dust Formation in Early Galaxies*, MNRAS, 343, 427

3 Astronomy Hiaku

Wise astronomers
sit and wait with hushed voices;
watching the room grow.

We listen intently
as the speaker weaves stories;
how dust plays a part.

Dark Astronomy
we sat in silence today;
all the great voices.

Haley Morgan, 2003

Contents

List of Figures

List of Tables

Chapter 1

Introduction

"We owe our existence to stars, because they make the atoms of which we are formed. So if you are romantic you can say we are literally starstuff. If you're less romantic you can say we're the nuclear waste from the fuel that makes stars shine."

Sir M.Rees, Astronomer Royal

1.1 An Introduction to Interstellar Dust

The Interstellar Medium (ISM) was once thought to be quiescent empty space, yet it is now known to have many different phases, temperatures and components, consisting of gas, high energy particles and magnetic fields. About 1% of the mass of the ISM is thought to be dust grains, tiny particles composed of heavy elements (mainly carbon and oxygen) which have been injected from stars. These dust grains affect our view of the Universe by blocking out optical light and changing the visible appearance of astrophysical objects. Dust grains scatter, absorb and re-emit light to longer wavelengths so effectively that observing techniques at wavelengths other than optical are needed to obtain a complete picture of the Universe.

Historically, dust grains were regarded as a nuisance element in observations which needed to be overcome to explain scattering and extinction of starlight. Today, dust is now regarded as an important area for study, particularly since the advent of infra-red and sub-millimetre telescopes. These observations show that dust plays an important part in the cooling processes of the gas and its interaction with the gas dynamically, as well providing greater understanding of stellar chemistry. The absorption efficiency of the dust allows gas clouds to cool and fragment into stars, with the limit of the dust opacity likely to be responsible for the final mass of the star formed (e.g. Ferrara 2003). Dust grains are attributed to be the source of molecular hydrogen in clouds since the abundance of H_2 cannot be explained by gas phase reactions only as they are too slow in the general ISM (Hirashita & Ferrara 2002). The grains act as a catalyst by accreting H atoms onto the surface which become attached (via physical absorption) and random walk on the surface until 'meeting' another H atom, recombining and releasing binding energy as they are ejected (e.g. Whittet 2003). In dense clouds, the grains provide cores on which mantles may grow, removing material from the gas phase and providing an explanation for the depleted levels of molecules observed in some environments with respect to solar values (Dwek 1998 - hereafter D98; Tielens 1998; Whittet 2003; Draine 2003).

Dust appears to be an integral part of the dynamics of many astrophysical sources e.g., around active galactic nuclei, young stars, evolved stars and in planetary nebula (see Figure 1.1). Stars are born in a cloud of gas and dust, with the dust providing the basic constituents of planetary systems and an efficient radiator of excess heat energy. Dust grains may even contain the molecules relevant to the origin of organic life (Whittet 2003). In evolved stars, dust which has condensed out of the gas phase can be important in driving winds by creating an extra opacity source to the ions and ultimately increasing the outflow rate of the star (Lamers & Cassinelli 1999).

(a) (b) (c)

Figure 1.1: Examples of dusty regions enshrouding astrophysical objects. (a) shows the famous horsehead nebulae in the optical, courtesy of VLT, ESO. (b) The Eagle nebula in the optical with the Hubble Space Telescope, courtesy of HST Image Gallery. (c) η Carinae, a dense star forming region, courtesy of NASA HST/Heritage.

In such cases, the mass of dust in the wind could affect the subsequent fate of the star during its last stages of evolution. A thorough knowledge of the degree of extinction of the starlight is therefore required to recover the basic properties of the astrophysical objects being hidden from our view. At high redshifts, significant extinction by dust may also obscure our view of cosmological star formation.

Although dust grains block the optical light, astronomers can observe the re-emitted starlight in the Infra-red. In Figure 1.2 the galaxy NGC891 is shown in both the optical and sub-mm regime at 850 μm. The dust lanes are prominent in the centre of the galaxy in the optical, but when we observe in the far Infra-red, we are directly observing the emission from the dust. The dust responsible for the emission in these images is at a temperature of about 15 - 20K (Alton et al. 1998) and has an order of magnitude more mass than predicted from the 60 - 100 μm fluxes alone.

One of the most suprising discoveries in recent years is the amount of energy in the IR extragalactic background. Observations with the Infra-red Astronomical

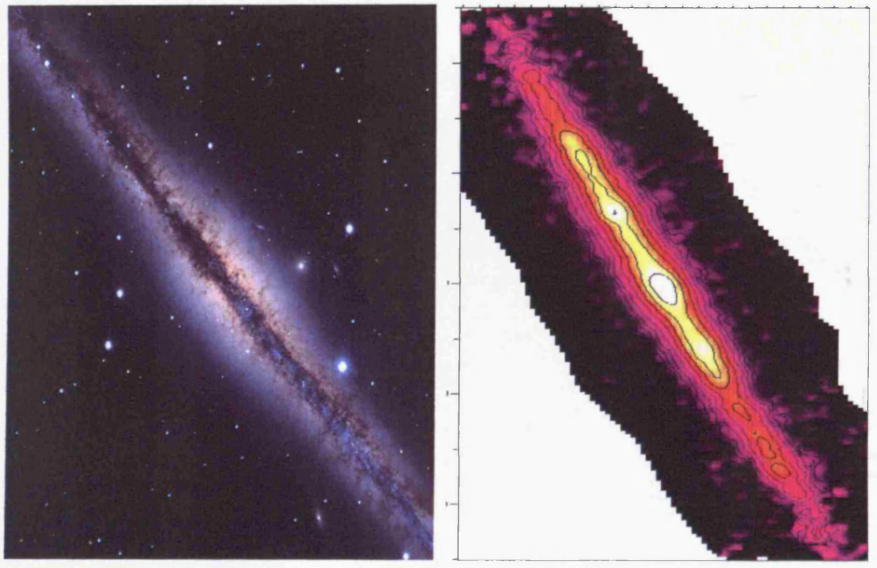

(a) (b)

Figure 1.2: Comparison of the optical (a) and sub-mm (b) emission from NGC891. There is a significant dust lane in the middle of the galaxy in (a), blocking our view of the central stars. The dust lane is extremely bright in the sub-mm. The optical image is courtesy of Howk et al. (/WIXN/NOAO/NSF, copyright WIYN.Inc.) and the sub-mm image is taken from Alton et al. 1998 using the Sub-millimetre Common User Bolometer Array (SCUBA).

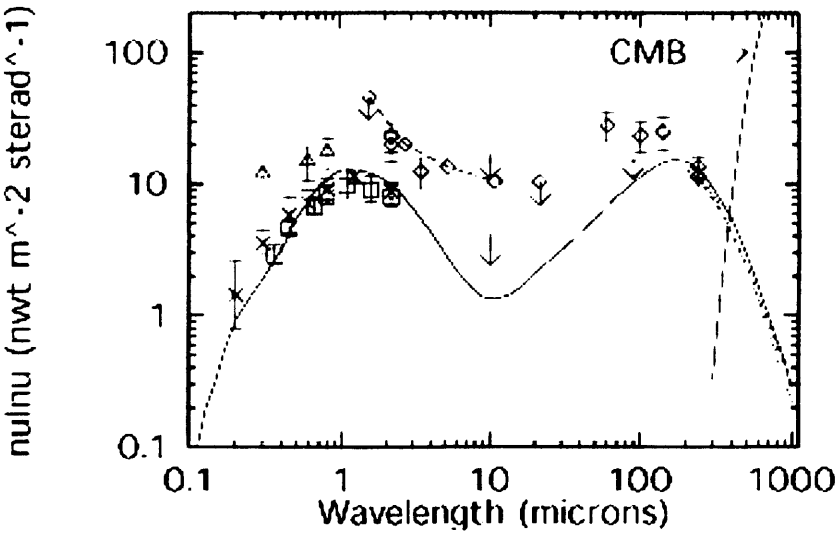

Figure 1.3: The integrated background energy in the Infra-red - optical regime predicted from cosmological models and the COBE results. This picture was taken from Pagel (2002).

Satellite (IRAS), the Infra-red Space Observatory (ISO) and the COsmic Backgound Explorer (COBE) measured the integrated energy in the waveband $125 < \lambda < 5000$ μm (e.g. Dwek et al. 1998; Pagel 2002). When this is compared to the integrated energy in the optical regime, astronomers found that an almost equal amount of energy existed in the two wavebands (Figure 1.3). This implies that almost half of the light emitted from stars and quasars since the Big Bang has been absorbed and re-radiated at IR wavelengths.

1.2 The Dust Cycle

Since dust is formed from the heavy elements in the gas phase, we can follow the evolution of dust by following the evolution and origin of the chemical elements (Tinsley 1980; Talbot & Arnett 1972; Whittet 2003; Tielens 1998; D98; Edmunds 2001 - hereafter E01). Stars are born and nuclear processing occurs and as they die, they inject more elements and dust into the ISM. This leads to an increase in the

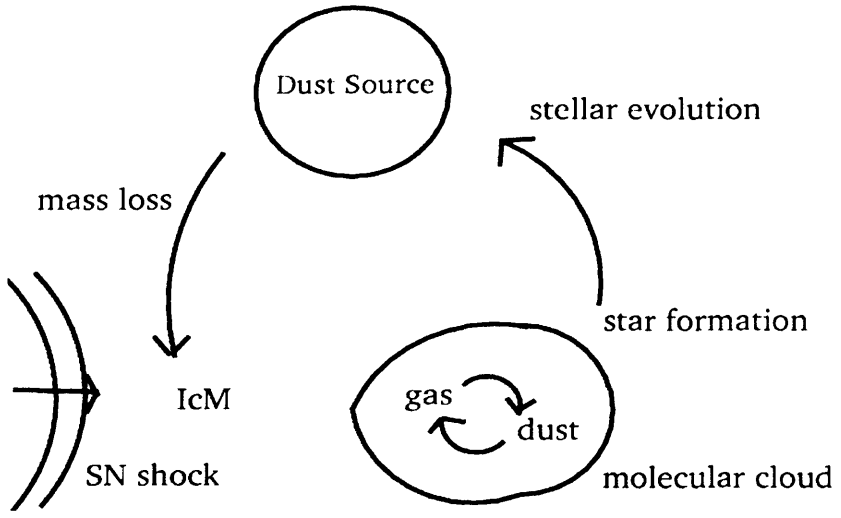

Figure 1.4: Schematic of cosmic dust cycle. Dust forms in the outflows of evolved stars, is injected into the ISM where it is subsequently processed by mantle accretion in dense clouds and destruction from supernovae shocks in the intercloud medium (IcM). Dust is then destroyed by new star forming regions which occur in dense molecular clouds. This figure is adapted from the schematic in Tielens & Allamandola (1987).

overall heavy element abundance (or metallicity) with time of successive star populations. Recent dust models have attempted to understand the evolutionary cycle of dust (Dwek 1998; Tielens 1998; E01) but there can be no real advancement whilst there still exists inherent uncertainties over dust sources, composition, destruction and the dependence of dust production on metallicity evolution.

Figure 1.4 shows a schematic of the cosmic dust cycle. Grains condense in the atmospheres and ejecta of evolved stars (red giants and supernovae) and replenish the ISM. The injected grains can provide a core to accrete mantles in dense molecular clouds and some grains are destroyed by passing supernova shocks. The next generation of stars is formed in the molecular clouds which destroy some of the dust grains.

In Sections 1.3.1 & 1.4.1, the possible sites of origin of dust grains are briefly

discussed.

1.2.1 Grain Growth

Grains can increase their mass by coagulation and/or mantle growth. Icy mantles accrete on the dust grains in dark molecular clouds ($n_H \geq 10^3$ cm^{-3}) either by chemical absorption or by freezing onto the grains (Tielens 1998; D98; E01; Whittet 2003; Draine 2003). Both processes become more efficient in higher density environments. The timescales for coagulation depends on the timescales for grain collisions, which in turn depends on the surface area of the grains, the grain velocity and the number density of grains. For a cloud of density 10^3 cm^{-3} and typical velocity ~ 0.1 km s^{-1}, the timescale is $\sim 3 \times 10^6$ yrs (Whittet 2003). The timescale for mantle growth depends on the surface area of the grains, grain velocity and the sticking coefficient of the absorbed material. With the same cloud parameters, mantles are accreted onto grains on timescales of 1 - 10 Gyr. Mantles can significantly increase the dust mass in cold, dark clouds.

1.2.2 Destruction

Dust is mainly believed to be destroyed by high velocity supernovae shocks (Tielens 1998, D98; Draine 2003) which compress, heat and accelerate the swept up gas, resulting in partial or total vaporisation of grains. The shocks move outwards and propagate through large volumes of gas during their evolution with speed dependent on the density of the surrounding gas. Dust is therefore destroyed more efficiently in the diffuse phases of the ISM rather than the dense clouds. The main destructive mechanisms from SNe shocks are due to grain-grain collisions and thermal sputtering (the removal of surface atoms by high velocity gas and dust). In head on grain-grain collisions between identical grains, complete vaporisation could occur (Draine 2003)

with most grains shattering and producing a smaller population in the ISM. Larger grains will fare better due to larger mass and a lower abundance of similar size particles. In a fast shock, sputtering is thought to be the most dominant destructive process (Jones et al. 1994; Dwek 1998; 2004), with almost complete destruction for shock velocities ≥ 200 km s^{-1} (Jones et al. 1994; 1997). Icy mantles can be removed from the grain via thermal sublimation when the grains reach temperatures > 100K (Draine 2003).

Evidence for grain destruction by supernova shocks is seen in depletion levels; as expected, there are fewer depleted elements in the diffuse phase than in dense clouds where SNe shocks are not as efficient at destroying dust (Whittet 2003). The timescales for destruction via supernova shocks is given in McKee (1989) and Jones et al. (1997). Using average shock velocities, supernova rates and the density of the warm phase of the ISM, dust destruction is thought to occur on timescales of $0.1 - 0.8$ Gyr. This may be an underestimate since the extent of the destruction by supernova shocks has recently been shown to be controversial (Gray & Edmunds 2004). Their work showed that sputtering is less efficient than originally thought, even at optimum energies (although this may be due to differences in the parameters used in the different models). Their work also showed that collisions may lead to grain growth since many incident particles are actually stopped by the grain and absorbed. Destruction processes are not well understood at the current time.

1.3 On the Origin of Dust - Stellar Winds

Astronomers in the early 1900s began to classify stars by their luminosity, effective temperature and mass using available observations. They found that when placed on the Luminosity-Temperature (L-T) plane, the locations of individual stars re-

vealed information about their evolution histories and mass loss rates. This relation is shown on a schematic representation of the Hertzsprung-Russell (HR) diagram in Figure 1.5 named after the two astronomers who independently discovered the relationship. One of the suprising results from this analysis was that not all of the L-T plane is populated. Instead stars are seen to occupy certain regions. Most of the stars lie on a narrow band running diagonally from hot bright stars to relatively cool ones known as the Main Sequence (MS) region which represent stars burning hydrogen in their cores. The H burning stops in the core and continues in a shell and the star leaves the MS, moving towards the red giant branch (RGB). Massive stars evolve towards the upper right corner of the diagram and may become supergiants (SGs) as they are cooler and bright. Supernovae are the endpoints of the bright, massive stars which occur along the end of this branch. White dwarfs, as the endpoint of cooler low mass stars, occupy the lower left corner.

The outflows from stars are extremely important in injecting dust and chemical products into the ISM. Such winds also crucially affect the evolution and subsequent fate of a star (particularly in massive stars where up to 90% of the mass of the progenitor could be lost in stellar winds (Maeder 1992)). The amount lost is dependant on the driving mechanisms contributing to the pressure on the material outwards from the star and is classified by a mass loss rate ($\dot{M}$) and terminal velocity (v_∞, the velocity of the wind at a large distance from the star). These parameters can be derived from observations of stellar spectra. The mass loss rates for different stellar phases are given in Table 1.1. These phases include O/B type stars which are the early phase of hot, massive stars. Theoretical models show that these massive stars will pass through an intermediate stage before their deaths, corresponding to either a Luminous Blue Variable (LBV) phase where the outer layers are stripped by fast winds, or for lower mass stars, a red supergiant phase. The higher mass stars may

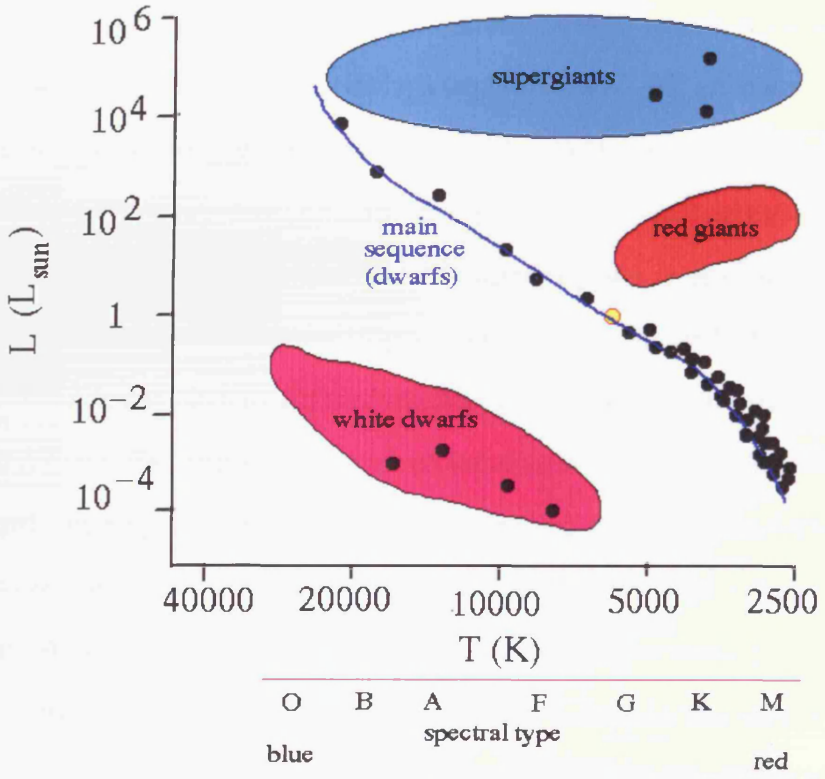

Figure 1.5: Schematic of the Hertzsprung-Russell diagram courtesy of the Department of Astronomy at University of Washington. This picture was taken from lecture resources at *http://www.astro.washington.edu.* Not all of the L-T plane is populated, instead stars are seen to occupy certain regions. The current position of the Sun is shown by the yellow circle on the Main sequence.

Stellar Type	$M_*(M_\odot)$	$L(L_\odot)$	$T_{eff}(K)$	$\dot{M}(M_\odot\ yr^{-1})$	$v_\infty(km\ s^{-1})$
AGB	$0.6 - 8$	$10^3 - 10^4$	2500	$10^{-8} - 10^{-4}$	5 - 25
RG/SGB	$8 - 50$	$10^2 - 10^4$	4000 - 20,000	$10^{-6} - 10^{-4}$	10 - 200
O/B	30 - 100	10^6	20,000 - 40,000	10^{-6}	2000
WR	30 - 100	$10^4 - 10^6$	30,000 - 50,000	$10^{-5} - 10^{-4}$	700 - 2500
LBVs	> 40	$10^6 - 10^7$	20,000	$10^{-3} - 10^{-1}$	200

Table 1.1: Summary of wind properties of stars in different phases of their evolution during the Asymptotic Giant Branch (AGB), Red Giant and Supergiant Branch (RG/SGB), Wolf-Rayet (WR) and Luminous Blue Variable (LBV) phases. The range of values were collated from Gomez (2004), Lamers & Cassinelli (1999) and Crowther (2000).

evolve into a Wolf-Rayet star (WR) after losing most of the outer layers via mass loss in the previous phase. Stars with mass $M_* < 8\ M_\odot$ will evolve onto the cool, Asymptotic Giant Branch (AGB) phase.

The individual phases of low mass stars, particularly their later stages are reviewed further in Chapter 2. Massive stars are also discussed further in Chapter 6.

1.3.1 Dust Formation in Stars

There are many observations which provide evidence for dust grain formation in stellar outflows: Infra-red emission around red giants, planetary nebulae, Wolf-Rayet stars and carbon stars. Indeed, stellar winds are thought to be the most important contributors to stardust into the ISM (Whittet 2003; Jones et al. 1997; Draine 2003). The dust around oxygen-rich red giants is characterised by a 10 μm silicate emission feature in their spectra, due to the Si-O bond. Around some IR bright stars, this feature is seen in absorption and suggests the presence of crystalline silicates (Draine 2003; Kemper et al. 2004). The correlation between the spectral features and stellar type suggests there is a correlation between the mass loss rates and the condensed dust (Waters 2003). In IR stars, emission features from amorphous silicates are present. Around IR stars with the highest mass loss rates, crystalline silicates and

olivine (molecules consisting of Mg, Si, Fe and O) features are seen. Around carbon stars the 10 μm Si feature is not present but there is a feature at 11.3 μm due to SiC. Meteorites provide evidence that grain formation occurs in outflows from evolved stars, since they contain isotopic anomalies of heavy elements thought to be nucleosynthesised in such stars (Whittet 2003).

There is no question that stellar winds are responsible for contributing dust to the interstellar budget. The question is *how much?* The chemistry of dust formation in stellar outflows is very complex (Salpeter 1974; Yorke 1988) and current models cannot realistically describe grain formation in such a dynamic environment. The majority of work has assumed that the formation of solids from a gas in stars can be described using classical nucleation theory (Salpeter 1974; Dominik et al. 1993; Gail & Sedlmayr 1999). Condensation of a species X occurs when its partial pressure[1] in the gas exceeds its vapour pressure in condensed phase, representing a transition between phase boundaries (Salpeter 1974; Whittet 2003). Subsequent particle growth occurs via random encounters leading to cluster formation. Chemical reactions will further assist cluster production (Salpeter 1974). The rate of grain growth will therefore depend on the temperature, T_g and pressure, P_g of the gas and the condensation temperature of a species, T_c. The optimum conditions for nucleation are thought to occur in the range $10^{-8} \leq P_g(Pa) \leq 10^5$ and $T_g \leq 1800$K (Salpeter 1974; Yorke 1988). This gives very strict restrictions on where nucleation can occur and this is thought to be satisfied in giant atmospheres at certain stages of evolution. Figure 1.6 shows when these conditions are thought to be reached. The strange shape for carbon is due to the differences in the available gas phase molecules at different pressures, e.g. at low pressures carbon is mainly in the form

[1]The pressure exerted by individual components of a gas if they are independent of the other components e.g. the total pressure of a gas is the sum of the partial pressures of the gaseous components which all have the same temperature $P_t = n_t kT$ where n is the sum of the number of moles.

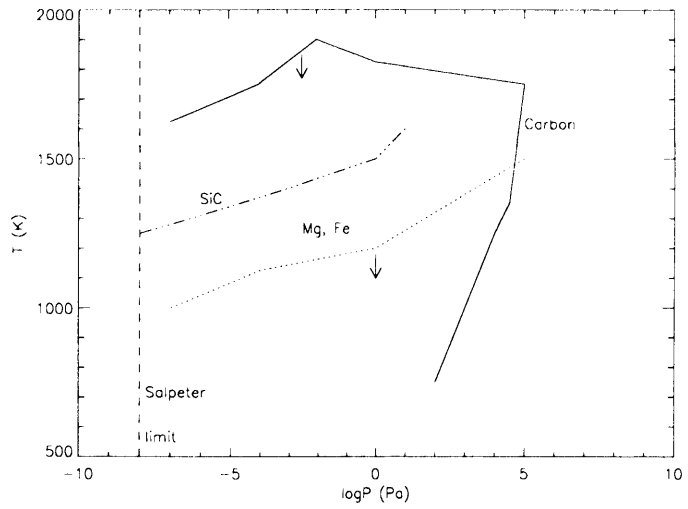

Figure 1.6: The nucleation conditions as adapted from Yorke (1988) and Salpeter (1974). The arrows show the direction in which nucleation conditions are satisfied for the elements shown. Carbon dust is likely to form in a gas with pressure range $-5 < logP(atm) < 5$ and temperatures below 2000K.

C, C_2 and C_3 whereas at high pressures hydrogenation occurs with the addition of H atoms (Salpeter 1974). At low pressures, dust does not condense since grain growth is inefficient.

The dominant component of dust formed will depend on the relative abundance of carbon or oxygen. The most abundant heavy molecule in stellar atmopsheres is CO, which is extremely volatile and does not condense into a solid. All of either the carbon and oxygen is locked up in the gas phase in CO and the most abundant element will be left to condense into dust. For environments with C/O < 1, we will expect oxygen-rich grains (silicates) and vice versa. From Figure 1.6, carbonaceous dust grains are able to form in gas temperatures $T_g \leq 1800$K . For silicates to form via condensation we require temperatures below 1500K (Salpeter 1974; Bode 1987; Whittet 2003).

Dust production in stars is hard to quantify observationally. Depending on the star's composition (whether it is carbon rich (C star) or oxygen rich (M star)) and

what fraction of a stellar population is in these stars, there will be a difference in the returned fraction of carbon and silicate type grains to the ISM. The problem compounds when O rich stars may become C rich as they ascend the AGB whilst undergoing pulsations which dredge up freshly synthesised carbon from the stellar core (Marigo et al. 1996). IRAS observations (Molster et al. 2001) and observations of AGB stars in the Large Magellanic Cloud (Trams & van Loon. 1999) show a high degree of silicate dust in C stars and it is yet unclear whether this is due to silicate formation in a previously O rich star or due to an O rich binary companion (Molster et al. 2001). It appears that the scenario is not as clear cut as once thought.

The composition of the dust observed in the ISM is therefore dependent on the heavy elements in the stellar atmopsheres and the mass loss rates during the final stages of the star's evolution. Observations of mass loss rates from stars suggest that they contribute 86 – 97% of the total dust mass injected from astrophysical sources (Whittet 1992; 2003).

1.4 On the Origin of Dust - Supernovae

Supernovae (SNe) represent the death of stars and are exceptionally bright explosions. There are two different spectral types: Type I and Type II which depend on the criterion of whether their spectra contain hydrogen lines (Type II) or no hydrogen (Type I). Type II SNe are produced from the collapse of massive stars ($M > 8\ M_{\odot}$), which evolve on timescales of a few million – 100 million years (Schaller et al. 1999a). Type I SNe consist of mainly two distinct sub-classes, Type Ia and Type Ib/c. The formation mechanisms for these explosive types are very different but all share the absence of hydrogen in the spectra. Type Ia's are seen in all types of galaxies (Longair 1994) but Type Ib/c's are seen exclusively in spirals suggesting

that the latter type are the result of explosions of relatively young population of stars. The stars which end up as Ia explosions would not produce SNe if they were single stars but are triggered to explode due to the mass transfer from a binary companion onto the surface of a white dwarf. The white dwarf accretes mass until exceeding the Chadrasekhar mass, by which time, explosive nucleosynthesis is ignited in the core (Panagia 2000). The explosions in Ia SNe are extremely luminous, fairly homogeneous as a class and are ideal candidates for standard candles in determining cosmological distances.

Type Ib/c SNe must be the endpoint of more massive stars since they are found only in young populations in spiral galaxies, suggesting progenitor masses above 5 $M_{\odot}$. This suggests that they are a sub-class of core collapse SNe (as in Type II SNe) which must remove the outer layers of H-rich material before the explosion. Massive stars in binary systems are often seen to lose most of the envelope before going SNe due to mass transfer (e.g. the possible evolution of the massive star η Carinae).

SNe are important astrophysical processes. Such events inject highly metal rich material (> 1 $M_{\odot}$, Woosley & Weaver 1995) and about 10^{51} ergs of kinetic energy into the surrounding medium. The blast waves produced by the explosion sweep out into the ISM and are powerful sources of X-ray and radio emission for thousands of years after the original event. During the last 2000 years, 9 events of SNe have been recorded (Panagia 2000) implying a rate of approximately 5 SNe per 1000 years. However, some SNe may not be bright enough or too far away and some may also be obscured by dusty clouds. If we assume that 10% of all SNe events are close enough/bright enough to be observed, then a more realistic rate for the Galaxy is 1 every 20 years (Panagia 2000).

The radio emission from SNe is thought to arise from acceleration of relativis-

tic electrons and compression of the strong magnetic fields both of which produce non-thermal synchrotron emission. The variation of the radio flux with frequency depends on the energy spectrum of the electrons, and is a power law described by spectral index $\nu^{-\alpha}$. The energy spectrum of electrons depends on the density of the ambient material (ISM or the stellar wind of the previous massive star phase) which is heated by the blast wave of the SNe. For shell like SNe, observations show steep spectral indices, $\alpha > 0.5$ (Longair 1994). Panagia (2000) notes that observationally, Type Ib/c have flatter spectral indices (i.e. $\alpha < 0.5$) than Type II suggesting that the former case is decelerated less by the ambient material i.e. the density of the surrounding medium is lower than in Type II, where the stronger shocks produce more radio emission. Type Ia have little radio emission (Panagia 2000) and hence flatter spectral indices (weaker shocks) which may be due to lack of prior stellar wind from the low mass stars which result in this type of explosion.

The evolution of a shell-like SNR follows a certain prescription (Figure 1.7, Chevalier 1977). The SN blast wave runs ahead of the expanding gas in a spherical shell and compresses/heats the surrounding material, producing hot X-rays. The shock front begins to decelerate as it ploughs into the medium and matter inside begins to pile up at the interface creating a contact disontinuity. A shock wave is then formed on the inner edge of the sphere and propogates backwards and is called the reverse shock (Chevalier 1977). Rayleigh-Taylor instabilities form between the dense shell and the ambient medium. The supernova ejecta will pass through 4 distinct phases (Chevalier 1977; Longair 1994; Reynoso et al. 1997). These are (i) rapid expansion phase, where the ejecta move freely through the surrounding ISM; (ii) adiabatic phase (also known as the Sedov phase) where the shockfront begins to decelerate as swept up interstellar material begins to dominate the mass; (iii) radiative phase, where the blast wave cools significantly and (iv) dissipative phase

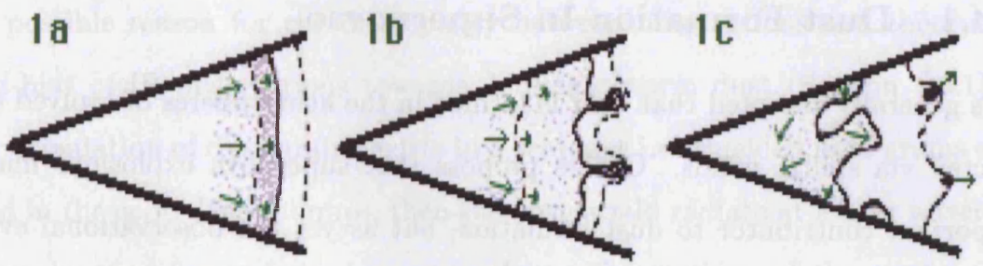

Figure 1.7: From Chevalier 1977. Schematic of the model of an early supernova remnant. The smooth shell interacts with the surrounding ISM, forming a reverse shock wave. Rayleigh-Taylor instabilities (fingers) form due to the flow of the two different density regions into each other. The dashed lines represent the shockfronts, solid lines represent contact discontinuities and the arrows repesent direction of motion. The hatched regions represent compressed ejecta whilst the ISM is plain.

in which the shock disappears and the SNe has merged with the surrounding ISM. These phases are characterised by a power law of radius of blast wave with time, $R \propto t^m$, where m is the expansion parameter. In the earliest stages of evolution, $m = 1$ as the mass swept up is much less than the ejected mass and so the ejecta are not decelerated as it moves outwards. As the swept up mass becomes larger, deceleration becomes stronger and m decreases to ~ 0.4 (this marks the transition into the Sedov phase). Interaction of the blast wave with a higher density medium will result in stronger deceleration and stronger radio emission. Alternatively, a more rapid expansion in a low density medium can become radio bright later on when the swept up mass begins to decelerate the shock (Bhatnagar 2001). If the shock is expanding into a medium of inhomogeneous density (i.e. a prior stellar wind with density profile $\rho \propto r^{-2}$), the shock slows as it enters the medium. The expansion parameter in this case is $m = 0.67$ when the evolution reaches the Sedov phase.

1.4.1 Dust Formation In Supernovae

It is generally accepted that dust is formed in the atmospheres of evolved stars and ejected via stellar winds. Others propose that supernova explosions must be an important contributor to dust formation, but as yet the observational evidence is weak.

Some major proponents of SNe as the dominant source of dust injection into the ISM include Dwek & Scalo (1980), Kozasa et al. (1989; 1991), D98, Todini & Ferrara (2000; hereafter TF01), Nozawa et al. (2003), but there was little observational evidence to support these models. Infra-Red observations of young supernova remnants with IRAS and ISO found only 10^{-3} and 10^{-4} $M_{\odot}$ of dust in Tycho and Kepler SNRs (Douvion et al. 2001b) and 10^{-4} $M_{\odot}$ in Cassiopiea A (Douvion et al. 2001a). Observations of SN1987A suggest a similar amount of dust (Dwek et al. 1992; Wooden 1997) although the elemental depletion seen in the ejecta suggests this could be a lot higher (Dwek 1992). This discrepancy could be explained if a colder population of grains exists and survives in dense clumps (Lucy 1991) since the estimated mass depends on the filling factor of the elements. The spatial correlation between the IR and the optical emission for the Tycho and Kepler SNRs (thought to arise from shock heating of surrounding circumstellar material (CSM)) implies that the dust is probably circumstellar in origin and not formed in the ejecta. The dust in Cas A was attributed to SN ejecta dust but the small amount observed is not nearly enough to prove significant dust formation in SNe. However, theoretical models of nucleation of dust grains in supernova gas suggest condensation efficiencies (the efficiency of the gas forming dust from the available heavy elements) of ~ 0.1 (Clayton et al. 2001) and $\sim 0.2 - 0.4$ (TF01) from a stellar population of supernovae. The model presented in TF01 concludes that $\sim 0.1 - 0.9$ $M_{\odot}$ of dust is formed in each Type II SNe regardless of initial metallicity.

A possible reason for the discrepancy between observations and theory is due to the bias of IR observations towards detecting warm dust (Section 1.6.1). If a colder population of dust grains exists in a remnant i.e. shielded dust grains or dust formed in the cool, dense clumps, then the dust would radiate at longer wavelengths in the submm regime. Indeed, recent submm observations of the young galactic SNR Cassiopeia A have shown that a colder population of dust grains exists in the remnant with an estimated $2 - 4$ $M_{\odot}$ of dust (Dunne et al. 2003) - four orders of magnitude more than detected by mid IR observations. If Cas A's progenitor star was 30 $M_{\odot}$, it would eject around 5 $M_{\odot}$ of heavy elements in the ejecta (Woosley & Weaver 1995), implying a condensation efficiency of 0.5 - 0.8. This result will be discussed more fully in Chapter 4 along with further evidence for significant dust formation in supernovae.

1.5 The Dust Budget Crisis

The injection rates of the above sources of dust into the interstellar medium are listed in Table 1.2. This Table has been reproduced from Whittet (1992) with revised values from Whittet (2003) included in brackets. The total minimum contribution from stars is 86% compared to a maximum of 14% from supernovae. There are two problems with this current understanding, which are desribed below.

1. Stars do not form enough dust to replenish the ISM

If 1% of the Galactic ISM mass is dust, using the revised stellar wind dust injection rate from Whittet (2003) in Table 1.2, the dust replenishing timescale is (Jones et

Stellar Type	$\dot{M}_G$	$10^{-3}[\dot{M}_G]_d$	%
M giants	2.0	14 (3)	37
OH -IR stars	2.0	14 (3)	37
Carbon stars	1.0	7 (0.2)	19
M supergiants	0.2	1.4 (0.1)	4
Planetary Nebulae	0.3	0.1	0.4
WC stars	0.01	0.07 (0.06)	0.2
Total stars	5.5	36.4 (6.3)	97 (86)
Novae	0.003	0.02	0.05
Supernovae	0.1	0.7? (1?)	2? (14?)

Table 1.2: Taken from Whittet 1992 and 2003. The table shows estimates of integrated mass loss rates in $M_\odot$ yr^{-1} for stars injecting dust into the ISM. Columns are (1) stellar type (2) total mass loss rate (3) dust mass loss rate calculated by $[\dot{M}_G]_d = Z_d[\dot{M}_G]$ where Z_d is the dust-gas ratio in the outflow (=0.007 here except for planetary nebulae which has observed values of 4×10^{-4}). Bracketed values show updated results from Whittet 2003. These are included since they give a maximum range from the current observations.

al. 1994; 1997):

$$t_{rep} = \frac{\text{dust mass}}{\text{injection rate}} = \frac{5 \times 10^9 \text{ M}_\odot \times 0.01}{6 \times 10^{-3} \text{ M}_\odot \text{yr}^{-1}} \sim 10^{10} \text{yrs}.$$

Dust is believed to be destroyed by supernova shocks and impacts on timescales $t_{des} \sim 4 - 6 \times 10^8$ yrs (Jones et al. 1997) which suggests that $t_{rep} \leq t_{des}$ i.e. there is not enough time to keep replenishing interstellar dust before it is destroyed. However, the dust mass observed in our Galaxy contradicts this analysis. This can be accounted for if AGB stars are much more efficient at producing dust than currently thought (by a factor of > 10) and/or destructive processes are much less efficient (recent work suggests that dust destruction rates are not as high - Gray & Edmunds 2004). The accretion of mantles has been proposed to explain this discrepancy (Jones et al. 1994) yet at least a first generation of dust grains is required in the first instance for the mantles to accrete onto. To make up for the dust discreprancy in the ISM without SNe we require a mantle mass injection rate

of ~ 0.02 $M_\odot$ yr^{-1}, which is five times as much as the dust core rate. This implies a small number of cores with large mantle mass.

2. AGB Stars evolve too slowly to form dust at high redshifts

Recent blank field submillimetre surveys and observations of distant quasars (Bertoldi et al. 2003) have discovered a population of extremely dusty objects at high redshifts implying that dust is present in the Universe at $z > 4$ (Smail et al. 1997; Eales et al. 2003; Ivison et al. 2003; Isaak et al. 2002). Figure 1.8 (a) shows an image of the high redshift sub-millimetre Universe at 850 μm with SCUBA and (b) shows the MAMBO observations of a high redshift QSO at $z = 6.2$. The sub-mm image is directly observing star formation heating dust in galaxies when the Universe was less than 1/10th of its present day age (Hughes et al. 1998). These distant galaxies have dust masses $> 10^8$ $M_\odot$ but it is difficult to identify these sources unambiguously since the large beam size of SCUBA does not always allow for correct identification with radio images. This has recently changed with the advent of the new Space IR telescope SPITZER. Using follow-up observations of the SCUBA fields, some of the sub-mm sources were recently detected (see press release: *http://outreach.jach.hawaii.edu/pressroom/2004-scubaspitzer/*). The lack of X-Ray detection of sub-mm sources in two deep fields imply that they are not powered by Active Galactic Nuclei (AGN) but are in fact extremely dusty starburst galaxies (Almaini et al. 1999; Waskett et al. 2003). These recent observations indicate a significant amount of dust is present in the high redshift Universe due to rapid star formation, hence dust could play an important part in the early evolution of galaxies.

However, it is difficult for the dust to have originated from the stellar winds of stars in such short timescales. The required cycle to produce dust in stars begins

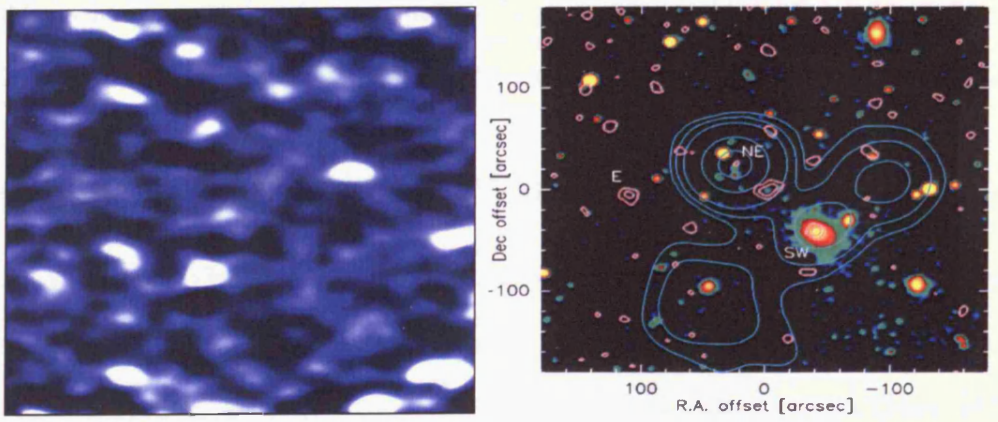

Figure 1.8: (a) SCUBA image of dusty galaxies in the Hubble Deep Field at high redshifts at 850 μm (taken from Hughes et al. 1998). Half of the objects in the entire image are beyond redshifts of 1 (Sarjeant et al. 2003). (b) Image of high redshift QSO at reshift 6.2 (taken from Bertoldi et al. 2003). The image is centered on the optical counterpart of the QSO with red-white contours of the MAMBO observations at 1200 μm and blue contours representing the emission at 21cm (VLA). The mass of dust in the QSO is estimated to be 10^8 $M_\odot$.

with enrichment of the ISM from the first population of rapidly evolving SNe, the incorporation of these elements into star formation and the evolution of the stars to the right atmospheric conditions before significant dust production can occur. If there is little or no dust formation occuring in supernovae then it is difficult to understand where the high redshift dust originated from. These problems suggest that dust formation in supernovae is required to explain both high redshift and present day observations. SNe dust would provide a direct source of dust in primordial systems within a few Myrs. This would comfortably explain the amount of dust seen in high redshift observations and bring dust replenishing and destructive timescales together.

1.6 Observing Dust

Dust grains absorb ultraviolet (UV) and optical photons which heat up the grain causing it to re-radiate the energy at longer wavelengths, although dust grains do not radiate as a perfect blackbody. The grains do not absorb energy at all wavelengths and the emission is not characterised by a blackbody but by the frequency dependence of the emission efficiency of the grains. If the grain is in thermal equilibrium, the efficiency with which a photon is absorbed Q_{abs}, is the same as the efficiency of the energy emitted Q_{em}. The efficiency varies with wavelength as a power law (Hildebrand 1983), $Q_{em} \propto \lambda^{-\beta}$ (or $\propto \nu^{\beta}$) where β is the wavelength dependence index ($\beta = 2$ for crystalline grains whereas $\beta < 2$ for more amorphous grains (Draine & Lee 1984; Whittet 2003)). We can observe grains in the submillimetre regime where the grain sizes are much smaller than the wavelength; $a \ll \lambda$ so $Q(\lambda) \ll 1$. In this long wavelength limit ($h\nu \ll kT$), the intensity drops off steeply and $S_\nu \propto \nu^{2+\beta}$. The Spectral Energy Distribution (SED) of the grains is given by a modified blackbody which is denoted by "greybody" (where in this work we take a greybody to represent a modified blackbody; this is not to be confused with dust grains that have a grey opacity i.e. $\beta = 0$),

$$S_\lambda = Q_{em} B(\lambda, T) \tag{1.1}$$

where $B(\lambda, T)$ is the Planck Function:

$$B(\lambda, T) = \frac{2hc^2}{\lambda^5} \frac{1}{exp\,[hc/\lambda kT] - 1} \quad or \quad B(\nu, T) = \frac{2h\nu^3}{c^2} \frac{1}{exp\,[h\nu/kT] - 1} \tag{1.2}$$

The wavelength corresponding to the peak in the emission spectrum is given

when $dS/d\lambda = 0$

$$\lambda_p = \frac{2900}{T}\left(\frac{5}{5+\beta}\right).$$

For $\beta = 0$ this is the normal form of Wiens Law. For $1 < \beta < 2$ and $10 < \lambda < 1000$ μm, the peak in the spectrum occurs at temperatures < 100K.

The temperature of a dust grain depends on the exchange of energy with their environment; generally the equilibrium dust temperature is determined by the interstellar radiation field (IRSF) (Whittet 2003). The power absorbed by a spherical grain is given by

$$W_{abs} = c(\pi a^2)\int_0^\infty Q_{abs} u_\lambda d\lambda \tag{1.3}$$

where u_λ is the energy density of the ISRF. The power radiated is

$$W_{rad} = 4\pi(\pi a^2)\int_0^\infty Q_{em} B_\lambda(T_d) d\lambda \tag{1.4}$$

In equilibrium, $Q_{abs} = Q_{em}$ and $W_{abs} = W_{rad}$ so we can replace by $Q_\lambda \propto \lambda^{-\beta}$ and equate the two expressions. This gives (Whittet 2003)

$$T_d \sim T_{IRSF} w^{1/5}$$

where T_{IRSF} is represented by a blackbody with temperature $\sim 10,000$K and w is the dilution factor ($\sim 10^{-14}$). Therefore an average interstellar grain has an equilibrium temperature of $T_d \sim 15$K.

However as discussed in Whittet (2003), this assumption is only valid when (i) the total kinetic energy of the grain is large compared to the energy received by the absorbed photon and (ii) when the absorbed energy is distributed throughout the whole grain on shorter timescales compared to photon emission. For smaller grains, these assumptions may no longer be valid and quantum events become more

important (e.g. surface effects (Krugel 2002)). The internal heat energy of a grain from lattice vibrations is proportional to $a^3T_d^4$ (Whittet 2003, p.202). If the grain absorbs a single photon then this gives a relationship between the initial and final temperatures. For classical grains with $a > 0.05$ μm, the change in temperature is small $\Delta T < 1$ K. For smaller grains however, $\Delta T \geq 10$ K. Smaller grains therefore radiate at shorter IR wavelengths whereas colder grains predominately radiate in the FIR and sub-mm.

1.6.1 Estimating Dust Masses

IR observations at $\lambda < 100$ μm are only sensitive to warm dust at T > 30K. The luminosity varies with temperature as $L_d \propto T^{4+\beta}$ and so a small amount of warm dust emits much more than cold dust. However, the dust mass is dominated by the cold dust. Since IR observations are only sensitive to dust with temperatures > 30K, we require observations in the sub-mm regime. If cold dust is present, these observations will detect a small rise in the long wavelength tail. Observations with the Sub-mm Common User Bolometer Array (SCUBA) on the James Clerk Maxwell Telescope (JCMT) in Hawaii at 450 and 850 μm are ideal to detect such cool dust components.

To determine the dust mass from sub-mm fluxes, we can assume that the grains are spherical with radius a such that the grain volume is given by $4/3\pi a^3$, and they are made from material with density ρ. The mass of a cloud of N dust grains is given by

$$M_d = \frac{4}{3}\pi a^3 N \rho \tag{1.5}$$

The radiative transfer equation with negligible background is $I_\nu = B(\nu, T)(1 - e^{-\tau_\nu})$ where τ is the optical depth. In the optically thin limit ($\tau \ll 1$), the solution

is $I_\nu = B(\nu, T)\tau_\nu$. The optical depth to the object is $\tau_\nu = \pi a^2 N_d Q_\nu$ where N_d is the column density of dust grains (N/area of cloud), πa^2 is the geometrical cross section of the grains and Q is the emissivity. The flux density from a cloud of dust grains in thermal equilibrium at T is therefore given by $S_\nu = I_\nu \Omega$, where Ω is the solid angle:

$$S_\nu = N \frac{\pi a^2}{D^2} Q_\nu B(\nu, T) \tag{1.6}$$

where D is the distance to the cloud. Rearranging the equation in terms of N and substituting into Equation 1.5, gives the total dust mass of the cloud as:

$$M_d = \frac{4a\rho D^2 S_\nu}{3Q_\nu B(\nu, T)} \tag{1.7}$$

The grain emissivity is poorly understood with estimates of a and ρ not well known observationally. These parameters can be grouped together to give the dust mass absorption coefficient, κ

$$\kappa_\nu = \frac{3Q_\nu}{4a\rho} \tag{1.8}$$

such that the mass of dust is given by:

$$M_d = \frac{D^2 S_\nu}{\kappa_\nu B(\nu, T)} \tag{1.9}$$

The effects of particle size, shape and composition on the value of the dust mass are discussed in Whittet (2003).

With an accurate value of κ, we should be able to determine the total mass of dust in a cloud to a good approximation. However, since κ is normally extrapolated from observations of Q in the mid-far IR, the value is very uncertain. This leads to an immediate uncertainty in the value of κ since the extrapolation depends on the range of β ($\kappa \propto \nu^\beta$) as well as the usual uncertainties in the observations. James et

al. (2002) determined the value of κ in the sub-mm regime by using galaxies with measured metallicities and determining their dust masses from the sub-mm emission obtained with SCUBA. They assumed that a constant fraction of metals condenses into dust in all galaxies and so estimated $\kappa_{850\ \mu m}$ to be 0.07 ± 0.02 m^2 kg^{-1}. This is consistent with extrapolation from the 100μm value of κ (Hildebrand 1983; Draine & Lee 1984) with a $\beta = 2$ power law. In this case, κ at other wavelengths is given by (in terms of wavelength)

$$\kappa = 0.07 \left(\frac{\lambda_0}{\lambda} \right)^{\beta}$$

where $\lambda_0 = 850$ μm. However, higher values of κ have been observed in certain environments e.g planetary nebula (Amure 2003) which suggests that the dust grain properties are affected by their surroundings and evolution. Studies measuring the optical properties in laboratories have also found higher values of κ suggesting that the dust in some environments may emit more efficiently than 'normal' interstellar dust. ISM dust studies suggest that κ is around $0.04 - 0.1$ m^2 kg^{-1} at 850 μm (Boulanger et al. 1996; Sodroski et al. 1997; Bianchi et al. 1998; James et al. 2002) which agrees with simulations of the optical properties of crystalline graphite and silicate particles given in Draine & Lee (1984). Other environments where the dust grain may not be so heavily processed (i.e. reflection nebulae, dark clouds and circumstellar envelopes) show higher values of $0.2 - 0.8$ m^2 kg^{-1} (Rowan-Robinson et al. 1986; Sopka et al. 1995; Amure 2003). Laboratory studies of 'fluffy' or fractal grains, amorphous particles rather than crystalline and agglomerates of smaller particles, show higher values still, with literature values ranging from $0.6 - 1.1$ m^2 kg^{-1} (e.g. Algadze et al. 1996). So for newly pristine dust, κ could be a factor of 10 higher than observations of normal interstellar dust suggests. The biggest uncertainty in our estimate of the dust mass is the value of the dust mass absorption coefficient.

1.7 Summary

This introduction has hopefully highlighted the importance of dust and our limited understanding of its most basic properties. Understanding how dust forms is necessary to understand cosmology and star formation, especially in the early Universe where our picture of dust grains may be very different to that of today's. I have summarised the current views and problems surrounding the issue of the origin of dust and have discussed the evolution of stars which may be responsible for polluting the Universe.

1.8 Thesis Outline

This thesis aims to understand *when* the conditions for dust formation are reached in stars and the *source* of dust at high redshifts. Chapter 2 gives an introduction to the current status of the field and estimates the condensation efficiency of dust in stars using published atmosphere and stellar evolution models. The chemical evolution equations with the detailed dust cycle from Edmunds (2001) are also presented. This model is modified to incorporate a time delay of dust yields from low mass stars and to determine the maximum redshift after which dust can be observed in the Universe for different star formation rates and cosmological parameters. In Chapter 3, the data reduction techniques used in the following chapters are outlined with a brief introduction to SCUBA data analysis. Chapter 4 uses these techniques to analyse the first sub-mm observations of the supernova remnants, Kepler and Tycho. The sub-mm emission is compared with the other wavelengths in Chapter 5 and we investigate the radial distribution of the emission. The possibility that iron whiskers are responsible for the sub-mm emission is also reviewed. In Chapter 6, arguments for and against a supernova origin of the dust are presented, along with

the first sub-mm observations of the massive star η Carinae. This is followed by the implications of the results of the thesis to the interstellar dust budget. Finally, Chapter 7 gives the conclusions obtained in this thesis and an outline of future work.

Chapter 2

Dust Production and Chemical Evolution

"Essentially every aspect of the subject needs further observational and theoretical study, so galactic [chemical] evolution will long be a fertile field for research."

B. M. Tinsley, 1980

2.1 Introduction

This chapter is concerned with determining the quantitative efficiency with which heavy elements ejected from stars are able to form dust. The questions posed and discussed are then: when are the conditions for dust formation reached in stars? What is the source of dust at high redshift? Is dust production dependant on metallicity? How much dust is present in high redshift galaxies and how will this affect observations? The aim of this chapter is to ask whether or not we can expect the build up of a significant amount of dust in the early Universe using our current understanding of stellar evolution and atmosphere models. The majority of work in

this chapter has been published in Morgan & Edmunds (2003).

2.2 Quantifying Dust Production in Stars

Unfortunately there is not yet nearly enough hard observational evidence to follow through the whole process of dust formation in stars so, in an attempt to investigate when nucleation conditions are reached in stars, we examine available extended atmosphere models for K and M giants (Plez et al. 1992a & 1992b, Hauschildt et al. 1999b, Brown et al. 1993). These models can be used to estimate the temperature and pressure in the gas out to a stellar radius where the visual optical depth has fallen to 10^{-6}. With the grids of temperatures, pressures and densities from these models, we can determine when the necessary conditions for dust nucleation are reached in the atmosphere. The atmospheric conditions depend on the mass of the star, M, its surface gravity ($g = \frac{GM}{R^2}$), and its effective temperature at the surface, T_{eff}. The published models assume spherical geometry with homogeneous stationary layers in local thermodynamic equilibrium (LTE) and use numerical codes to simulate the gas properties in stellar atmospheres (e.g. PHOENIX (Hauschildt et al. 1999a) with these models available from the website: http://phoenix.physast.uga.edu/NG-giant). Although this is not likely to give a realistic detailed description of conditions in real stellar atmospheres where pulsations, mass loss and inhomogeneities will surely exist, it will serve to make an estimate of the mean condition for the processes occurring, since better models are beyond the scope of this PhD.

Model atmospheres for C stars were obtained from Jörgensen et al. (1992) and an observational model (Harper et al. 2001) of the red giant AlphaOri is included for comparison (with T_{eff} = 3600K, M = 12 $M_{\odot}$, $log(g)$ = 0.0). The model P-T curves are shown in Figure 2.1 (a) for T_{eff} < 3000K, and Figure 2.1 (b) for

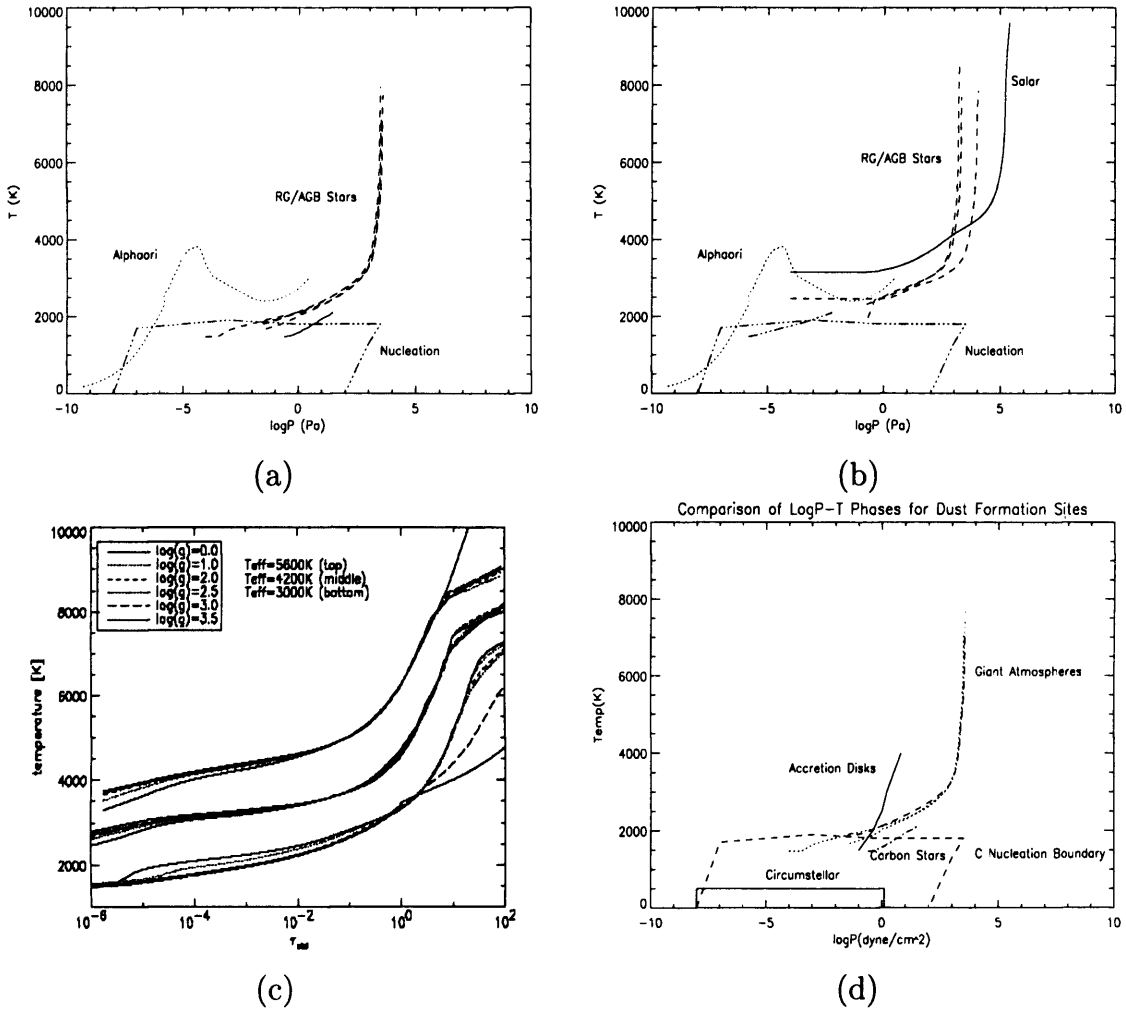

Figure 2.1: The gas properties of the model atmospheres with $T_{eff} \leq 3000K$ (a) and $T_{eff} = 3600 - 3800K$ (b) with the solar model added for $logT_{eff} = 5.5K$ (Hauschildt et al. 1999b). An empirical atmosphere (Harper et al. 2001) and the carbon nucleation boundary are included. Figure (c) shows the results from the modelling of extended atmospheres with the PHOENIX code taken from Hauschildt et al. (1999b). This suggests that only atmospheres with $T_{eff} < 4000$K will reach gas temperatures below 2000K. Figure (d) compares the average temperatures and pressures reached in different proposed dust formation sites, including circumstellar disks, binary accretion disks and stellar winds (K & M stars, Carbon stars). The accretion disk model is theoretical and is for a specific set of parameters only.

$T_{eff} = 3600 - 3800$K. They clearly show the models do not extend to the low gas temperatures observed in AlphaOri, and we will assume the boundaries do in fact extend downwards in a similar manner. It is also clear that as T_{eff} increases, the

likelihood of the gas temperatures reaching the nucleation boundary decreases as expected. Hauschildt et al (1999b) show for various values of $log(g)$, that only those atmospheres with $T_{eff} < 4000$K will reach gas temperatures below 2000K and hence attain C nucleation conditions (Figure 2.1 (c)). However, in order to reach the silicate nucleation boundary, we require $T_{eff} \leq 3000$K. As a summary, Figure 2.1 (d) shows the average properties of the gas in some proposed dust production sites. This includes stars, circumstellar disks around young stars (Bode 1988) and binary accretion disks (van Zadelhoff et al. 2001). The circumstellar disks around stars satisfy the conditions for dust nucleation but such disks are eroded on timescales of $\leq 10^6$ yrs, with no apparent ejection mechanism for the dust to escape.

These model atmospheres apply to stars with a given luminosity and temperature. The luminosity was calculated using Equation 2.1 and simply placed on a Hertzsprung-Russell diagram using their respective T_{eff} values (Figure 2.2).

$$L_* = 4\pi\sigma R_*^2 T_{eff}^4 \tag{2.1}$$

The stars do indeed correspond to the evolved stages expected, but for dust nucleation properties to be reached we require the stars to lie on or just beyond a late AGB phase (evolutionary tracks of solar metallicity, $Z_\odot = 0.02$, from Schaller et al. (1992)). It appears then that low - intermediate mass stars seen to produce dust using the arguments given here, only satisfy the conditions at the very latest stages of their evolution which is only a very small fraction of their life ($10^4 - 10^6$ years). This phase is the TPAGB (Thermally Pulsating Asymptotic Giant Branch) as described further in Section 2.2.1. We found that using the stellar evolution models from the the Padova group instead of the PHOENIX code (http://pleiadi.pd.astro.it) also gives the same conclusion. The stellar tracks for stars can reach lower effective temperatures for the same luminosities (Pols et al. 1995) depending on the opacities

of the ions, overshooting[1] and mixing parameters used. A recent study of these models suggest there is still more to be done in this area (Young et al. 2001). Further progress on new tracks given by this group using their new stellar evolution code, TYCHO should investigate how these properties affect the effective temperatures of stars and thus the dust conditions reached. From this simple argument, we assume,

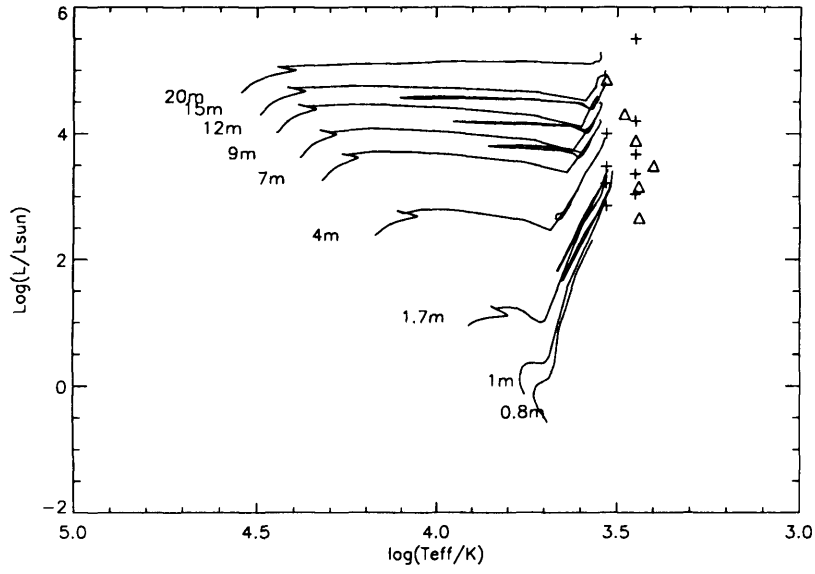

Figure 2.2: The HR diagram with added stars corresponding to the model atmospheres used which reach the dust formation stages. The triangles represent the K & M giants whilst the crosses represent the C stars.

in further sections, that only those stars with $T_{eff} < 4000K$ and which lie on this evolutionary branch are significant producers of dust (although this is actually a maximum limit since these are the conditions for carbon nucleation and we would expect to require much lower temperatures for the formation of silicate dust).

[1]This is a parameter which was added to the models to explain a variety of theoretical predictions which did not match observations e.g. the over-abundance of oxygen observed in TP-AGB stars and the phenomenon of 'dredge-ups' since overshooting allows the He rich shell to penetrate the CO core and cause a mixing of the nuclear products of the core to the surface. Adding overshooting to the stellar evolution models enhances the number of dredge-ups and the abundance of C and O in AGB stars (Herwig et al. 1999).

It is important to note that, at this stage of the thesis, we have ignored dust production in the atmospheres of stars with $M_i > 25\ M_\odot$. Observationally however, dust shells are seen around a class of massive stars which suffer large mass loss ($\sim 10^{-5}\ M_\odot\ yr^{-1}$) in the late stages of their evolution (Williams et al 1987; Marchenko et al. 2002). These are the Wolf-Rayet (WR) stars, which have three phases characterised by the dominant species of O, C and N in their spectra. Dust shells are only seen around the very cool, carbon rich WR (Marchenko et al. 2002; Dwek 1998), and will therefore contribute to the production of carbon dust in the ISM. Could this be a significant dust formation site? Recent observations of a WR binary system have shown that the formation of dust in these stars may be increased via wind-wind interactions with at least 20 per cent escaping and thus enriching the ISM (Marchenko et al 2002). Their results find a total dust mass of $2.8 \times 10^{-5}\ M_\odot$ which coupled with the mass loss rate gives an estimate of the condensation efficiency of dust in WR of $\sim 6\%$. But WR stars are also very rare in galaxies as compared to low-intermediate mass stars, with the fraction of stars in a given population with $M > 25\ M_\odot \sim 10^{-4}$ implying that the yield of dust from such a process will not be significant. Model atmospheres for WR stars do not suggest that dust could nucleate prolifically in them due to the high temperatures and diffuse gas, but dust formation is thought to occur in the interacting region of colliding wind binaries (CWB) (Usov 1991). This will be addressed further in Chapter 6.

2.2.1 Mass Loss and the TP-AGB Phase

The dominant processes in stellar mass loss are pulsational and line driven winds with mass loss rates [2] of $\sim 10^{-4} - 10^{-6}\ M_\odot\ yr^{-1}$ and $10^{-7} - 10^{-10}\ M_\odot\ yr^{-1}$ (Lamers

[2]Dust driven winds only become important at high metallicities where there is sufficient dust production to drive the gas outwards (Willson 2000).

& Cassinelli 1999). The important question to ask is how much of these outflows are in the form of *condensed* material? Whether or not dust is formed from the gas will depend on the temperature and the density inside the wind (Section 2.2). A rough estimate of the dust production in these winds can be made by investigating condensation conditions in stellar atmosphere models which in turn are tied to stellar evolutionary models which predict T_{eff} and $\dot{M}$ throughout the star's evolution.

M_i	τ_m	M_R	ΔM_{ej}	ΔM_{SNe}	ΔM_{SW}	M_{SW} (E-AGB)
1	10^4	0.5	0.5	/	0.5	0.30
3	350	0.6	2.4	/	2.4	0.07
4	160	0.7	3.3	/	3.3	0.05
5	94	0.8	4.2	/	4.2	0.08
7		0.9	6.1	/	6.1	0.20
9	26	1.2	7.8	5	2.8	0.40
12	16	1.4	10.6	8, 10	2.6, 0.6	0.48
15	11	1.7	13.3	10, 11	3.3, 2.3	1.42
20	8	2.2	17.8	12, 18	5.0, 0.0	3.48
25	7	2.7	22.3	13, 23	9.4 0.0	9.42
40	4	1.8	38.2	6, 27	32.2, 11.2	31.90

Table 2.1: The mass lost in stars with initial mass of $1 \leq M \leq 40$ $M_\odot$ for stellar winds and SNe at $Z = Z_\odot$. Columns are (1) Initial mass of star. (2) Main sequence lifetime in Myrs (Schaerer et al. 1993). (3) Remnant masses taken from Maeder (1992). (4) Total mass ejected from star in SNe and stellar winds. (5) Total mass lost in SNe (Maeder 1992; Woosely & Weaver 1995). (6) Total mass lost in SWs i.e. (4) - (5). (7) Mass lost in the E-AGB phase, corresponding to those from Schaller et al. (1992). This is negligible for low-intermediate mass stars.

The total mass lost by the progenitor star is believed to satisfy the initial-final mass relationship shown in Weidermann (1987) and Marigo (2000) following hydrodynamical modelling of yields from stars using current mass loss prescriptions. Thus for low-intermediate mass stars $1 \leq M_i \leq 7$ $M_\odot$, the mass lost in stellar winds and novae is the difference between the initial mass, M_i and the final remnant mass, M_R. For high mass stars ($7 < M_i \leq 40$ $M_\odot$) the mass is lost via both winds and SNe. Stars with mass beyond 40 $M_\odot$ may become a black hole and swallow up the elements produced (Maeder 1992) so they are ignored here.

We have followed the evolutionary model grids in Schaller et al. (1992)[3], up to the end of central C burning for high mass stars, the early AGB phase for intermediate stars and up to the He flash for low mass stars. The points of greatest mass loss up until the end of the evolutionary grids were multiplied by the duration, τ, to give the total mass lost during that phase. In the TP-AGB & stellar wind phases, $\dot{M}$ & τ were taken from Blöcker (1995a) and Marigo (1996). From the gross mass loss given in Table 2.1 it is clear that some mass is lost in the very late AGB phase or after (the mass lost in low-intermediate mass stars in column 7 is much less than the total mass lost in winds in column 6), but how and where does this occur? As a star ascends the AGB it is thought that (depending on the previous mass loss history), it may undergo some He flashes and will pulsate periodically. This is the TP-AGB phase and as a result of mixing, will create a dredge up of material within the star to its surface. Consequently, there will be not only a change in the composition in the atmosphere but also the composition of the dust (Garcia-Lario et al 2001, Herwig et al 1999; Waters 2003). The TP-AGB phase has mass loss rates comparable to the AGB phase and lasts for approximately $10^4 - 10^6$ years depending on the initial stellar mass ($7 - 3$ $M_\odot$ respectively) and the number of thermal pulses in the phase (Blöcker 1995a). So there is an opportunity here to create and inject dust into the ISM, but are the conditions right? The conditions for dust formation do appear to be satisfied in the TP-AGB phase as shown in Figure 2.3 where the evolutionary tracks of stars undergoing thermal pulses from Marigo et al. (1996) are added to those in Schaller et al (1992) for low-intermediate mass stars. The TP-AGB tracks pass through the area where dust forming atmospheres exist on Figure 2.2.

The future evolution of the star may depend on where the thermal pulses occur as they ascend the AGB. If the TP occurs just before the AGB ends, the star will

[3]As distributed by the astronomical data center at NASA Goddard Space Flight Centre.

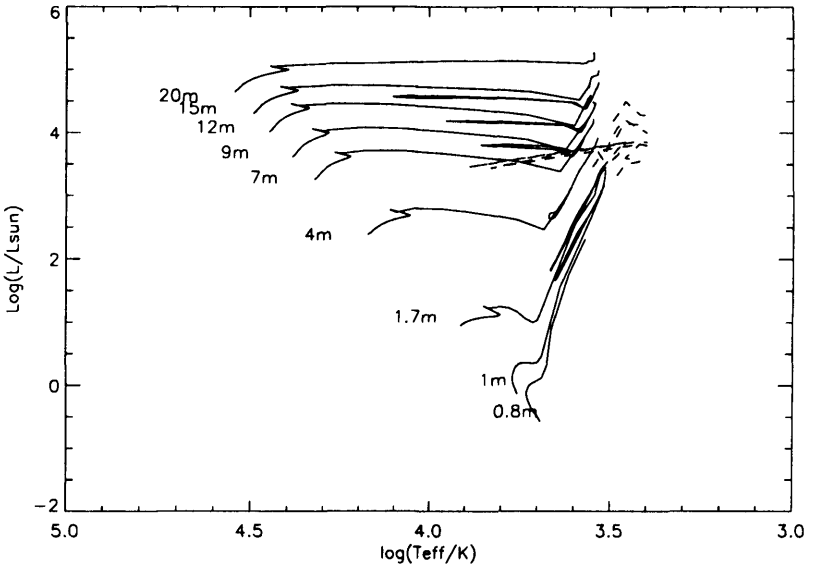

Figure 2.3: The evolution of low-intermediate mass stars up to the end of C burning (solid line) and up through TPAGB phase (dashed line) for $Z = Z_{\odot}$. The PAGB tracks are given in Blöcker (1995b), and are not included here.

experience dredge up and may become C rich. A superwind is then thought to occur with $\dot{M} \sim 10^{-4}$ $M_{\odot}$ yr^{-1} (Schönberner & Steffan 2001, Blöcker 1995b). If the TP occurs after the AGB ends, then it will evolve on a constant luminosity track for $\sim 10^3$ years to a Planetary Nebula (PN) phase - and the star is now PAGB (Post AGB). This is characterised by an increasing T_{eff} and a decreased mass loss (Schönberner & Steffan 2001, Blöcker 1995b, Fujii et al. 2001), with temperatures reaching above 30,000K. The central star begins to ionise the surrounding material to create a PPN (proto-planetary nebula). This phase does not seem suitable for dust formation. It does not satisfy the low temperatures or the high mass loss rates needed, so we can ignore this as a significant phase of dust production (although circumstellar dust shells are seen around PAGB stars, they are thought to have survived from their previous AGB phase (Lorenz-Martins et al 2001) but any further

mass ejection from the central star may affect the shells (Blöcker et al 2001)). If the TP occurs when He burning has ceased then the star will evolve on a white dwarf cooling track and will again not be suitable for dust condensation.

So in these later evolutionary stages we have a clear candidate for a dust formation site - stars in the TP-AGB and the superwind phases. Those stars which have had their composition changed from O rich to C rich are now more likely to form C rich dust. It is interesting to note that from Section 2.2, not only is it difficult to reach the low temperatures in stars for silicates to form but we are now faced with the problem that those O rich stars are likely to become C rich in the most significant dust formation stages! This may suggest that silicate dust may not be the dominant component of returned dust from stars as previously thought (Bode 1988). Dust formation in the TP-AGB phase will also be highly dependant on metallicity as dredge ups are found to be more efficient at low Z. This is due to a number of factors (i) lower mass loss rates at lower metallicities prolong the TP-AGB lifetimes and there are more dredge up events; (ii) yields of C and O are more efficient at low Z since the dredge-ups affect the composition more strongly if there is relatively lower abundance in the shells (van de Hoek & Gronewegen 1997); (iii) The core mass at the first pulse affects the amount of dredge-up material. At low Z, the core mass is higher and hence more is dredged-up in this phase. The TP-AGB is reached earlier on in the star's lifetime and more C stars may be formed (Groenewegen 1998, Marigo 1998, Marigo et al. 1999). The enhanced conversion of O stars to C stars at low Z may then imply a large abundance of carbon dust in the early universe (although at Z=0.001 we need at least 1×10^8yrs for $M \leq 5\ M_\odot$ to reach the TP-AGB phase).

It is worth mentioning that if it is mainly carbon dust forming in stars during the TP-AGB phase then it may be formed from freshly synthesised elements in the

star and may be considered differently to dust formed from pre-existing heavy elements in stellar atmospheres. This may have consequences in models which separate the formation of dust into two classes as in E01. In the evolutionary dust model presented there, our TP-AGB phase may be considered as a χ_1 source (condensation efficiency of dust from freshly synthesised elements - see below) instead of a χ_2 (condensation efficiency in stellar winds).

2.2.2 Estimating the Condensation Efficiency in Winds

To estimate the condensation efficiency in winds we can use the models in Schaller et al. (1992) and Marigo et al. (1996) to give the mass fraction lost in winds (as listed in Table 2.2), and the fraction which satisfies the conditions for nucleation given in Section 2.2. Equation 2.2 will then give an estimate of χ_2 (although this is actually a maximum as we assume 100% condensation wherever the nucleation conditions are satisfied).

$$\chi_2 = \frac{\text{Mass into dust in stars}}{\text{Mass of heavy elements lost in Stellar Winds}} \tag{2.2}$$

To determine the average condensation efficiency over a stellar population we need to sum over the stellar mass spectrum, with Salpeter initial mass function (the distribution of mass in a stellar population, normally fitted as a power law), $\phi(M) \propto M^{-2.35}$. The uncertainty of whether or not the TP-AGB phase represents χ_2 or χ_1 does not allow a clear estimate to be made, and initially we estimate χ_2 for the models in Schaller et al. (1992) up to the E-AGB stage (Table 2.2 column 3), and χ_2^* which also includes the TPAGB and the superwind phase (Table 2.2 columns 3 & 3). So for solar metallicity and using Table 2.2,

M_i	mp_C	mp_Z	$M_{dust}{}^a$	$M_{dust}{}^b$	Total M_{dust}	Implied χ_2
1	2.4E-5	2.4E-5	8.0E-6	5.2E-6	1.3E-5	0.55
3	3.5E-2	3.0E-2	6.0E-4	1.9E-2	2.0E-2	0.65
4	1.5E-2	2.0E-2	2.3E-4	1.5E-2	1.5E-2	0.76
5	5.0E-3	1.2E-2	1.7E-4	9.0E-3	9.2E-3	0.76
9	2.7E-2	1.7E-1	1.0E-4	<6.0E-4	<7.0E-4	<< 0.7
12	7.1E-2	6.9E-1	1.4E-4	<6.6E-4	<8.0E-4	<< 0.8
15	1.4E-1	1.32	2.6E-4	<3.4E-4	<4.8E-4	<< 0.6
20	2.2E-1	2.73	5.6E-4	<2.4E-4	<8.0E-4	<< 0.8
25	3.0E-1	4.48	0	0	0	0
40	4.88	8.01	0	0	0	0

Table 2.2: The maximum mass M_{dust} lost in winds from stars, $M_\odot$, which satisfy the conditions for dust nucleation, for $Z = Z_\odot$. The columns are (1) Initial mass. (2) Total carbon yield for low mass stars taken from Marigo (2000) and for high mass stars from Maeder (1992). (3) As (2) for heavy elements, Z. (4) Mass of dust from winds in the RG/E-AGB phase. Mass loss rates and effective temperatures used to estimate the maximum dust mass that could form were taken from the models in Schaller et al. (1992). (5) Maximum dust mass in the TP-AGB/superwind phase. Carbon dust formed in TP-AGB assumes $\sim$ 80% of the freshly synthesised carbon satisfies the nucleation conditions. (6) Total dust mass produced. (7) Implied condensation efficiency calculated from Equation 2.2. For massive stars the condensation efficiency can not be estimated as there appears to be no corresponding dust production phase since the gas temperatures in the atmosphere models are too high.

$$\chi_2 \sim 0.16$$

$$\chi_2^* \sim 0.45$$

If the condensation efficiency of dust nucleating from the available metals in the gas is < 100% then this would serve to decrease χ further. χ is simply calculated by assuming that when the right conditions are met, then all the available elements lost in that phase will condense so these efficiencies are upper limits. The efficiency of dust forming from the available metals in stellar winds (and not the efficiency of the star at forming dust) can be modelled theoretically via grain growth from a single monomer to give $\sim 0.3 - 0.7$ for condensation of Si, Fe, Mg, O (Dominik et al. 1993) and $\sim$ 0.3 for carbon (Cadwell et al. 1994). The numbers given in

Table 2.2 are a maximum and could be as low as 0.1 if we assume only 30 per cent nucleation efficiency when conditions are right. In the elementary model given in E01, this is the minimum condensation efficiency in stars required to reach the observed dust masses in the solar neighbourhood. From these simple arguments, it appears that the TP-AGB and superwind phases (M_{dust} [b] in Table 2.2) may be the most significant dust production phase in the stars lifetime.

2.2.3 Estimating the Condensation Efficiency in SNe

As discussed in Chapter 1, observational studies of SNe (until the work of this thesis) estimate condensation efficiencies of $\ll 0.01$. Theory is still a long way from reliably estimating the condensation efficiency of dust in SNe of different progenitor mass and evolutionary phases. The most acceptable theories begin with nucleation via chemical or kinetic rates, but these models can not match the observations of SN1987A (with that of Kozasa et al. (1989; 1991) predicting lower gas temperatures than actually seen). (For a detailed discussion on the IR observations of SN1987A see Wooden 1997.) Interestingly the models in Clayton et al. (2001) allow for a greater production of carbon dust even in ejecta with $C/O < 1$ compared to the more classical nucleation models (Kozasa et al. 1991). We take the elementary model published in TF01 to estimate the condensation efficiency in SNe (although this is based on the nucleation theory given in Kozasa et al, which has been shown to be incorrect for SN1987A). The model gives the dust mass produced per supernova as a function of the mass of the progenitor star and the metallicity. TF01 have modelled two cases of dust production - (a) and (b) - corresponding to low and high energy SNe explosions respectively.

To estimate χ_1 for these two cases, we require information on the heavy element yield from the ejecta (as we are interested in finding the condensation efficiency of

dust forming from freshly synthesised elements as in Equation 2.3).

$$\chi_1 = \frac{\text{Mass of dust formed in ejecta}}{\text{Mass of freshly formed heavy elements in ejecta}} \tag{2.3}$$

M_i	12	15	20	25	30A	35A	40A
					30B	35B	40B
C	8.1E-02	1.6E-01	2.1E-01	3.2E-01	2.9E-01	3.0E-01	3.1E-01
					2.9E-01	3.2E-01	3.6E-01
O	2.1E-01	6.8E-01	1.9E+00	3.3E+00	3.7E+00	3.1E+00	2.4E+00
					4.8E+00	5.8E+00	6.0E+00
Mg	8.2E-03	2.7E-02	3.1E-02	1.1E-01	2.1E-01	1.2E-01	6.8E-01
					2.8E-01	2.9E-01	2.3E-01
Si	9.1E-02	1.1E-01	2.9E-01	3.2E-01	9.8E-02	4.2E-02	2.5E-02
					3.2E-01	1.1E-01	5.5E-02
Al	1.0E-03	4.0E-03	4.0E-03	2.4E-02	3.9E-02	3.0E-02	2.1E-02
					5.1E-02	6.4E-02	6.5E-02
Ni	4.3E-02	1.2E-01	8.8E-02	1.3E-01	2.5E-02	2.8E-02	2.8E-02
					2.5E-02	2.8E-02	2.8E-02
Fe	1.2E-02	1.4E-02	1.8E-02	2.2E-02	1.1E-01	1.3E-09	7.7E-10
M_Z	4.4E-01	1.1E+00	2.6E+00	4.2E+00	4.3E+00	3.6E+00	2.8E+00
					6.3E+00	6.6E+00	6.8E+00
M_d	2.0E-01	4.7E-01	5.0E-01	1.0E+00	1.0E+00	5.8E-01	4.2E-01
					2.0E+00	1.3E+00	8.0E-01
χ_1	0.45	0.42	0.19	0.24	0.25	0.16	0.15
					0.32	0.19	0.12

Table 2.3: The yield of heavy elements from supernovae for solar metallicity ($Z = Z_\odot$) and progenitor star ranging from $M_i = 12 - 40$ M$_\odot$. Cases A and B represent low and high energy SN explosions as published in Woosley & Weaver (1995). M_Z is the total amount of heavy elements ejected in the SNe and M_d is the ejected dust mass from TF01. The implied condensation efficiency is χ_1 per SNe.

The yields were obtained from the tables given in Woosley & Weaver (1995), for a grid of stellar masses and metallicities $Z/Z_\odot = 0, 10^{-4}, 10^{-2}, 1$. The heavy element yield for $Z = Z_\odot$ is given in Table 2.3. Weighting the values over the stellar mass

spectrum for solar metallicity, gives:

$$\chi_1(a) \sim 0.22$$

$$\chi_1(b) \sim 0.23$$

Other theoretical models suggest efficiencies of $\sim 0.1 - 0.3$ (Kozasa et al. 1991; Clayton et al. 2001). The available data allow for a comparison of χ_1 values at different metallicities as discussed in the next Section. The condensation efficiency in SNe is re-evaluated in Chapters 4 & 5 with new sub-millimetre observations.

2.3 The Dependence of Dust Sources on Metallicity

Now we can ask the question does the condensation efficiency as estimated here vary with the metallicity evolution of a galaxy? It seems obvious that there will be less dust formation at low Z due to higher temperatures and less pre-existing heavy elements for grain growth or shielding, but can we actually quantify this relationship? Using the same arguments as given in Section 2.2.2, the condensation efficiencies, χ_2 and χ_2^* at different metallicities have been estimated.

It is useful at this stage to re-define the condensation efficiencies used in previous Sections:

- χ_1 - efficiency of dust condensation from new heavy elements for the (a) high energy (b) low energy SNe explosions.
- χ_2 - efficiency of dust condensation from pre-existing heavy elements in stellar winds of stars during their RG/AGB phases.

- χ_1^* - condensation efficiency of dust from stellar winds of evolved stars during their TPAGB phase if we assume the available heavy elements are freshly synthesised in the star.

- χ_2^* - condensation efficiency of dust from pre-existing heavy elements in the stellar winds of evolved stars during their RG/AGB phase *and* their super-wind/TPAGB phases (i.e. $\chi_2 + \chi_1^*$).

The criterion for nucleation is the same with the mass loss rates and effective temperatures for the E-AGB stage taken from Schaller et al (1992), Schaerer et al (1993), and Schaller et al. (1993). For zero metallicity, it has been shown that the TP-AGB phase does occur but at higher temperatures, $T_{eff} > 4500$K (Marigo et al. 1999). Therefore the TP-AGB phase at low metallicities is not considered here as a source of dust production. For $Z = 0.008$, the star does appear to reach the low temperatures but for a shorter period of time as compared to those at solar metallicity (as shown in Marigo et al. 1996). The problems in trying to calculate the condensation efficiency at different Z become apparent when trying to determine the mass loss rates and the time spent in the nucleation conditions. With lack of any concrete information it is assumed that the TPAGB properties at $Z = 0.001, 0.008$, 0.04 are similar to those at $Z = 0.02$ but at lower metallicities less dust is formed per star due to less time being spent in this phase.

The published models allowed estimates to be made for dust nucleation for $Z = 0.001, 0.008$ and 0.04[5]. Their corresponding χ_2 values are listed below in Table 2.4. χ_1^* represents the condensation efficiency in the TP-AGB phase *if* it is considered as a χ_1 source i.e. freshly synthesised dust production. For χ_1, the same process of estimating the condensation efficiency seen in Section 2.2.3 was applied to the yields at higher metallicities from Woosley & Weaver (1995). The values are given

[5]as distributed by the astronomical data center at NASA Goddard Space Flight Centre

$Z/Z_\odot$	0.0	10^{-4}	10^{-2}	0.05	0.2	1.0	2.0
χ_2	0	/	/	/	0	0.16	0.10
χ_2^*	0	/	/	0.10	0.10	0.45	0.21
χ_1^*	0	/	/	0.10	0.11	0.22	0.22
$\chi_1(a)$	0.46	0.15	0.18	/	/	0.22	/
$\chi_1(b)$	0.27	0.18	0.21	/	/	0.23	/

Table 2.4: The maximum stellar weighted condensation efficiencies, χ_2, χ_2^*, χ_1^* and χ_1 in stars at different metallicities, $Z/Z_\odot$.

in Table 2.4 where (a) and (b) still represent the low and high energy cases. Note that this will be a maximum estimate of χ_2.

We found that there is no correlation between the metallicity and the condensation efficiency in SNe for the high energy case so we assume χ_1 is roughly constant, ~ 0.23. The variation of χ_2 with metallicity can also be approximated by a constant. The small variation can be fitted by a parabola with:

$$\chi_2(Z) = -162Z^2 + 9Z$$

$$\chi_2^*(Z) = -676Z^2 + 33Z$$

$$\chi_1^*(Z) = -5807Z^3 - 612Z^2 + 21Z.$$

Whether this small variation with metallicity would affect dust evolution is investigated in Section 2.9.

2.4 Modelling Chemical Evolution

Using the notation given in Pagel (1997) and Henry et al. (2000), we can follow the build up of heavy elements over time in a closed galactic system. Initially we have a mass of gas, g, which is converted into stars, s, via a star formation rate - SFR,

$\psi(t)$ and an IMF, $\phi(m)$. The total mass of the closed system will then be

$$M = g + s$$

Using an infall model (such as the one described in D98), the extra dilution of the ISM limits the metallicity reached and hence the dust mass will be slightly less. Edmunds & Eales (1998) show that the simple model produces the maximum dust yields for a given gas fraction hence we assume no inflows or outflows (the effects of which are discussed elsewhere (e.g. Köppen and Edmunds 1999; E01)). The gas mass, g will be depleted by star formation and enriched by the mass ejected from stars, e(t).

$$\frac{dg}{dt} = -\psi(t) + e(t) \tag{2.4}$$

The evolution of the heavy element abundance in the ISM (Zg) is governed by the ejection of metals by stars (e_z) and those going into forming stars.

$$\frac{d(Zg)}{dt} = -Z(t)\psi(t) + e_z(t) \tag{2.5}$$

Therefore the metallicity evolution is described by Equation 2.6

$$\frac{dZ}{dt} = \frac{e_z(t) - Z(t)e(t)}{g} \tag{2.6}$$

Assuming that mass loss occurs suddenly at the end of stellar evolution, the ejected mass and the ejected heavy elements are (Tinsely 1980)

$$e(t) = \int_{m_{\tau_m}}^{m_2} [m - m_R(m)]\, \psi(t - \tau_m)\phi(m)dm \tag{2.7}$$

$$e_z(t) = \int_{m_{\tau_m}}^{m_2} ([m - m_R(m)]\, Z(t - \tau_m) + mp_z)\psi(t - \tau_m)\phi(m)dm \qquad (2.8)$$

where mp_z is the stellar yield of heavy elements from a star of initial mass m (values taken from Maeder (1992) and Marigo (2000) for massive stars and IMS respectively). $m_R(m)$ is the remnant mass, τ_m is the lifetime of a star of mass m such that a star formed at $t - \tau_m$ has died at time t, and m_{τ_m} is the stellar mass whose τ_m corresponds to the age of the system. This expression includes the contribution of the metals which have been recycled through star formation and metals from freshly synthesised elements in stars. This analysis also includes the finite age of the stars ejecting the material into the ISM. The integrated yield, P_x, which defines the mass

Mass Ranges	Z	P_Z	P_c
$1 - 5M_\odot$ [a]	0.004	3×10^{-3}	2×10^{-3}
	0.02	5×10^{-4}	4×10^{-4}
$9 - 120M_\odot$ [b]	0.001	0.018	2×10^{-3}
	0.02	0.015	8×10^{-3}

[a] From Marigo (2000) and van de Hoek & Groenewegen (1997).
[b] From Meader (1992)

Table 2.5: The integrated yields, P_x of heavy elements (P_Z) and carbon (P_c) from massive and intermediate mass stars at different metallicities, Z.

fraction of stars (mp_x) formed in the mass range m_1 and m_2 and eventually expelled as new element, x,is given in Equation 2.9 and Table 2.5.

$$P_x = \int_{m_1}^{m_2} mp_x(m)\phi(m)dm \qquad (2.9)$$

$\phi(m)$ is the initial mass function which is the normalised Salpeter Initial Mass Function (IMF,) with $b = 1.35$

$$\phi(m) = \left(\frac{1-b}{m_2^{-(1-b)} - m_1^{-(1-b)}}\right) m^{-(1+b)} \qquad (2.10)$$

where $m_2 = 120\mathrm{M}_\odot$ and $m_1 = 0.8\mathrm{M}_\odot$.

It is not straightforward to solve these equations without making some simple assumptions so from Talbot et al. (1973) we approximate the remnant mass $m_R(m)$ as

$$m_R(m) = \begin{cases} 0.11\mathrm{m}{+}0.46, & m \leq 6.86\ M_\odot; \\ 1.5\ \mathrm{M}_\odot, & 6.86 < m \leq 120\ M_\odot \end{cases}$$

The star formation rate, $\psi(t)$ scales as the gas density to some power η (Henry et al. 2000) where

$$\psi(t) = kg^\eta \tag{2.11}$$

and k is the star formation efficiency. η is thought to lie between 1 and 2 - although here we assume $\eta = 1$ for simplicity.

The code was written with a logarithmic time step with initial conditions for the gas and metallicity of the system:

$$g(t=0) = M_{tot} = 1 \ ; \ Z(t=0) = 0$$

The yields from Maeder (1992) and Marigo (2000) were tabulated and interpolated to find the stellar yield mp_z corresponding to a given metallicity (for the models of $Z = 0.001,\ 0.02$) and mass. The overall yields calculated in our model were compared with the original to check the validity of the code and were found to agree to within 3%.

The stellar lifetimes, τ_m were initially estimated via the relationships given in Equation 2.12 following the method of Talbot & Arnett (1973)

$$\tau_m(m) = \frac{11.7}{m^2} + 1 \times 10^{-3}\ \ (Gyrs) \quad \Rightarrow \quad m_{\tau_m} = \sqrt{\frac{11.7}{t - 1 \times 10^{-3}}}\ \ (M_\odot) \tag{2.12}$$

However, we found that for a given mass, the lifetime of a star estimated with

this method is larger than hydrodynamical models of stellar evolution suggest. This in turn will underestimate the $\psi(\tau - \tau_m)$ values (see Figure 2.4). Thus we used tabulated values of lifetimes from the Schaller et al models which were interpolated to find the relevant value for m. This also allows us to input a metallicity variation of stellar mass with lifetime. Equations 2.4 & 2.6 were then solved at each timestep with each increment of Z and g added to the previous solution.

With the parameters for our nominal galaxy, after 10 Gyrs we obtain the fraction of matter locked up in stars, $\alpha = 0.8$, the returned fraction $R = 0.2$ and a gas mass of 0.13 which represents the Milky Way with g = 5×10^9 $M_\odot$ and k = 0.25 Gyr^{-1}. We calculate the returned yield at this time to be $P_x \sim 0.016$ with a true yield ($p = P_x/\alpha$, defined as the mass of new element x ejected by all stars per unit mass of matter locked up in stars) of ~ 0.019. The metallicity reached after 10 Gyrs is ~ 0.03 which, although higher than the nominal 0.02 value used for solar metallicity, agrees with the metallicity estimated using an analytical approach where $Z = p\alpha kt$ for the same value of p (see next Section).

2.4.1 Further Assumptions

The Instantaneous Recycling Approximation

For the instantaneous recycling approximation we can assume that all evolutionary processes (i.e. the recycling of heavy elements into the ISM) occur instantaneously as compared to galactic timescales ($> 10^9$ years). This provides a simplified approach to the above equations since we can now neglect the finite lifetime of a star and set τ_m to zero. Consequently the returned fraction of gas and metals and the fraction of mass locked up in long lived stars (α) will now become constant for a constant IMF - this is not a realistic assumption when considering the yield and dust production from low mass stars which take $> 10^8$ years to evolve (see Section 2.4.1). This

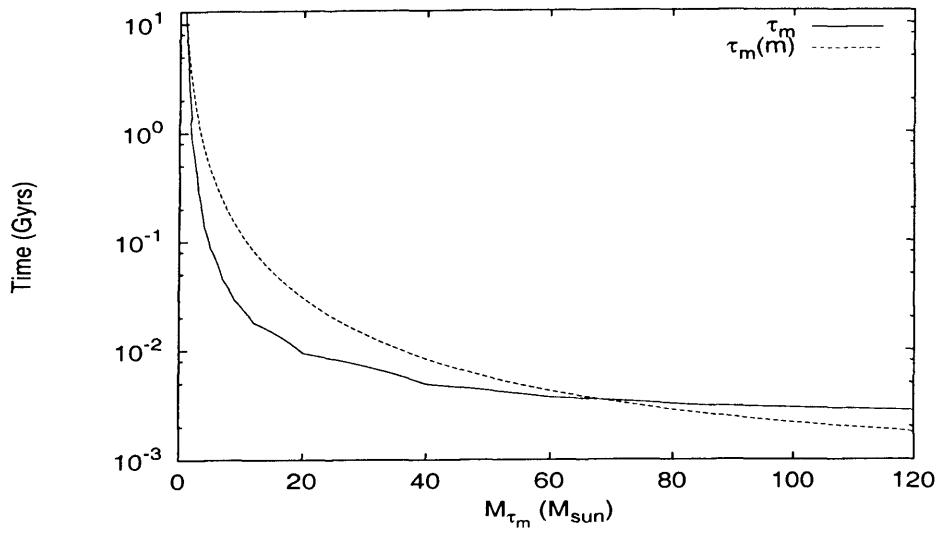

(a)

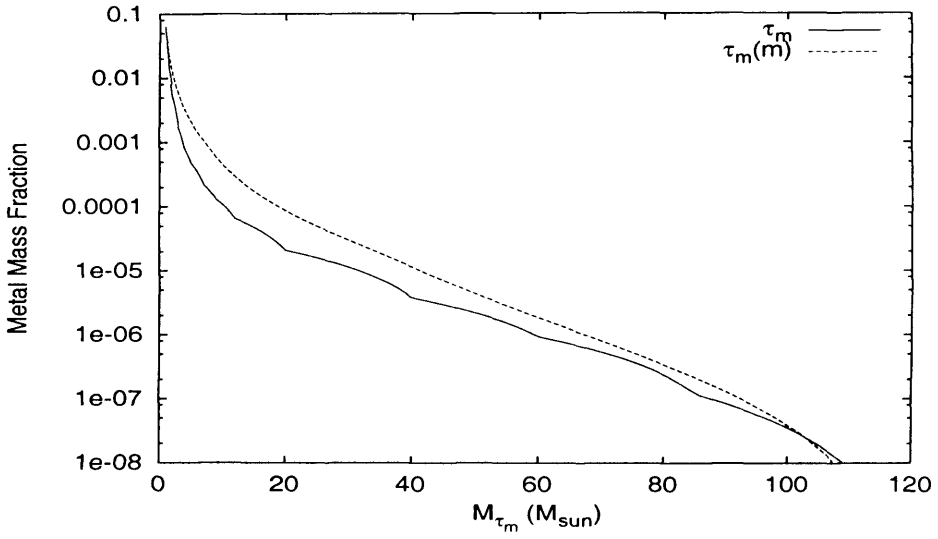

(b)

Figure 2.4: The comparison of the mass of star whose lifetime corresponds to the age of the system, m_{τ_m} with (a) time and (b) metallicity using the functional approximation in Equation 2.12 (curve $\tau_m(m)$) from Talbot & Arnett (1972) and the tabulated lifetimes from the Schaller models (curve τ_m). At a given time and metallicity, m_{τ_m} is higher using the functional approximation which means that the integral over mass is over a smaller mass range. The 'bumps' in the τ_m curve are due to the finite step size of the interpolation.

approximation is not applicable if the star formation rate strongly decreases as a function of time since $\psi(t-\tau_m) \neq \psi(t)$. Equations 2.7 & 2.8, for the instantaneous approximations now become

$$\int_{m_1}^{m_2} [m - m_R(m)]\,\phi(m)dm \Rightarrow (1-\alpha)$$

$$e(t) \Rightarrow (1-\alpha)\psi(t)$$

$$e_z(t) \Rightarrow p\alpha\psi(t) + (1-\alpha)Z(t)\psi(t)$$

$$\psi(t) = kg \Rightarrow ke^{-t/t_o}$$

where p is the true yield from stars (P_x/α) and $t_o = 1/\alpha k$ is the star formation timescale.

$$\frac{dg}{dt} = -\alpha\psi(t) \tag{2.13}$$

$$\frac{d(Zg)}{dt} = p\alpha\psi(t) + (1-\alpha)Z\psi(t) - Z\psi(t) \tag{2.14}$$

Therefore the metallicity evolves as Equation 2.15

$$\frac{dZ}{dt} = \frac{p\alpha\psi(t)}{g} \tag{2.15}$$

The terms in Equation 2.15 & 2.13 are therefore equivalent to those in the previous section for a one zoned model, with no inflow or outflow. These are easily solved to

give

$$g = e^{-\alpha k t} \tag{2.16}$$

$$Z = -p ln(g) \Rightarrow p\alpha k t \tag{2.17}$$

The evolution of gas mass and metallicity with time using the full chemical evolution model is shown in Figure 2.5. These figures are similar to the chemical evolution model presented in Talbot & Arnett (1972) and Tinsley (1968) with slight differences due to differences in heavy element yields and chemical evolution coefficients such as τ_m etc. The instantaneous approach breaks down at low gas masses and begins to diverge from these solutions when $g < 0.1$. For the same value of the integrated yield, the instantaneous approach overestimates the metallicity at earlier times as expected.

Time Delay Approximations

We can introduce time delays into the model for elements which are "delayed" in their return to the ISM as compared to those released quickly via Type II SNe (e.g. iron from Type Ia SNe released only after $\sim 10^9$ years). Suppose that an element x is delayed by a time τ_x and then suddenly released, we can follow the evolution of x using a step function such that

$$H(x - x_0) = \begin{cases} 1, & x \geq 0; \\ 0, & x < 0 \end{cases}$$

and with a star formation rate now given by $\psi(t-\tau_x)$. We can associate a metallicity increment with τ_x to give $Z_x = p\alpha k\tau_x$ and thus follow the evolution of any delayed element with slightly more accuracy. This is often used to describe the evolution of nitrogen and carbon to fit the observed abundance ratios (Henry et al. 2000) and we can use the same idea for dust (Section 2.5).

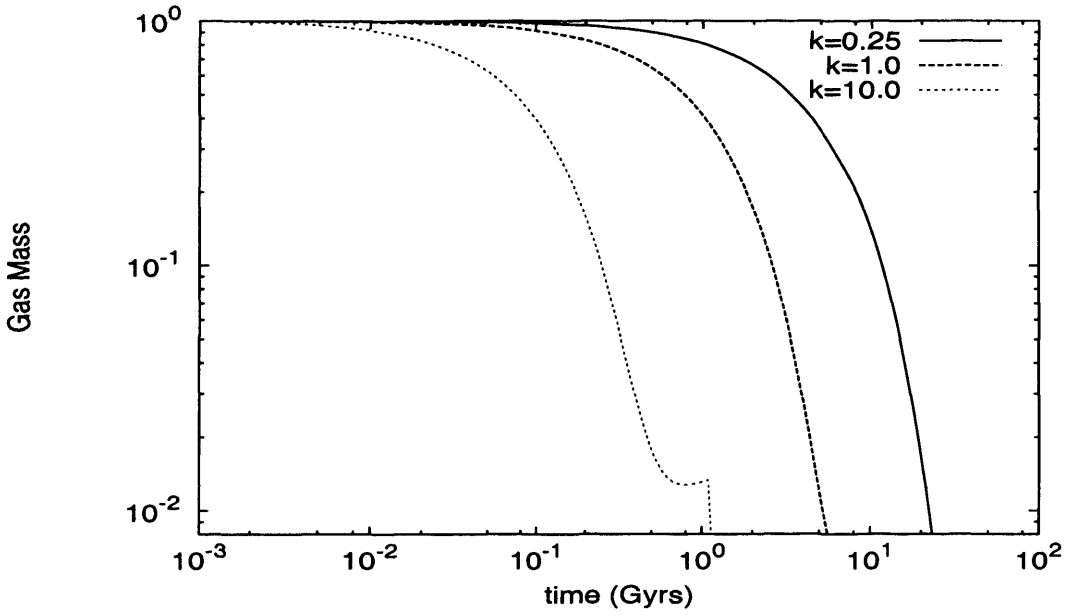

(a)

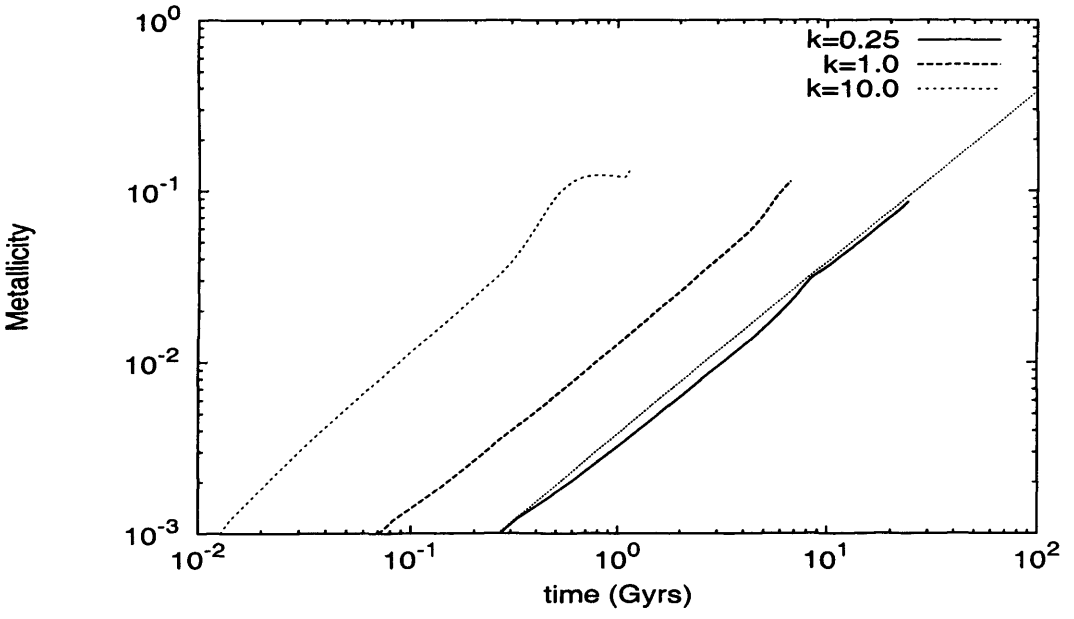

(b)

Figure 2.5: Evolution of (a) gas mass and (b) metallicity (Z) with time for different star formation efficiencies, k = 0.25, 1.0, 10.0 Gyr^{-1} for the chemical evolution model. The metallicity evolution expected using the instantaneous approach from Equation 2.17 is also shown in (b) by the small dotted line.

2.5 Dust Evolution

From E01, the elementary model uses the instantaneous recycling approximation and follows the evolution of gas mass (g), metallicity (Zg) and grain core mass (yg) as a mass ds forms stars as in equations 2.18, 2.19 & 2.20. The destruction of grains is ignored here. The terms in Equation 2.20 represent the relative contributions of dust sources to the grain mass as a mass ds forms stars. The first term gives the contribution from SNe, the second from stars and the third from grains lost in forming stars.

$$dg = -\alpha ds \tag{2.18}$$

$$dZ = \frac{p\alpha ds}{g} \tag{2.19}$$

$$d(yg) = p'\chi_1 ds + (1-\alpha)\chi_2 z ds - y ds \tag{2.20}$$

If the TP-AGB can be considered as a 'new element' dust production mode then this will affect the elementary model. We can now propose an additional term allowing for the grain cores formed in the TP-AGB phase with condensation efficiency, χ_1^* and the fraction of C stars in a population, γ. γ will depend strongly on the metallicity - the number of C stars increases at lower Z due to an increase in the efficiency of dredge-ups (Marigo et al. 1999). This relationship is shown in Groenewegen (1998, Figure 3), and from this we can roughly quantify a function for the variation of γ with Z, as in Equation 2.21.

$$\gamma(Z) = \left[1 + \left(\frac{Z}{0.0046}\right)^{\frac{3}{2}}\right]^{-1} \tag{2.21}$$

The integrated yield of carbon produced in low-intermediate mass stars during the TPAGB phase (p^*) can be estimated at different metallicities using Figure 12 in

Marigo (2000). Qualitatively, if we assume that 10% (50%) of the solar C/O value is carbon returned by these stars (Henry et al. 2000) we obtain $p^* \sim 0.00073$ (0.00365). The simple model including the TPAGB phase is then described by Equation 2.22.

$$\begin{aligned} d(yg*) &= p\alpha\chi_1 ds + (1-\alpha)(1-\gamma(Z))\chi_2 Z ds \\ &\quad - y ds + \gamma(Z)(1-\alpha)p^*\chi_1^* \, Z ds \end{aligned} \tag{2.22}$$

We can compare our dust model with the work presented in D98 which also follows dust formation via chemical evolution (although the model presented here is much more simplistic with fewer parameters). As both models assumes a fraction of the heavy elements will condense into dust, it is interesting to compare the differences in the yields used. In Figure 2.6 we plot the carbon and oxygen yields used in both models from stars in the range $1 \leq M \leq 40$ $M_\odot$ for solar metallicity. In (a) we attempt to reproduce Figure 6 in D98 in which the yields for IMS and massive stars are taken from Renzini & Voli (1981) and Woosley & Weaver (1995) respectively, and in (b) we plot the yields from this work as given in Table 2.2. This work takes the more recent results for IMS yields from Marigo (2000) in which a metallicity dependant mass loss prescription is used. This produces higher carbon yields for IMS than those in Renzini & Voli (1981) and negligible carbon yields in stars with $M > 6$ $M_\odot$ (as is also shown in the TPAGB models presented in van de Hoek & Groenewegen 1997). This is thought to occur due to a drop in the TP lifetime (hence lower number of dredge ups). In this scenario, higher mass stars can end up processing the dredged-up material from the core at the bottom of the burning shells, the result of which is a conversion from C and O to nitrogen (Marigo 2000). The Renzini & Voli (1981) model also uses a lower mass loss parameter, which will produce optimistic yields in the $M > 3$ $M_\odot$ range. The differences between these

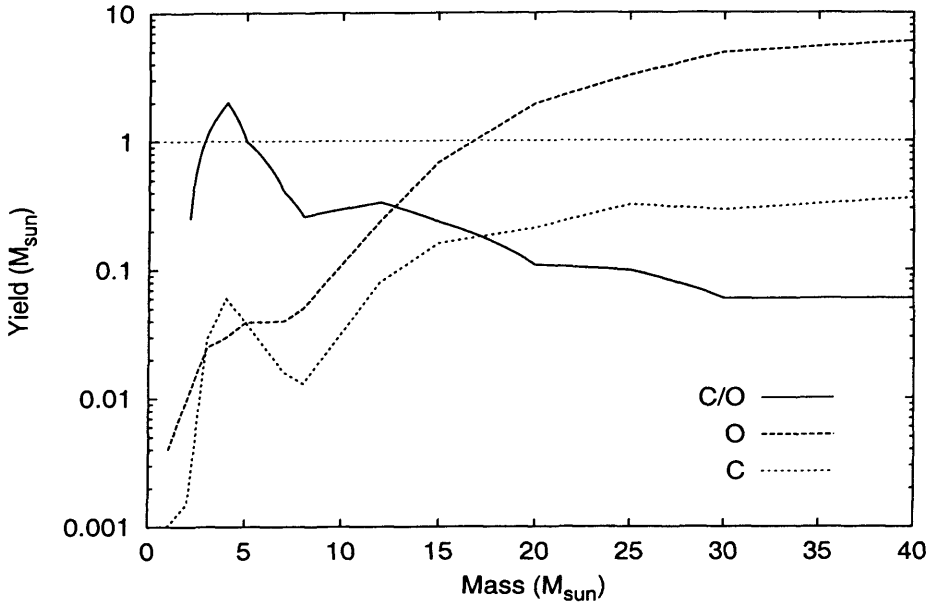

(a)

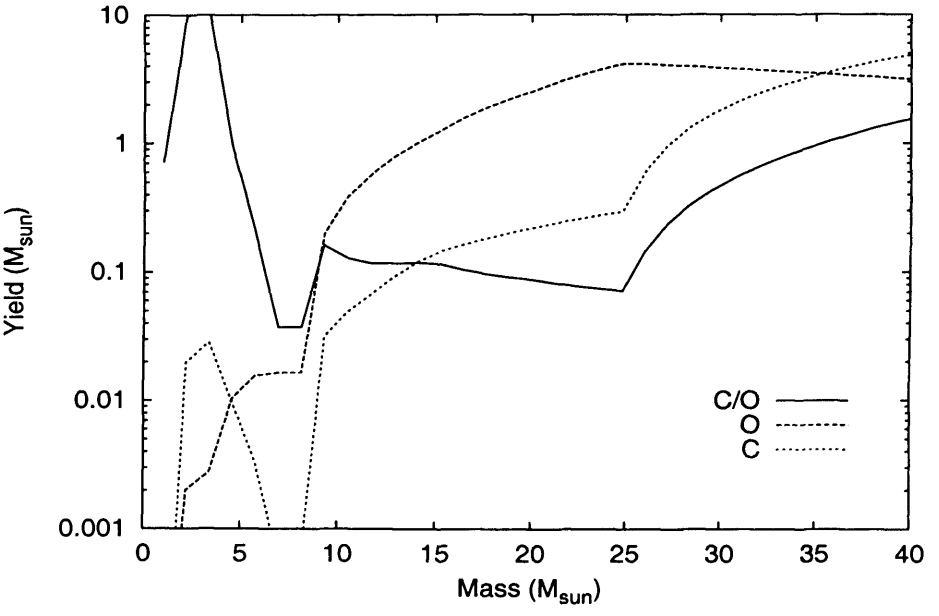

(b)

Figure 2.6: The carbon and oxygen yields from stars with $1 \leq M \leq 40$ $M_\odot$ at $Z = Z_\odot$ from (a) D98 and (b) this work. The C/O ratio is also shown in both figures. This work (b) shows a higher C/O ratio for both low mass ($M < 5$ $M_\odot$) and massive stars ($M > 25$ $M_\odot$) than in the Dwek model. The yield from stars with $6 < M < 8$ $M_\odot$ is much lower in this work than D98 due to the negligible yields in AGB stars in this mass range (Marigo 2000; van den Hoek & Groenewegen 1997).

models are clearly seen in Figure 2.6 (a) and (b) with this work having a high C/O ratio produced in IMS but lower yields overall over the whole mass range. This in turn leads to a lower dust yield in this work in comparison with D98 which is shown in Figure 2.7. Again in (a) we attempt to reproduce the model in Figure 7, D98 in which the stellar mass spectrum weighted dust yields are shown for solar metallicity and are compared with this work in Figure 2.7(b). As originally shown in D98, and reproduced in Figure 2.7(a) and (b), the majority of carbon dust is produced in IMS whereas the silicate dust is from massive stars. In this work, (b), we have a greater yield of carbon dust from more massive stars (M > 25 $M_{\odot}$) than D98 (a), due to the higher C/O ratio in massive stars in the Maeder (1992) yields. It is interesting to note that due to differences in the stellar evolution models and yields chosen on which to base the chemical models, we get a remarked difference in the production of dust in stars and SNe. Including a time delay (Section 2.4.1) for the production of dust in stars (assuming it is all produced in stellar winds at the end of stellar lifetimes) we can set (in Gyrs)

$$\tau_{d2} = 0.1$$

$$\tau_{*} = 2.4$$

as the delay of dust production in stars producing χ_2 and χ_1^* dust respectively. Thus the dust will evolve with time as

$$\begin{aligned} d(yg*) &= p\alpha\chi_1\psi(t) + H(t-\tau_{d2})(1-\alpha)(1-\gamma(Z))\chi_2 Z(t-\tau_{d2})\ \psi(t-\tau_{d2}) \\ &\quad - y\psi(t) + H(t-\tau_{*})\gamma(Z)(1-\alpha)p^{*}\chi_1^{*}Z(t-\tau_{*})\psi(t-\tau_{*}) \end{aligned} \tag{2.23}$$

The solutions for the dust mass y(g) and y*(g) were obtained numerically using a fortran 90 code, with the values of χ from the estimates given in Section 2.2.2 for

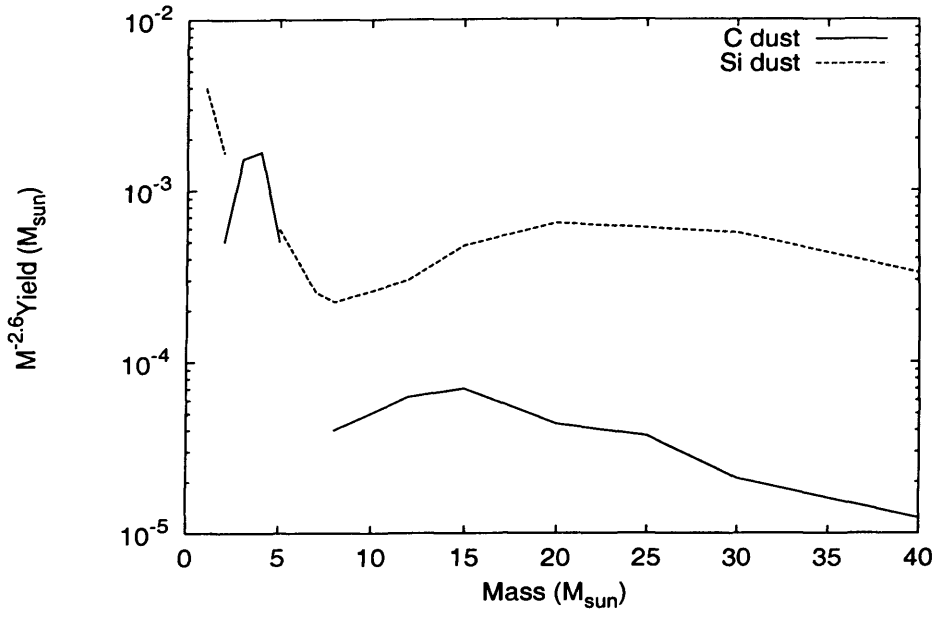

(a)

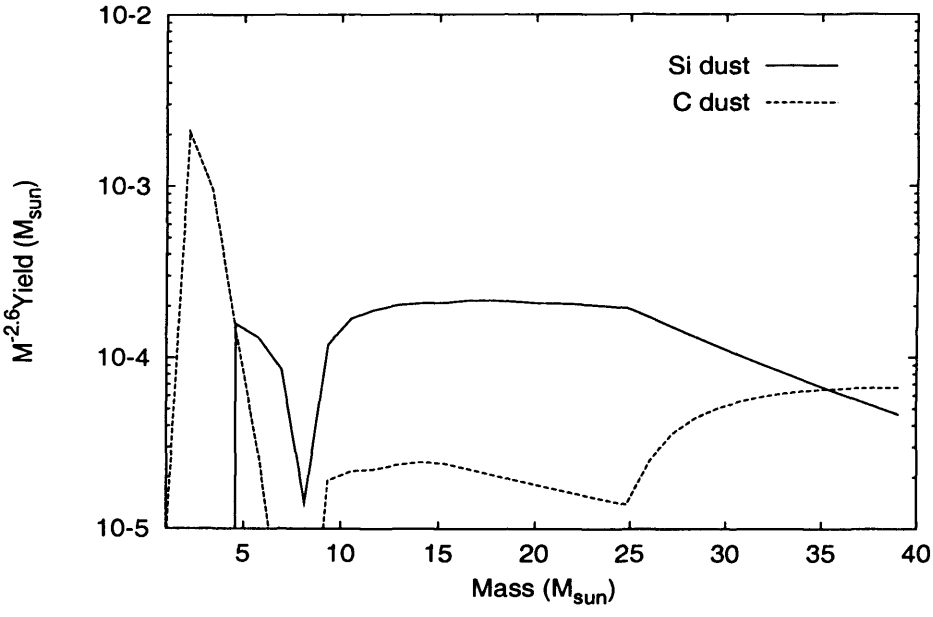

(b)

Figure 2.7: Carbon and silicate dust yields weighted with a stellar mass spectrum as in D98 for $Z = Z_{\odot}$. In (a) we attempt to roughly reproduce the dust yields from D98 Fig 6 and plot our own results in (b) to compare the dust yields from the two models. As in D98, the majority of carbon dust is produced by low mass stars (< 5 $M_{\odot}$) whereas most of the silicate dust is produced by massive stars (> 10 $M_{\odot}$). However, in (b) the amount of dust produced by stars > 5 $M_{\odot}$ is less by a factor of 10 than in D98 due to differences in the yields and the condensation efficiencies chosen.

$Z_{\odot}$.

Since the chemical evolution code used here no longer uses the instantaneous recycling approximation, it is worthwhile to compare our results with the results published in E01. The condensation efficiency for dust in stellar winds and supernovae in E01 were assigned values to represent the following cases: (a) $\chi_1 = \chi_2 = 0.16$; (b) $\chi_1 = 0$, $\chi_2 = 0.79$; (c) $\chi_1 = 0.1$, $\chi_2 = 0.39$; and (d) $\chi_1 = 0.2$, $\chi_2 = 0$. In this work we have etsimated theoretically that, $\chi_1 = 0.23$ and for stellar winds, (a) $\chi_2 = 0.16$ or 0.45 and (b) $\chi_1^* = 0.8$. Comparing the models demonstrates that the dust evolution from this work is similar to the instantaneous model but has slight differences due to the slow build up of elements rather than the immediate return from stars. In Figure 2.8 we show the differences between the dust evolution (y/z) with gas mass (g), with the quoted parameters in E01 (his Figure 2a) with the dust evolution from this work with our parameters. We also compare the elementary model (χ_1 and χ_2 only) to Equation 2.22 in (b) (Equation 2.23 is not compared here as it is only important when looking at temporal variation of dust mass. If our estimates are representative of the real processes governing dust formation in stellar winds, we find there may not be a significant amount of dust production in stars (only 16 per cent efficiency). If the stellar evolution models were to reach lower T_{eff} during their greatest mass loss stages then more dust would be produced and this value would be higher. The model for χ_2^* gives such a high dust mass at low gas masses due to the high condensation efficiency of the dust in the TPAGB phase. However, the TP model in which some of the dust from winds represents freshly synthesised elements is not significantly different to the simple model but will continue to be used here. It may be useful in tracing the evolution of carbon and silicate dust in the galaxy.

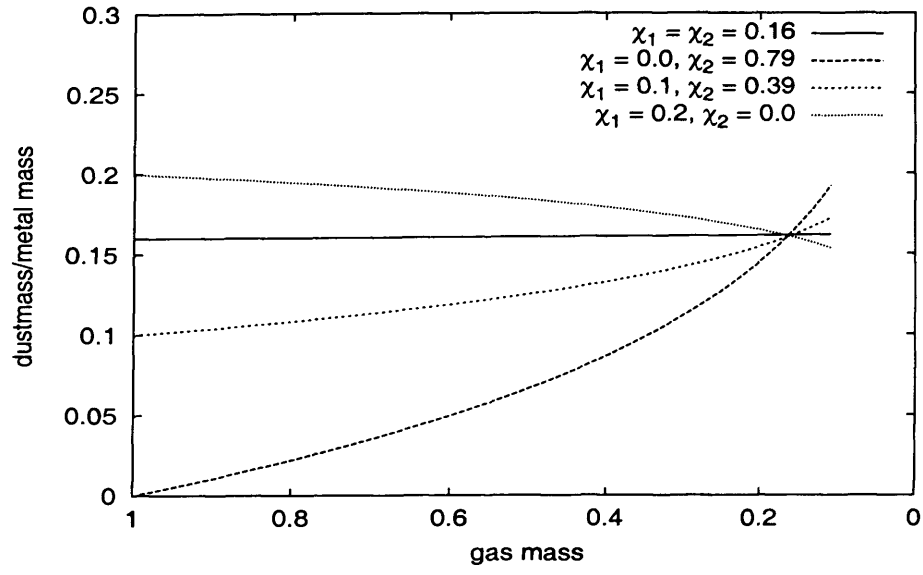

(a)

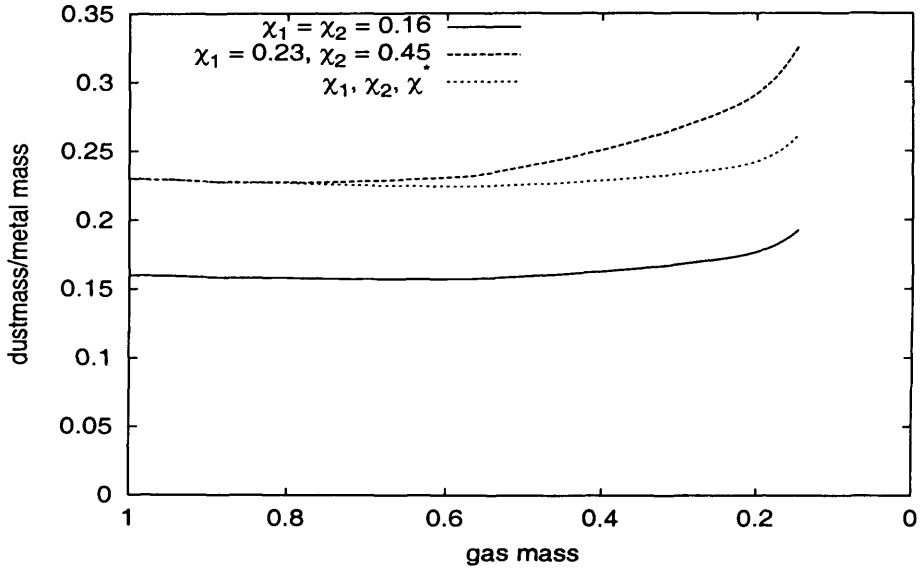

(b)

Figure 2.8: The evolution of the ratio of grain core mass to ISM metal mass (y/z) with gas mass. The evolution using the instantaneous approximation is shown in (a) as in E01 and in (b) we compare our results with our estimated condensation efficiencies. χ_1 is the condensation efficiency of SNe and χ_2 is the condensation efficiency of stellar winds. The solution of Equation 2.22 is shown in (b) by the χ_1, χ_2, χ_1^* in which $\chi_1 = 0.23$, $\chi_2 = 0.16$, $\chi_1^* = 0.22$ (see Section 2.3, Table 2.4). In this model, the dust produced during the TPAGB is considered as a separate dust mode - one in which freshly synthesised carbon is produced and is now a χ_1-type source. The value of p^* (the integrated yield of carbon produced during this phase) is taken as 0.00073 - see text.

2.5.1 Dust Evolution with Metallicity

Putting the relationships from Section 2.3 into the elementary model we obtain Figure 2.9. The variation of χ with metallicity as proposed here does not appear to differ significantly from the elementary model. The only differences are in the decreased grain core mass at low Z and at very low gas masses since it takes longer for the stellar wind dust to build up. The increased yield of carbon from the models given in Marigo (1998) as compared to those in Henry et al. (2000), will also lead to an increased χ_1^* dust mass at low g. This suggests that the theoretical dust production from stellar winds and supernovae does not vary significantly with metallicity.

2.6 Dust in Early Galaxies

The earliest stages of star formation remain a mystery, but one important factor is likely to be the role of dust. The first heavy elements could not have been created until the first stars were formed, but how and when did dust formation turn itself on? Studying high redshift galaxies and the obscuration effects of dust at these epochs should provide some answers. Some differences between early galaxies and our own are quite obvious, these galaxies will certainly have higher temperatures and higher supernova production rates than that found in the Milky Way. Conditions at these earlier times may have not been right for the accretion of mantles within the ISM. The primary source of dust cores here would be Type II SNe, introducing heavy elements into the ISM on timescales of $\sim 10^6$ yrs (if SNe are important as dust formation sites).

When modelling early galaxies we can no longer rely on the instantaneous recycling assumption as used in Section 2.5 to describe the dust production in stars. To

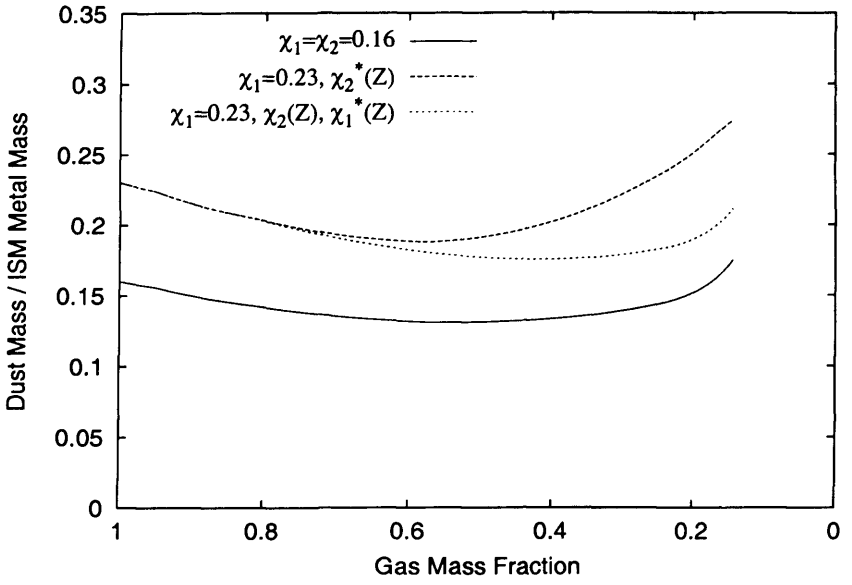

Figure 2.9: The comparison of dust evolution models with galactic evolution (represented by the gas mass). Here we show the grain core mass / ISM metal mass, y/z for different dust condensation efficiencies - the equal χ case and $\chi(Z)$ which includes the variation of χ with metallicity as given in Section 2.3. 'Equalchi' then represents equal condensation efficiencies in SNe and stars, $\chi_1 = \chi_2 = 0.16$. 'Chi2(b)' represents the simple model in which $\chi_1 = 0.23$ and we take the condensation efficiency in stars (including the TPAGB phase), $\chi_2^*(Z)$ (from Section 2.3). The solution of Equation 2.22 is represented by '0.00073' in which $\chi_1 = 0.23$, $\chi_2(Z)$ and χ_1^* vary as functions of Z with $p^* = 0.00073$. This shows the evolution of dust cores/ISM metal mass if we include the dust formed during the TPAGB phase as separate to other stellar winds. we include

be thorough, we require the detailed modelling of dust from stars using yield calculations and the variation with metallicity of the condensation efficiency in stars (Section 2.3). From Section 2.4, we can model dust in early galaxies using Equation 2.24 where χ_2, χ_1 and χ_* are now the *unnormalised* condensation efficiencies. The first term corresponds to the dust produced from recycled yields in stellar winds, the second the dust from freshly synthesised elements produced in massive stars and the third from freshly synthesised carbon in IMS stars with $C/O > 1$. Equation 2.24

was solved numerically with the code described in Section 2.4.

$$y(t') = \int_0^{t'} \int_{m_{\tau_m}}^{m_2} ((1-\gamma(z))[m - m_R(m)]\, z(t-\tau_m)\chi_2 + mp_z\chi_1 + \gamma(z)[m - m_R(m)]\, z(t-\tau_m)\chi^* mp_*)\psi(t-\tau_m)\phi(m)dm\, dt' \quad (2.24)$$

We can compare with another dust evolution model (Hirashita et al. 2002) which represents a young starburst galaxy, SBS 0335-052 with a star formation rate of 1 $M_\odot$ yr^{-1} (Figure 2.10 - note that this only shows the contribution from SNe dust). The model presented here predicts a similar increase in dust mass with time but is offset due to a difference in the average χ_1 term chosen (taken conservatively in our case to be $\sim$ 0.2 for M < 40 $M_\odot$) and the yields from massive stars (in this work taken from Maeder 1992). An indicative dust mass derived from fitting a two component temperature model to the IRAS and ISO observations of SBS 0335-052 gives $M_{dust} \sim 2400$ $M_\odot$ (Dale et al. 2001). The published errors in estimating the flux emitted and the temperatures of the dust are $\sim 20 - 30\%$ leading to large uncertainties in the dust mass derived. As a guide, the model presented here cannot produce this amount of dust until $\sim 10^7$ yrs instead of 4×10^6 yrs from the Hirashita model. This is still consistent with the observed age of the starburst modelled in Hirashita et al. (2002) and places an extra burden on the timescales needed to create dust in galaxies.

Our predictions for a general galaxy with gas mass $g = 2 \times 10^{10}$ $M_\odot$ and star formation rate of 5 $M_\odot$ yr^{-1} are shown in this section. This represents galaxies similar to the Milky Way, with a gas fraction of 15 per cent reached after $\sim$ 10 Gyrs. The delay from long lived stars returning dust to the ISM is evident in Figure 2.11 with significant dust production only seen for $t > 2$ Gyrs. Even if the condensation efficiency is increased from 0.16 to 0.45 which is the maximum value of

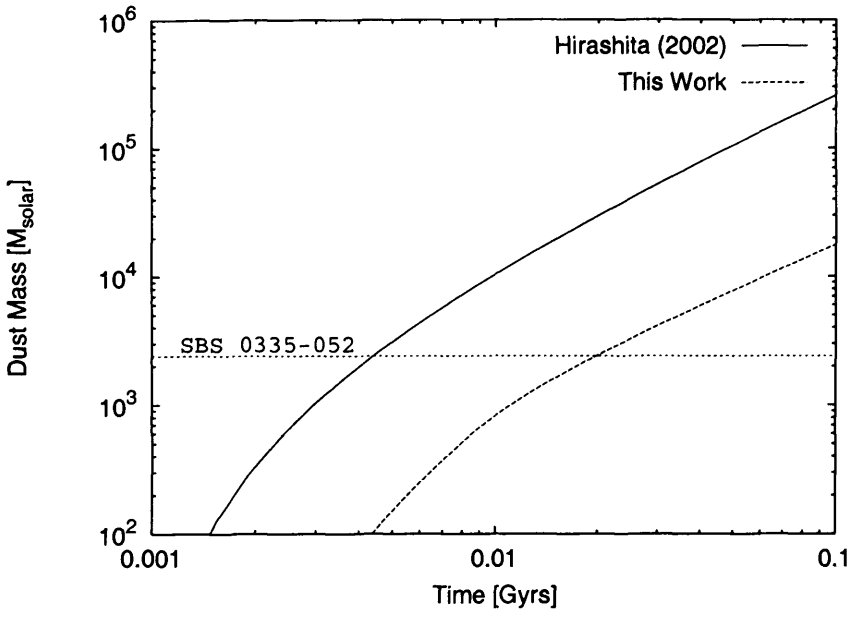

Figure 2.10: The evolution of dust mass with time for a young starburst galaxy using our model with $g = 2 \times 10^{10}$ $M_\odot$, $k = 0.05$ (corresponding to a SFR of 1 $M_\odot$ yr^{-1}) and comparing to the model in Hirashita et al. (2002). The observed value of a galaxy (SBS 0335-052) which matches these properties is given also.

χ_2 allowed (i.e. 45 per cent of all returned metal mass in stellar winds is in the form of dust), we still only have appreciable dust mass after 2 Gyrs. Increasing the SFR rate by five times will result in a higher dust mass at a given time, but the delay from stars is still visible (Figure 2.12). SNe create more dust from a higher SFR, but we still have the delay from SWs. From Figures 2.11 & 2.12 we can clearly see that for significant dust to be available in metal poor, young galaxies it must come from SNe unless star formation rates are very high. This is further highlighted when mapping redshift onto time for different cosmologies as seen in Figure 2.15. To map redshift with time we need to know the cosmology i.e. the values of Ω_m and Ω_Λ. Current values taken from observations of the Cosmic Microwave Background power spectrum and distant Type Ia SNe favour values of 0.3 and 0.7 respectively (i.e. a flat universe with nonzero cosmological constant) known as the concordance model. Other scenarios include $\Omega_m = 1$ and $\Omega_\Lambda = 0$ (again flat but with zero cosmological

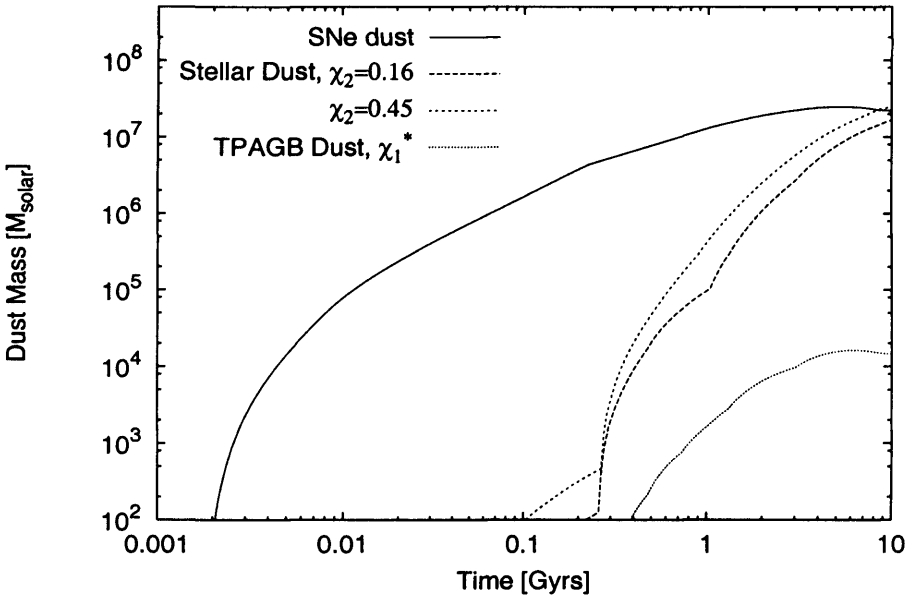

Figure 2.11: Evolution of dust mass fraction, y with time for a galaxy with initial gas mass $g = 2 \times 10^{10}$ $M_\odot$ and SFR of 5 $M_\odot$ yr^{-1} ($k = 0.24$). This is representative of the Milky Way in which the gas fraction reaches 15 per cent after approximately 10Gyrs. 'SNe' corresponds to dust formed in supernovae only with $\chi_1 = 0.23$, $\chi_2 = 0$. 'SW=0.16' represents a condensation efficiency of 16 per cent ($\chi_2 = 0.16$) and 'SW=0.45' represents the max condensation efficiency in winds of 45 per cent. The TP-AGB phase is given by χ_1^*.

constant) or $\Omega_m = 0$ and $\Omega_\Lambda = 0$ (i.e. an open universe). The age of the universe can be calculated from these models using,

$$t = H_o^{-1} \int_z^\infty \frac{dz}{(1+z)^{3/2}\sqrt{\Omega_m(1+z)^2 + \Omega_\Lambda}} \tag{2.25}$$

where H_o is the Hubble constant (chosen here to be 65 km s^{-1} Mpc^{-1} - for a higher H_o the corresponding time for a given redshift is lower) and for the simplest cases Equation 2.25 reduces to

$$\Omega_m, \Omega_\Lambda = \begin{cases} 1, 0, & t = \frac{2/3 H_o^{-1}}{(1+z)^{3/2}} \\ \\ 0, 0, & t = \frac{H_o^{-1}}{(1+z)} \end{cases}$$

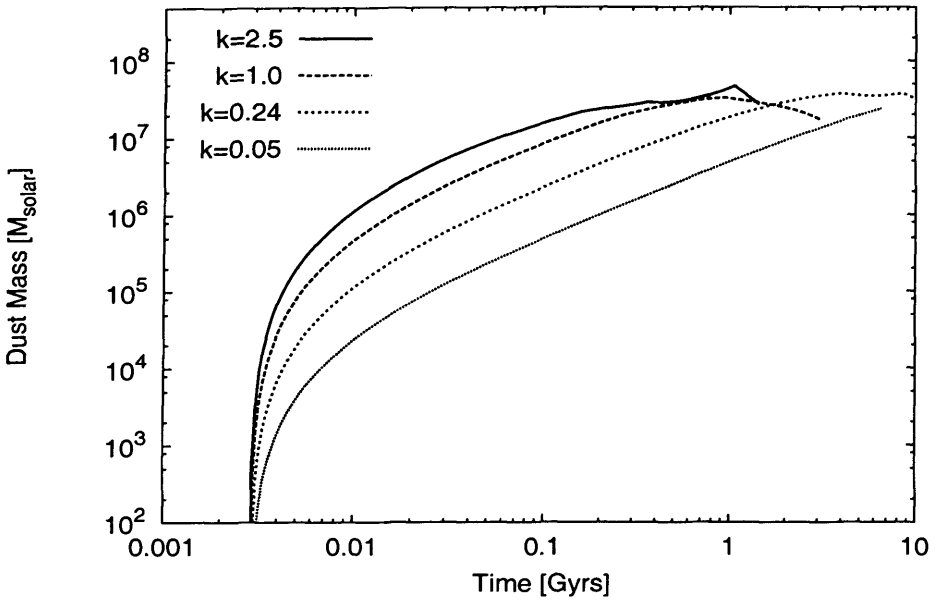

(a)

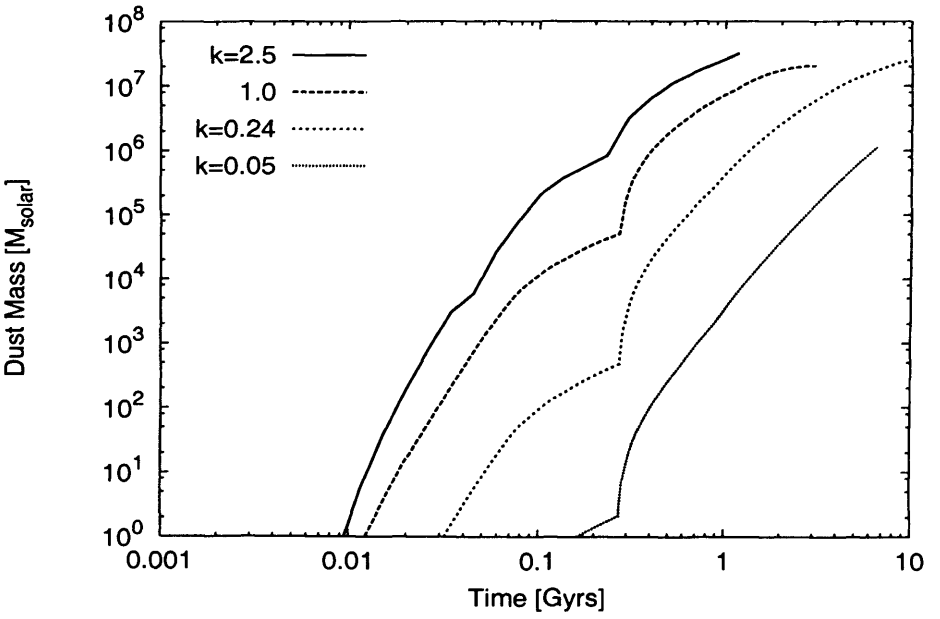

(b)

Figure 2.12: The evolution of dust mass from SNe (a) and stellar winds (b) with time for a given star formation efficiency, k (χ_1 = 0.23, χ_2 = 0.45). For initial gas mass of 2×10^{10} $M_\odot$, we have a SFR for k=0.05, 0.24, 1.0, 2.5 of 1, 5, 20 & 50 $M_\odot$ yr^{-1} respectively. This sequence is likely to represent galaxies from spirals to ellipticals.

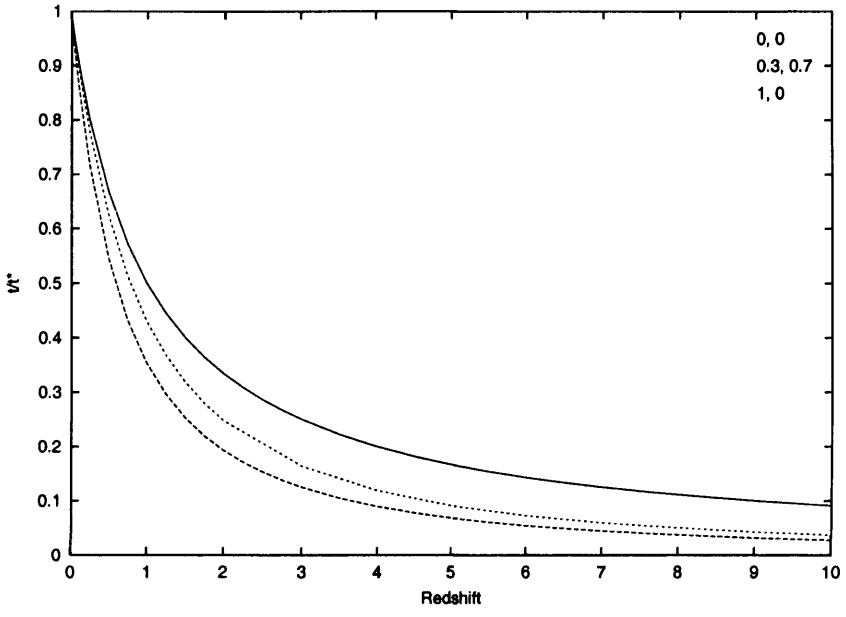

(a)

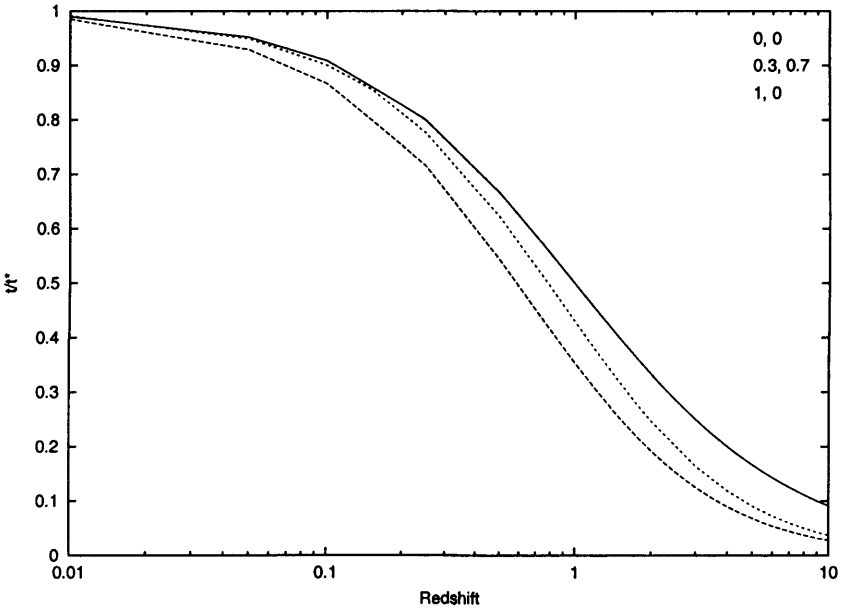

(b)

Figure 2.13: The age of the Universe at a given redshift for the different cosmological models (i) Ω_m=1, Ω_Λ=0; (ii) Ω_m=0, Ω_Λ=0; and (iii) Ω_m=0.3, Ω_Λ=0.7 using Equation 2.25 and H_o = 65 km s^{-1} Mpc^{-1}. The age of the Universe is normalised to the present age (i.e. when $z = 0$) for each model, taken to be the values 1×10^{10}, 1.5×10^{10} and 1.4×10^{10} respectively. Figure (b) shows how the age of the Universe varies over redshift intervals. By a redshift of 1, the Universe is half its current age.

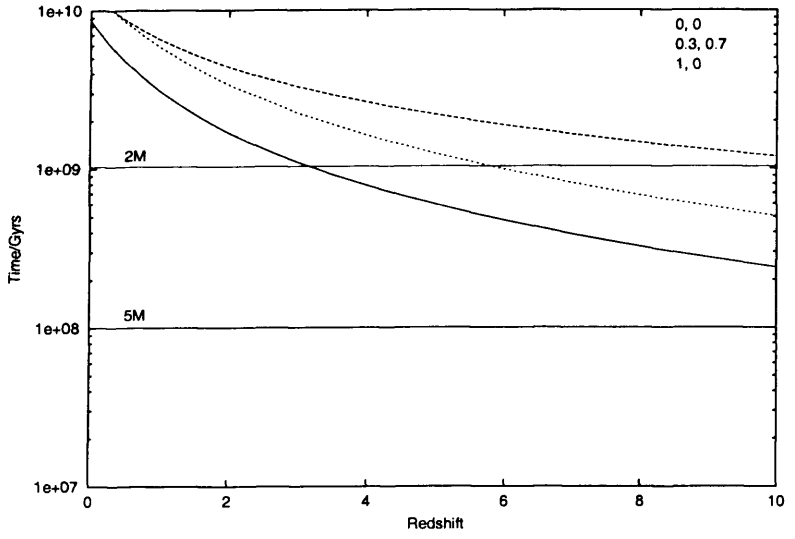

Figure 2.14: The age of the Universe at a given redshift for the three different cosmological models. The lifetimes of stars with mass 2 and 5 $M_\odot$ are shown, with the 2 $M_\odot$ forming earlier on in a concordance cosmology to a 1,0 Universe.

These equations are plotted in Figure 2.13 where the time corresponding to a given redshift is clearly different for each cosmological model. The timescales needed for IMS stars to evolve to the AGB phase is shown in Figure 2.14 where the lifetime of a 2 and 5 $M_\odot$ star is shown vs. redshift. The 2 $M_\odot$ will have evolved earlier on for the concordance model in comparison to the 1, 0 model. Thus when determining the dust evolution with redshift we will show the evolution with different cosmologies. We arbitrarily start star formation at 3×10^8 years corresponding to a redshift of 10 for 1, 0 cosmology and 14 for 0.3, 0.7 model. It is believed that the first generation of star formation may lie between z = 10 - 15 (Mackey et al. 2002) and it allows us to 'push' the time available for dust formation. The evolution of grain core mass with time/redshift starting from $t = 3 \times 10^8$ years is plotted in Figure 2.15. These figures clearly show that for the different cosmologies given and a SFR efficiency of 0.24 (corresponding to a SFR of 5 $M_\odot$ yr^{-1} for a 2×10^{10} $M_\odot$ galaxy), we require redshifts of less than 2, 8, or 4 respectively for dust production in stellar winds

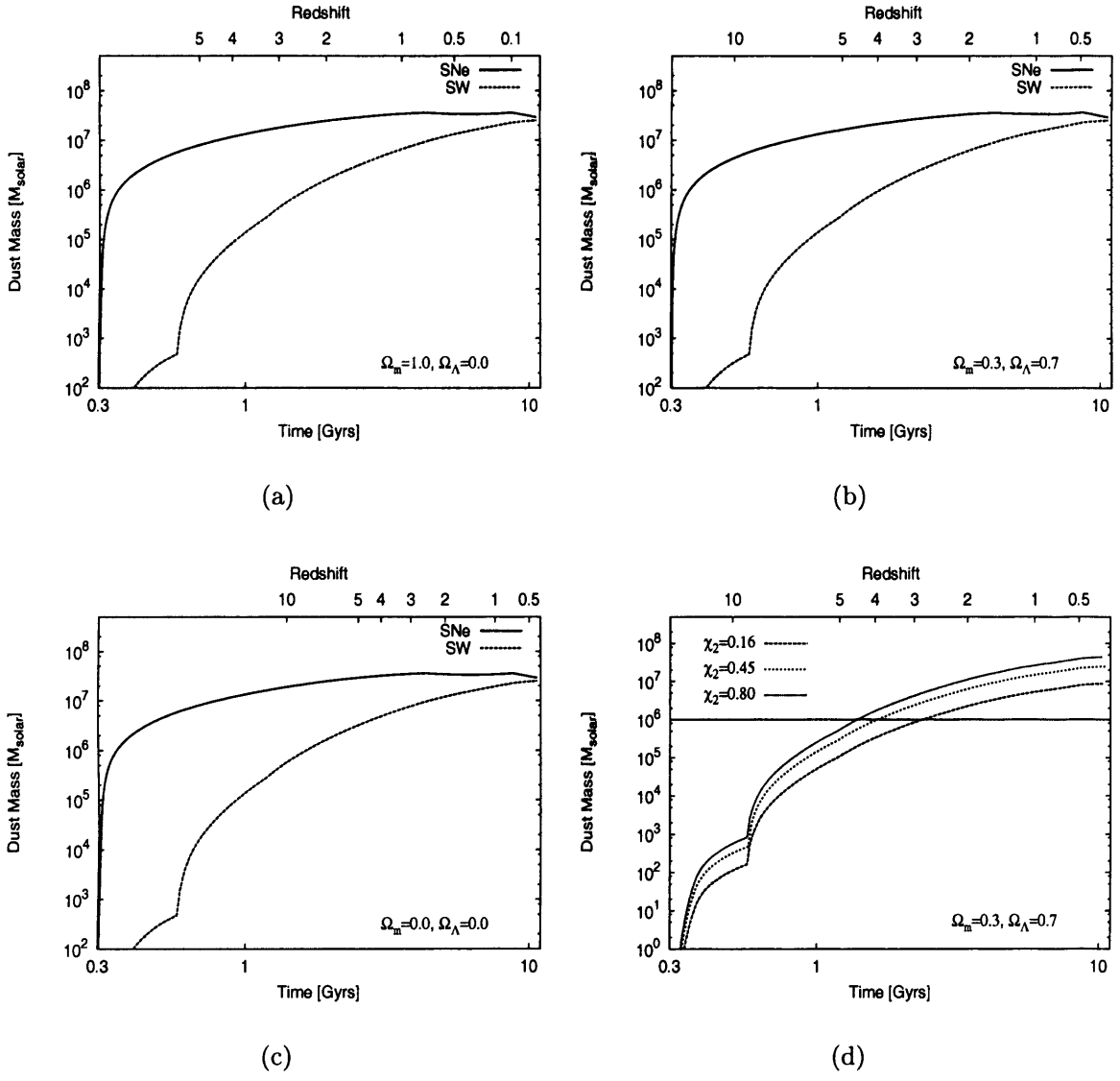

Figure 2.15: The evolution of grain core mass yg ($M_\odot$) with time and redshift for $g = 2 \times 10^{10}$ $M_\odot$, k=0.24 Gyr^{-1}. (a), (b) and (c) represent redshifts calculated for Ω_m=1, Ω_Λ=0; Ω_m=0, Ω_Λ=0; Ω_m=0.3, Ω_Λ=0.7 respectively with star formation 'turned on' at $t = 3 \times 10^8$ yrs (which is the zero point of the x axis for the above graphs). 'SNe' and 'SW' again represent the dust production in SNe and stellar winds with values as above with $\chi_2 = 0.45$. (d) shows what would happen in we take case (c) and alter the value of χ_2 from 0.16, 0.45, 0.8. The solid line represents the value of dust mass we have taken to be a significant amount and the arrow shows the direction of increase in χ_2.

to be significant (i.e. when the dust mass fraction of the ISM (y) is $\geq 10^{-4}$ or alternatively when dust mass for the above system is $\geq 10^6$ $M_\odot$). Even if the the condensation efficiency in stellar winds is increased to 80 per cent, we obtain similar results, Figure 2.15 (c). The amount of dust mass produced depends more on the coefficient of the star formation rate than χ_2. Indeed if the SFR efficiency is 2.5 (50 $M_\odot$ yr^{-1} for this system), dust production in winds reaches this level at redshifts less than 10, 30, 11 for the given cosmology (note: if χ_2 *is* actually 0.16 as proposed here then the problem deepens - significant dust production would require $z < 3$ for $\Omega_m = 0.3$, and $\Omega_\Lambda = 0.7$). So if present cosmology is to be believed we may have a problem for the creation of dust in these high redshift 'dusty' galaxies where z could be as large 10 (Steve Eales - priv.comm.). If no dust is produced in SNe then to observe such galaxies we must set the condensation efficiency in winds at the maximum estimate ≥ 0.45 and have a high star formation efficiency (rate) of $k \geq 1.0$ (SFR ≥ 50 $M_\odot$ yr^{-1} for $g = 2 \times 10^{10} M_\odot$). If this is not the case then significant dust is not available until $z < 5$. If we assume that dust is heated in regions of intense star formation by massive stars then we may relate the observed FIR luminosity from high redshift sources to the current SFR of massive stars ($SFR \propto L_{60}/L_\odot$). The flux densities reached in such observations suggest that SFRs in the early Universe could be as high as 1000 $M_\odot$ yr^{-1} (Gear et al. 2000). With a galactic mass of order 10^{10} $M_\odot$, a SFR as high as this could only sustain itself for about 10^7 years. For the most massive galaxies observed (10^{12} $M_\odot$), a SFR of 1000 $M_\odot$ yr^{-1} (e.g. Scott et al. 2002), represents a star formation efficiency of ~ 1 and is consistent with our nominal galaxy. We would require SFRs greater than this to produce enough dust at redshifts < 5.

For the present day Galaxy, the time-averaged dust injection rate estimated from Figure 2.15 is $\sim 6 \times 10^{-3}$ $M_\odot$ yr^{-1} from stellar winds with a similar amount from

supernovae. The value for stellar winds is in agreement with the dust injection rates given in Whittet (2003) (and Section 1.5). However, present day observations of SNe suggest injection rates which are at least, a factor of 10 lower. Hence we require SNe to have comparable rates to stellar winds to solve the current long-standing issues on the dust budget and the origin of high redshift dust.

2.7 Summary

In this Chapter, I have briefly reviewed the current status of dust production in stars and supernovae. I have also presented the chemical evolution models which can be used to follow the evolution of the gas and metal history of a galaxy. Assuming that the metals condense into dust allows us to use such models to follow the dust evolution. The simple model with an instantaneous approach is presented and extended to include the condensation efficiencies of dust in different sites - stellar winds and supernovae - to determine the source of dust at high redshifts. The low yields of dust estimated in this chapter from stellar winds places a heavy burden on supernovae to produce dust. The conclusions reached in this Chapter are:

- Published literature studies indicate that stars only reach the conditions necessary for dust nucleation during their last (and shortest) evolutionary stage. We found this is the TP-AGB for IMS and the RGB/superwind phase for stars with mass $9 - 20\ M_{\odot}$. No corresponding phase was found for massive stars since their extended atmosphere models do not reach temperatures low enough.

- The most crucial unknown at the current time, in any model of dust evolution is the origin of the dust, i.e. the relative contribution of supernovae and stellar winds to the ISM. By considering current evolution tracks and atmosphere

models we can predict a condensation efficiency of dust formation in stellar winds. We estimated this amount by determining the amount of time the star spends in the right conditions and how much mass is lost in metals during that time. We found that:

  - The normalised dust condensation efficiency in stellar winds can be set to a maximum of 0.45 and is likely to be much lower (0.16). This factor varies with metallicity with lower efficiencies at lower metallicities due to the hotter stellar atmospheres yet this does not affect the overall dust evolution with time.
  - The TPAGB phase appears to be very efficient for dust nucleation, due to the low temperatures and high mass loss rates in this phase. This may produce more carbon dust since during this phase, freshly synthesised carbon is dredged-up from the core. We suggest that this may lead to a dichotomy in the stellar wind condensation efficiency - (1) dust from recycled elements in stellar winds and (2) dust from freshly synthesised elements.

- We compare the chemical yield and dust model with the widely accepted model in D98 and we find differences due to the differences in chosen yields and the values taken for the condensation efficiency of dust from these metals. The lower dust yields in this work place a greater burden on producing dust in the early Universe and even in our own Galaxy today.

- There is no difficulty in producing dusty galaxies at redshifts above 5 if SNe are an important contributor to interstellar dust. If grain core destruction is mainly a result of supernova shocks the process cannot be efficient if grains from the source are to survive. We note that we have ignored dust destruction

mechanisms in this initial model, believing (E01) that such mechanisms may not be efficient and require an extended timescale ($> 10^9$ yrs) before they can significantly alter the grain core content of the ISM. Further studies will be required to demonstrate this is indeed so.

- If SNe are not a dominant dust source, significant dust masses can only be generated at redshifts above 5 by galaxies with very high star formation efficiencies.

- SNe and stellar wind dust production mechanisms are likely to be contributing equal amounts of dust into the ISM at the present time, but this work suggests that SNe may be far more significant in the past.

This Chapter has quantitatively shown that SNe are required to input dust in the early Universe. In the next Chapter, the data reduction processes for reducing sub-mm data with SCUBA are outlined.

Chapter 3

Data Reduction and Analysis

"..the dust that is merely opaque in the visible is self luminous in the infra-Red, and so in the midst of this optical darkness there has appeared a great infra-red light"

N.J.Woolf, 1978

3.1 Introduction

The data used in the next few chapters of this thesis were taken with the Sub-millimetre Common User Bolometer Array (SCUBA) camera on the 15m JCMT telescope on Mauna Kea in Hawaii. SCUBA simultaneously observes at 450 and 850 μm using bolometer arrays of 91 and 37 pixels respectively (Figure 3.1). The arrays are arranged in a close packed hexagon with field of view (fov) $\sim$ 2.3 arcmin which is slightly smaller at 450 μm. At these wavelengths the beam size (Full Width Half Maximum - FWHM) is $\sim$ 8 and 14 arcsecs respectively. Bolometers work by measuring the heat input from incident photons with a 'thermometer'. Electrical connections measure the change in resistance due to the heat change and the voltage drop is recorded. The telescope chops on and off the source at a frequency of 7.8 Hz

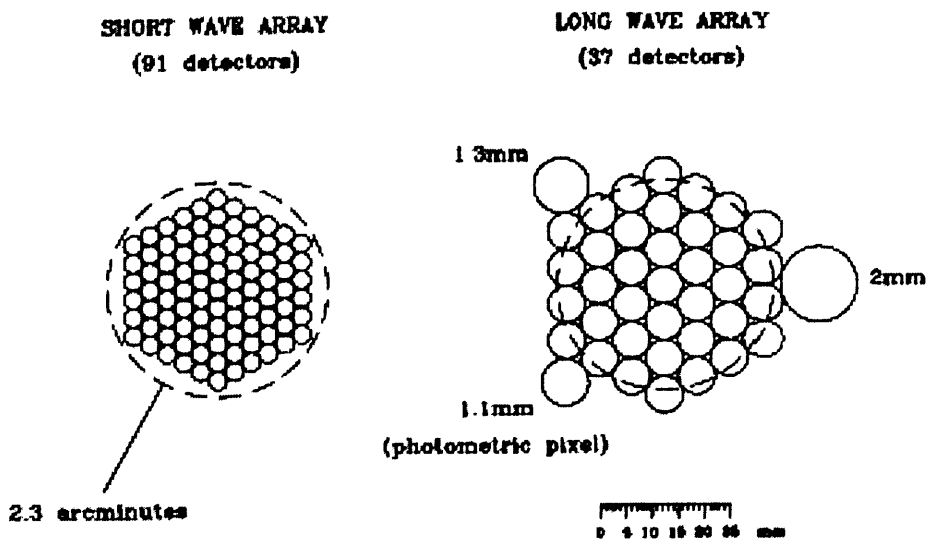

Figure 3.1: The SCUBA bolometer arrays at 450 and 850μm from Holland et al 1999. The larger pixels around the edge of the 850μm array are used for photometry observations.

to cancel out the sky noise.

SCUBA has four different modes, mapping (×2), photometry and polarimetry. The mapping mode has two separate methods, the first called JIGGLE MAP mode in which the camera is jiggled over a region. This ensures that the sky is fully sampled as the hexagonal structure of the bolometers actually serve to undersample the sky (Figure 3.2(a)). The other mode of mapping is SCAN MAPPING. In this mode the beam is scanned over the area and is usually used in objects where the fov of the beam is not large enough to encompass the object, i.e. for extended sources (Figure 3.2(b)). The scanning and chopping occurs in the same direction such that the final image is convolved with the chop. The arrays have to be scanned at three different chop throws (20, 30 and 65 arcsec) and two different directions (RA and Dec) to produce a fully sampled map due to the spacing of the pixels and to ensure the zeros of the chops do not overlap. These two methods are used in the reduction of data in this thesis.

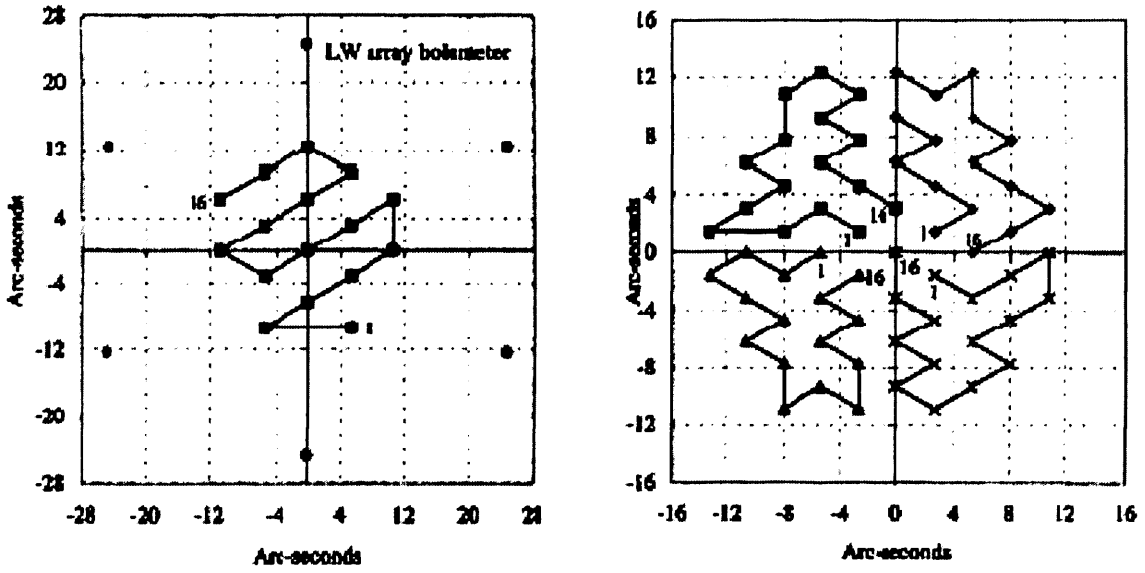

(a)

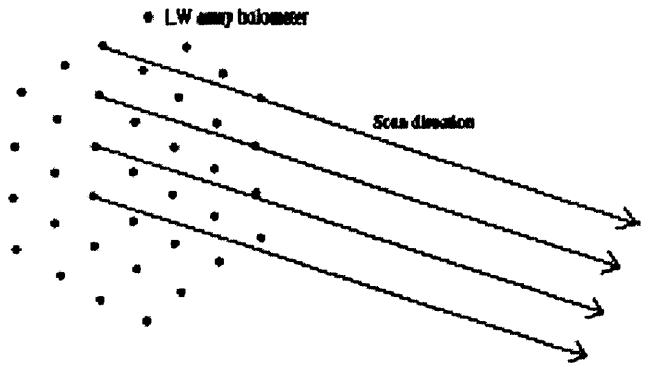

(b)

Figure 3.2: The different mapping modes of SCUBA (a) jiggle map and (b) scan map (shown in one direction only). From Holland et al. 1999.

Observing in the sub-mm regime with ground based telescopes is severely hindered by the atmosphere which absorbs and scatters the incoming sub-mm rays. There are only a few transparent windows through the atmosphere available and even these change on short timescales. The biggest atmospheric absorber is water vapour with the amount of transmission strongly dependent on the wavelength where the shorter wavelength windows are more opaque. Frequent measurements of the opacity are critical in order to calibrate sub-mm data. At 850 μm this is less crucial since in good weather, a 20% error in the opacity alters the source flux observed by 5 - 10% (see Archibald et al. 2002). At 450 μm the same error can affect the measured flux by 50 - 80%. To account for this, SCUBA performs skydip measurements which measure the sky brightness with elevation at regular intervals in the night and fits an optical depth to it. Unfortunately, at 450 μm this process isn't accurate enough due to the fact that the opacities can vary wildly on the same night. The skydips only fit a few points, which will not predict the τ values accurately enough for the given time of the observation of the source. This could create a large uncertainty when measuring the flux levels. Instead, the opacity at 225 μm is measured by the Caltech Submillimetre Observatory every 10 minutes and can be converted to the optical depth in the sub-mm (τ_{850} and τ_{450}) via the following relationships:

$$\tau_{850} = 4.02(\tau_{CSO} - 0.001) \tag{3.1}$$

$$\tau_{450} = 26.2(\tau_{CSO} - 0.014) \tag{3.2}$$

The CSO tau determines the weather band for a given night. Originally, the data were processed by hand using SURF, the SCUBA Reduction Facility, using the SCUBA Reduction Cookbook (Sandell et al. 2001, hereafter S01) and the JCMT website. A faster processing pipeline was used in the following chapters (XORACDR)

which is vital in obtaining accurate fits to the optical depth, due to its automatic option for using CSOFITS (see below). The standard tools for reducing SCUBA data along with the options required for this research project are given below.

3.2 Jiggle Map Reduction

All of the following reduction programs were used in the reduction of the data on Kepler's supernova remnant presented in Chapter 4.

- **Reduce Switch**

  The telescope chops on and off the sky by tilting the secondary mirror in order to remove some of the background signal. Selecting the chop throw (the distance between the source and the sky region) is extremely important when observing as this may affect the amount of signal observed. For Kepler's Supernova Remnant, the radio emission map was used to check the telescope would not chop onto the supernova ring and miss any flux (Section 4.2.1). The telescope also nods the primary mirror to on off positions to produce positive and negative beams. This command actually subtracts the OFF nod position from ON in the raw data.

- **Flatfield**

  Removes sensitivity variations in the bolometers by dividing by a standard flatfield.

- **Extinction**

  The opacities (τ_{850} and τ_{450}) can be derived using skydip measurements taken with SCUBA during the night of the observations. The first two steps in the data reduction are applied to the skydip files and when processing in SURF,

the command **skydip** is used. Following the prompts for date and time of observations, τ is given which should then be inputted when prompted when running the command **extinction**. The fits to the CSO taumeter opacities can also be used automatically when running XORACDR.

- **Change Quality**

  This option allows the user to flag noisy bolometers as 'bad'. After inspecting the data using the graphical interface KAPPA, the bad bolometers are clearly seen and can be thrown out of the data set using **change_quality ndf:b37** which takes the file **ndf** and removes bolometer 37. Using **scunoise** showed that for the Kepler data, three bolometers were consistently noisy at 850 μm - 7, 30, 37. Bolometer 37 was removed from all data sets as it lay on the edge of the array but due to not knowing which bolometers were on the source (not really knowing whether there was a source), the others were kept in order to minimise any loss of information.

- **Scuclip**

  This clips the data to a given σ (normally 4σ at this point) from the mean value of *each individual* bolometer. This removes the largest spikes from all the bolometers.

- **Remsky**

  The sky noise from thermal radiation of the atmosphere is obvious when looking at the data in KAPPA, producing horizontal stripes seen across the array. If the object is small ($d < 1'$), there are a number of pixels which are staring at the blank sky. These off-source bolometers can be chosen as inputs to **remsky** when prompted and the program then subtracts the mean signal from the array (taking this as background sky level). This signal can be added back but

this is normally not done (type **remsky noadd**) as the level is often negative. This process is a little more dubious in the Kepler reduction as it can remove some of the real source if the object is extended. This was dealt with and described in Section 4.2.1.

- **Sigclip**

  This is another clipping method which now clips the data to a given σ (normally 3σ) from the mean value of the *whole array* of bolometers. This affects the noisiest bolometers. This may be done a few times until it stops removing lots of spikes. It is customary to then run **scuclip** on the data again to a 3σ level. This should remove any remaining large spikes (Dunne - private communication).

- **Setbolwt**

  This is used when co-adding multiple data files of the same object. It weights all the files in an input list e.g. kepler850_rebin.inp (which contains a list of all the filenames reduced so far), by comparing the noise in each bolometer in each map to the central bolometer of the first input file. These weights are added onto the input file automatically. Multiple files can be weighted using the command

  setbolwt -filelist = rebin.inp

  where rebin.inp includes the filenames of the NDFs to be rebinned.

  For single maps, a measure of the noise is given using apertures off the source with a weighting of 1 given to the map with the lowest noise.

- **Rebin**

  This command coadds the data and regrids it to an image with specified pixel

sizes (chosen by the user - taken here to be 1 arcsec pixels). When there is more than one data file for a given object, the files may be co-added in rebin using the input file e.g. rebin.inp. This will take the bolometer weightings from **setbolwt** and coadd all the maps of the same object and produce a final image in RA/DEC.

3.3 Scan-Map Reduction

Scan mapping employs a technique in which the telescope is chopped in two orthogonal directions with three different chop throws. This is in order to fully sample the sky and to be sensitive at different spatial frequencies. Consequently the reduction of the data is different to the Jiggle map mode as we now have six maps for each observation. Firstly however, the reduction steps are similar, we run the data through **reduce_switch**, **flatfield** and **extinction**. Noisy bolometers are blanked in the same way but then we change direction a little. The removal of sky noise is a little harder in scan maps as the telescope sweeps over a large region of sky and therefore could have differing emission (S01). Also there is no nodding in the scan map mode so sky subtraction is not carried out on the raw data. This means that there are no longer bolometers continually looking at the sky so the sky noise in scan maps can be a severe problem.

The steps required for data reduction are:

- **Despike**

  Using the surf tool **despike_2** we can clip the data to a standard level above the noise (normally 3 - 4σ). Large spikes are removed using **sclean**.

- **scan_rlb**

This fits a linear baseline for each scan by taking a region free of emission at the end portions of the scan and using this as a base. If the source is weak, the residual can be removed using the option *median* which will take a median instead of a linear fit.

- **Sky removal**

  The SCUBA tool **calcsky** is generally used on scan maps as a way of reducing sky noise. This command uses an in-built algorithm to place each data point into a square bin. Since we expect the mean sky emission to be zero during an observation, the median value in each bin is treated as the source model (e.g. Amure 2003). The source model is subtracted from the data for all bolometers (remembering now that we have no 'sky' bolometers), leaving the sky emission which is then subtracted by **remsky**. If more than one map has the same chop throw and direction they can be coadded. The sky variations can then be examined with linplot and removed using **remsky**. Unfortunately calcsky does actually require significant emission from the object to be able to model it against the background and with extended objects with faint emission, it is likely to actually remove some of the emission. Amure (2003) found that running remsky after calcsky in order to remove the sky emission in faint images actually makes no difference to the image at all. He also showed using **remsky** with the option **all bolometers** will produce optimum results. The sky emission is still correlated across the array so this should pick up the median level as in the Jiggle Map reduction. However, because the array is scanning over a large area and not just jiggling over a small one, we cannot add back the median level to replace any lost source emission due to any variations in the source emission at each point. Not using addback has been shown to have no significant affect on the levels (Amure 2003).

- **Rebin**

  Finally we need to make one map for each chop throw in each direction with identical dimensions and pixel sizes. Each map should be corrected for pointing and each source should show up as a positive and negative in the maps (as they are still convolved with the chop). The size of the maps should be made slightly larger and then cut after rebinning so that they all have the same dimensions. These are finally coadded into one map using **remdbm**. Remdbm forces the sum of all pixels to be zero and hence leaves a negative background level on the map ($\sim$ 0.3 V). This can be added back on using **cadd**.

After original data reduction using the SURF software, a perl script written by Remo Tilanus (priv.comm) was modified and used which ran through the above sequence with no calcsky.

3.4 Calibrating the Maps

The calibrator maps of planets and other point sources were reduced in the same way as the normal source maps *without* clipping (as this procedure confuses the bright central planet for a large spike in the emission and flags it as a noisy region) and were rebinned in ALT/AZ co-ordinates. For a perfect Gaussian beam with FWHM Θ, the beam area is given by $1.134\Theta^2$. However, there is an error lobe associated with the SCUBA beam such that the beam area is $1.134\Theta_A^2\ (E-1)$ where E is the error lobe contribution and Θ_A is the SCUBA FWHM. This must be taken into consideration when calibrating the images.

To measure the flux from an extended source, an aperture containing as much flux as possible should be placed on the source map which gives the signal in Volts (S_{obj}(V)). The same aperture should then be placed over the calibrator map and

the signal measured (S_{cal}(V)). After obtaining the flux of the planets in Jy from the SURF program FLUXES, the calibrated object flux is (Dunne 2000)

$$S_{obj}(Jy) = \frac{S_{obj}(V)}{S_{cal}(V)} \times S_{cal}(Jy \tag{3.3}$$

This method of calibrating has the useful advantage that the error lobes in the beam are automatically accounted for in both the calibrator and the source by the aperture (if it is big enough).

To convert the map from Volts into Jy/beam, we need to obtain the conversion factor (also known as the Flux Conversion Factor (FCF)). This method allows us to compare our calibrators with the nominal SCUBA FCF values. The beam shape during the observations of the planets was measured in GAIA using **cut slices** horizontally across the object. This produces a graph of the beam profile and the Full Width Half Maximum (FWHM) can be read off this to give θ_{m1} (the difference between the x co-ordinates corresponding to the FWHM on either side of the curve). The same method was applied vertically across the source to give the semi-minor axis, θ_{m2}. The beam size for an unresolved calibrator (e.g. crl2688) is then $\theta_A = \sqrt{\theta_{m1}^2 \times \theta_{m2}^2}$. For planets, which are not true point sources, the FWHM measured is related to the Half Power Beam Width (HPBW) by

$$\theta_{A1} = \sqrt{\theta_{m1}^2 - \left(\frac{ln2}{2}W\right)^2} \tag{3.4}$$

where W is the diameter of the planet. The same procedure should be applied with θ_{m2} to give θ_{A2} and $\theta_A = \sqrt{\theta_{A1}^2 + \theta_{A2}^2}$. The flux in the beam is calculated by accounting for the coupling of the planet to the beam

$$K = \frac{x^2}{1 - e^{-x^2}}, \quad \text{where} \quad x = \frac{W}{1.2\theta_A} \tag{3.5}$$

If S_{tot} is the true flux of the planet, the flux in the beam is given by

$$\mathrm{S_{beam}} = \mathrm{S_{tot}/K} \qquad \text{(Jy/beam)} \tag{3.6}$$

We can now convert the original voltage map into a calibrated flux map via the relationships:

$$\mathrm{FCF} = \mathrm{S_{beam}/V_{peak}} \qquad \text{(Jy/V/beam)} \tag{3.7}$$

$$\mathrm{FCF} = \mathrm{S_{beam}/V_{tot}} \qquad \text{(Jy/V/pixel)} \tag{3.8}$$

where $\mathrm{V_{peak}}$ is the peak value in Volts from the object and $\mathrm{V_{tot}}$ is the total flux in a given aperture placed over the object. For a perfect Gaussian beam shape, the area under the beam should be $1.134\theta_A^2$. The FCFs would then be related by

$$1.134\theta_{\mathrm{A}}^2 = \frac{\mathrm{Jy/beam/V}}{\mathrm{Jy/pixel/V}}$$

but in reality, the error lobe of the beam will contribute further to the flux such that

$$1.134\theta_A^2 E = \frac{\mathrm{Jy/beam/V}}{\mathrm{Jy/pixel/V}} \tag{3.9}$$

with error lobe $E - 1$. This is accounted for when using the same apertures on the same objects but it affects Jy/V/pix measurements quite significantly and is a good measurement of the quality of the observations. The nominal FCF values taken from the SCUBA website[1] during 2003 are $\sim 203 - 220$ Jy/beam/V at 850 μm and $280 - 333$ Jy/beam/V at 450 μm.

[1] http:www.jach.hawaii.edu/JCMT/

3.5 Errors

The errors in each observation can be attributed to (S01):

Shot Noise

This is known as statistical noise of the map and is normally given as $\sigma_{shot} = \sigma_{pix}\sqrt{N_{ap}}$ where σ_{pix} is the standard deviation of pixels in a region off the source and N_{ap} is the number of pixels in the aperture used. Due to the correlation between 1 arcsec pixels in a SCUBA map this formulation cannot be used as it underestimates the noise. Studies by Dunne (2000) show that the shot noise for a 1 arcsec-pixel map at 850 and 450 μm is given by

$$\sigma_{shot} = 8\sigma_{pix}\sqrt{N_{ap}}$$

$$\sigma_{shot} = 4.4\sigma_{pix}\sqrt{N_{ap}}$$

Sky Noise

This error arises from a non zero background sky level which remains even after correct reduction of the data. This can be measured using (Dunne, 2000)

$$\sigma_{sky} = \sigma_{ms}N_{ap}$$

where σ_{ms} is the error in the mean sky level -

$$\sigma_{ms} = \frac{1}{\sqrt{n}}\left[\frac{\sum_i^n (S_i - F_{ms})}{n}\right]^{1/2}$$

S_i is the sky level in the ith aperture out of n apertures (taken to be 10 in this work) and F_{ms} is the mean sky value of the apertures.

Calibration Error

From Dunne (2000) the calibration error, σ_{cal} is thought to be $\sim$ 10% at 850 μm and $\sim$ 15 – 20% at 450 μm. For less careful work, σ_{cal} is > 15% and 20 – 30% respectively.

The final error is given by

$$\sigma_{tot} = \sqrt{\sigma_{shot}^2 + \sigma_{sky}^2 + \sigma_{cal}^2}$$

After these basic reduction techniques were applied to the data, simulated noise maps made by a program written by Steve Eales (see Eales et al. 2000) were produced. This produces 1000 artificial data maps from the standard deviation of the bolometer arrays which are analysed with SURF in the same way as the real data. Using **mstats** in KAPPA, the 1000 maps were stacked to produce a noise map, giving the noise at each pixel. A signal-to-noise (S/N) map can then be made by dividing the real map by the noise map (using **div** in KAPPA). This has the advantage that the edge-effects and noisy bolometers should disappear as well as producing a higher quality image by increasing the signal strength. Problems may arise as these S/N maps may contain more false 3σ detections than expected randomly (Dunne 2000) so thorough checking of the noise levels is required in data reduction.

3.6 Summary

In this Chapter, we have discussed the reduction techniques used in reducing sub-mm observations, which are used in analysing the observations presented in Chapters 4 and 5. SCUBA has been a significant and powerful tool for submillimetre astronomy in a wide range of topics. It has been responsible for revolutionising our ideas from the largest scales in the high redshift Universe down to protoplanetary clouds. It has detected dusty galaxies at high redshifts (Isaak et al. 2002; Eales et al. 2003), a significant fraction of the population of galaxies producing the Far infra-red (FIR) background (Smail et al. 1997) and provided the first statistical survey of local sub-mm sources (Dunne et al. 2000; Dunne & Eales 2001). It has also discovered new populations of Class 0 protostars (Motte & Ward-Thompson. 2001) and potential planetary systems around a number of stars (e.g. Greaves 1998). The impact of SCUBA on astronomy in the sub-mm regime has been enormous and as reported here, this work will suggest that current knowledge on the origin of dust may not be as clear cut as once thought (see Chapters 4 & 5).

Chapter 4

Dust Production in Supernovae I

4.1 Introduction

In this Chapter, from observations of young remnants in the sub-mm regime, I present evidence that significant amounts of dust may be produced in supernovae. The observations of Kepler are presented, analysed and the dust mass of the remnant is calculated with a statistical treatment of the errors. Our suggestive observations of Cassiopiea A are given a brief overview and I include the recent but incomplete observations of a third remnant, Tycho. The work in this chapter has been published in Morgan et al. (2003) and Dunne et al. (2003).

4.2 Kepler's Supernova Remnant

Kepler's SNR has been observed at many wavelengths, but never before in the sub-mm regime. The supernova was first observed in 1604 with an absolute magnitude of -3 and was closely studied by Johannes Kepler. The remnant is clearly shell-like with an observable shell at around $\sim 3'$ in diameter. The distance to Kepler is hotly debated with previous estimates placing the remnant at 3 - 12 kpc. A recent study

by Reynoso & Goss (1999) determined a distance of 4.8 - 6.4 kpc. Here we take the distance to the remnant as 5 kpc (+1.4 -0.2 kpc). At this distance, the remnant has a diameter of 4.8 pc (+1.5 -0.1) pc.

The progenitor and type of Kepler's SN is controversial. Originally it was thought to be a Type Ia SN due to its light curve and its distance from the Galactic plane ($\sim$ 600 pc) indicating the progenitor was an old population II object (low mass, evolved star). However, slow moving optical knots, present in the region around the SNR, show substantial overabundance of nitrogen which is most naturally explained by the Carbon-Nitrogen-Oxygen cycle in massive stars (as discussed in Bandiera 1987; Borkowski et al. 1992). The slow expansion velocity and high densities of the knots ($n \geq 1000$ cm^{-3}, Blair et al. 1991) suggest they were not ejected in the SN explosion but rather in an earlier stellar wind which again suggests a massive star progenitor. Further evidence for a previous stellar wind comes from recent models for the X-Ray emission from the remnant. These models require ambient densities of a few H atoms per cubic centimetre (Kinugasa & Tsunemi 1999) which is a 100 times greater than the local ambient density of the hot, tenuous ISM expected at 600 pc above the galactic plane (Whittet 2003). All these observations indicate that there is dense circumstellar material (CSM) predating the SNR which is at odds with the theory of Type Ia SNe in which typically no CSM is present. The evidence appears to indicate that Kepler's SN should be classified as a Type Ib (Section 1.4). In this scenario, significant mass loss occurs during the red supergiant phase of a massive star, exposing the stellar core just before the explosion (Borkowski et al. 1992). Such an explosion would then create a light curve similar to that seen in Type Ia SN but the progenitor is now a young, massive star (M $>$ 10 M$_{\odot}$) with Type II SN-like ejecta (without Hydrogen in the spectra). Extensive studies of radio emission from SNRs have shown that most Type II progenitors were RSGs

and Type Ibs were more compact members of binary systems (Panagia 2000 and refs therein). Bandiera (1987) suggested that Kepler was a massive star, ejected from the Galactic plane and moves through its own stellar wind. This would compress the wind material into a bow shock in the direction of motion and produce the N-S asymmetry seen in the X-Ray and radio observations. This model also explains why a massive star (normally confined to the Galactic plane) is at the location of Kepler's SNR.

We can also determine whether or not Kepler is a Type II-like SN by studying the dynamics of the shell. The position of the shockfront in each of the SN phases (Section 1.4) is characterised by a power law, $R \propto t^m$, where m is the expansion parameter. This relationship changes if the ejecta are expanding into an inhomogeneous surrounding medium as this will change the evolution of the shock. Ejecta with power law density profile characterised by n expand into circumstellar material with density index s expands via the following relationship:

$$R \propto t^{\frac{(n-3)}{(n-s)}}$$

(Hughes 1999). If the ambient density and the ejecta are uniform then $s = 0$. If the ejecta expand into dense material from a prior stellar wind phase then $s = 2$. For these cases, $m = 0.4 - 0.57$ for $s = 0$ and $m = 0.67 - 0.8$ if $s = 2$. This allows us to distinguish between Type Ia and Type II progenitors since Type Ia explosions will have no ambient material from a prior stellar wind phase and will hence follow an $s = 0$ evolution. Observations in the X-ray and radio wavebands for Kepler suggest that the expansion rates are 0.239 % yr^{-1} and 0.11 % yr^{-1} respectively. This allows us to calculate m since $m = dlnR/dlnt$ giving $m = 0.93$ and 0.54 respectively. With the CSM density profile characterised by $s = 2$ and $m = 0.93$, the density

profile of the ejecta is $n \sim 15$ giving a steep density distribution similar to RSG atmospheres (Hughes 1999). If $s = 0$ then to explain the high X-ray expansion rate, we need $n > 40$ i.e. without the presence of a dense CSM, we require a much steeper and more unrealistic density distribution of the ejecta to explain why the X-Ray emission is expanding so fast. The expansion parameter for Kepler is higher than $m = 0.4$ expected for the Sedov phase (suggesting it is in a phase which is not yet dominated by swept up material) and it appears to correspond with the $s = 2$ case (SN expanding into a surrounding dense CSM). This suggests a massive star progenitor with expanding ejecta in an early evolutionary phase.

Kepler is therefore an ideal SNR to study not only for the investigation of dust formation in SNe but also to determine whether or not dust can form in massive stars in the early Universe in timescales $< 10^7$ years.

4.2.1 The Data

The observations of the Kepler SNR were originally taken by Rob Ivison and Steve Eales on five different nights during 05/2001 - 05/2002 in Jiggle map mode. Four maps were made in four quadrants around the centre of the remnant (RA $17^h\ 30^m\ 41^s$, Dec $-21°\ 29'\ 30''$) to encompass the whole shell which is approx. 3 arcmin in diameter. Each observation was made with a chop throw of $180''$ using the radio image as a guide to ensure chopping and nodding off the source. The data were taken in Grade 1/2 weather with the atmospheric opacities ranging from $0.11 < \tau_{850} < 0.25$ and $0.34 < \tau_{450} < 1.30$. The details are listed in Table 4.1.

The data were reduced using the SURF software package (S01). Corrections for atmospheric absorption using the opacities (τ) were applied at both 850 and 450 μm derived using skydip measurements with 'CSO-fits' processed through ORACDR using the CSO-fit option. Noisy bolometers were flagged and large spikes were

Date	Name	Run N^o	N^o Ints[a]	τ_{850} [b]	τ_{450} [b]
12/05/2001	kepler1	60	10	0.25	1.30
	kepler1	66	5	0.25	1.26
	kepler1	68	10	0.24	1.25
	kepler1	70	25	0.24	1.23
	kepler1	75	15	0.24	1.21
18/03/2002	kepler2	12	25	0.11	0.34
	kepler2	14	25	0.14	0.59
	kepler3	21	25	0.19	0.90
	kepler3	23	12	0.20	0.97
20/03/2002	kepler3	61	25	0.24	1.24
	kepler3	63	13	0.24	1.22
	kepler4	69	25	0.24	1.22
	kepler4	72	25	0.25	1.29
21/03/2002	kepler4	76	20	0.13	0.53
04/05/2003	keplernew	47	19	0.25	1.27
	keplernew	51	19	0.23	1.19
	keplernew	58	14	0.23	1.13
	keplernew	60	12	0.24	1.12
	keplernew	62	12	0.22	1.14

[a]Number of integrations.
[b]τ values calculated from CSO polynomial fits to the skydip data.

Table 4.1: The sub-mm observations of Kepler's SNR taken over a period of two years. This table includes all the data files reduced to obtain the final map.

removed from all the bolometers using a 4σ clip. Any noise correlated across the array (i.e sky noise) was removed using the SURF program REMSKY and the data were clipped to 3σ from the mean level of the array. The individual bolometers were once again clipped to remove any further spikes to the 3σ level. The program SETBOLWT was used to weight the noise in each bolometer relative to the central bolometer in the first map and the maps were rebinned. The mean sky noise was removed from all the bolometers in the array, which should reduce the background level to zero. However, a measure of the sky noise in apertures around the source showed the background was actually negative so the mean value of the level in the apertures was added back on. This should then account for any flux lost from the source during REMSKY. This slightly affected the flux levels by adding on an extra flux level of $\sim 0.5\times$ the noise level in the maps.

Monte-Carlo noise maps were made using a program written by Steve Eales (following the method in Eales et al. 2000) and the real image was divided by the noise map. After the original data were reduced, there appeared to be a high level of noise still present in the outer regions of the remnant. Dividing by the noise maps suggested that this could be real emission but was confused with the noise at the edges. To determine if this was indeed real signal from the source, we carried out further observations with SCUBA in service mode to look at the north and south eastern quadrants again. These new observations greatly improved the S/N in the centre of the northern limb by $\sim 3\sigma$ at 850 μm. The southern regions however remained quite noisy even with the extra integrations. The final coadded S/N images at 450 and 850 μm along with the corresponding noise maps are shown in Figure 4.1. At 850 μm, the peak signal is in the northern limb ($\sim 12\sigma$) with a peak of 6σ in the south-west. At 450 μm these peaks are 5 and 4σ respectively (the peaks on the original data maps were only 3 and 2σ).

The north-eastern and south-western (north is up and east is on the left) quadrants were observed on nights with the worst atmospheric conditions which could explain why there is less emission in these regions especially at 450 μm which is very sensitive to the weather conditions. The average optical depth for these two quadrants was 1.26 and 1.1 at 450 μm respectively. The observations for the N-W and S-E quadrants had much lower opacity with $\tau_{450} = 0.99$ and 0.47 and hence more signal would be observed in these regions. The overlapping region in the centre will also have a higher noise especially at 450 μm where the smaller field of view has meant that this has been considerably undersampled. The high levels of noise in these regions are clearly seen as bright spots on the noise maps (Figure 4.1 (c) & (d)). **Note:** in the N-W region of the remnant there appears to be some flux at 450 μm which is not present in the 850 μm image at all. Overlaying the 450 contours onto the 850 shows that there is definitely a discrepancy between the two wavelengths. At first glance this may appear confusing as both wavelengths are observing the same population of dust. On careful consideration however, we realised that the bolometers in the 850 μm array during these observations were very noisy, particularly in this region and due to the good weather conditions when observing this quadrant, the 450 μm observations were actually comparable to the 850. After creating the artificial noise maps, the bright region in the 850 noise map quite clearly shows that this is a particularly noisy part of the array, whereas in the 450 noise map, there are no problems with the bolometers in that part of the array. Thus the 450 emission here was included in the flux measurements, although it must be stressed that this emission hidden from us at 850 μm may have produced a lower flux measurement at this wavelength. This is a nice example of the noise maps visually showing which parts are particularly noisy and why the 450 and 850 measurements may not always agree.

Date	Name	Run	Ints	τ_{850}	HPBW	S_{tot}	Jy/b/V	Jy/p/V	E
12/05/01	crl2688	79	3	0.2	15.4	5.9	231	0.8	9%
18/03/02	Uranus	27	3	0.2	14.4	60.9	270	0.9	29%
20/03/02	Uranus	76	3	0.3	15.9	61.5	280	0.9	11%
	Mars	16	3	0.3	15.8	278.9	245	0.8	5%
21/03/02	Uranus	80	3	0.1	15.3	62.7	250	0.8	12%
04/05/03	Mars	54	2	0.2	15.3	1375.3	256	0.7	34%
						Av.	*255*		

Table 4.2: The primary calibrators used to obtain the FCFs for the 850 μm data for each night using the methods in Chapter 3 and Equation 3.7. Columns are (1) Date of observation. (2) Name of calibrator. (3) Run number. (4) Number of integrations in secs on the source. (5) Atmospheric opacity at 850 μm. (6) Half Power Beam Width, θ_A. (7) Total flux of source from the program FLUXES. (8) Flux Conversion Factor in units of Jy beam^{-1} Volts^{-1}. (9) Flux Conversion Factor in units of Jy pixel^{-1} Volts^{-1}. (10) Error lobe contribution (Equation 3.9) measured in an aperture of radius 65″.

How realistic are the simulated noise maps? To check the noise levels on the artificial noise map, an aperture was placed on both the noise map and the original sub-mm maps (taking care to be off source) and the mean level standard deviation of the pixels in the aperture was measured for the two maps respectively. The noise levels from the smoothed 850 μm and 450 μm maps were $\sim$ 8 and 46 mJy/beam respectively. Correspondingly, in the artificial map these levels are $\sim$ 6 and 47 mJy/beam so the two methods agree quite well. Are the peaks in the S/N map real? The number of beams in each image is $\sim$ 64 at 850 μm and $\sim$ 180 at 450 μm with a probability of getting a random 3σ detection of 0.0026. We therefore estimate the number of false 3σ detections to be less than 1 in both images.

To obtain the observations in Janskys, the method outlined in Chapter 3.4 was used to obtain the FCF for each night (Tables 4.2 & 4.3). These conversion factors were not actually used for calibrating the final map but are useful to show how widely the maps on different nights vary in calibrating the data. The FCF's were within 10% at 850 μm and 20% at 450 μm. These conservatively give calibration errors of 15% and 20% respectively.

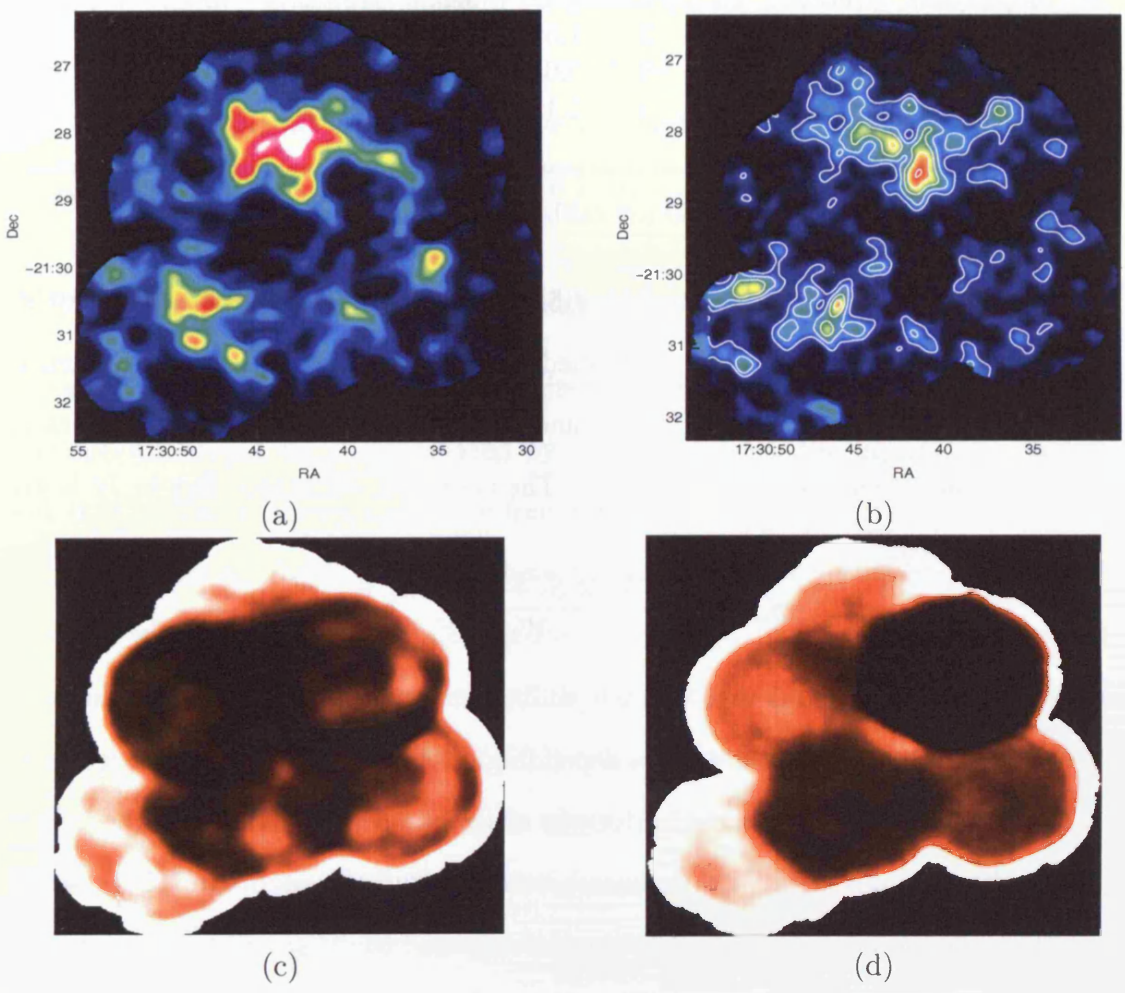

Figure 4.1: Signal/Noise maps of the Kepler SNR with SCUBA at (a) 850 μm smoothed by 14″ (mean background noise level is 7 mJy/beam with peak signal of 12σ). (b) 450 μm smoothed by 14″ with contours $1.5\sigma + 1\sigma$ ($1\sigma \sim 46$ mJy/beam). The emission at 850 μm follows the N-S asymmetry seen in observations at other wavelengths whereas the 450 μm is distributed differently. This is likely to be due to synchrotron contamination at the longer sub-mm wavelengths. (c) 850 μm smoothed simulated noise image with bright regions showing the highest level of noise. (d) 450 μm smoothed simulated noise image. North is up and East is on the left for all images.

Date	Name	Run	Ints	τ_{450}	HPBW	S_{tot}	Jy/b/V	Jy/p/V	E
12/05/01	crl2688	79	3	1.2	9.5	23.2	335	5.1	28%
18/03/02	Uranus	27	3	0.9	7.9	160.8	451	5.2	23%
20/03/02	Uranus	76	3	1.4	9.4	162.4	458	4.5	10%
	Mars	16	3	1.5	9.4	1003.6	337	4.4	17%
21/03/02	Uranus	80	2	0.6	8.4	161.2	313	3.6	8%
04/05/03	Mars	54	3	1.1	6.3	5062.9	293	1.6	104%
						Av	*365*		

Table 4.3: 450 μm calibrators. Columns as in Table 4.2.

The final image was actually calibrated by co-adding calibrators with the same chop throws. The files were rebinned once the relative offsets were taken care of using the KAPPA **centroid** command to produce one final '*super*' calibrator map in the same way as the Kepler files. The co-added calibrator flux in Jy is given by (Dunne 2000)

$$S_{cal-co} = \frac{W_1 \times S_1 + W_2 \times S_2 + ...W_n \times S_n}{W_1 + W_2 + ...W_n} \tag{4.1}$$

where S is the total flux of each calibrator using FLUXES. W is the weighting factor applied to the calibrators depending on how many integrations were spent on Kepler for the night the calibrator was observed. The flux in Volts was measured in 10 elliptical apertures with diameter $\sim 80''$ around the remnant. This aperture was then placed on the co-added calibrator map and the final calibrated flux in Jy was found using

$$S_{kep}(Jy) = \frac{S_{kep}(V)}{S_{cal-co}(V)} \times S_{cal-co}(Jy) \tag{4.2}$$

As a check, each planet map was also calibrated to obtain the FCF for the maps each night and we multiplied the individual maps by the FCF. These were then co-added to give a final map of Kepler in Jy/beam. This will have more errors as the calibrator apertures will have to be different on each night so a constant aperture cannot be used all over the map. The final Jy/beam map was similar to the one

obtained using the *super* calibrator map.

The noise in the aperture was estimated by directly placing the calibration aperture on the Monte Carlo noise maps or by measuring the standard deviation in the aperture on the original map. The total errors at 850 and 450 μm data are estimated to be $\sim$ 15% and $\sim$ 24% respectively. The final sub-mm fluxes with errors are $S_{850} = 1.0 \pm 0.16$ Jy and $S_{450} = 3.0 \pm 0.7$ Jy.

4.2.2 The Spectral Energy Distribution

Is the sub-mm emission due to thermal emission from circumstellar dust? To explore if the sub-mm could be contaminated by free-free we use the argument given in Dwek (1987). The contribution of the free-free for supernovae is different to that of a classical stellar wind (Chapter 6), where the large mass of optically thick ionised gas in the wind provides for a high free-free luminosity. In SNe however, the mass of the ionised material is small relative to the mass shocked by the expanding ejecta and also decreases with time. Dwek (1987) estimates the free-free contamination in the IR for Cas A to be ~ 7 M_{ion} $(M_{\odot})$Jy where M_{ion} is the mass of ionised material. Estimates of the optically emitting material range from $0.01 - 0.25$ $M_{\odot}$, only some of which will be radiating free-free and hence the free-free emission is negligible at IR ($<$ 1% at 100 μm and $<$ 2% at 850 μm). For Kepler, the relationship is $\sim 2.5 M_{ion}(M_{\odot})$Jy (scaling for the difference in distance). The mass of optical material is less than that in Cas A's remnant, i.e. $\ll 0.1$ $M_{\odot}$ and hence the free-free flux would be $\ll$ 1Jy in the IR.

However, supernovae are strong sources of synchrotron radiation which may contaminate at the longer sub-mm wavelengths (Green 2001). The five radio measurements from the literature (plotted in Figure 4.3) are well fitted by a power law slope, $S_{\nu} \propto \nu^{\alpha}$ where $\alpha = -0.71$. The sub-mm flux is in excess of this slope hence the

emission appears to be from cold dust. A point by point comparison of the sub-mm maps with the radio also implies that there is submillimetre emission in excess of the synchrotron especially in the south of the remnant where there is very little radio emission but a significant amount of sub-mm flux. The radio image shows the well known N-S asymmetry associated with the presence of a bow shock, which is clearly seen in the 850 μm image but is not present in the 450 μm map. Using Equation 4.3, the contribution to the sub-mm flux from the synchrotron is 30% at 850 μm and 6% at 450 μm,

$$S_{850} \propto S_6 \left(\frac{\nu_{850}}{\nu_6}\right)^{\alpha} \tag{4.3}$$

Perhaps the strongest evidence for the sub-mm emission resulting from the emission from cold dust is the ratio of the sub-mm fluxes. The fact that this is ~ 3 makes it practically impossible to explain this by some synchrotron process. The VLA radio image of Kepler (kindly provided for us by T. Delaney and shown in Figure 4.2 (a)) was used to correct for the contamination from the synchrotron. To remove the contribution, the radio images were first convolved to the beam size of SCUBA (after changing the pixel sizes to 1 arcsec pixel^{-1}). This was smoothed to the same resolution as the 850 μm and scaled to produce an image in Jy/14″ beam. The synchrotron emission was then subtracted from the sub-mm images (Figure 4.2 (b)). The N-S asymmetry previously seen in the 850 μm regime has now been removed showing that the two sub-mm wavelengths now have similar dust distributions, implying that this is in fact emission from cold dust. The peaks on the 450 and 850 μm synchrotron subtracted maps do not appear to coincide with each other but this may be due to the low signal-to-noise on the 450 map and the fact that we are extrapolating a long way in frequency from 5GHz to the sub-mm waveband. Estimating the synchrotron contribution to the sub-mm assumes that the spectral index is constant over the remnant. This is not true with α known to vary from

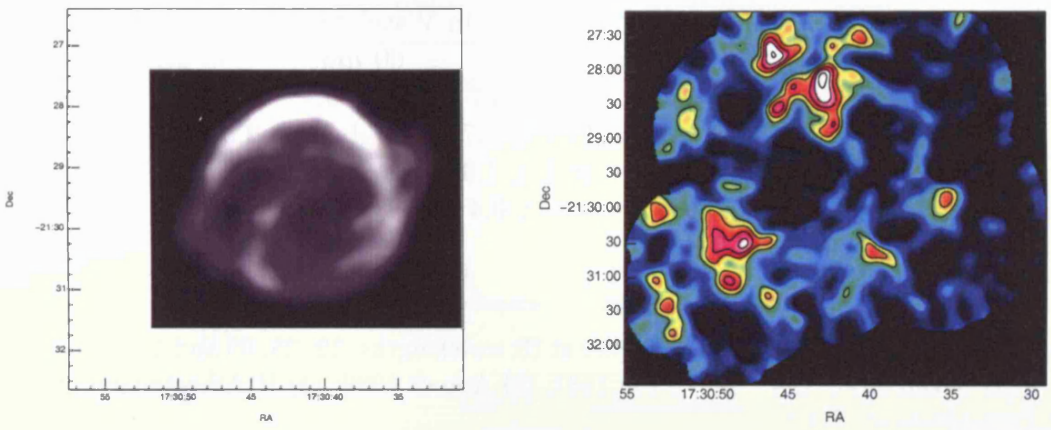

(a) (b)

Figure 4.2: (a) The smoothed 5GHz VLA image of Kepler kindly provided by T.Delaney (private communication). (b) The synchrotron removed 850μm signal-to-noise image with contours 3σ, 4σ, 5σ etc.... The peak S/N in the northern limb is now 7σ which is a 40% decrease from the unsynchrotron subtracted 850 map. In the southern regions, the peak S/N is still 6σ as expected since there is hardly any radio emission in this region.

-0.65 to -0.85 ($\pm$15%). However the fact that the 450 and 850 μm images seem to follow the same distribution means that this is not a problem. We include this error in the sub-mm subtraction and present the final sub-mm fluxes (minus synchrotron) for Kepler's SNR as 0.7 ± 0.2 Jy and 2.8 ± 1.3 Jy at 850 μm and 450 μm respectively.

The removal of the original symmetry after subtracting the synchrotron contribution was also observed in the analysis of Cas A (Section 4.3) - although to a more extreme extent. After subtraction, the 850 μm emission was identical in distribution to the 450 μm hence implying that the sub-mm flux is due to dust and not synchrotron processes. The peaks in the two sub-mm wavelengths are aligned far better than in Kepler and this is probably due to the brighter signal and lower noise levels in the Cas A observations (Dunne et al 2003).

The Spectral Energy Distribution (SED) can be fitted by thermal emission from

Flux (Jy) in Wavelength				Ref
12 μm	25 μm	60 μm	100 μm	
1.8 ± 0.9	8.1 ± 3.7	7.2 ± 0.9	< 8.2	(1)
1.6 ± 0.2	11.7 ± 1.7	10.5 ± 1.1	2.5 ± 0.3	(2)
1.0 ± 0.5	10.1 ± 1.0	7.1 ± 0.6	2.9 ± 1.1	(3)
0.6 ±0.1	2.9 ± 0.4	4.7 ± 0.6	5.6	(4)
1.0 ± 0.2	..	..	..	(5)

Table 4.4: Observed fluxes of Kepler at IR wavelengths, 12, 25, 60 and 100 μm. References - (1) Saken et al. 1992; (2) Braun 1987; (3) Arendt 1989; (4) IRAS catalogue, various; (5) Douvion et al. 2001b.

a greybody (Section 1.6):

$$S_\nu = N\nu^\beta B(\nu, T) \tag{4.4}$$

where N is a normalisation term depending on the mass and optical depth. We firstly tried fitting a single temperature greybody to the SED using a χ^2 test but we could not obtain an acceptable fit. A two temperature greybody component was fitted, where

$$S_\nu = N_w\nu^\beta B(\nu, T_w) + N_c\nu^\beta B(\nu, T_c) \tag{4.5}$$

and β is assumed to be constant with wavelength.

The IR fluxes (Table 4.4) and radio observations of Kepler were fitted using a χ^2 test to the observed fluxes until the minimum χ^2 was obtained, Figure 4.3. It is instructive to make the fits with a fixed β to ensure the validity of the χ^2 test. The parameters we require to be returned are T_w, T_c and N_c/N_h. In this case there are two degrees of freedom. The results are listed in Table 4.5 and show that the 'true' value of β lies around 1.0. The quality of the fit, Q gives the probability that χ^2 should exceed a particular value of χ^2 by chance, such that larger Q values have a better quality of fit. Allowing β to be unconstrained (i.e. a fit parameter), the best fit gives $\beta = 0.9$, $T_{\rm warm} = 114$K and $T_{\rm cold} = 20$K. This shows that allowing all

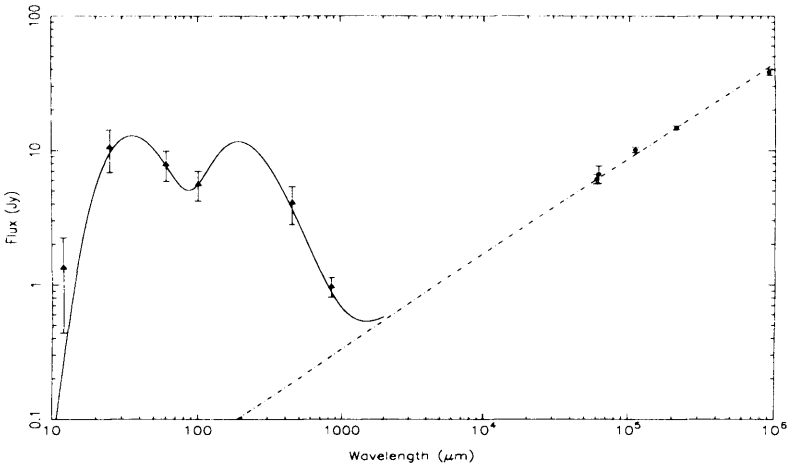

Figure 4.3: Kepler's IR - Radio SED for the IRAS 12, 25, 60 and 100 μm fluxes (Table 4.4) and the 850 and 450 μm measurements from SCUBA. The radio measurements were taken from Delaney et al (2002) and the NED database and are well fitted with spectral index $\alpha = -0.71$. The solid line represents a two temperature, greybody fit to the data points with $\beta = 0.9$, $T_{warm} = 114K$, $T_{cold} = 20K$. This SED implies a best fit dust mass of $\sim 3\ M_\odot$ for $\kappa_{850} = 0.07\ m^2\ kg^{-1}$.

four parameters to vary in a fit to only 5 points does not significantly change the quality of the fit when compared to a fixed β. The best fit model favours a lower β in agreement with the less constrained modelling in Table 4.5.

Many different pairings of β and T will fit the same data set, but increasing the best fit temperature moves the peak to shorter wavelengths so we can be reasonably confident that for accurate fluxes, we can have a good estimated temperature. Increasing β serves to increase the gradient required to fit the sub-mm data (long wavelength tail of the spectrum) and hence decrease the temperature. Increasing β will increase the dust mass whereas decreasing β provides a higher temperature fit and less dust[1]. The errors on the SED fit parameters were obtained using a program provided by Loretta Dunne. 3000 sets of artificial fluxes were created from the original data using the bootstrap technique. A fit was made to each individual set and 1σ errors were derived from the distributions of β, T_{warm} and T_{cold}. The

[1]The situation becomes worse if β varies with temperature or even wavelength.

β	T_{warm} (K)	T_{cold} (K)	M_{dust}	N_c/N_h	χ^2	Q
0.5	132	23	0.84	211	0.47	0.79
1.0	108	19	1.22	540	0.05	0.98
1.5	96	17	1.55	1816	0.58	0.75
2.0	84	15	2.08	4456	0.95	0.62
0.9	*114*	*20*	*1.07*	*795*	*0.03*	*0.99*

Table 4.5: The best fit parameters for Kepler with constant β. N_c/N_h is the ratio of the mass of dust in the cold component and the mass in the warm component. The resulting minimised value of χ^2 is given with the quality of the fit Q. The dust mass is calculated from the 450 μm flux with $\kappa_{450} = 0.27$ m^2 kg^{-1} which is scaled from the 850 μm value in James et al. (2002) with a $\lambda^{-\beta}$ dependency. The best fit parameters obtained when we allow β to vary are shown in italics.

fits with $\chi^2 < 3$ are shown in Figure 4.4 with clear evidence of two peaks in the spectrum remaining in all trials. The distribution of these parameters are shown in Figure 4.5.

The mid IR - Radio SED for Cas A (Figure 4.8 (a)) is extremely similar to Kepler's. Both have two distinct peaks and both have sub-mm emission far in excess of the synchrotron contribution. Using the bootstrap technique to fit Cas A's SED shows a similar distribution to Kepler's with a clear second peak around 200 μm. In Cas A, the 850/450 μm ratio is 1.4 instead of the higher value of 3 observed in Kepler. The fact that both Kepler and Cas A appear to have this second peak is strong evidence for the existence of a colder population of grains which was not seen in the IR.

4.2.3 Estimating The Dust Mass

The dust mass can be measured directly from the flux at sub-mm wavelengths using Equation 4.6 (Hildebrand 1983)

$$M_d = \frac{S_\nu D^2}{\kappa_\nu B_\nu(\nu, T)} \tag{4.6}$$

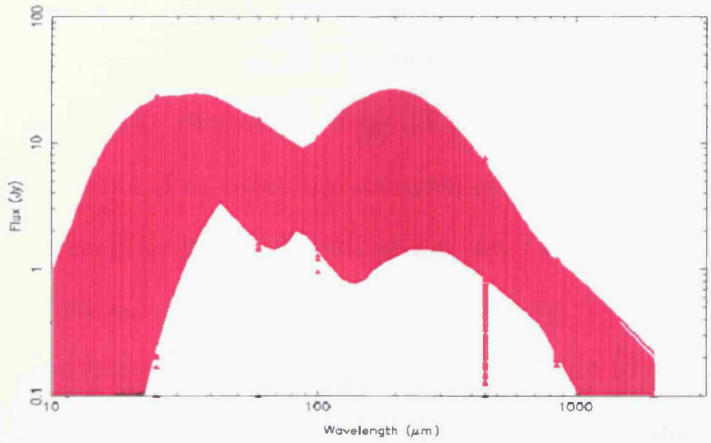

Figure 4.4: Modelling the SED using the bootstrap technique. 3000 fits were made from the original data points and those with $\chi^2 < 3.0$ (satisfied by 2684 fits) are shown. Although there is no data point to confirm the existence of the second peak around 200 – 400 μm, it appears to remain even when fitting extremes to the SED.

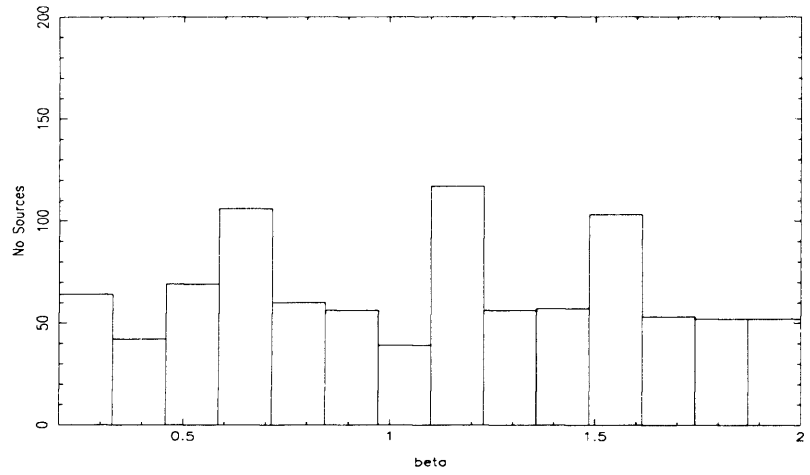

(a)

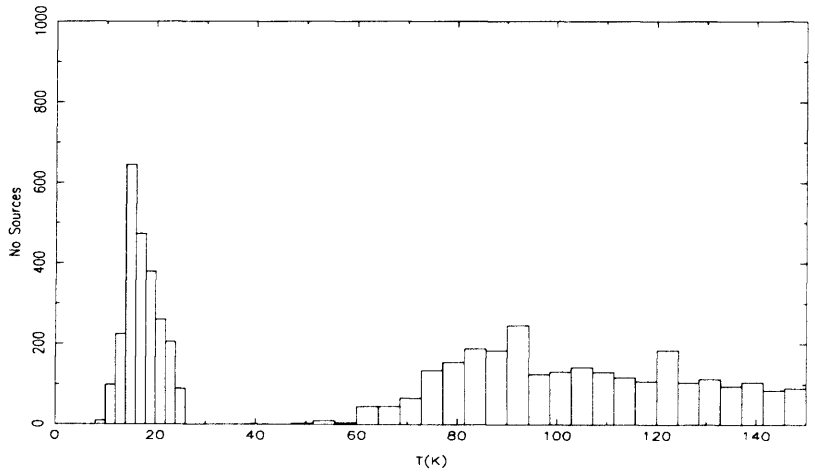

(b)

Figure 4.5: The distribution of the parameters obtained by fitting the IR-Radio SED of Kepler's SNR using the bootstrap technique. The fits shown are with $\chi^2 < 3.0$ and account for 2684 trials out of 3000. (a) shows the distribution of β which was allowed to vary between 0.2 and 2.0 and (b) shows the distribution of warm and cold temperatures fitted to the SED. The value of $T_{\rm warm}$ fitted was allowed to range from 50 - 160K whereas $T_{\rm cold}$ ranged from 5 - 25K.

where S_ν is the flux density measured at frequency ν, D is the distance and B is the value of the Planck function at frequency, ν with dust temperature T. κ_ν is the dust absorption coefficient of grains at a given frequency. For a two component temperature model, the dust mass is given by

$$M_d = \frac{S_\nu D^2}{\kappa_\nu} \left[\frac{N_w}{B_\nu(\nu, T_w)} + \frac{N_c}{B_\nu(\nu, T_c)} \right] \tag{4.7}$$

The largest error is introduced by the uncertainty in the value of κ (see Section 1.6). The value of κ_{850} from James et al. (2002) is determined from observations in the diffuse ISM where dust is likely to have encountered extensive processing. As discussed in Dunne et al. (2003), this may not be the case for newly formed supernovae dust. In such environments (i.e. reflection nebulae, circumstellar envelopes), the emissivity of the grain may be more efficient and κ could increase. Recent studies of such environments find κ_{850} could be as high as 0.5 m^2 kg^{-1} (Amure 2003). In Dunne et al. (2003), three κ values were taken from the literature to determine the dust mass in Cas A, (1) $\kappa_{850} = 0.04 - 0.15$ m^2 kg^{-1}, the range observed in diffuse ISM studies; (2) $0.16 - 0.8$ m^2 kg^{-1}, the range observed in reflection nebulae/circumstellar environments and (3) $0.6 - 1.1$ m^2 kg^{-1}, the range observed in laboratory studies of clumpy aggregates. In Cas A, the maximum κ values were required to produce a sensible dust mass range of 2 - 4 M$_\odot$. Using the maximum κ for Kepler gives a lower range of $0.2 - 0.4$ M$_\odot$ whereas the lowest values suggest that 1 - 3 M$_\odot$ of dust is present in the remnant. The bootstrap analysis allows us to place errors on the parameters with 90 per cent of the trials having a dust mass of at least 1 M$_\odot$ for $\kappa_{850} = 0.07$ m^2 kg^{-1} (James et al. 2002).

Table 4.6 shows the statistical properties given by the SED fittings for different values of κ. The distribution of the dust masses calculated from the 450 μm and

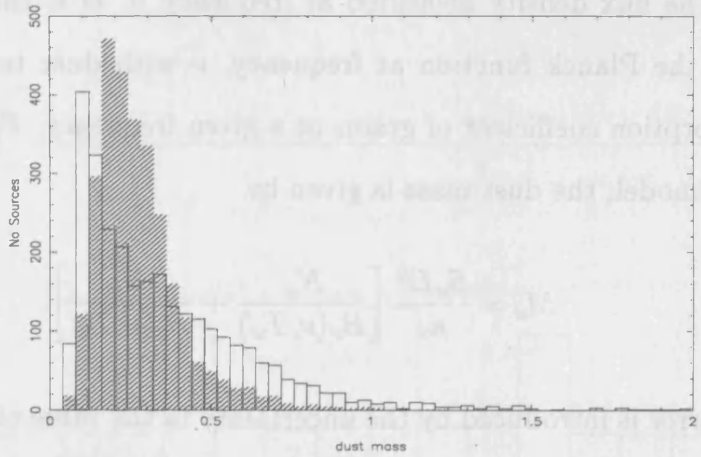

(a)

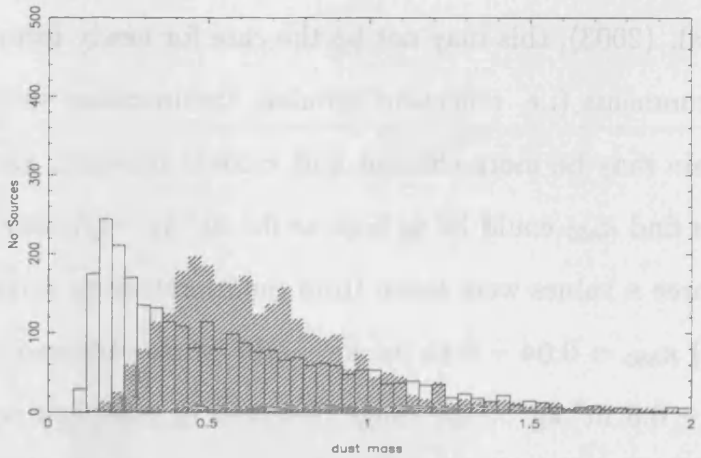

(b)

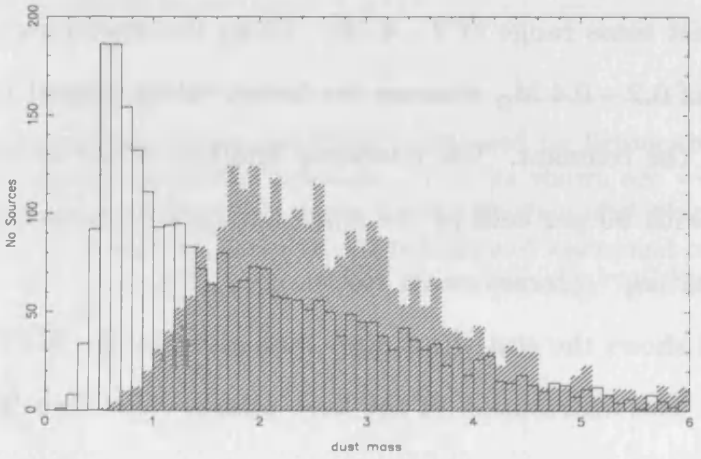

(c)

Figure 4.6: The comparison of the distribution of dust masses calculated from the bootstrap technique for the 450 (solid) and 850 μm (hashed) fluxes for (a) κ_1, (b) κ_2 and (c) κ_3.

Parameters			Dust Mass ($M_\odot$)		
β	T_{warm} (K)	T_{cold} (K)	κ_1	κ_2	κ_3
1.2 ± 0.4	102±12	17^{+3}_{-2}	$M_{450} = 0.3^{+0.2}_{-0.1}$	$0.5^{+0.3}_{-0.2}$	$1.7^{+0.9}_{-0.6}$
			$M_{850} = 0.3 \pm 0.1$	0.6±0.2	$2.7^{+0.6}_{-0.5}$

Table 4.6: The parameters obtained from the SED fitting for Kepler's supernova remnant. The dust masses are the median of the distribution from the bootstrap technique with 68% confidence interval quoted as the error. The values of κ are (as in Dunne et al. 2003) $\kappa_1(450) = 1.5$ m^2 kg^{-1}, $\kappa_1(850) = 0.76$ m^2 kg^{-1} (laboratory studies). $\kappa_2(450) = 0.88$ m^2 kg^{-1}, $\kappa_2(850) = 0.3$ m^2 kg^{-1} (observations of evolved stars). $\kappa_3(450) = 0.26$ m^2 kg^{-1}, $\kappa_3(850) = 0.07$ m^2 kg^{-1} (observations of the diffuse ISM).

850 μm fluxes and the best fit parameters using Equation 4.6 are shown in Figure 4.6. The dust masses obtained from the fluxes at each wavelength converge for the higher κ values as was also seen in Cas A (Dunne et al. 2003). Regardless of the value of κ used, we obtain at least *three orders of magnitude more dust* than that previously obtained in mid-IR observations. This is an order of magnitude lower than the dust observed in Cas A but the far greater brightness of Cas A than Kepler at all wavelengths may be due to a difference in the dynamics of the explosions or the progenitor star.

The Effect of Fluxes on the Dust Mass

Difficulties arose when computing the best fit to the SED mainly due to the uncertainties in the 100 μm and the 450 μm observed fluxes. Choosing the IRAS fluxes to fit the SED was also difficult due to the large range observed via different methods (Table 4.4). Ultimately a weighted average of the IRAS survey results (taken from refs (1), (2) and (3) in the Table) for the 12, 25 and 60 μm fluxes was taken to be the most sensible result with errors taken to be the largest error quoted. However, the larger 100 μm flux of 5.6 Jy was used in calculating the SED as this serves to

Case	Parameters			Dust Mass ($M_\odot$)		
	β	T_{warm} (K)	T_{cold} (K)	κ_1	κ_2	κ_3
I	$0.9^{+0.7}_{-0.1}$	114^{+12}_{-24}	20^{+3}_{-5}	$M_{450} = 0.2^{+0.3}_{-0.1}$	$0.3^{+0.5}_{-0.1}$	$1.1^{+1.5}_{-0.3}$
				$M_{850} = 0.3 \pm 0.1$	$0.5^{+0.3}_{-0.1}$	$2.2^{+1.1}_{-0.5}$
II	2.3 ± 1.0	80^{+7}_{-4}	11 ± 1	$M_{450} = 1.5^{+0.6}_{-0.2}$	$2.6^{+0.8}_{-0.6}$	$8.7^{+2.0}_{-1.9}$
				$M_{850} = 0.6^{+0.1}_{-0.2}$	$1.5^{+0.4}_{-0.3}$	6.6 ± 1.4

Table 4.7: As in Table 4.6. The parameters from the SED fitting with different fluxes. CASE I represents the new data with the lower 100 μm flux i.e. $S_{100} = 2.9$ Jy, $S_{450} = 3.0$ Jy. CASE II represents the old sub-mm data with the lower 100μm flux i.e. $S_{100} = 2.6$ Jy, $S_{450} = 4.1$ Jy. Thus with a lower 100 μm flux we have already doubled the dust mass. The new data were invaluable in constraining the dust mass.

minimise the cold dust mass and ensures a lower limit on the dust mass is calculated for Kepler. Taking the lowest 100 μm of 2.6 Jy (instead of 5.6 Jy) would, for example, produce a larger dip in the SED between the two peaks seen in Figure 4.3. This would decrease the cold dust temperature required to fit the SED, hence increasing the dust mass by a factor > 2. If the lower 100 μm flux is used, the SED properties are completely different to those presented in Section 4.2.2. The best fit dust mass would be doubled to ~ 6 $M_\odot$ for $\kappa_{850} = 0.07$ m^2 kg^{-1}. The SED parameters obtained in this case are shown in Table 4.7 (CASE 1). The analysis of the original data set had completely different properties than the best fit parameters in Table 4.6. In this case, the 450 μm flux was higher - the SED parameters for the original data are given in CASE II in Table 4.7 for comparison with the new observations.

It is quite clear that in CASE II, the 850 and 450 μm dust masses do not converge for any of the values of κ given in the Table which implies a high β (> 2) is needed to fit the slope. The main issue is probably the lower signal of Kepler at the IR

wavelengths where the poor resolution of IRAS has meant large uncertainties in the flux levels calculated in different observations. Further observations using SPITZER at 70 and 160 μm and SHARCII at 350 μm will help constrain the IR fluxes and determine the height of the second peak.

4.3 Cassiopiea A

It is instructive at this point to present a brief overview on the sub-mm results of Cas A published earlier this year in Dunne et al. (2003). Although I did not directly reduce the results, I was a collaborator and involved with the work. It is therefore useful to summarise these results since they were the first published evidence of dust existing in a supernova remnant.

Cassiopeia A is the brightest radio source in the sky and is believed to be the remnant of the explosion of a massive ($M > 20\ M_{\odot}$) star. The explosion occurred around 320 years ago and is thought to be at a distance of 3.4 kpc. There have been many multiwavelength studies of Cas A - the most recent from Rudnick et al (in prep) but none have included the sub-mm regime. The data were taken from the JCMT archive (originally observed in 1995 in scan map mode) and were reduced by Loretta Dunne. There were large artefacts on the sky after the initial reduction and further photometry measurements at several positions on the remnant were taken in December 2002 at 850 μm. These allowed a more accurate flux level to be determined. In Figure 4.7, the sub-mm images at 850 and 450 μm are shown (kindly provided by Loretta Dunne) with a ring like morphology clearly seen in the 850 μm. Comparison with the radio map at 3mm (Figure 4.7 (b)) shows a similar morphology which is due to the contamination of the synchrotron emission at the longer sub-mm wavelengths. In Dunne et al. (2003), the synchrotron was estimated to be

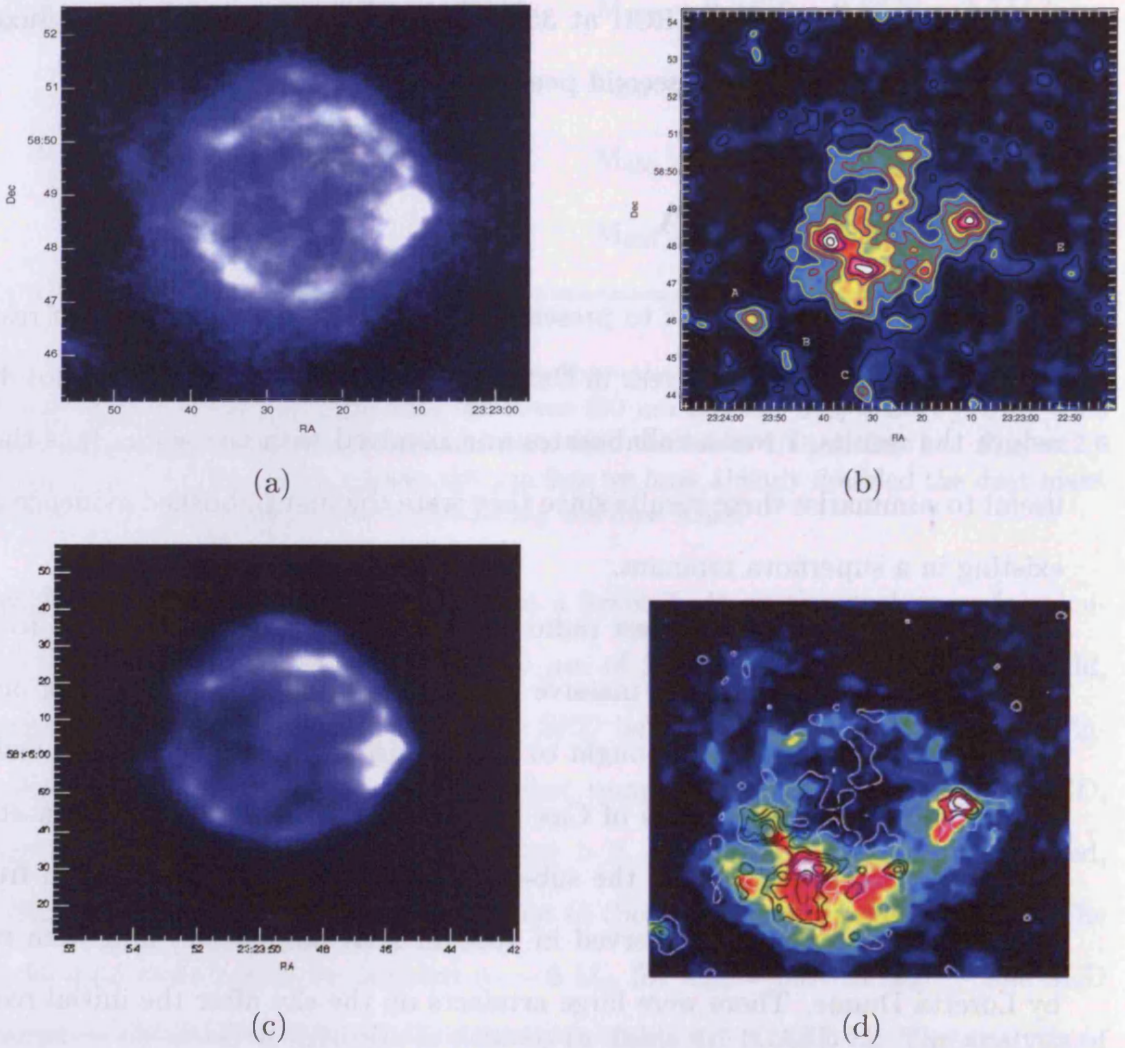

Figure 4.7: SCUBA Images of Cas A at (a) 850 μm smoothed by 6 arcsecs (b) 450 μm signal-to-noise image smoothed by 21″ Gaussian with contours $2\sigma + 1\sigma$. Notice the clumps of emission in the southern part of the remnant labelled A - E. (c) 86 GHz map (3mm) taken with the Berkeley Illinois Maryland Association (BIMA) millimetre array and (d) synchrotron subtracted 850 μm with 450 μm contours. Cas A is brighter than Kepler by $\sim$ 50 Jy at 850 μm and thus the former has a much higher S/N than Kepler. The ring like morphology is apparent in both young SNR's. These figures were kindly supplied by Loretta Dunne and are published in Dunne et al. 2003 and Morgan et al. submitted, 2004.

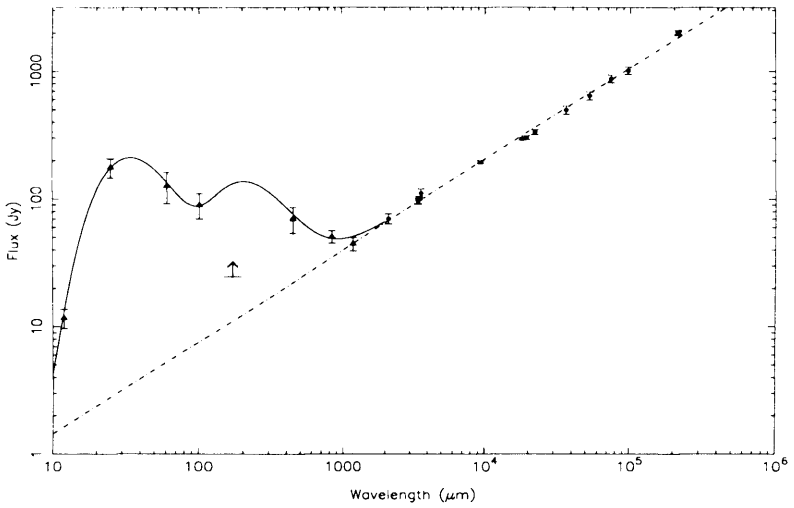

Figure 4.8: The mid IR-radio SED for Cas A with SCUBA fluxes of 50.8 ± 5.6 Jy at 850 μm and 69.8 ± 16.1 Jy at 450 μm. The lower limit is the integrated flux from ISO at 170 μm. The radio data is well fitted by a power law slope $\alpha = -0.72$ and have been corrected for radio decay to the epoch of the Cas A observations (1998). The best fit SED gives $\beta = 0.9$, $T_{hot} = 112$K and $T_{cold} = 18$K. This figure was kindly supplied by Loretta Dunne and is published in Dunne et al 2003.

responsible for two thirds of the 850 μm emission and they removed it from the sub-mm image using the relationship $S_\nu \propto \nu^\alpha$ to scale the radio map. The synchrotron subtracted map is therefore obtained by subtracting the two (see Section 4.2.2 for Kepler). In (d) the 850 μm synchrotron subtracted image is shown. The ring like morphology has disappeared leaving an asymmetrical distribution which now closely follows the 450 μm (shown here by the contours).

The SCUBA fluxes for Cas A are 50.8 ± 5.6 Jy at 850 μm and 69.8 ± 16.1 Jy at 450 μm with synchrotron contributions at the sub-mm wavelengths of 35 and 22 Jy respectively. The best fit SED parameters for Cas A are $\beta = 0.9$, $T_{hot} = 112$K and $T_{cold} = 18$K. The parameters from the bootstrap technique for Cas A are shown in Table 4.8. Note the similarities of the fitting parameters between Cas A and Kepler.

The dust masses estimated from the SED of Cas A are too large using the absorption properties of normal interstellar dust ($7-27$ $M_\odot$). We require a factor of

Parameters			Dust Mass ($M_\odot$)		
β	T_{warm} (K)	T_{cold} (K)	κ_1	κ_2	κ_3
$0.9^{+0.8}_{-0.6}$	112^{+11}_{-21}	17±3.6	$M_{450} = 2.6^{+0.8}_{-0.6}$	$4.4^{+1.4}_{-1.0}$	$15.0^{+4.6}_{-3.4}$
			$M_{850} = 2.5^{+0.6}_{-0.4}$	$6.4^{+1.5}_{-1.1}$	$26.3^{+6.1}_{-4.4}$

Table 4.8: The parameters obtained from the SED fitting to Cassiopeia A (Dunne et al 2003). The dust masses are the median of the distribution from the bootstrap technique with 68% confidence interval quoted as the error. The values of κ are (as in Dunne et al, 2003) $\kappa_1(450) = 1.5$ m^2 kg^{-1}, $\kappa_1(850) = 0.76$ m^2 kg^{-1} (laboratory studies). $\kappa_2(450) = 0.88$ m^2 kg^{-1}, $\kappa_2(850) = 0.3$ m^2 kg^{-1} (observations of evolved stars). $\kappa_3(450) = 0.26$ m^2 kg^{-1}, $\kappa_3(850) = 0.07$ m^2 kg^{-1} (observations of the diffuse ISM).

ten greater efficiency in absorption properties to lower this to more reasonable values of $0.7 - 2.7$ $M_\odot$. Alternatively, it is possible that we are observing some of the dust in clouds in front of the remnant (since Cas A is located in a spiral arm). Recently it has been suggested that up to half of the dust seen in the sub-mm emission could be from molecular clouds due to the alignment of peaks in the sub-mm with peaks in foreground CO observations of the clouds (Wilson, submitted 2004). They conclude this shows that some of the sub-mm is not associated with the remnant and estimate the mass of dust from the CO peaks is $\sim 0.1 - 1$ $M_\odot$ i.e. about half the dust in the sub-mm peaks from Dunne et al. (2003). However, there are a number of problems with this scenario. Firstly, the CO peaks also align with the radio peaks which are of supernova origin. Secondly, the sub-mm peaks are located between the forward and reverse shocks of the remnant which disagrees with a foreground component which should be more diffusely distributed and should not be confined between the shocks. Finally, if the dust is from the foreground clouds, it would be similar to normal interstellar dust which has much lower absorption properties than the supernova dust. If the sub-mm emission is from normal IS dust then the estimated dust mass

is far higher than can be explained from the CO observations. Other observations mapping the entire region around the remnant show CO emission distributed all over the region with no resemblance to the shell-like shape seen in the SNe (Wilson et al. 1993). If the sub-mm was due to the foreground clouds, we would expect some correlation with the CO outside the remnant as well. To solve this issue, HI and CO observations towards Kepler would help provide information on the correlation (if any) of CO/HI peaks with the sub-mm in a remnant which does not have much evidence for foreground clouds.

What is the likelihood of a 1 $M_\odot$ dust cloud lying along our line of sight (los) to Kepler? If the clouds are randomly distributed with number density N and cloud radius r, along a los with length l, the number of clouds intercepted in our los to the remnants is $\pi r^2 l N$. The virial radius of these clouds can be estimated by assuming virial equilibrium (Lawrence 2001) to be

$$R_{vir}(m) = 1.46 \times 10^{15} M_g \left(\frac{T}{7}\right)^{-1} \tag{4.8}$$

where T is the temperature of the cloud. For $M_d \sim 1$ $M_\odot$, and gas-to-dust ratio of 100, $M_g = 100$ $M_\odot$. For $T = 20$K, $R_{vir} = 1.7$ pc and for 7K, $R_{vir} = 4.9$ pc. If we assume $\kappa_d = 0.07$ m^2 kg^{-1}, $D = 5$ kpc and $M_d = 1$ $M_\odot$, the clouds would have flux ≤ 500 mJy at 850 μm. From Lawrence (2001), the mass density of the clouds can be estimated using Equation 4.9

$$\rho(\mathrm{M_\odot\ pc^{-3}}) = 1.8 \times 10^{-3} (M_g)^{-1/2} N \left(\frac{T-2}{5}\right)^{-3} \tag{4.9}$$

The number density, N of sources with fluxes of order a few 100 mJys at 850 μm is ~ 55 deg^{-2} (Barnard et al. 2004). Therefore $\rho \sim 10^{-4}$ $M_\odot$ pc^{-3} i.e. these clouds are fairly sparse (as also shown in Lawrence 2001).

The number of clouds intercepted is therefore quite small for Kepler which is located 600 pc out of the disk. In this case, $l \sim 200$ pc (out of the disk) and $n \sim 0.02 - 0.15$ for $r = 1.7 - 5$ pc. For Cas A, which exists inside the Galactic disk at a distance of 3 kpc, $l \sim 3000$ pc and $n \sim 0.3 - 2.3$. Therefore, we would expect to see more clouds along the line of sight to Cas A than Kepler.

4.4 An Aside on Tycho's Supernova Remnant

Tycho's supernova remnant is the remnant of an explosion which occurred 430 years ago. It has a shell like morphology which is 8 arcmin in diameter. Distance estimates to the remnant place it at $\sim 3 \pm 1$ kpc (Reynoso et al. 1997) just in front of the Perseus arm. Tycho is generally believed to be a Type Ia SNe. Originally it was argued so because of the similarities in the light curve to Kepler! Although we have seen that Kepler is more likely to be a Type Ib which has a light curve similar to a sub luminous Type Ia, this is not the case for Tycho. Van den Bergh (1993) tested this hypothesis out by comparing the light curve of Tycho with two well observed SNe - the sub luminous Type Ia SN1991bg and the more normal Ia - SN1980N. Tycho's light curve agreed well with SN1980N near maximum light but after ~ 200 days, the Tycho observations dropped by a magnitude. In contrast, Tycho's light curve was in excellent agreement with the sub luminous curve of SN1991bg. This result lead Van den Bergh to tentatively conclude that Tycho is a sub luminous Type Ia.

Further evidence for a Type Ia explosion comes from the expansion parameter, m derived from X-ray and radio observations. Comparing two CHANDRA images taken 5 years apart gives an expansion rate of 0.124 % yr^{-1} and hence an expansion parameter $m = 0.54$ (Hughes 2000). This varies in different regions with $m = 0.71$

in the outermost rim and $m = 0.34$ on the inside edge. In the radio, observations with the VLA taken 10 years apart give $m = 0.47$ (Reynoso et al. 1997; Katz-Stone et al. 2000). Although the X-ray derived expansion rate is slightly higher than the radio (as is the case in Kepler), both suggest that the SNR has not yet entered the Sedov phase ($m = 0.4$) implying that the ejecta dominate the mass. Both sets of observations are consistent with a constant density ejecta expanding into a uniform ISM. This implies that Tycho is a Type Ia SN as there is no significant density contrast in the surrounding medium. If Tycho were a Type II, then we would expect m to be higher due to the expansion of the blast wave into the previous mass lost from stellar winds (c.f. Kepler and Cas A).

Although a proposal was accepted on the JCMT for further observations of Tycho in Grade I-II weather, only 20% of the observations were completed during my PhD. For this reason, I have reduced the data taken so far to determine if anything was present and the flux levels (if any) we expect to get when comparing with Kepler and Cas A. Unfortunately, the noise level in the final image is rather high and it is difficult to make significant conclusions from it, yet as this is the first reduction of the sub-mm data of a Type Ia supernova remnant, it is important to include the work in progress here. In the following section the observations are presented with the first (but inconclusive) images of Tycho's SNR.

4.4.1 The Data

As mentioned in Section 3.3, the removal of the sky noise in scan maps is a difficult process. The normal method of using CALCSKY to fit a model of the sky from the data (S01, David Nutter: priv.comm.) has been shown to work on images in which the source is bright and clearly above the sky. For images in which the source is extremely faint and extended, the calcsky method of fitting the sky cannot determine

Date	τ_{850} [b]	τ_{450} [2]
12/05/2001	0.24	1.22
22/03/2002	0.22	1.10
08/09/2003	0.15	0.74
27/12/2003*a*	0.16	0.71
27/12/2003*b*	0.25	0.99
11/01/2004	0.19	0.92

Table 4.9: The sub-mm observations of Tycho's SNR taken over a period of 3 years. This table includes all the data files reduced to obtain the final map with each date containing one set of six scan maps (in two different directions at three angles).

between sky noise and source emission and ends up producing images in which there are extended patches of emission. As in the case of Cassiopeia A at 450 μm, it is likely that the low flux expected in Tycho's remnant over such a large area, will not show up in calcsky. In Figures 4.9 and 4.10, we show the affect of using the various sky removal methods and the resulting images this produces. In Figure 4.9 (a) we show the original extinction corrected data file for one of the observations. The sky noise is seen as the dark noisy lines across the array (x axis) during the observation integration (y axis). This data file clearly has sky noise at times of 1000, 1400, 1600. If we try removing this using calcsky to first fit the sky model and then remsky to remove it, we find that the sky noise is not removed (b) and in fact it seems noisier. When reducing the entire data set, this method produces an image which looks similar to tilting planes of emission sometimes seen in sky noise (Figure 4.9 (c)).

Similarly, in Figure 4.10 we show the same data file (a) and the effects of removing the sky noise using REMSKY only (b). The overall image this produces is a lot less noisier ($\sim$ 13 mJy/beam) and has no extended emission regions as was seen in Figure 4.9 (c).

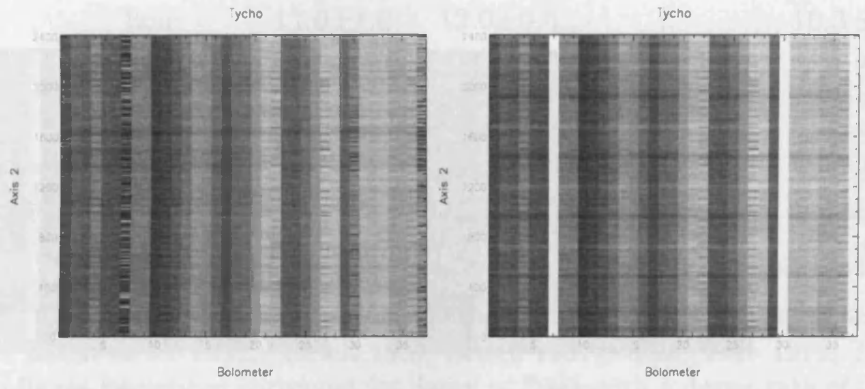

(a) (b)

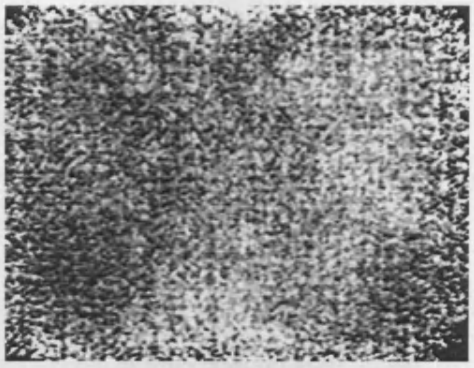

(c)

Figure 4.9: Removing sky noise across the array with the SURF command CALCSKY. In (a) we have the original extinction corrected data file. In (b) we show the file after the sky removal (the lines are now in fact plainer to see!) and (c) presents the final coadded picture of Tycho's SNR using this method. The lines which have no data are the bolometers which have been termed 'bad' and have thus been removed in the data reduction process. The failure of this method to work in a faint object is evident from the negative and bright planes it produces. The 1σ noise level on this image is ~ 17 mJy/beam.

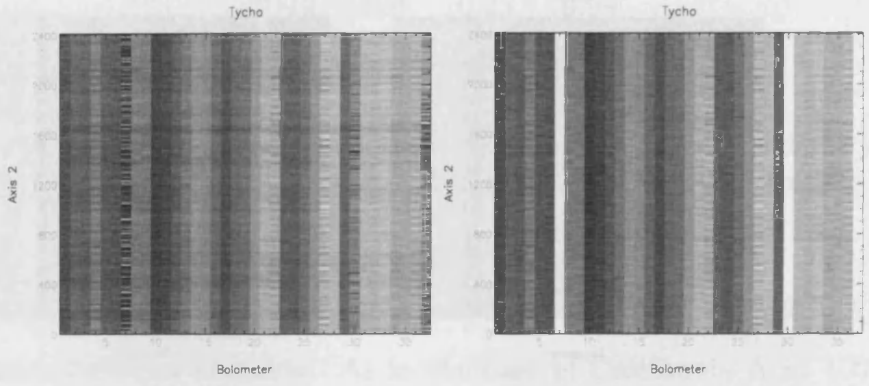

(a) (b)

(c)

Figure 4.10: Removing sky noise across the array with the command REMSKY only. In (a) we have the original extinction corrected data file. In (b) we show the file after the sky removal in which we can clearly see that the sky noise has been removed and (c) presents the final coadded picture of Tycho's SNR using this method. The 1σ noise level on this image is $\sim$ 13 mJy/beam. This method likely to remove some of the source flux as it subtracts the median level from all of the bolometers.

Wavelength	Integrated Flux (Jy)			Average (Jy)
12μm	3.7±2.5	1.8 ± 0.8	3.1±0.3	3.0 ± 2.5
25μm	22.0 ± 2.0	24.3 ± 2.1	23.7 ± 0.2	23.0 ± 2.4
60μm	39.0 ± 6.0	40.2 ± 3.1	41.5 ± 0.4	39.9 ± 6.0
100μm	21.0 ± 6.0	18.1 ± 2.2	11.3 ± 0.1	17.6 ± 6.0
2cm	11.0±1.0	12.0±0.5	..	10.3 ± 1.0
3cm	13.1±0.8	..	..	11.7 ± 1.0
6cm	19.2±1.0	21.2±0.4	..	18.1 ± 1.0
11cm	29.2 ± 0.5	28.5 ± 2.0	..	25.9 ± 2.0
21cm	43.1 ± 2.1	41.9±1.9	39.4 ± 2.6	37.0 ± 2.6
40cm	62.9 ± 2.1	..	..	5.4 ± 2.1
50cm	73.0±3.7	..	..	65.4 ± 3.7

Table 4.10: Observed fluxes of Tycho's supernova remnant at IR - radio wavelengths. References - Saken et al. 1992; Arendt 1987; Braun 1987; Klein et al. 1979; The average of the radio fluxes have been corrected for decay to 2003 with a decay rate of 0.5 % yr^{-1}.

4.4.2 An Upper Limit on the Dust Mass

Tycho's radio flux was observed to decay over a period of 16 years from 41.9 Jy to 39.4 Jy at 21.4 cm (Klein et al. 1979). This gives a decay rate of 0.5 % yr^{-1}. The radio observations taken from different epochs were corrected for this to represent the same radio flux of the sub-mm observations (Table 4.10). The radio spectral slope exponent ranges from $\alpha = -0.52$ (Katz-Stone et al. 2000), -0.61 (Green 2001) to -0.67 (Glushak 1985). Including this range in α, we can estimate the contribution of the synchrotron to the 850 and 450 μm emission. For the average value of $\alpha = -0.61$, this contribution is $\sim 1.3^{+0.6}_{-0.3}$ and $0.9^{+0.5}_{-0.2}$ Jy.

We can estimate the amount of flux we would expect to see in Tycho's supernova remnant using the colours of Cas A and Kepler. The 60/850 μm ratio for Cas A and Kepler are 8 and 12 respectively. Using the average 60 μm flux for Tycho and assuming the dust in Tycho is similar to the dust seen in the other remnants (since the IR SEDs are very similar), we obtain an estimate of the 850 μm integrated flux as 5.1 or 3.3 Jy. The same at 450 μm gives 15.7 or 14 Jy. If the dust is distributed

over 10% of the area of Tycho ($\sim$ 50 sqarcmin) then we expect Tycho to have an average surface brightness of 190 mJy/beam at 450 μm and 6 mJy/beam at 850 μm. The sensitivity in the observations presented here are therefore not low enough to make any conclusive statements to whether or not dust exists in Tycho. Using the 1σ noise level at 850 μm as an upper limit, we plotted the SED and found that the maximum dust in Tycho is 8 $M_{\odot}$ for $\kappa_{850} = 0.07$ m^2 kg^{-1}. To obtain the required sensitivity level to obtain the correct sub-mm fluxes, a further 30 hours of data are required.

4.5 Summary

The main results of this Chapter are:

- The first submillimetre observations of Kepler's supernova remnant are presented. This shows the first published sub-mm images of a Type Ib remnant showing high levels of emission at both 850 μm (12σ) and 450 μm (6σ). This is the first direct proof of dust in Kepler's SNR.

- We find that there is synchrotron contaminating the longer sub-mm wavelengths but estimate this to be only 30% of the submm flux using the radio flux measurements. Therefore there is 0.7 Jy at 850 μm due to emission from cold dust.

- The median dust mass responsible for this emission ranges from *at least* 0.3 – 2.7 $M_{\odot}$ depending on the value of the absorption coefficient (κ) used and the chosen 100 μm flux from the literature. The median dust mass increases to 0.6 – 7 $M_{\odot}$ if normal ISM dust is assumed.

- We use the mid Infra-Red to Radio SED to constrain the dust properties with

median parameters estimated as $\beta = 1.2 \pm 0.4$, $T_{warm}(\mathrm{K}) = 102 \pm 12$ and $T_{cold}(\mathrm{K}) = 17^{+3}_{-2}$. We show that Kepler's SED has the strange 'two-bump' property that was seen in Cas A and probably suggests that there two populations of dust grains at different temperatures.

- We do not require the high absorption coefficients which were needed to explain the large amounts of sub-mm flux in Cas A. This may be due to the much higher signal-to-noise in Cas A or the difficulty in obtaining accurate IR fluxes for Kepler at $60 < \lambda < 100\mu$m from the literature.

- We present an overview of the results of the first sub-mm observations of the Cassiopiea A remnant.

- We briefly outline the sub-mm observations and background of the young galactic remnant Tycho and present the data taken so far. Using the flux levels on the images suggests that the dust mass in Tycho is < 8 $\mathrm{M}_{\odot}$ for normal interstellar dust.

The sub-mm observations show that *three orders of magnitude* more dust exists in Kepler's supernova remnant than previously detected. Along with Cas A, this is further evidence of significant dust production in supernovae ejecta. In the next Chapter, we try to determine the distribution of the dust and its dynamics with emission at other wavelengths. The possible heating mechanisms are also reviewed.

Chapter 5

Dust Production in Supernovae II

"..dust does make a difference" *P.G.Martin, 2003*

5.1 Introduction

The aim of this chapter is to analyse further the sub-mm observations of the two remnants Cas A and Kepler. The images at different wavelengths are compared with the dust emission to determine whether dust exists within the ejecta or outside of the shockfronts. We discuss the possibility of a new estimate of the position of the forward shock front for Kepler and the apparent anti-correlation between the emission from the cold dust and other wavelengths. This is a rather lengthy discussion and is included for completeness. The summary of this analysis is given in Section 5.3.3 and some extra figures are given in Appendix A.

In Section 5.4, we discuss the reasons why the dust is so cold even though it may be mixed with hot X-ray gas. An extreme alternative to the origin of the sub-mm emission using the thermal emission from iron needles is investigated. Some results from the work in this Chapter have been submitted for publication in MNRAS,

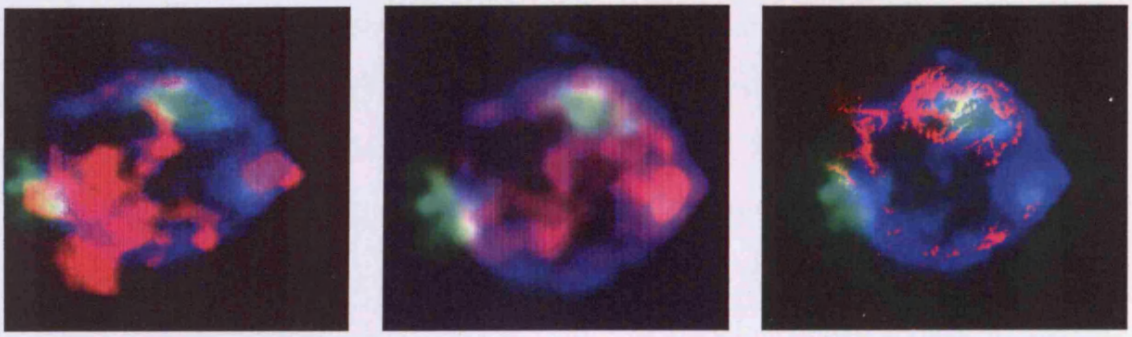

Figure 5.1: Multi-wavelength images of the Cas A Supernova remnant made by splitting each wavelength into colour channels. **Left:** 850 μm, 450 μm and X-ray FeK image. Red = 450 μm, Blue = 850 μm, Green = FeK emission. **Middle:** 850 μm, X-ray FeK line and X-ray continuum. Red = Continuum, Blue = 850 μm, Green = FeK emission. **Right:** 850 μm, optical and X-ray FeK image. Red = optical, Blue = 850 μm, Green = FeK emission.

Morgan, H.L., et al. 2004.

5.2 Multiwavelength Cassiopeia A

The sub-mm emission in Cas A is anti-correlated with every other wavelength, particularly the optical and warm IR dust, as is also seen in Kepler. This suggests that although the overall distribution of the emission is not the same in both remnants, the properties needed for the dust to exist, form and survive may be. In Figure 5.1, multiwavelength colour images made from the emission of hot X-ray gas (from archival images of XMM-Newton, courtesy of T.Waskett), synchrotron and optical (courtesy of L.Dunne), are compared with the emission at different wavelengths corresponding to a colour using Red-Green-Blue channel splitting. Figure 5.1 shows that there seems to be a segregation of the plasmas. The optical and the 850 μm 'avoid' each other and the 850 emission is further out than both of the X-Ray components and the optical filaments. In terms of relative strengths, we can compare the flux in the sub-mm with the X-Ray continuum and FeK line (Figure 5.2). The

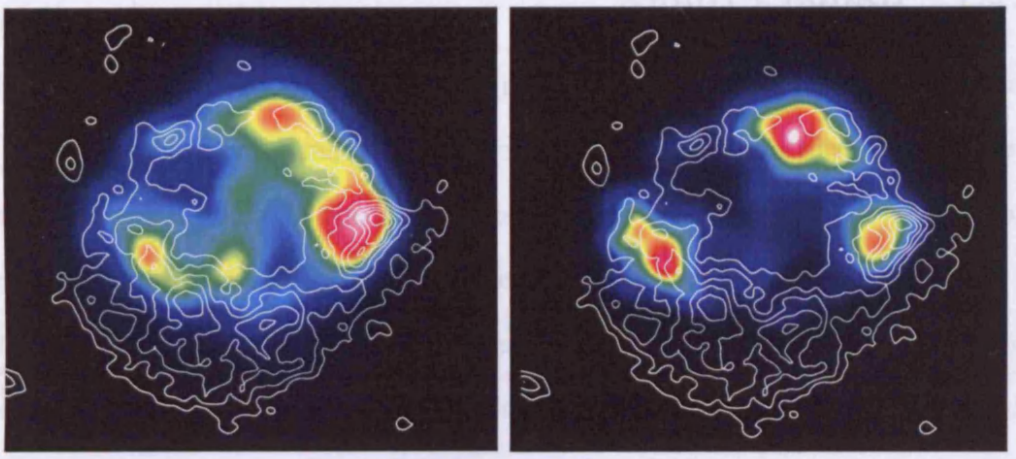

(a) (b)

Figure 5.2: Cassiopeia A's SNR in the (a) X-Ray continuum and (b) FeK line overlaid with 850 μm synchrotron subtracted contours. The X-Ray and the 850 μm images are smoothed to a resolution of 21″. The contours start at $3\sigma + 1\sigma$. The reduced X-Ray data were kindly provided by Tim Waskett.

X-Ray emission as seen by recent CHANDRA observations (Gotthelf et al. 2001) is more filamentary than seen here (due to the low angular resolution of XMM-Newton). The FeK emission which traces the hot ejecta, has a peculiar clumpy nature with three distinct clumps of emission seen in the northwest, south and west-south west regions. The FeK emission lies within the continuum boundary suggesting again that the forward shock is traced by the continuum and like Kepler (Section 5.3.2), the continuum emission in the south appears to extend further out than the Fek. The hotter part of the remnant is towards the centre, providing evidence for emission from a reverse shock (Delaney & Rudnick 2003).

To determine the comparison of the emission at all wavelengths, radial profiles were constructed.

5.2.1 Radial Profiles

Cas A is well studied in most wavelengths with previous authors publishing radial profiles of the radio and X-Ray emission, most recently in Gotthelf et al. (2001). In their work, they identified a new outer shock front position using secondary peaks in the emission profiles outwards from the centre of the remnant. This result was obtained by angle-averaging the emission at positions -5° – -60° and 110° – 230° which we will label north-west and south respectively. We reproduced these profiles using the XMM-Newton X-Ray images with the sub-mm and a 3mm BIMA image (courtesy of Ned Wright) and identified the same outer position of the shock front (Figure 5.5). We also chose to look at another region which incorporated some of the dust features in the sub-mm in the west (-90° – -130°). The radial profiles of Cas A in the sub-mm at 450 and 850 μm are shown in Figure 5.3, where we compare the sub-mm emission in (a) the original maps and (b) the synchrotron subtracted maps averaged over the whole remnant. The higher signal-to-noise in Cas A has meant that the profiles are very smooth so we do not weight the emission with noise. We also show the comparison with the radio and X-Ray[1] over the whole remnant in Appendix A.1, Figure A.1.

Averaged over the whole remnant, there is evidence for a main peak in the sub-mm at 104″ and an outer peak at 270″ which is $\sim$ 20% of the main. This corresponds to the position of faint clumps of emission seen on the sub-mm image of Cas A which could be due to prior stellar wind dust (Figure 4.7 (b)). When removing synchrotron from the images, the outer peaks become more significant. A second peak increases in height relative to the main peak at around 150 - 180″ from the centre which is

[1]The original comparison was made with smoothed X-Ray and radio images to the 850 μm resolution but we found that this smeared out most of the outer structure in the profiles. After checking that the positions of the peaks in the emission at other wavelengths were the same with or without smoothing to the 850 μm resolution, we decided to use the lesser smoothed profiles in some of the regions as they highlight the important structure far better.

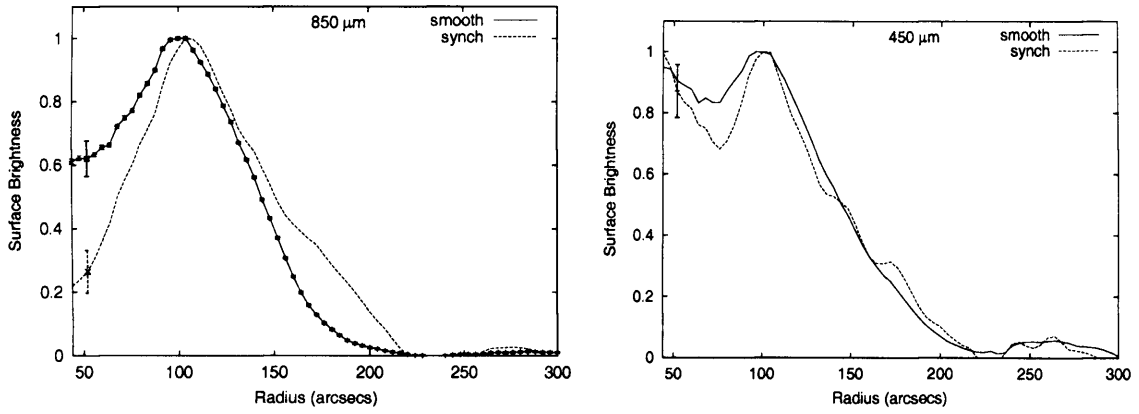

Figure 5.3: Radial profiles of Cas A averaged over the whole remnant for the smoothed sub-mm and synchrotron subtracted sub-mm at (a) 850 μm and (b) 450 μm. The images were smoothed at 450 μm by 7″ gaussian and at 850 μm by a 6″ gaussian per 3arcsec pixel, resulting in a final resolution of $\sim$ 22″. A 1σ error bar is shown. The profiles are normalised to the maximum value and by area. The centre was chosen to be the centre of the outer shock in Gotthelf et al. (2001) at $\alpha_{2000} = 23^{h}\ 23^{m}\ 26.98^{s}$, $\delta_{2000} = -58°\ 48'\ 45.9''$.

seen at both 850 and 450″. This corresponds to the position of the outer shock front at 153″ determined in Gotthelf et al. (2001). The main peak in all the wavelengths is in the same place but the sub-mm emission extends further out than the bright X-ray and radio ring (Appendix A.1, Figure A.1). The outer bump at 270″ is not seen in either the X-ray or the radio as these images only extend to $r < 230''$.

In Figure 5.4 the synchrotron subtracted sub-mm emission is compared over the three regions of the remnant mentioned above - south, western and northwestern. These were chosen to include the dust feature in the South and west and to compare with the regions in Gotthelf et al. (2001). The northwestern region has very little dust. It must be noted here that in the original radio map used to remove the synchrotron contamination from the sub-mm images, a negative hole was seen in the southern parts of the remnant. Careful analysis showed this would contribute to $< 25\%$ of extra flux in this region when subtraction was carried out from the sub-mm map. The synchrotron subtracted map therefore has a slightly higher level

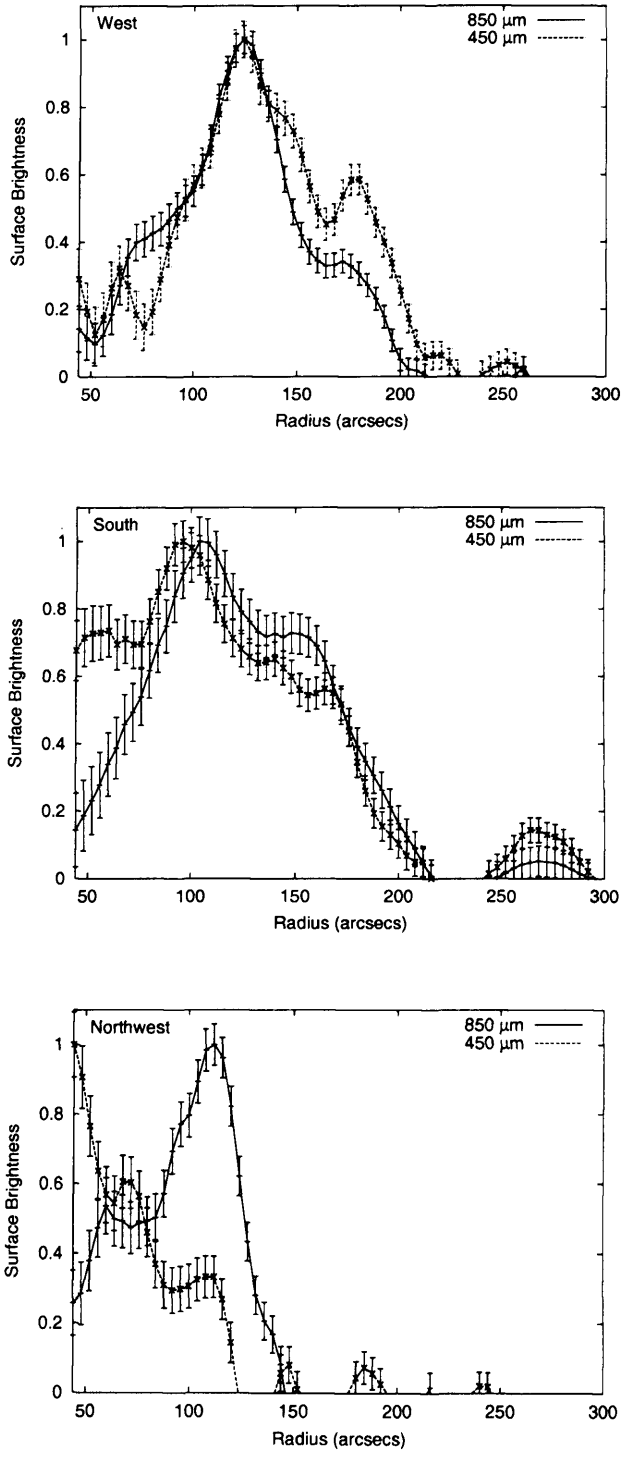

Figure 5.4: The radial profiles of Cas A in the sub-mm averaged over the (a) West ($-90°$ - $-130°$) (b) South ($110°$ - $230°$) and (c) northwest ($-5°$ - $-60°$) regions of the remnant and normalised by area. The south and northwest regions were chosen to reproduce the results in Gotthelf et al. (2001). The flux in the southern part is the highest of the three regions with the peak flux in the Northwest only 18% of the South. There is very little dust in the northwest region. The error bars show the normalised error in an aperture from the sub-mm images. The centre is the same as in Figure 5.3.

in this region than the original 850 μm map had. Due to differences in this negative level per pixel, it could not be subtracted from the map so instead we left the flux levels intact and note that the height of the second peak in the 850 μm in the southern region could be $< 25\%$ less (but the position is the same regardless of flux level). The fact that the second peak in the emission is present in the 450 μm is encouraging since this is less affected by the synchrotron subtraction. The 850 and 450 μm emission trace each other well. The second peak is evident in both the south and the west with a third peak seen at $\sim 270''$. These peaks are not seen in the northwest.

In Figure 5.5 we compare the profiles in terms of wavelength and region to determine if there are any patterns in the emission profiles. The FeK profiles are compared in Appendix A.1 to show the position of the line emission (hot ejecta) with respect to the dust and continuum in these regions.

Some key patterns seen in these profiles are: (i) the X-Ray continuum and radio are coincident in the south with an extra peak at $\sim 150''$. (ii) The radio leads the X-Ray continuum in the northwest with secondary peaks seen at both wavelengths at $\sim 150''$ as was shown in Gotthelf et al. (2001). There is very little sub-mm emission in this region. (iii) The outer peaks in the X-ray and radio emission in the west is not as significant than the south and northwest regions. (iv) The sub-mm emission has outer peaks in the west and south coincident with the outer shock from the X-Rays but none in the northwest. The evolution of the blast wave depends on the density of the medium surrounding it, if the medium is dense i.e. from a previous stellar wind phase, the blast wave will be significantly slowed down as compared to the evolution into the diffuse ISM. The overall patterns for Cas A suggest that the expansion of the remnant in all three wavelengths is being hindered in the south by the presence of a dense ambient material.

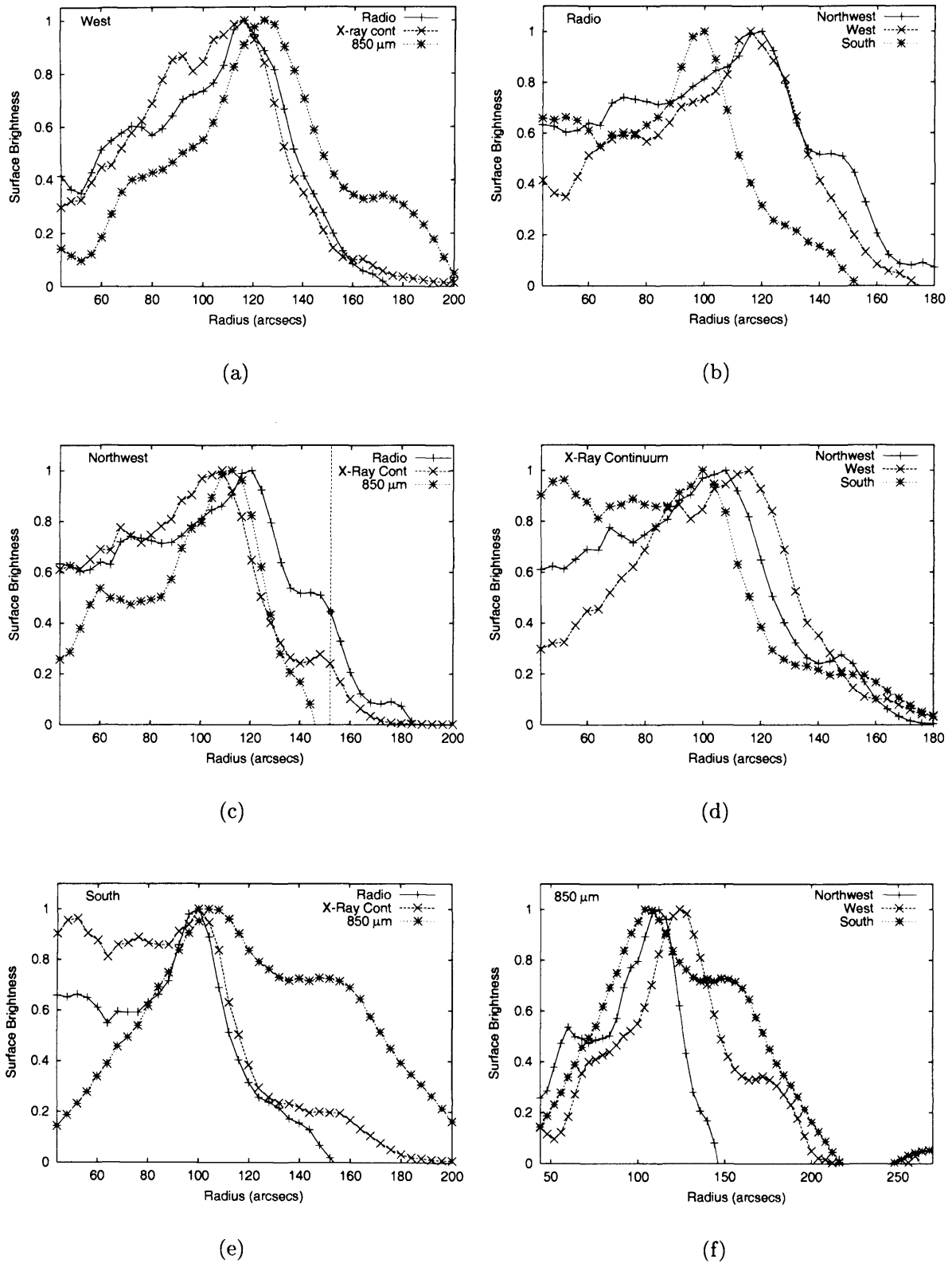

Figure 5.5: The radial profiles of Cas A in the radio, X-Ray and sub-mm in the West, South and North-western regions of the remnant. The vertical line in the Northwest image identifies the position of the forward shockfront from Gotthelf et al (2001) at 153″ from the centre. This is identified from extra peaks in the emission, further out than the bright ring. These peaks are also seen in the South and to a much lesser degree, in the West.

There does not appear to be any global correlations between the evolution of the emission in Cas A **except** for the presence of significant sub-mm flux outside the main peak of emission in all other wavelengths.

5.3 Multi-wavelength Kepler

There are many observational studies of Cas A at different wavelengths due to its extremely bright nature. However, Kepler has not had the advantage of being observed in many different wavelengths. In this Section I present a multi-wavelength analysis of Kepler with some discussion on the origin of the emission.

5.3.1 Images and Observations

The observations of Kepler used in this Section are summarised below.

X-Ray

X-ray emission in young SNRs is dominated by the line emission from heavy elements (Si, Fe, S) in the shocked ejecta (possibly due to encountering the reverse shock - Kinugasa & Tsunemi 1999). This is due to X-Ray emission being proportional to density squared, hence the brightest emission mainly arises from the shocked ejecta which is usually denser than the ambient medium. There are possibly three X-ray components - (1) ejecta (fast moving enriched material); (2) clumpy CSM (slow moving not heavily enriched material traversed by outer shock) and (3) diffuse CSM (continuum emission outer shock). The ejecta are freely expanding until it hits the reverse shock and is possibly decelerated.

We used two different X-ray images in our analysis of Kepler's SNR. Firstly we obtained an archival 50ks CHANDRA broadband image taken in 1999 by Stephen

Holt. This was used originally to compare the broadband X-ray evolution due its arcsecond resolution. However, in order to determine the position of the forward and reverse shock, we needed to separate the line emission from the continuum (the broadband image is dominated by line emission from the ejecta). For this reason, we used archival images of Kepler and Cas A taken in 2001 with XMM-Newton which were reduced by Tim Waskett. These images are not as deep (~30ks) and the resolution is far less ($\sim 6''$) but sufficient for our purposes when comparing to the $14''$ 850 μm images. Images of the continuum (4 - 6 keV) and FeK line emission (6.1 - 6.8 keV) were used to compare emission from the ejecta and the interaction with the CSM. The continuum was subtracted by using the overall spectrum to derive a ratio of continuum-to-line energy and comparing this with the level of continuum emission in an adjacent band with no line contamination. A bright ring is seen at a radius of $\sim 95''$ from the centre of the remnant and is brighter in the north (particularly in the northwest). This is suggestive of the forward shock encountering a denser CSM in the north than the south (Bandiera 1987; Borkowski et al. 1992). Strange features, dubbed as 'ears', are seen in the northwest and northeast outermost edges. The X-ray line (minus continuum) and continuum images of both Kepler and Cas A were kindly provided by Tim Waskett.

Radio

There are two major radio components in a supernova shock - flat spectrum and steep spectrum emission which are thought to trace the forward and reverse shocks respectively (Delaney et al. 2002). The synchrotron emission can be enhanced by increasing the number of relativistic electrons and amplifying the magnetic fields. The synchrotron emission in Cas A is thought to be due to the amplification of magnetic fields around the ejecta clumps (Anderson & Rudnick 1996). In this sce-

nario, a bow shock is created in front of the clump as it traverses the reverse shock and a shock is created on the surface. This decelerates the clumps and generates turbulence in layers which amplifies the magnetic field.

The radio image used in this thesis is a 6 cm Very Large Array (VLA) image taken in 1997 and was kindly provided by Tracey Delaney (Delaney et al. 2002; hereafter DKRD02). The radio looks remarkably like the X-Ray but is expanding at a much slower rate (Hughes 1999). This suggests an evolutionary connection between the X-ray and the Radio in which the shocks 'turn on' the synchrotron. The ears observed in the X-ray and the north-south asymmetry are also seen in the Radio.

Optical

The Hα optical image used in this Thesis was kindly provided by William Blair (Blair et al. 1991) and was taken in 1987 at the Dupont Telescope, Las Campanas Observatory. Two optical components exist in the remnant - shocked diffuse circumstellar medium and clumpy CSM. Both are due to the outer shock over-running the ambient material and heating/compressing the different density regions. Bright radiative optical filaments are seen mainly on the northwest edge where the brightest X-ray exists. Fainter optical emission is seen in the north just outside the X-ray and radio shell. This faint Hα emission is filamentary and at a larger radius than the dense clumps (visible in [NII]) and is likely to be from the diffuse CSM (has a broad component which suggests emission from a shock encountering neutral material). There is no optical emission in the south (as in Cas A).

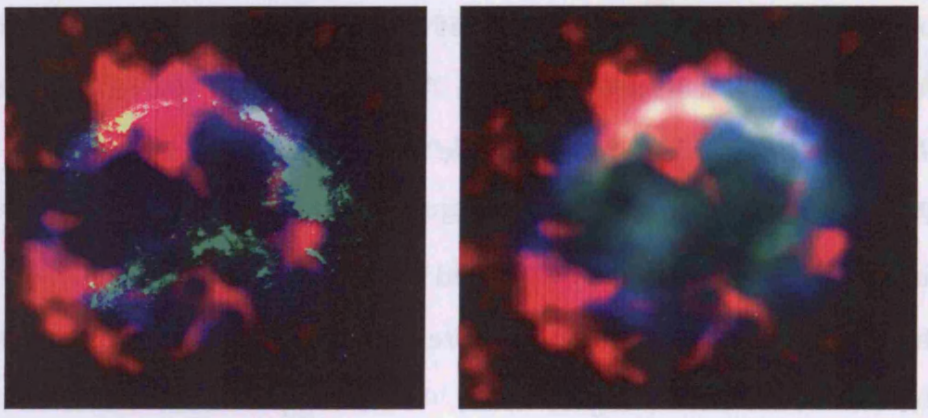

Figure 5.6: Multi-wavelength images of Kepler's Supernova remnant made by splitting each wavelength into colour channels. **Left:** 850 μm, X-ray and optical image. Red = 850 μm, Blue = X-ray continuum, Green=optical emission. **Right:** 850 μm, X-ray Fe line and X-ray continuum. Red = 850 μm, Blue = X-ray continuum, Green = Iron (FeK) emission.

Infra-Red

Kepler was observed in 1996 with ISO with a spatial resolution of 6″ at 12 μm (Douvion et al 2001). They found that the total flux over a circle of 1.8 arcmin radius was 1.0 ± 0.05 Jy. The IR image looks remarkably like the optical, again demonstrating the North-South asymmetry seen in the other wavelengths. As the optical is thought to be from shocked circumstellar material (Blair et al. 1992), this suggests that the IR is also CSM. The spectrum is well fitted by dust thermal emission composed of astronomical silicates with single grain temperature of 107K with total dust mass of 10^{-4} $M_{\odot}$. Hence Douvion et al. (2001b) concluded that the IR emission was from circumstellar dust.

It is intuitive at this stage to show the different wavelengths together visually. By splitting each wavelength into RGB colour channels and adding them up we can see clearly where the emission in each wavelength originates and its evolution. This is a popular method when analysing supernova data as it is a powerful tool for tracing the multiwavelength plasmas. Figure 5.6 shows that, like Cas A, there

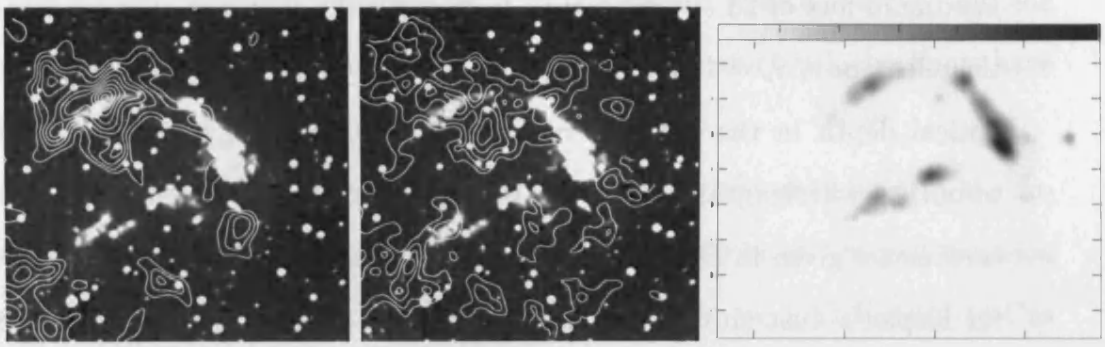

(a) (b) (c)

Figure 5.7: The (a) 850 μm emission contours ($3\sigma+1\sigma$) and (b) 450 μm contours ($1\sigma+1\sigma$) emission overlaid onto the smoothed optical image (Blair et al. 1991). (c) The 12 μm image with ISO showing the emission from warm dust at 100K (Douvion et al. 2001a). This image was taken from the website *http : //www.astro.umn.edu/tdelaney/kepler/* and observations only exist of the northern part of the remnant. The sub-mm emission appears to be anti-correlated with the optical and the IR as was seen in the SNR Cassiopiea A.

seems to be a segregation of the plasmas, the optical and the 850 μm 'avoid' each other and the 850 emission is further out than both of the X-Ray components and the optical filaments. This will be discussed further in Section 5.3.2 and Section 6.2.

5.3.2 Sub-millimetre vs. Other Wavelengths

Evidence for the sub-mm dust not being mixed with the emitting gas comes from direct comparison with the other wavelength images. If we overlay the 850 μm and 450 μm emission onto the optical image from Blair et al. (1991), we can clearly see that the dust is mainly situated where there is little or no optical emission (Figure 5.7). This suggests that the dust could be blocking the optical light from reaching us in those parts where dust exists and that the sub-mm emission is not from circumstellar dust. This was also seen in the observations of Cas A (Section 5.2). Yet are the sub-mm clumps optically thick enough to block the optical light?

The size of these clumps at the distance of Kepler is approximately 0.75pc with

maximum flux of 28 Jy/20″ beam. In an optically thin medium the flux density at the telescope is $S_\nu = \Omega B(\nu, T_d)\tau$ where τ is the optical depth. This gives a maximum optical depth in the sub-mm regime of $\tau(850\mu\text{m}) \sim 5.5 \times 10^{-4}$. Extrapolating to optical wavelengths via the relationship between sub-mm and visual absorption coefficients given in Bianchi et al. (2003) where $\tau_v \sim \tau(850)\kappa(850)/\kappa_v$, gives $\tau_v \sim 2$ for Kepler's dust clumps[2]. This suggests that some of the optical emission could be blocked by the dust clumps and explains why there is no optical emission in the south where most of the sub-mm resides. A similar calculation for Cas A results in an optical depth of ~ 6. Alternatively, the anti-correlation may also result from conditions for dust formation/survival not being reached in areas of strong optical emission.

These figures show that a lot of the sub-mm emission appears to lie outside the bright ring in the X-ray and the radio remnants. Previous analysis of the X-ray and radio suggests that the forward shockwave is traced by the bright emission shells in these images, located at a radius of $\sim 100''$ from the centre of the remnant and the reverse shock front is located at $\sim 90''$ (e.g. DKRD02). The ratio of the radii of the two shockfronts is therefore $r_f/r_r \sim 1:1$. If the identification of the shock fronts are correct, then half of the sub-mm emission does not reside between the forward and reverse shocks, implying that the sub-mm dust is not associated with the remnant. There are several ways we can explain this:

(i) The dust is from a prior stellar wind stage and is about to be swept up by the blast wave.

(ii) The dust is newly synthesised supernova dust which formed in cool, dense bullets in the ejecta which has penetrated the material swept up by the shocks with-

[2]This is calculated using $\kappa(850) = 0.75$ m^2 kg^{-1}. For lower ISM κ values, the optical depth would be higher.

out significant deceleration. This is similar to the optical FMKs observed outside the remnant of Cas A (Fesen et al. 2001) although such extreme velocity knots have not yet been observed in Kepler.

(iii) The leading edge of the shock front is not the bright shell seen in the radio, instead the forward shock front is further out than the bright ring of emission suggests. There is little work on this subject for Kepler so we look instead to Cas A, where the shock fronts have been analysed in detail. Firstly, the sub-mm emission observed in Cas A when overlaid onto the radio, also shows that there is dust emission outside the bright radio and X-ray ring (e.g. Figures 5.2 & 5.1). The high resolution X-ray data for Cas A showed that the forward shock was $\sim 153''$ from the centre which is a further $\sim 45''$ from the radio ring seen in the radio (and is believed to trace the reverse shock). Gotthelf et al. (2001) show that, at this location, an extra peak exists in the X-ray and radio emission profile outside the previously determined shock front (as shown in Figure 5.5). The ratio of the radii of the two shocks in Cas A is then $r_f/r_f \sim 3:2$. If the positions of the new shock fronts are imposed onto the Cas A dust images, the sub-mm emission is now confined between the two shock fronts (Figure 5.8).

Kepler is in a similar evolutionary phase to Cas A with a similar range of observed expansion parameters (Dickel et al. 1987; Hughes 1999; Delaney & Rudnick 2003). The time-averaged expansion rates of the shockfronts in both remnants should be the same (Hughes 1999). Therefore the overall dynamics of the two remnants should be closely related (Chevalier & Oishi 2003) and the ratio of the shockfronts should be similar i.e. r_f/r_r should be $\sim 3:2$. This ratio predicts the forward shock in Kepler should be $\sim 120-130''$ from the centre which would encompass all of the 850 μm emission.

In Figure 5.9, the images of Kepler at different wavelengths are compared with

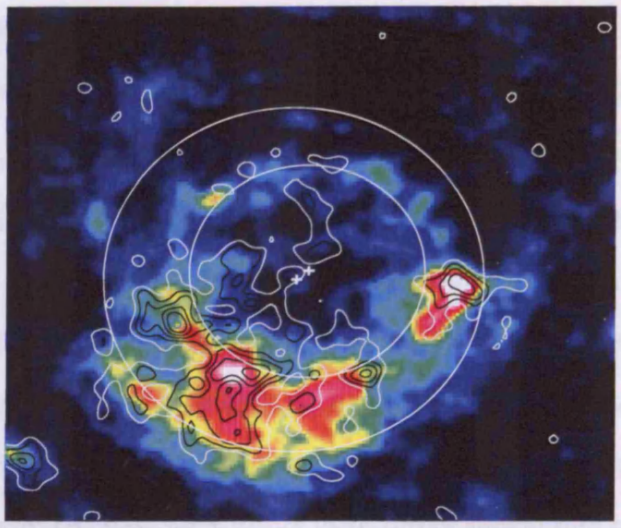

Figure 5.8: The 850 μm image of Cas A (courtesy of L. Dunne) with the position of the new shock fronts (Gotthelf et al. 2001) overlaid. The forward shock is moving out from the centre and is situated at a radius of $153 \pm 12''$ and the reverse shock is at a radius of $95 \pm 12''$. The ratio of the two shockfronts is 3:2. The contours show the 450 μm emission levels starting at $3\sigma + 1\sigma$.

the shockfront position at 100″ overlaid. The sub-mm emission is clearly outside the bright ring seen in the radio (b) and the X-ray (c). DKRD02 suggest that the bright 'ears' seen in the radio and X-ray are actually the outer most edge of the radio and not the bright ring. If we assume that the outer edge of the wisps are due to the leading shock, then the forward shock lies between $\sim 120 - 135''$ from the centre (Figure 5.9 (e)). If we use this outer radius as the position of the forward shock, it encompasses all of the 850 μm emission (Figure 5.9 (f)). Although this argument is not very strong evidence (we have to wait for further X-ray analysis on Kepler to be confident that this outer radius does actually trace the forward shock), the fact that the X-ray appears to be expanding at a rate faster than the radio is promising (Hughes 1999).

To determine if outer peaks in the X-ray and radio emission exist in Kepler's remnant, radial profiles were constructed using the sub-mm, X-ray broadband image,

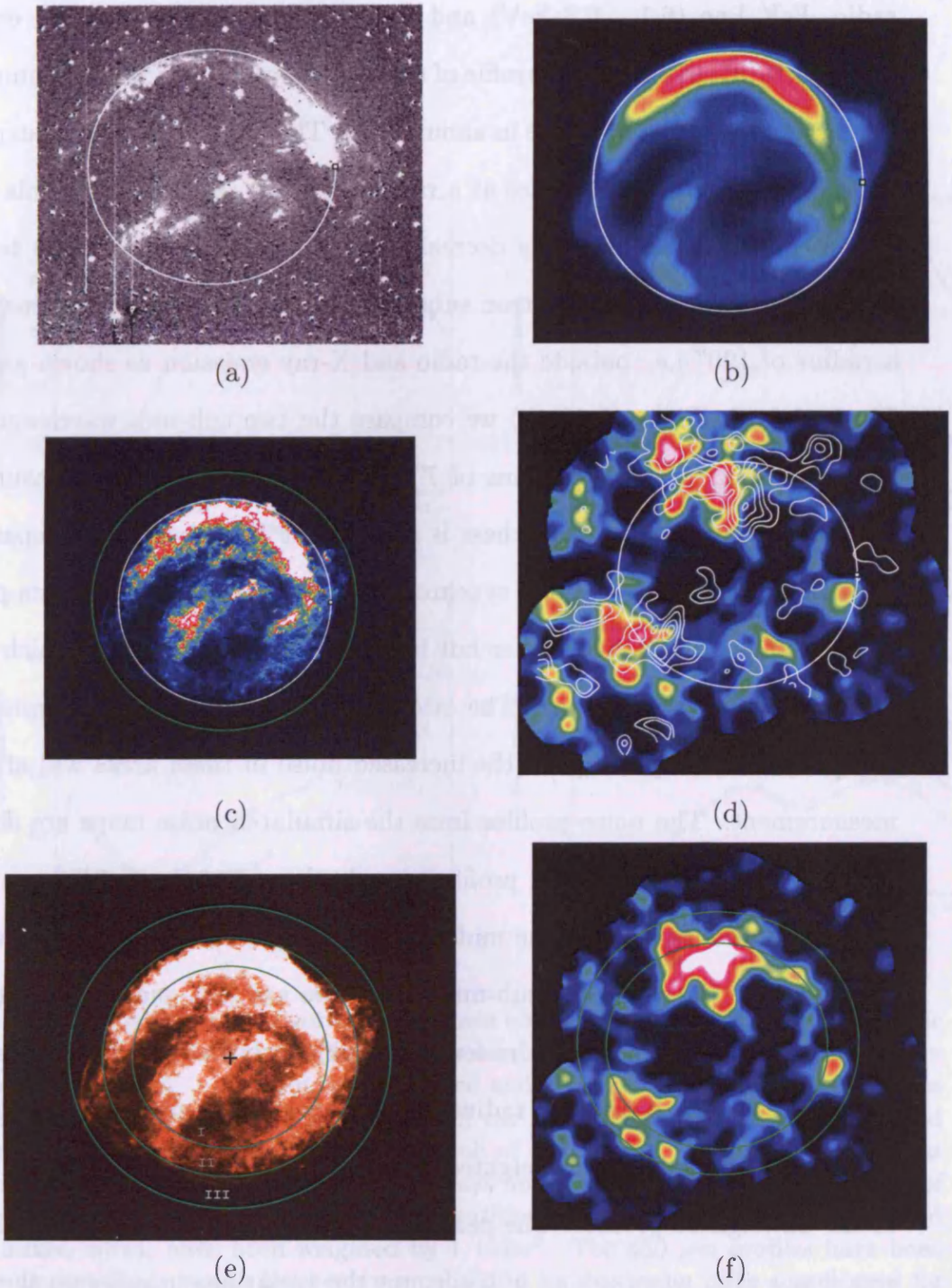

Figure 5.9: Comparison of Kepler at different wavelengths. A circle with radius 100″ centred on $\alpha_{2000} = 17^{h}\ 30^{m}\ 41.25^{s}$, $\delta_{2000} = -21°\ 29'\ 29.7''$ is overlaid onto (a) the optical image; (b) the smoothed VLA 6cm Radio image; (c) the Chandra X-ray 50 *ks* exposure image and (d) the smoothed 850 μm image with 450 μm contours ($1.5\sigma + 1\sigma$). In (d) it is clear that some of the dust lies outside the 100″ ring. (e) shows a possible new identification of the shock fronts using 'wisps' identified in the X-ray as the outer shock (circle III). The reverse shock is represented by circle I with radius 80″ which corresponds to the first peak in the intensity profiles. The position of the forward shock as represented by the outer blast wave is shown by circle II with radius 105″ (f) shows circle III and II overlaid onto the synchrotron subtracted 850 μm emission. The dust emission is confined in the two shockfronts if the 'wisps' determine the 'true' position of the outer shock.

radio, FeK line (6.1 - 6.8 keV) and X-ray continuum (4 - 6 keV) emission. In Figure 5.10(a), the intensity profile of the 850μm smoothed image is compared to the synchrotron subtracted image in annuli of 7″. The difference is not unexpected. The radio contamination dominates at a radius of $\sim 80 - 90''$ and once this is removed, the intensity in this region is decreased by around 30% and is due to dust only. Consequently, in the synchrotron subtracted sub-mm image, the intensity peaks at a radius of 120″ i.e. outside the radio and X-ray emission as shown graphically in Figure 5.9. In Figure 5.10 (b) we compare the two sub-mm wavelengths over the whole remnant averaged in bins of 7″ and 4″ respectively. This ensures that the 850 and 450μm surface brightness is sampled at least twice in comparison to the relative beam sizes. In (b), the synchrotron subtracted 850 and 450 μm peaks do not exactly coincide with each other but in general they both agree (which is probably due to low S/N at 450 μm). The evidence for peaks in the dust emission outside 100″ radius is compelling but the increased noise in these areas will affect the flux measurement. The noise profiles from the simulated noise maps are shown in (c). The large bump in the noise profile towards the centre in the 450 μm emission is due to the missing data in the middle of the image. It is important to note that at a distance $>$ 140 pc in the sub-mm images we are just encountering the edges of the jiggle maps where the noise level is significantly increased, thus we will ignore any sub-mm flux beyond this radius. In (d) the sub-mm emission is weighted by the noise. The 850 and 450 μm weighted flux density profiles are shown with comparison to the unweighted profiles. The peaks outside 100″ in the sub-mm still appear to be significant even when taking into account the variations in noise on the map.

Included in Appendix A.2 are the radial profiles of the X-ray, radio and 850 μm over the whole remnant. In this Section, we follow DKRD02 by comparing the flux density at each wavelength for three different regions of the remnant. These were

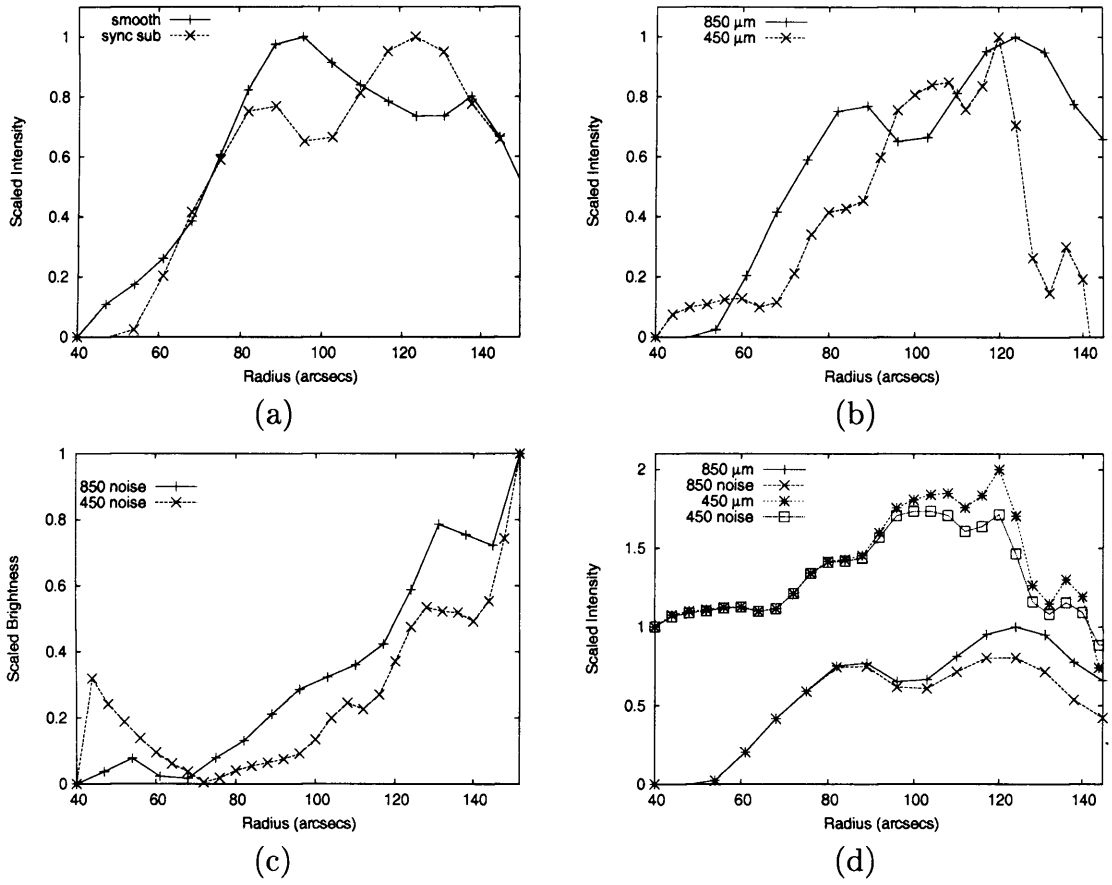

Figure 5.10: Comparison of the surface brightness emission from Kepler's SNR over the entire remnant for the (a) 850 μm smoothed sub-mm image compared to the synchrotron subtracted image. (b) 850 synchrotron subtracted and 450 μm smoothed sub-mm images (both convolved with the 850 μm beam) and (c) the intensity profiles from the 850 and 450 μm simulated noise maps averaged in annuli of 7″ and 4″. The sharp increase at small r in the 450 μm emission is due to the arrays not quite overlapping in the centre of the image. In (d) we compare the sub-mm intensities from (b) with the noise weighted sub-mm fluxes, which have been weighted by $1/\text{noise}^2$. The 450 μm profiles have been scaled for clarity. Each profile has been normalised to its maximum. The centre used for the averaging is $\alpha_{2000} = 17^{\text{h}}30^{\text{m}}41^{\text{s}}.25$ and $\delta_{2000} = -21°29'29''$.

chosen to incorporate all the features seen in the Radio without including filamentary structures. These are labelled: North - Northeast (-15° – 45°); Northwest (-75° – -40°) and South (145° – 225°) and the intensity profiles are shown in Figure 5.12 and Figure 5.11.

The optical and infra-red profiles are given in DKRD02 and are reproduced here. Some key patterns from these are: (i) the X-ray, radio and 850 μm appear to be expanding slower in the NW than in the other regions. (ii) Small peaks with low S/N are seen outside the radius of the bright ring in the X-ray profiles at $110 - 120''$ (S, NW) and are also seen in the radio at the same radius (S). Extended emission is seen in the radio in the NW at $100 - 130''$. This corresponds to significant peaks in the 850 μm emission[3]. (iii) All three wavelengths trace each other extremely well in the NE region with similar peak positions, apart from the presence of a second peak in the sub-mm. (iv) The radio and X-Ray emission regions in the South appears to be further out than that seen in the north, again implying that there is a steeper density gradient in the northern regions hindering the expansion of the ejecta. (v) The Hα and IR emission both lead the X-ray and radio in NE and S and trace them in the NW. The sub-mm emission does not appear to be tracing the same conditions as either the optical or the warm dust.

Radial profiles constructed on regions which only incorporate the dusty features seen in the south and northwest are given in Appendix A.2, Figure A.4. These show more evidence for dust peaks outside the ring of bright X-ray emission.

How does the sub-mm emission compare with the forward and reverse shocks in the different regions? Do the ejecta and forward shock follow different profiles in each medium? In Figure 5.13 the 850 μm synchrotron subtracted emission is compared to the X-ray continuum and FeK line emission. The X-ray continuum

[3]The extra peak may be missed in the NW of the sub-mm emission because this region is hindered by noisy bolometers which may have affected our flux measurements

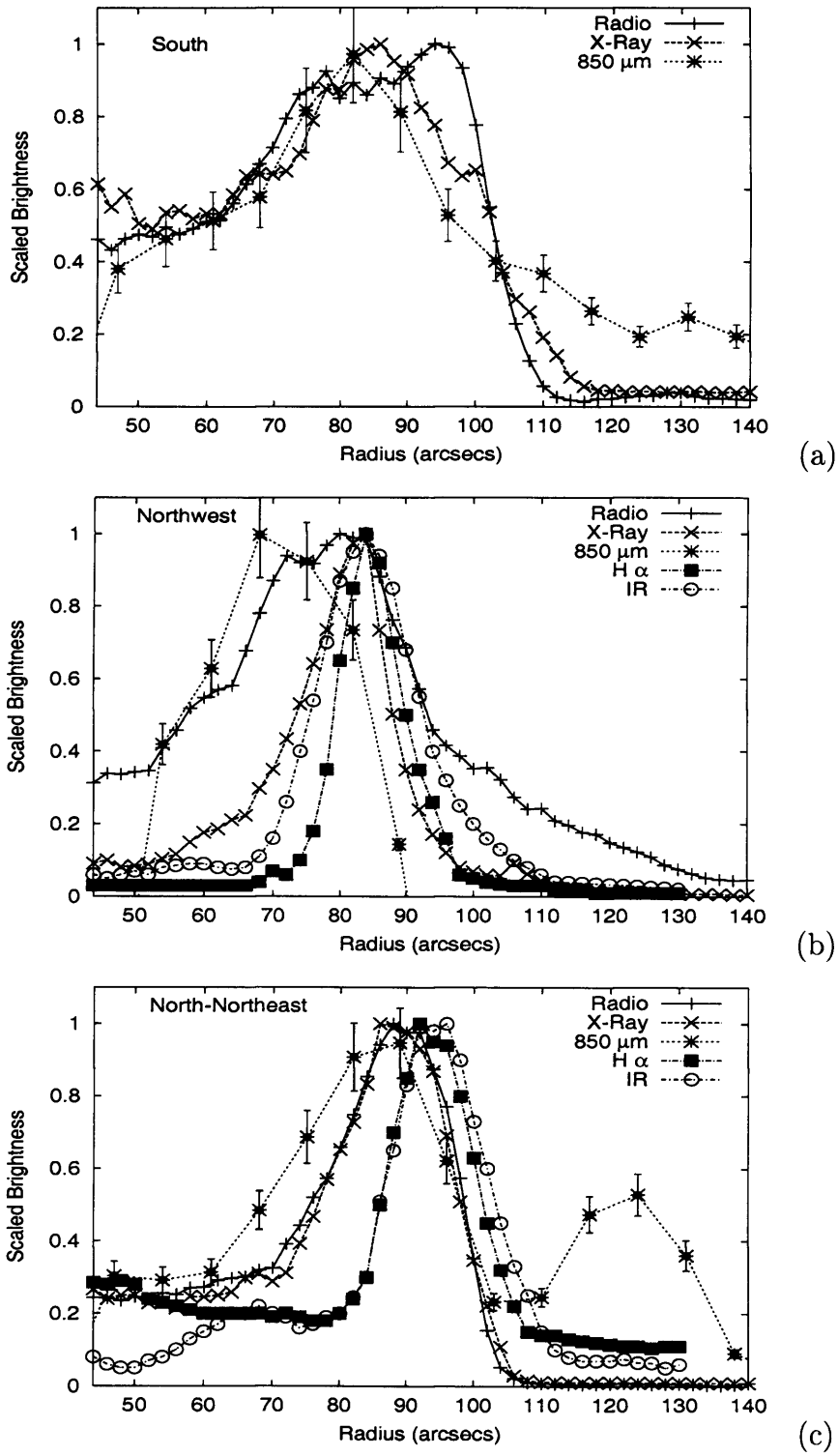

Figure 5.11: Comparison of the radial profiles normalised by area for the smoothed X-Ray, Radio, Infra-Red and optical (Hα) and the noise weighted, synchrotron subtracted 850 μm emission averaged over the (a) Southern (145° – 225°) (b) Northwestern (-40° – -75°) and (c) North - Northeast (-15° – 45°) regions of the remnant.

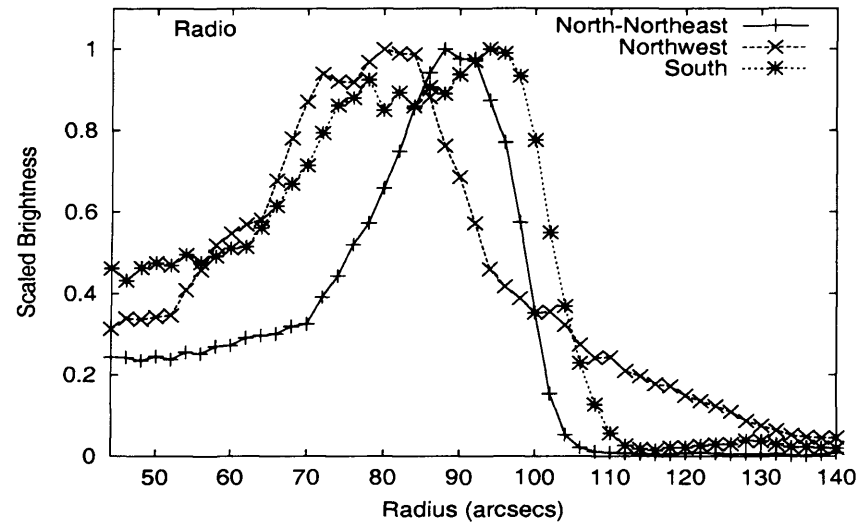

(a)

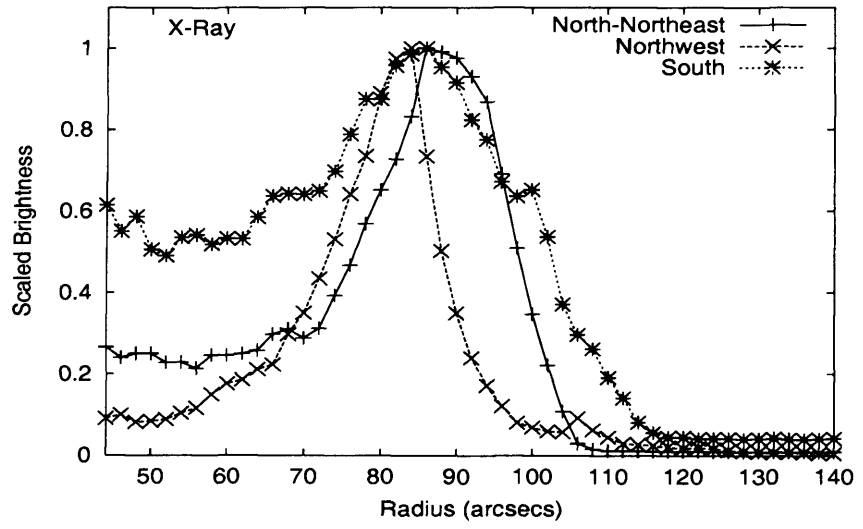

(b)

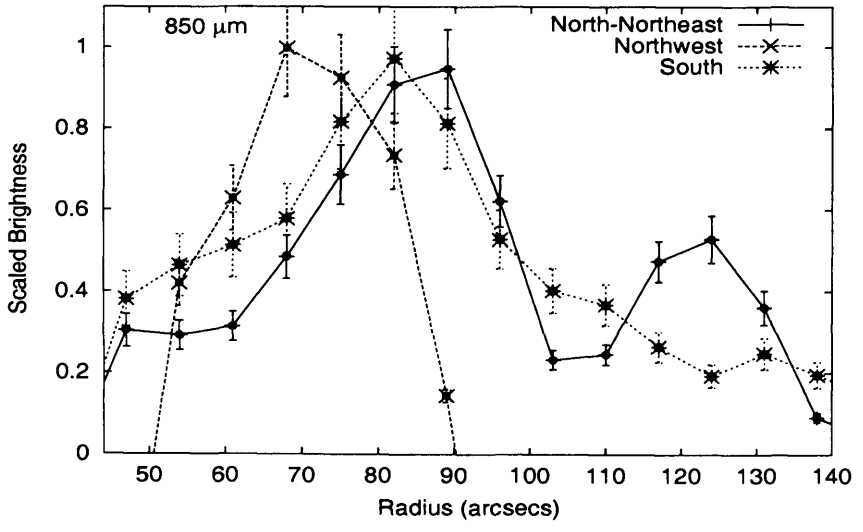

(c)

Figure 5.12: Comparison of the radial profiles normalised by area over the North-West, South and North Eastern regions of the remnant for (a) radio (b) X-Ray (c) noise weighted, synchrotron subtracted 850 μm.

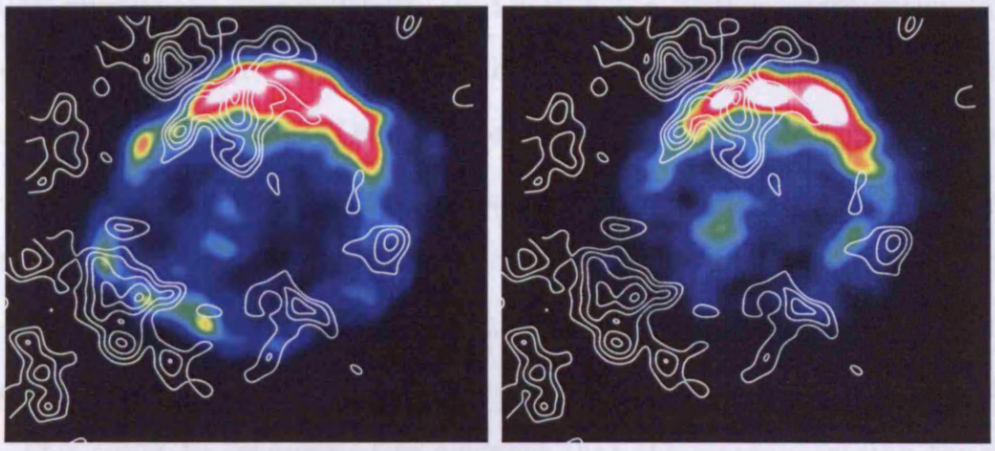

(a) (b)

Figure 5.13: Kepler's SNR in the (a) X-Ray continuum and (b) FeK line overlaid with 850 μm contours. The contours show the synchrotron subtracted 850 μm emission with levels starting at $2\sigma + 1\sigma$.

extends further out than the ejecta, particularly in the south as was seen in Cas A. The sub-mm emission is much further out than the X-ray, even in the continuum emission which traces the forward shock.

In Figure 5.14, we compare the radial profiles of the X-ray line emission and the X-ray continuum from the archival XMM-Newton observations and the noise weighted 850 μm synchrotron subtracted emission. This allows a direct comparison of the profiles of the sub-mm 'shell' with the forward and reverse shocks (in comparison to the previous images which looked at the global emission at all wavelengths). In (c) we also show the same Figure made by T.Delaney using the CHANDRA X-ray data with better resolution.

The ejecta peaks earlier than the outer shock which peaks at $\sim 100''$. The two shockfronts are very close to each other in the NE yet further separated in the South. The 850 μm profile in both regions traces the ejecta (X-ray line emission) for $r < 100''$. However as seen in the previous profiles, the 850μm has a second peak

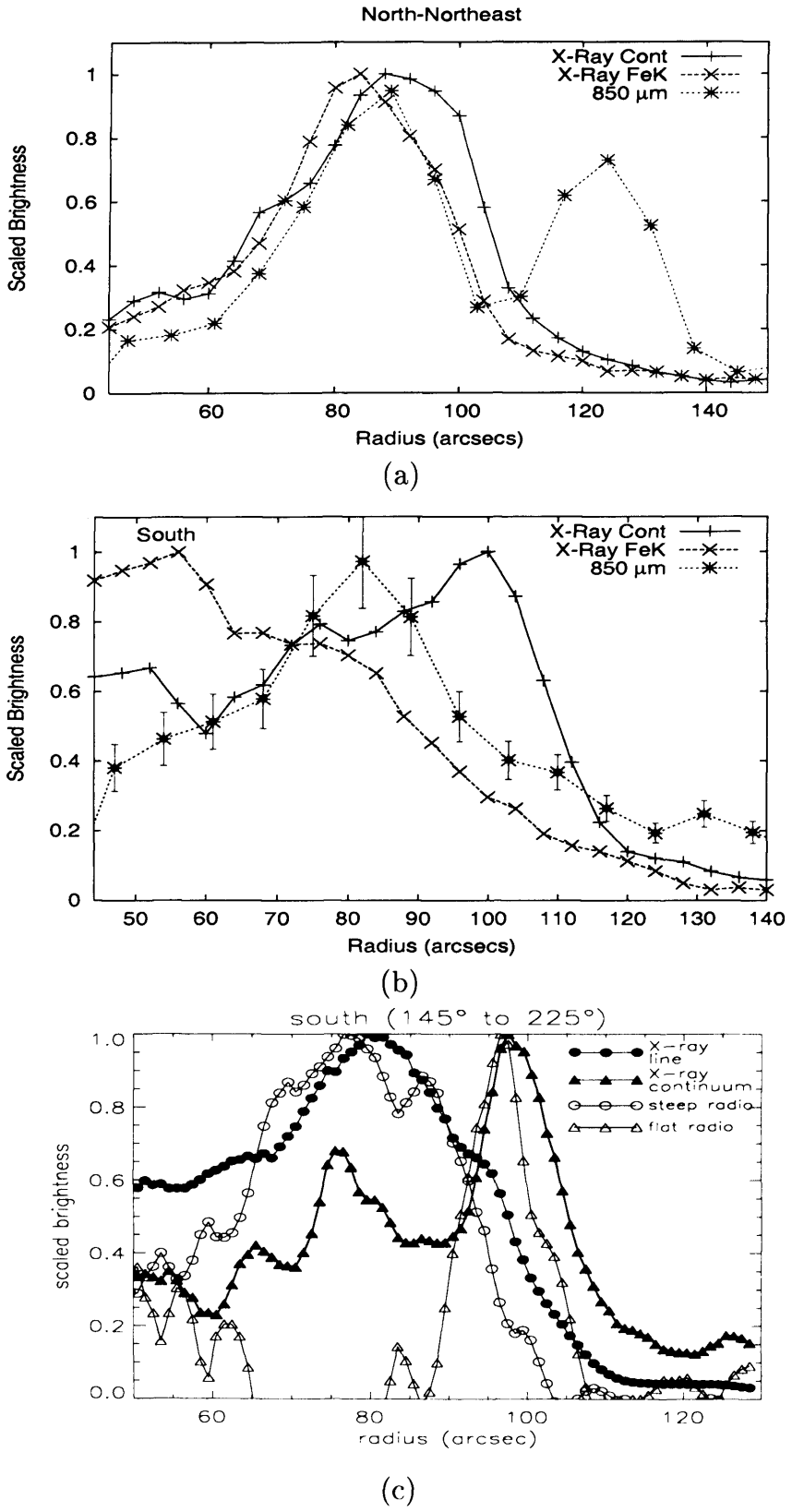

Figure 5.14: Comparison of the surface brightness with radius for the FeK emission, X-ray continuum and the noise weighted, synchrotron subtracted 850 μm emission averaged over (a) North - Northeast (-15° - 45°) and (b) Southern (145° - 225°) regions. In (c) the X-ray profiles from CHANDRA in the south is shown compared to the flat and steep radio spectrum (courtesy of T.Delaney).

at $\sim 120''$ outside the forward shock. In DKRD02, a further investigation into the radio emission was made by separating the two radio maps at 6cm and 20cm into flat and steep radio emission. The flat represents flux with spectral index lower than $\alpha = -0.72$ and the steep is due to emission with $\alpha > -0.72$. DKRD02 found that morphologically, the steep traces the reverse shock and the flat the outer forward shock (Figure 5.14 (c) courtesy of T.Delaney). In the NW, the X-ray is similar to the flat spectrum, yet in the South, the steep tracks the X-ray and trails the flat radio. This could be interpreted as evidence that the steep is tracing the reverse shock. The similarity between the X-ray line emission and the steep radio (ejecta) and the X-ray continuum and the flat radio (outer shock) is remarkable. (c) also shows second peaks in the X-Ray at $130''$ and in the flat radio at $120''$ which may identify the forward shock as being much further out than previously believed. The flux from these peaks are $\sim 0.1 - 0.2$ times the main peak, yet in Figure 5.14 the peaks are far less significant at < 0.1, due to the far better sensitivity of CHANDRA w.r.t. XMM-Newton.

If the small (but low S/N) outer peaks in the X-Ray and radio seen in these images at $\sim 110 - 130''$ are due to the interaction of the forward shock with the ISM, the ratio of the shockfront positions would be $\sim 3 : 2$ which agrees with the result in Gotthelf et al. (2001) for the shock front positions of Cas A. Unfortunately, the low level of flux in the outer peaks in Kepler are not high enough to determine whether they truly trace a forward shock and deeper X-ray observations are required to detect any faint emission. We look forward to future, deeper observations with CHANDRA which may shed some light on this issue.

5.3.3 Morphology of Kepler's remnant

To compare the morphology of the emission in the North where the bright region of the X-Ray and Radio trace the most shocked ejecta/CSM, we can trace the azimuthal dependence of the emission (50°—−50°). Here we include the sub-mm observations to the radio, X-ray profiles as was originally done in DKRD02. The intensity from the 850 μm image was averaged in a annulus of radius $70 - 100''$ from the centre in 5° increments. In Figure 5.15, we show the results for the 850 μm image and include the results for all other wavelengths as published in DKRD02.

From (a) we see that the Hα and IR are closely correlated and peaks are seen in the NE and NW regions. The radio brightness is concentrated symmetrically, directly north and is similar to the flat emission. The steep emission is brighter in the NW (although at $r = 50 - 80''$ there is also emission in the NE). The steep is similar to the Hα and IR. This suggests that the steep, X-ray, IR and Hα are all tracing variations in the circumstellar density in the North. What is interesting about this comparison is that the sub-mm trend appears to be anti-correlated with all of the above with a peak in the NE and none in the NW. This is even more marked at the larger radii suggesting the cold dust could be a different component of the CSM or tracing a different density/temperature region of the shocked ejecta. Alternatively it could be indicating something important about the conditions for dust formation/survival in SNRs.

We summarise all of the above multiwavelength analysis in terms of the remnant morphology[4]:

- **NW** - High density medium surrounding the remnant in this region due to presence of bow shock. This medium immediately slows down the outward moving blast wave and as the ejecta is constantly being ploughed into this

[4]An aside on the X-ray and Radio morphology is given in Appendix A.2

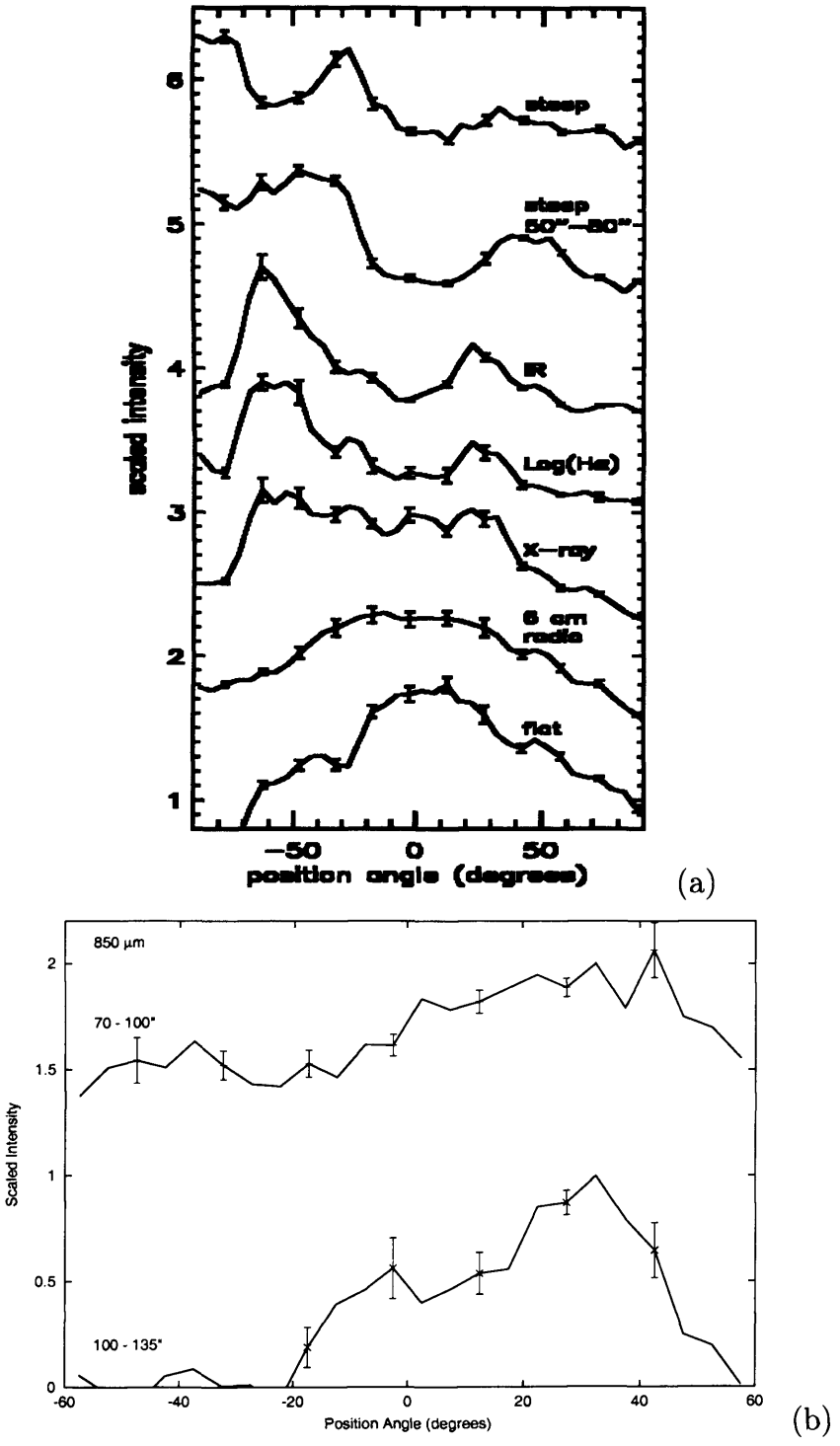

Figure 5.15: Intensity averaged every 5° in position angle for an annulus in radius 70–100″ around the Northern ring (−60° - 60°). In (a) we show Fig. 17 from DKRD02 in which the intensity of the IR, optical, X-ray, Radio (flat, steep and whole) are compared (with the steep also being shown at a radius of 50 – 80″). In (b) we present the azimuthal averaged 850μm profile at a radius of 70 – 100″ and 100 – 135″. The errors bars are taken from the standard deviation of the flux in each section and are shown for every third azimuth bin. The centre used for this plot is the same as in Figure 5.10.

high density medium, the reverse shock is set up immediately due to the compression of the ejecta behind the outer shock. The strong shocks leads to bright emission in the X-ray and radio. The distance between the two main peaks in the X-ray continuum and FeK emission is $\sim 15''$.

- **NE** - Lower density stellar wind medium encountered such that both X-ray and Radio are further away from the remnant than the NW emission. This also explains the short distance between the two shockfronts in this region ($< 5''$) as the density of the surrounding medium isn't high enough to create as strong reverse shock as seen in the NW.

- **S** - Less dense surrounding material in this region so shock fronts are less decelerated. The distance between the main peaks in the X-ray continuum and FeK is $\sim 20''$. Since the blast wave has not encountered a high density medium, any reverse shock set up will not be strong enough to accelerate the electrons sufficiently enough to shine in the radio (as seen by the lower emission in the radio image in the southern regions). The shock region spreads outwards and becomes thin as the shock energy is dissipated. The forward blast wave is still moving outwards. Dust is prevalent in this region whereas the FeK emission which traces the hottest ejecta is absent.

This scenario is in agreement with the model proposed by Bandiera (1987) in which Kepler's progenitor was a massive star moving into its own stellar mass loss and provides tantalising clues for the conditions needed for dust formation/survival. A full hydrodynamical model to investigate the future evolution of the shell is beyond the scope of this thesis.

Comparing the radial profiles of both Cas A and Kepler, there seems little correlation between where the dust is and the position of the X-Ray relative to the

Radio and the hot dust in the IR (the reasons for which are beyond the scope of this thesis). The significant result from this work is that in both remnants there is sub-mm emission outside of the main peak in the X-Ray and radio *and* the sub-mm emission is anti-correlated with the warm dust and optical. It could be possible that, like Cas A a few years ago, the position of Kepler's forward shock front is still to be identified by X-Ray observations.

5.4 Understanding the Cold Dust Temperature

An important question to ask is how did the grains become so cold? The previous analysis suggests that the cool dust may not reside in the hot, X-ray plasma. If dust does exist in the X-ray gas, one may imagine that the grains should exist at much higher temperatures than those emitting at sub-mm wavelengths. Dwek (1999) has shown that spherical dust grains mixed with a warm X-Ray gas should remain at a steady state of $\sim$ 100K. The steady state dust temperature is found by equating the heating and cooling processes acting on the grain (Equation 5.1).

$$H_{coll}(a, T_e) + H_{rad}(a) = L = 4\pi a^2 \sigma T_d^4 < Q(a, T_d) > \tag{5.1}$$

where L is the luminosity and $< Q >$ is the Planck averaged absorption coefficient (Draine & Lee 1984). The heating processes are given by $H_{rad} = \pi a^2 < Q_\nu > cU$ and

$$H_{coll} = \pi a^2 \left(\frac{32}{\pi m_e}\right)^{1/2} n_e (kT_e)^{3/2} h(a, T_e).$$

$h(a, T_e)$ is the grain heating efficiency ($\sim$ 1 for most temperatures and grain sizes - Dwek 1987; Arendt et al. 1999) and U is the radiant energy density. However, in SN shocks, the collisional heating rate is dominant over the radiative heating so we

can assume that H_{rad} is negligible. Therefore T_d is given by

$$\pi a^2 \left(\frac{32}{\pi m_e}\right)^{1/2} n_e (kT_e)^{3/2} h(a, T_e) = 4\pi a^2 \sigma T^4 < Q(a, T_d) >$$

$$T_d = \left[\frac{(\frac{32}{\pi m_e})^{1/2} n_e (kT_e)^{3/2} h(a, T_e)}{4\sigma < Q(a, T_e) >}\right]^{1/4} \tag{5.2}$$

If the grains emit with a λ^{-2} dependency then $< Q(a,\ T_d) >$ is given in Draine & Lee for a range of temperatures. In Dwek (1999), this prescription was used to show that the dust grains emitted in the mid-IR should be $\sim$ 100K. They assumed that the dust temperatures were $>$ 150K and thus from Draine & Lee (1984), the absorption coefficient for silicate grains was $Si < Q >= 0.25a$ (μm). For an X-ray gas with typical shock density and temperature, they found that T_d = 180K or 58K for $a = 0.01$ and 1 μm respectively.

In this work however, we know that the grains must have $T_d < 50$K since they are detected in the sub-mm only. $< Q(a, T_d) >$ for silicate grains at this temperature is $< 0.01a$ (μm). From models of the X-ray spectra, the properties of the gas in the forward and reverse shocks of Kepler are thought to be: $n_e = 2$ cm^{-3}, $T_e = 10^{7.13}$K, $n_e = 4$ cm^{-3}, $T_e = 10^{6.97}$K (Kinugasa & Tsunemi 1991). Using Equation 5.2, this implies that the dust grains mixed in the X-ray gas should remain at a steady state temperature of $\sim$ 165K and 52K for $a = 0.01 - 1$ μm respectively. If the grains are larger, the grain temperatures will be cooler since the absorbed energy is less than the internal energy of the grain and it reaches thermal equilibrium quickly (see Section 1.6 and Whittet 2003). A 10 μm grain would reside at a temperature of 30K. Alternatively, if $< Q >$ is larger by a factor of 10, this decreases the temperature to $T_d \sim$ 30K respectively for $a = 1$ μm. For $a = 0.01$ μm, the temperature would be 93K. Changing the density and temperature of the X-ray gas will also serve to

decrease the dust temperature. If the density remains the same then we require $T_e < 10^5$K, to give $T_d < 20$K for $a = 1$ μm. If the gas temperature is constant, we require the density to be ~ 0.1 cm^{-3} to give $T_d < 20$K for $a = 1$ μm.

To summarise, the low temperature of the sub-mm dust can be explained if the grains are large or more efficient emitters than normal interstellar dust and reside in the X-ray plasma. Alternatively, the low temperatures could be due the grains existing in a more diffuse or lower temperature phase of the plasma. If the grains are below a critical size they are subject to stochastic heating from electron collisions (Dwek 1987). A negative charge will build up on the grain and therefore protons will start bombarding. If $a < 0.005$ μm, the collisional rate is less than the cooling rate so there maybe enough time between collisions for the grains to cool down (Arendt et al. 1999). A very unusual grain size distribution would be required to explain the shape of the observed SED of the remnants.

5.5 Weird Dust - Iron Whiskers

Conducting needles have been proposed as an alternative explanation for the large amounts of sub-mm flux we observe in the sub-mm for Cas A. Such needles, if they exist, are highly efficient emitters at sub-mm wavelengths and are collisionally heated by hot X-ray gases to temperatures less than 10K (Dwek 2004a). The high emissivity of the needles gives rise to even larger values of the dust mass absorption coefficient κ than the amorphous aggregates or the laboratory values from Chapter 4 and would thus decrease the dust mass in the remnant by several orders of magnitude. Due to the efficient emitting properties, the needles would also cool faster than normal grains and would easily exist at the low temperatures obtained from fitting the SED even when mixed in the hot X-ray gas.

The needles are thought to form via a 'screw dislocation' mechanism in which the inital spherical condensation grows along one axis preferentially, producing elongated grains with high axial ratios l/a (e.g. Dwek 1987; Hoyle & Wickramsinghe 1988). In Cas A, these grains have recently been proposed to have formed in metal-rich ejecta, flung out at high velocities into the ambient medium (Dwek 2004a). An important issue of contention (between the theory of conducting needles and more normal dust being the main cause of the sub-mm) is the calibrated value of the ISO 170 μm observation of Cas A (Tuffs 1999). This observational flux was treated as a lower limit in Dunne et al. (2003) because Tuffs had subtracted a background flux level from the image, resulting in the subtraction of dust with temperatures less than the background i.e. with T < 20K. This method would have subtracted any emission from cold dust. The fit to the SED in Cas A ignoring the ISO measurement resulted in a predicted 170 μm flux of $\sim$ 100 Jy which is three times higher than the 35 Jy published in Tuffs (1999). Dwek (2004a) used this to show that if the ISO 170 μm flux measurement of Cas A was an actual true detection at 35 Jy, the cold dust temperature required to fit the IR - sub-mm SED would be 8K (and not 20K as found in Dunne et al. 2003) (see Figure 5.16). This requires a dust mass of at least $\sim$ 20 $M_{\odot}$ to provide the emission, even for the highest laboratory κ values. This estimate of the dust mass is far too high to be explained with normal dust and hence conducting needles (particularly iron needles) would provide an alternative explanation. Unfortunately, there is a severe lack of understanding of the absorption properties of elongated grains (e.g. Li 2003). Most models assume a Rayleigh approximation with criterion given by (following Li 2003 and derived in Appendix C)

$$l_{max} \approx \frac{1}{20\pi}(\lambda\rho c)^{1/2} \tag{5.3}$$

where l_{max} is the maximum length of the needle for which the approximation is

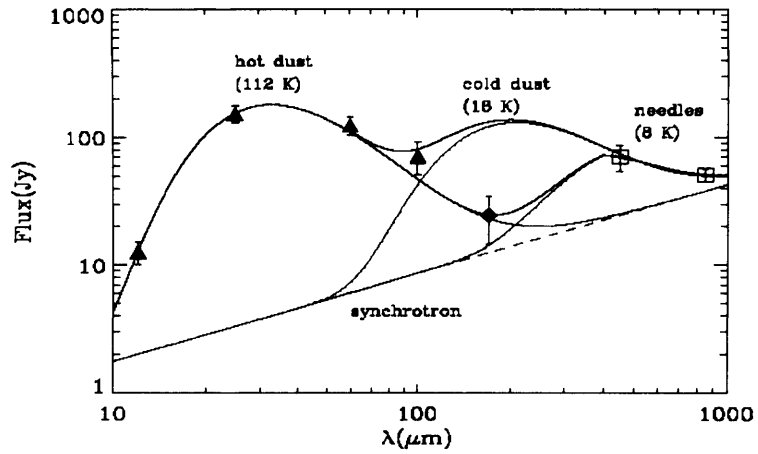

Figure 5.16: The SED of Cas A as published in Dwek 2004a. The solid lines show the best fit greybody to the IR-submm fluxes. The labels hot and cold dust refer to the fit made in Dunne et al. 2003 (also in Section 4.3) with dust radiating at 18K. However, Dwek has shown that to fit the observed ISO 170 μm component then dust at 8K is required to fit the SED.

valid and ρ is the resitivity of the material (which is temperature dependant). This limit to the needle size must be satisifed because the high absorption properties only occur when all elements within the particle radiate in phase. At 850μm and for a physical range of resistivites, the range of lengths are $l_{max} \ll 0.3$ μm. For l/a ratios of 1000, the radius of the grains become very small $a \ll 2$Å which are quite unphysically small (even a few layers of iron atoms would be comparable or greater than these radii).

The mass absorption coefficient for this approximation is given by (Equation C.4)

$$\kappa_0 = \frac{4\pi}{3}\left(\frac{1}{\rho c \rho_d}\right) \tag{5.4}$$

where ρ_d is the dust density ($\sim$ 8150 kg m^{-3}). κ_0 ranges from $5 \times 10^7 - 2 \times 10^5$ m^2 kg^{-1} for pure iron at 20K and 300K[5]. These values are therefore dependent on the temperature of the dust. However, there is a long wavelength cutoff, λ_0

[5] ρ values are quoted in Dwek (2004) as $\rho = 3 \times 10^{-8}$ Ω cm for pure iron at 20K and $\rho = 9.6 \times 10^{-5}$ Ω cm at 300K. 1 Ω cm $= 1.139 \times 10^{-12}$ s.

(Appendix C, Equation C.5)

$$\lambda_0 = \frac{1}{2}\rho c \frac{(l/a)^2}{\ln(l/a)}$$

after which $\kappa(\lambda) \propto \lambda^{-2}$.

Dwek finds that the best combination of values to reproduce Cas A's SED (**with** the 170 μm flux) are $\lambda_0 = 400$ μm, $10^2 < l/a < 4 \times 10^3$. However these are only valid for certain electron densities and temperatures of the X-ray emitting gas (in the forward and reverse shocks) of $n_e = 16$ cm^{-3}, $kT_e = 3.3$ keV and $n_e = 61$ cm^{-3}, $kT_e = 0.45$ keV which constrains the needle resistivity to be $2 - 5 \times 10^{-6}$ Ω cm (see Section 5.5.1). If these values are representative of the dust population emitting the sub-mm emission, then the cold dust mass in Cas A is only $10^{-4} - 10^{-3}$ M$_\odot$. There are a large number of parameters in this analysis which can physically have quite extreme ranges. However, to explain the observations of Cas A, we require that the parameter space is narrowed with only a certain combination able to reproduce the correct results. As the proposal of iron needles has the highly significant result that dust is not significantly formed in SNe ejecta, it is worthwhile to investigate this for Kepler's SNR.

The absorption coefficients of iron needles from Equation 5.4 are several orders of magnitudes higher than the observed κ of interstellar dust and even the laboratory values. In Figure 5.17, we show how the absorption coefficient varies for iron antennae grains with (a) axial ratio and (b) wavelength for a given resistivity. At 850 μm, κ can be as much as $\sim 10^6$ m^2 kg^{-1} compared to 0.8 m^2 kg^{-1} from Chapter 4.

This method works very well for Cas A if the 170 μm flux is the lower value given in Tuffs. However, it does not work so well for Kepler, particularly considering the 450/850 flux ratio for Kepler is higher than Cas A which implies that the parameters in Dwek's work may not be suitable. Also, the plasma temperatures in Kepler's gas inferred from the X-Rays are about a factor of 10 less than Cas A and hence cannot

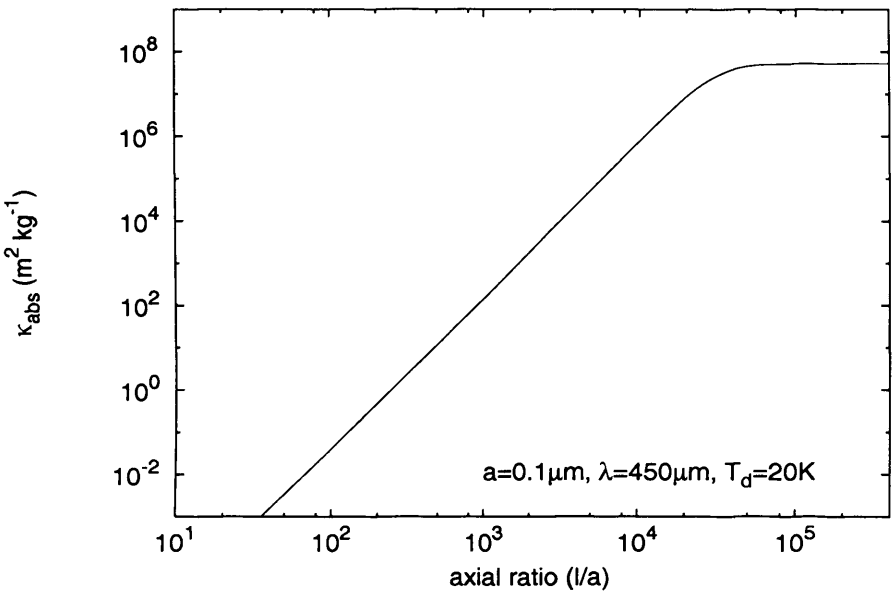

(a)

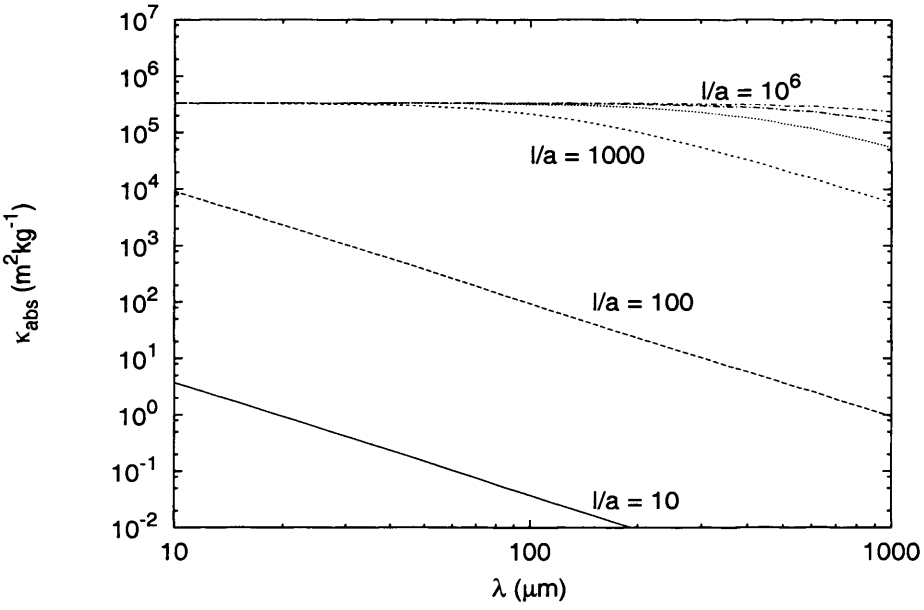

(b)

Figure 5.17: Absorption coefficient (κ) in m^2 kg^{-1} for iron needles modelled as antenna. In (a) we compare the absorption coefficient at 450 μm as a function of axial ratio l/a with $a = 0.1$ μm. For comparison, the average value of the absorption coefficient estimated from laboratory studies of amorphous aggregates is 1.5 m^2 kg^{-1}. In (b) we show how the absorption coefficient varies with wavelength for different l/a ratios with resistivity of 10^{-5} Ω cm.

heat the iron needles to such high temperatures.

To determine whether the iron needles approach is suitable for Kepler, we can follow the same argument as Dwek. If we use the observational IR - sub-mm data of Kepler (Figure 4.3), then we have observational constraints on the fitting of the SED, mainly (notation as in Dwek 2004a) $F_1 = 450/850 \sim 4.3$ and $F_2 = 450/170 \sim 0.28$ where 170 μm is just taken from the blackbody fit to the $60 - 850$ μm fluxes. In Dunne et al. (2003), the results for Cas A were: $F_1 \sim 3.0$ and $F_2 \sim 0.5$. Dwek has used the added 170 μm flux from the ISO observations of Cas A to revise F_2 to be $\gg 1$. Using the 100/170 flux ratio of Cas A from Dwek (2004a) we can estimate a corresponding 'Dwek' flux for Kepler by scaling it to the 100 μm flux for Kepler. In this case, F_2 for Kepler slightly increases to 0.8 (still less than 1). From Dwek's analysis, the needle temperature for Kepler has to be $>$ 10K to fit the observational flux ratios *even* when we use the lower 170 μm estimate. A good fit to the observational fluxes for Kepler requires a cut off wavelength $200 < \lambda_0 < 400$ μm and needle temperature $10 < T_d < 30$K (with best fit value of 20K). The lowest temperature of 10K can only be fitted if we use the lowest value of the 100 μm flux from the literature (as discussed in Section 4.2.2). In Figure 5.18, we used these properties to estimate the range of parameters which would be required to fit the data with iron needles.

The dust mass estimate for iron needles in Kepler is lower than estimated for Cas A due to the higher temperature required to fit the IR - submm SED. The sub-mm flux ratios suggest that the cutoff wavelength is much lower which decreases the resitivity for a given l/a and dust mass. From Figure 5.18, Kepler's sub-mm spectrum can be fit with iron needles with $T_d = 10$K and long wavelength cutoff $\lambda_0 = 200$ μm only *if* we assume that the 170 μm flux is lower than our SED predicts. Using the range of resistivities given in Dwek 2004 gives a maximum dust mass (i.e.

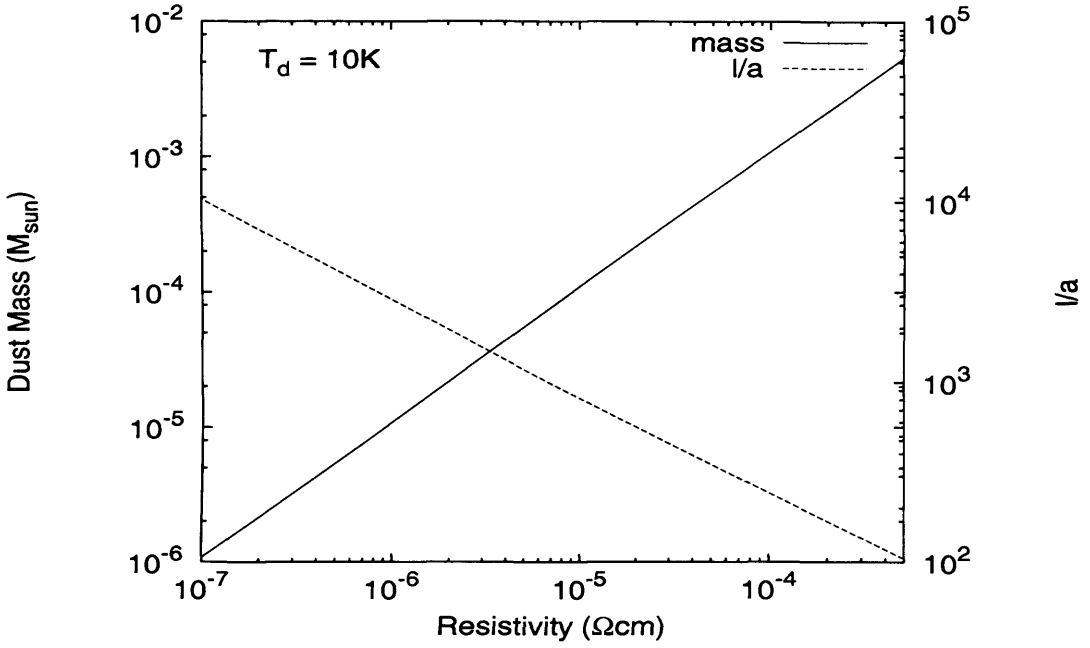

(a)

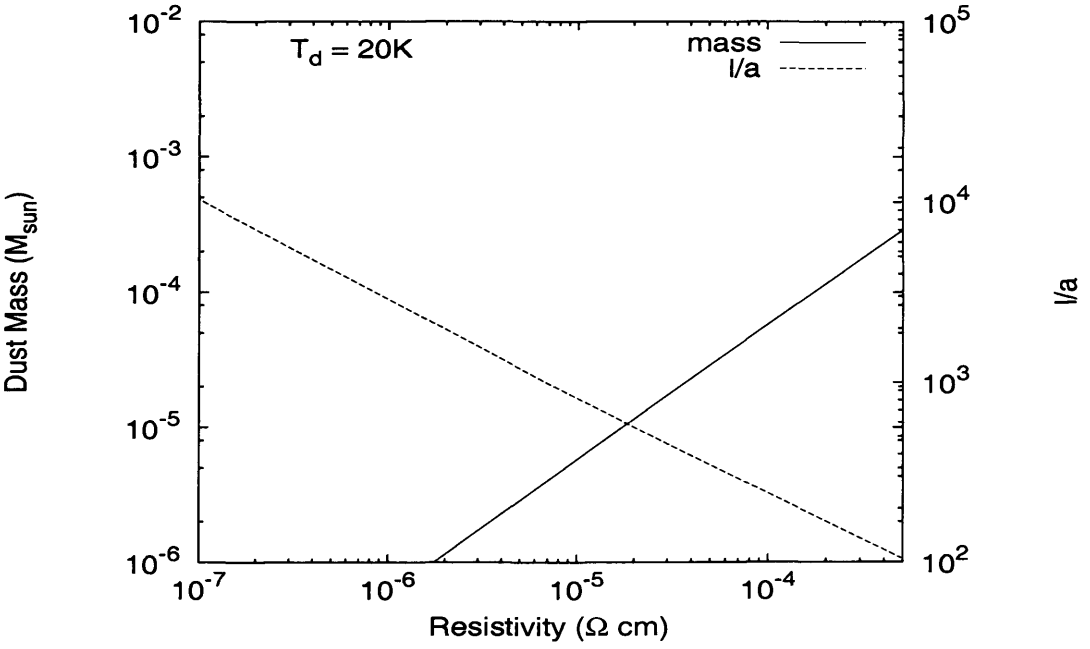

(b)

Figure 5.18: The mass of needles required to fit the SCUBA data for Kepler's SNR and the axial ratio (l/a) with resistivity ρ (1 Ω cm = 1.14×10^{-12} s). In (a) we use the cutoff wavelength and temperatures for Kepler *if* we fit the low 170 μm measurement to give $\lambda_0 = 200$ μm, $T_d = 10$K. This graph is the same type as shown in Dwek (2004a, Figure 3) with grain density $\rho_d = 8150$ kg m^{-3} and $a = 0.1$ μm to allow direct comparison between this work. In (b) we show the range of M_d and l/a with cutoff wavelength $\lambda_0 = 200$ μm and our best fit temperature 20K. For higher cutoff wavelength, $\lambda_0 = 400$ μm, the dust mass is lower with maximum at 10K of $M_d = 2 \times 10^{-3}$ M$_\odot$.

for 10K grains) of $\sim 10^{-6} - 6 \times 10^{-3}$ $M_{\odot}$ and axial ratio (l/a) between 100 and 8000 (c.f. 100 - 4000 for Cas A). For the higher temperature dust grains at 20K obtained from the SED fit to the observational fluxes, the dust mass ranges from $\sim 10^{-6} - 5 \times 10^{-4}$ $M_{\odot}$.

5.5.1 Heating and Cooling of Needles

The iron needles are heated by collisions with electrons and then cool via emission. The temperature of the dust grain is therefore dependent on the absoprtion efficiency, the density of electrons in the plasma and the plasma temperature. In Dwek (2004a), the electron densities required to explain the iron needle temperature of the grains in Cas A, were close to observational values (although the highest observed values published). In Kepler, however, the grain temperature is higher (since we cannot fit the SED with temperatures less than 10K). For a similar gas temperature, this suggests that the electron density must be higher to allow for the extra heating. X-ray observations suggest that the densities in Kepler are *lower* than Cas A so this is an important way of investigating if iron whiskers can exist in Kepler. Balancing the heating and cooling rate of the needles will also provide a greater constraint on the resitivities when comparing to observational plasma densities and temperatures.

We can no longer use Equation 5.2 since we are not dealing in spherical particles with normal ISM dust properties. To predict the electron densities for a wide range of parameters with our predicted absorption values for iron needles, we use the prescription given in Dwek 2004a. The heating rate is given by

$$H = 2\pi a l n_e (1 - f_r) \left[\int g(E) v(E) E_{dep}(E) dE \right] \tag{5.5}$$

where n_e is the electron density, f_r is the fraction of electrons that are reflected

from the surface of the grain and $g(E) = 2\pi^{-1/2}(kT)^{-3/2}E^{1/2}exp(-E/kT)$ is the Maxwell-Boltzmann distribution of electron energies with velocity $v(E)$. E_{dep} is the amount of energy deposited in the neddle by the incident electrons. Substituting for $m_d = \pi a^2 l \rho_d$ gives

$$H = 2m_d n_e(1 - f_r)\left[\int g(E)v(E)\frac{E_{dep}(E)}{\rho_d a}dE\right] \tag{5.6}$$

At low energies, up to a maximum E_*, the incident electrons are mostly stopped in the needle and the energy deposited is equal to the energy of the electron, $E_{dep} = E$. For energies above E_*, electrons can travel through the needle, depositing some energy but not all. At very high energies, the needles are almost transparent to the electrons as they are not stopped at all, and deposit very little amounts of energy. In this case $E_{dep} = x(dE/dx)$ where x is the average length travelled by an electron through the needle ($\sim 2a$) and dE/dx is the energy lost in the needle per unit length travelled by the electrons. Equation 5.6 becomes

$$H = 2m_d n_e(1 - f_r)\left[\int_0^{E_*} g(E)v(E)\frac{E}{\rho_d a}dE + \int_{E_*}^{\infty} g(E)v(E)\frac{1}{\rho_m}\frac{2dE}{dx}(E)dE\right] \tag{5.7}$$

dE/dx can be estimated using the range of electron energies given in Dwek (2004):

$$R_e(\mu\text{m}) = 2.59 \times 10^{-3}\left(\frac{\rho_\text{d}}{\text{kgm}^{-3}}\right)^{-1}\text{E(eV)}^{1.492} \tag{5.8}$$

Differentiating w.r.t E and setting $R_e = 2a = 0.02$ μm gives

$$\frac{dE}{dx}(\text{eVm}^{-1}) = 2.59 \times 10^{8}\left(\frac{\rho_\text{d}}{\text{kgm}^{-3}}\right)\text{E(eV)}^{-0.492} \tag{5.9}$$

The maximum energy in which electrons are stopped (E_*) can be estimated by equating the two different integrated regimes at E_* i.e. $dE/dx = E_*/2a$. In this

case,

$$E_*(\mathrm{eV}) = 1.89 \left(\frac{\rho_\mathrm{d}}{\mathrm{kg\ m^{-3}}}\right)^{0.67}$$
$$\sim 1.6 \times 10^3\ \mathrm{eV}, \qquad \text{for } \rho_\mathrm{d} = 8150\ \mathrm{kg\ m^{-3}}.$$

In Dwek (2004a), this number was quoted as 1.64×10^3eV but when using his Equation 10 instead of Equation 5.7, the code does not find the solutions to the integral. This is because the Dwek had failed to account for the extra factor of two multiplied by dE/dx in Equation 5.7 due to the substitution of xdE/dx for E_{dep}. He should have used

$$E_*(\mathrm{eV}) = 1.89 \left(\frac{\rho_\mathrm{d}}{\mathrm{kgm^{-3}}}\right)^{0.67}$$
$$\sim 790\ \mathrm{eV}, \qquad \text{for } \rho_\mathrm{d} = 8150\ \mathrm{kg\ m^{-3}}.$$

Using $E_* = 1.6 \times 10^3$ eV to solve Equation 10 in Dwek creates a discontinuity in the variation of dE/dx with E and the equations are not solved properly using a standard Euler method. In Figure 5.19, dE/dx is plotted against E to show the difference between the two values of E_* from this work and Dwek (2004). There is a sharp fall at the peak of the energy distribution using the stopping energy in Dwek (2004a) whereas, including the factor of 2 in Equation 5.7, the distribution is continuous even at the edge of the two energy regimes ($E < E_*$ and $E > E_*$).

The cooling rate is given by the luminosity of the grain. The Planck averaged emissivity ($< Q(\mathrm{a,T}) >$) is now replaced by the Planck averaged absorption coefficient ($< \kappa(\mathrm{T}) >$) where (Draine & Lee 1984),

$$< \kappa(\mathrm{T}) >= 15 \left(\frac{\mathrm{hc}}{\pi \mathrm{kT}}\right)^4 \int_0^\infty \frac{\kappa_\mathrm{abs}(\lambda)}{\lambda^{-5}} \left[\exp\left(\frac{\mathrm{hc}}{\lambda \mathrm{kT}}\right) - 1\right]^{-1} \mathrm{d}\lambda \qquad (5.10)$$

$\kappa(\lambda) = \kappa_0$ for $\lambda < \lambda_0$ and $\kappa_0 \left(\frac{\lambda}{\lambda_0}\right)^{-2}$, for $\lambda > \lambda_0$.

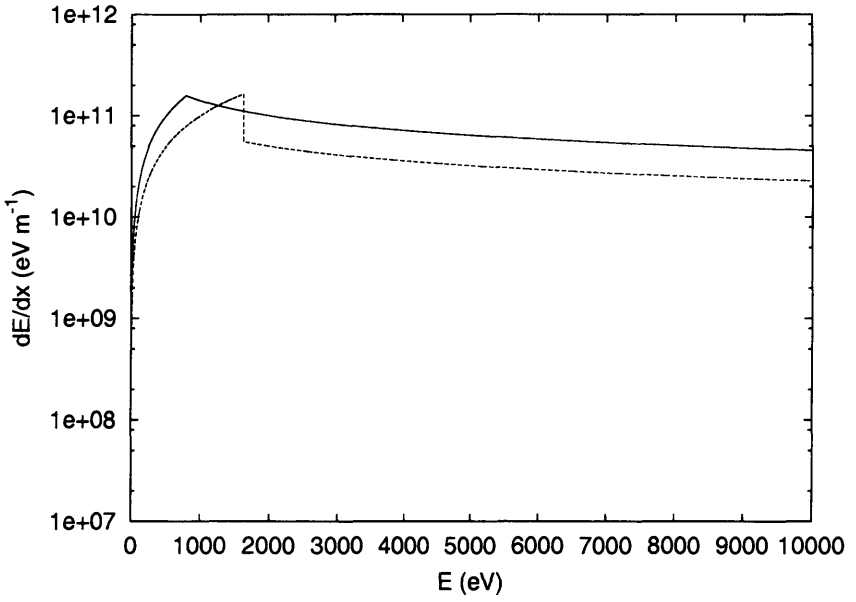

Figure 5.19: The energy lost in the iron needle dE/dx per unit length travelled by the electrons against the energy of the incident electrons E. The solid line represents the distribution with $E_* = 790$ eV from this work solving Equation 10 in Dwek (2004a) (scaled by 2 for clarity), and the dashed curve with $E_* = 1.6 \times 10^3$ eV. The energy distribution should be continuous over the two regimes ($E < E_*$ and $E > E_*$) to solve Equation 5.7 but if we use the form of the Equation in Dwek (2004a), the latter curve does not meet at the energy boundary given by E_*. This sharp fall in dE/dx is not seen if we use our estimate of what E_* should be from Equation 10 in Dwek.

The luminosity of the dust grain is therefore given by:

$$L_d = 4m_d\sigma T^4 < \kappa(T_d) > \tag{5.11}$$

The electron density is then given by the ratio of the heating-to-cooling rates. In Figure 5.20, the electron density required to heat the iron needles to 8.2K for Cas A is shown using the parameters in Table 5.1. This is a reproduction of Figure 4 in Dwek (2004a) using the model described above. These results suggest that at resistivities of $(2-5) \times 10^{-6}$ Ω cm, the temperature of the iron whiskers in Cas A can be explained by collisions with the electrons.

The electron density of the gas is required to be much higher in Kepler to heat

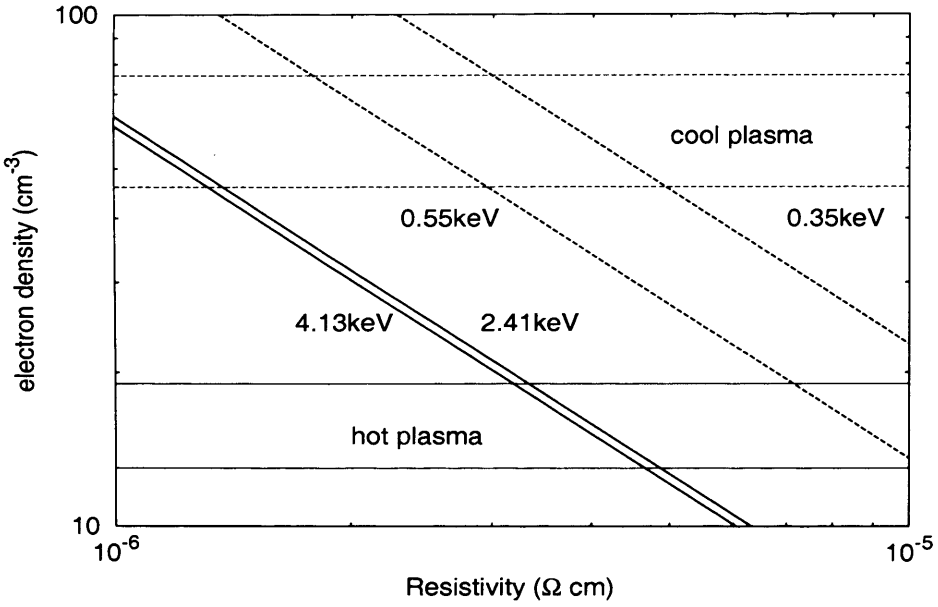

Figure 5.20: Electron density required to heat a needle of 8.2K in Cas A for different plasma temperatures. The lines show the electron temperature of the plasma in decreasing order from left to right. The hot and cool plasmas are outlined and are defined by $\{n_e, T_e\} = \{61 \pm 15\ cm^{-3},\ 0.45 \pm 0.10\ keV\}$ and $\{16 \pm 3\ cm^{-3},\ 3.27 \pm 0.86\ keV\}$ from Willingale et al. (2003). This is a reproduction of Figure 4 in Dwek (2004a) to show the model created here reproduces their work.

Name	Symbol	Value
Cut-off wavelength	λ_0	400 μm
Initial resistivity	ρ_0	9.6×10^{-7} Ω cm
Max. Energy for stopping electrons	E_*	790 eV
Fraction of reflected electrons	f_r	0.83
Grain temperature	T	8.2K
Grain density	ρ_d	8150 kg m^{-3}
Grain size	a	0.01 μm

Table 5.1: The parameters used to determine the electron density in Cas A.

the grains to T > 10K and for the lower plasma energies. This is because we require more collisions to replenish the lost energy if we have a similar or lower electron temperature. Figure 5.21 shows the electron density required for the different plasma temperatures to heat a needle to 10K with cutoff wavelengths (a) $\lambda_0 = 400$ μm and (b) $\lambda_0 = 200$ μm.

For $\lambda_0 = 400$ μm, the needle resistivity needs to be $\sim (3 - 40) \times 10^{-5}$ Ω cm to reside in the hot or cold components. This requires that iron needles in Kepler must have a resistivity of two - three orders of magnitude greater than those in Cas A *or* that the density must be greater than 40 cm^{-3}. Using Figure 5.18, the mass of needles is therefore $\sim 10^{-3}$ M$_\odot$ in the cold plasma and $\sim 4 \times 10^{-3}$ M$_\odot$ in the hot plasma, with axial ratios of $l/a \sim 100-600$. For $\lambda_0 = 200$ μm, the densities required to heat the needles to 10K for the same plasma temperature are lower, since the absorption coefficient is smaller and the needles do not cool as effectively. In this case the resitivity ranges from $\sim (1-7) \times 10^{-5}$ Ω cm with axial ratios of $l/a \sim 300-600$. The mass of iron needles with these constraints is $\sim (4 - 10) \times 10^{-3}$ M$_\odot$.

The lower densities required to explain the X-Ray observations of Kepler therefore require higher resistivity values than Cas A but overall lead to a similar estimate of the dust mass. However, to fit the iron needle emission to the SED of Kepler requires dust temperatures $\geq$ 10K. If the dust temperatures are higher with the same

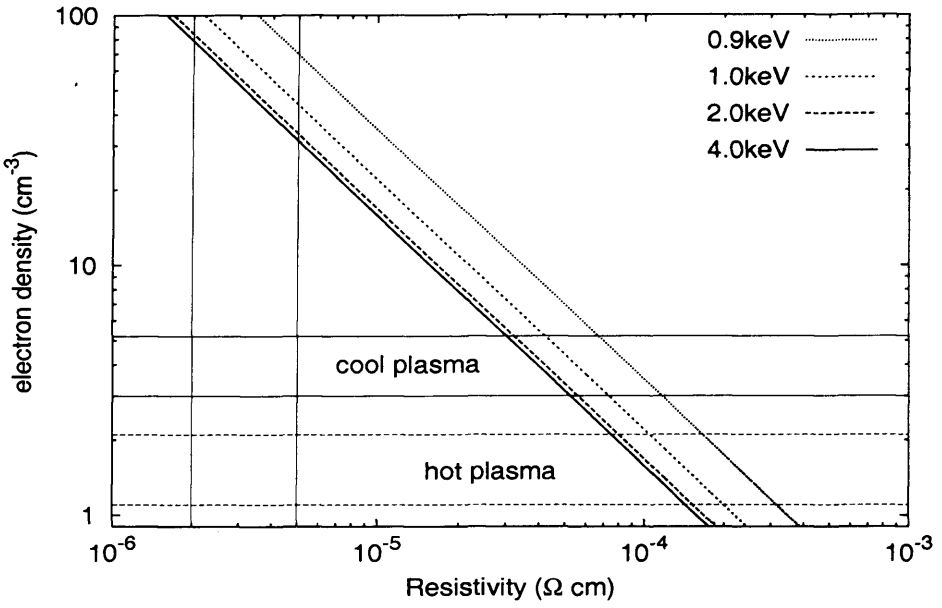

(a)

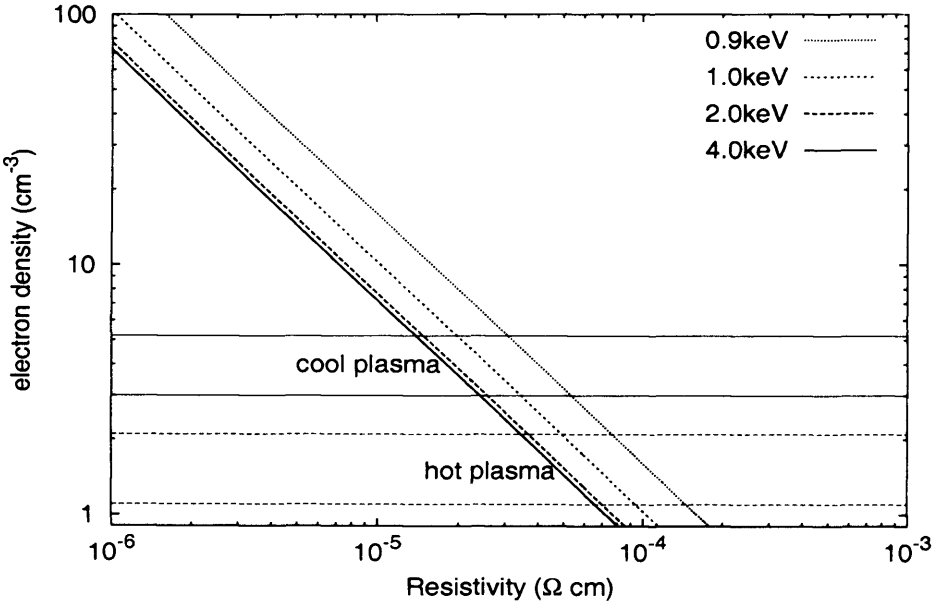

(b)

Figure 5.21: Electron density required to heat a needle of 10K in Kepler for different plasma temperatures with (a) $\lambda_0 = 400$ μm and (b) $\lambda_0 = 200$ μm. The horizontal lines show the electron temperature of the plasma in decreasing order from left to right. The hot and cool plasmas are defined by $\{n_e, T_e\} = \{4.0 \pm 1.0$ cm^{-3}, 0.80 ± 0.2 keV$\}$ and $\{1.6 \pm 0.5$ cm^{-3}, 3.0 ± 0.9 keV$\}$ from Kinugasa & Tsunemi (1999) with 30% errors. The vertical lines in (a) represent the range of resistivities required to explain the Cas A observations. With a lower value of λ_0, the absorption coefficient is much less in the sub-mm regime since when $\lambda > \lambda_0$, κ_0 decreases by λ^{-2}. The needles therefore emit less efficiently and are generally hotter.

plasma energy, the collisional heating must be even larger and hence the densities must be higher. This contradicts the observations of low densities in Kepler and suggests that it becomes more difficult to explain the sub-mm emission in Kepler with iron needles unless $T_d \leq 10K$.

Using the derived resistivities for the needles in Kepler, the Rayleigh criterion for which this approximation is valid (Equations 5.3 and C.7) gives a maximum needle length of $0.05 - 0.2$ μm (Li 2003). With the range of axial ratios derived, the minimum size of the grains is $a_{min} \sim 0.8$ Å and the maximum is $a_{max} \sim 5.7$ Å. These needles would be extremely small and could only be explained by a few layers of atoms at the most and we would question whether or not such needles coudl exist or survive. The minimum radius is actually less than the radius of one layer of iron atoms which would have $a \sim 1$ Å (Li 2003).

5.5.2 The Evidence for Iron Needles and Implications

If iron needles exist in abundance in the Universe, it will have significant implications on estimates of dust masses at high redshift, the polarization and extinction of interstellar grains and the origin of the CMB. The polarisation of iron needles in the ISM should be detectable in the sub-mm regime. Dwek (2004b) has reviewed the current evidence for iron needles and uses these grains to explain the excess of extinction over the expected values in the mid IR extinction curve. There should exist a minimum in the extinction curve at around 3 - 8 μm since the graphite and silicate particles are no longer producing much extinction at these wavelengths (except for the Si-O strecthing bond which causes extinction at 9.7 μm) (Whittet 2003). However, observations have shown that there is an excess which can be explained by the presence of iron needles (Dwek 2004b) since these grains have much higher absorption coefficients at these wavelengths. To fit the observed extinction

curve, Dwek requires needles with axial ratios $l/a \sim 600$, since grains with higher values would be too efficient at 'extincting' and would predict too high an excess over the observed values. This value of l/a is an order of magnitude lower than the estimated value of ~ 3000 required to fit the SED of Cas A in Dwek (2004a). It does, however, agree with our analysis for Kepler's SNR, where l/a was required to be around $300-600$ to reproduce the X-ray electron densities and plasma temperatures of the SNe gas. These iron needles are too short to provide significant extinction at cosmological distances, since at a reshift of 2, the optical depth is $\tau < 0.02$ for $\kappa_{100} = 10^5$ m^2 kg^{-1} (Dwek 2004b). Therefore, if these iron needles are the source of the sub-mm emission in high redshift galaxies, we would still be able to see them. The absorption coefficient at 850 μm for needles of this ratio is 10^3 m^2 kg^{-1} (Figure 5.17) and so the large dust masses in high redshift galaxies with $M_d > 10^8$ $M_\odot$ (Eales et al. 2003) would decrease to $\sim 10^3$ $M_\odot$. If we assume that each massive star SNe event produces the same mass of iron needles as Cas A and Kepler, then with a SN rate of 1/30 per year (Panagia 2000), we have an iron dust injection rate of $\sim 10^{-4}$ $M_\odot$ yr^{-1}. After a Gyr, the total iron dust mass from SNe (with no destruction) would be 10^5 $M_\odot$. The timescale for replenishing the interstellar dust budget would be $\sim 8 - 9 \times 10^9$ yrs which would bring current dust destruction and dust replenishing timescales closer (Jones et al. 1997).

This extreme explanation for the SCUBA observations shows that the sub-mm emission may be due to a small mass of cold needles and not the large mass of more 'normal' dust as estimated in Chapter 4. If this is the case, then SNe are not significant contributors to the dust *mass* of the ISM and stellar winds will therefore dominate the interstellar dust budget. However, if iron needles are formed in SNe, then the large sub-mm fluxes observed in high redshifts galaxies can be attributed

to small masses of dust. The issue with explaining the large dust masses in the early Universe then disappears. Future observations of Cas A with the polarimeter on the JCMT should provide some evidence on whether iron needles do exist in supernovae.

5.6 Summary

- Multiwavelength images of Cassiopiea A's SNR are presented. The position of the outer shockfront as was originally identified in Gotthelf et al. (2001) was reproduced here with significant amounts of sub-mm emission found to exist outside the bright X-ray and radio ring.

- Multiwavelength images of Kepler's SNR are presented. Kepler's North-South asymmetry is seen at all other wavelengths but not in the sub-mm. There are no global patterns in the intensity profiles but there is significant sub-mm emission outside the main bright radio and X-ray ring (as in Cas A). We propose that the small peaks in the Radio and X-ray profiles at a radius 120 - 130″ trace the forward shock. With this new position most of the dust exists within this radius and can be associated with the ejecta.

- The sub-mm emission in Kepler and Cas A is anti-correlated with the optical and warm dust suggesting that the dust is either blocking the optical light or that the cold dust does not reside in the same regions where the IR or optical emission arises. The latter point could be explained if the conditions for cold dust formation or survival are not reached in the optically bright regions.

- We find that the dust can exist at the low temperatures seen in the sub-mm if the grains are larger or more efficient at radiating its energy. Alternatively, the dust grains can be colder if they exist in a more diffuse phase of the gas

than the hot X-ray.

- We review the proposal that iron needles could be responsible for the sub-mm emission. Using a physical range of needle resistivities of $10^{-6} - 10^{-3}$ Ω cm, the mass of iron needles required to produce the sub-mm emission is only $10^{-4} - 10^{-3}$ $M_{\odot}$ at $T_d = 20$K and $\sim 10^{-7} - 10^{-6}$ $M_{\odot}$ if $T_d = 10$K for different material properties.

- The electron densities required to heat the iron needles to 10K were found by equating the heating rate of the needles to the cooling rate. To match the X-ray observations of the ejecta density, we require a narrow range of resistivities $\sim (3 - 40) \times 10^{-5}$ Ω cm for $\lambda_0 = 400$ μm (and $\sim (1 - 7) \times 10^{-5}$ Ω cm for $\lambda_0 = 200$ μm). This is 10 - 80 times higher than the resistivities required to match Cas A's plasma conditions. The maximum mass of needles responsible for the sub-mm emission is therefore $\sim 10^{-2}$ $M_{\odot}$. This suggests that most of the iron ejected from the SNe is in the form of dust grains.

- The assumptions under which the Rayleigh approximation is valid are only satisfied with extremely small needles. It is unclear how such tiny needles could exist in astrophysical environments.

In the next Chapter, we discuss the possible origin of the dust if it is not freshly synthesised in the ejecta. The sub-mm observations of the massive star η Car are also presented to determine if massive stars are prolific producers of dust.

Chapter 6

Dust In Massive Stars - Revisiting the Model

"..the man of science ought not to recoil, either before the obscurity of a phenomenom or before the difficulty of a research ....However little ground he gains, he will always enlarge it by returning to his problem with that persistence which is the indispensible condition of study. "

F G W Struve, 1847

6.1 Introduction

In this chapter, we investigate the origin of the dust seen in the sub-mm, showing that, although it does appear possible to explain the lower observational estimate of the dust mass found in Kepler's SNR via dust formation in stellar winds, we cannot account for the higher end in Kepler or the large amount of dust seen in Cas A. The sub-mm observations of the massive star η Carinae are presented to determine if the pre - SN evolution phase can produce enough dust to explain the

sub-mm emission in the remnants. We discuss the implications for the dust budget and destruction efficiencies in the interstellar medium and revisit the dust evolution model from Chapters 2 and 3 to follow the cycle of dust in galaxies.

6.2 The Origin of the Submillimetre Dust

In order to determine if the dust observed in the sub-mm is actually due to freshly forming dust in the ejecta, we need to explore if any other source is responsible. The main scenarios which may produce a shell of dust similar to that seen in the SNe which do not involve condensation in the ejecta are: (i) the ejecta has swept up dust in the surrounding interstellar medium, (ii) the ejecta are sweeping up a previous Wolf Rayet wind and/or previous mass loss in the past supergiant phase and (iii) the interaction of the blast wave with the stellar wind producing cool shock regions for dust condensation to occur.

6.2.1 Pre-existing Dust in the ISM

The mass swept up by a blast wave sweeping into uniform density ISM is $M_s = 4/3\pi R^3 \rho_o$. For $n_H = 6$ cm^{-3} (Kinugasa & Tsunemi 1999; Cassam-Chenai et al. 2004) - 10 cm^{-3} (Blair et al. 1991), and interstellar gas-to-dust ratio of $\sim$ 160 (average of values in Frisch & Slavin (2002)), the maximum dust mass swept up for Kepler is $\sim 0.06 - 0.09$ M$_\odot$. The surrounding interstellar medium can be argued to be an order of magnitude denser than quoted here and thus the amount of dust swept up would then explain the lower limit of Kepler's sub-mm observations. It seems unlikely though that this is the case as this would imply more than 100 M$_\odot$ of material is swept up. This is not seen in the measured expansion velocities and dynamical behaviour of the blast wave which imply that only a few solar masses has

been swept up and shocked ($3 - 8$ $M_\odot$ - Kinugasa & Tsunemi 1999). We can also discount the possibility that the dust is swept up from the ISM with the circular argument that if it is interstellar dust then κ_{850} would be the 'normal' value of 0.07 m^2 kg^{-1} and thus the lower limit of the observed dust mass becomes 3 $M_\odot$ for Kepler and 15 $M_\odot$ for Cas A. This is far more than we would predict from normal ISM gas/dust ratios of > 100 and would suggest swept up gas masses of > 1000 $M_\odot$. We can therefore reject the possibility that the SN dust is swept up from the surrounding ISM.

6.2.2 Pre-existing Dust from a Stellar Wind

To determine the mass lost from the progenitor star requires some knowledge of the evolution of Kepler's progenitor star before it exploded. This is difficult since the history of Kepler is not well known. The X-Ray observations suggest that the total mass ejected is ~ 5 $M_\odot$ suggesting that the progenitor star was < 15 $M_\odot$ (Woosley & Weaver 1995) yet it is thought that Kepler was a Type Ib which implies it was ~ 30 $M_\odot$ (Bandiera 1987). Alternatively, the range of dust mass estimated here for Kepler and the dust models in TF01, suggests that the progenitor star lies in the range $12 < M(M_\odot) < 30$ for solar metallicity. These stars will undergo extensive mass loss during RSG phases and WR phases. Here we will assume that Kepler's progenitor star was towards the more massive end of this range as this gives us more heavy elements and hence a lower limit on the condensation efficiency of dust formation. Detailed hydrodynamical modelling of the evolution of the circumstellar gas around massive stars has shown that the final circumstellar shell of mass lost from a 35 $M_\odot$ star will have a radius of ~ 10 pc from the central star (García-Segura et al. 1996). This is much further out than the dust shell seen in the sub-mm and hence would not be responsible for the observed dust. However, the final radius

of the shell could match the sub-mm radius at $\sim$ 3 pc if the velocity of the wind during the RSG phase is $\leq$ 15 km s^{-1}. The ensuing WR wind will then expand outwards into this wind and will be decelerated. The bright ring seen in the X-ray could be due to the ejecta sweeping all of this material up. These two phases can be characterised by mass loss rates of 10^{-5} M$_{\odot}$ yr^{-1}, wind velocities $\sim 10 - 75$ km s^{-1} and can last up to 10^6 years. We would then expect a maximum of $5 - 20$ M$_{\odot}$ of circumstellar material to be present from these two phases (García-Segura et al. 1996). The gas-to-dust ratio in RSGs is estimated to range from $160 - 500$ (Knapp 1985; Salasnich et al. 1999; van Loon et al. 2000). The dust mass formed in the stellar wind and swept up by the supernova blast wave would only range from $0.01 - 0.1$ M$_{\odot}$. This analysis suggests that the lower end of dust mass in Kepler could be explained with dust formation in the stellar winds of the RSG and WR phases. The argument is not applicable to Cas A.

We can also estimate the dust mass formed in the previous WR phase which would then have been swept up by the SN ejecta. A recent study of dust in WR binaries has shown that the maximum dust mass loss in WR winds is $\sim 6 \times 10^{-7}$ M$_{\odot}$ yr^{-1} (Marchenko et al. 2002). The location of the shell will constrain this as violent mass loss for a number of years will blow the WR wind material outwards. If the outer radius R(t) is the radius of the wind material at time t, then we can estimate the length of time the WR wind has been losing material using Equation 6.1 (Lamers & Cassinelli 1998, p367)

$$R(t) = \left(\frac{25 L_{\omega}}{14 \pi \rho_o}\right)^{1/5} t^{3/5} \tag{6.1}$$

where $L_{\omega} = 1/2 \dot{\mathrm{M}} v_{\infty}^2$. If $\dot{\mathrm{M}} \sim 10^{-5}$ M$_{\odot}$ yr^{-1}, $v_{\infty} \sim 2000$ km s^{-1}, $n_o \sim 10$ cm^{-3}. If the sub-mm emission is from dust formed during this phase, the radius of the shell after 5×10^5 yrs is $\sim$ 16 pc which is far too large. After only 2×10^4 yrs, the radius of the WR wind is $\sim$ 2.4 pc which corresponds to the physical size of Kepler's shell.

ZAMS	Yield SW		Yield SNe			Cond.Effic.
	Ma	WW	Ma	WW	LC	Kepler
15	0.0	2.2	1.3	1.1	0.7	0.9
20	0.0	3.1	2.8	2.6	2.0	0.4
25	0.0	3.3	4.5	4.2	3.5	0.2
30	..	4.1	..	4.3 - 6.3	5.0	0.2
35	..	5.5	..	3.6 - 6.6	6.5	0.2
40	6.5	5.9	1.6	2.8 - 6.7	..	0.2

Table 6.1: The yield of heavy elements (carbon, oxygen, iron etc.) in $M_\odot$ ejected from massive stars during their stellar wind (SW) and supernova phases (SNe). The ejected mass is estimated from the three published models: Ma - Maeder (1992); WW - Woosley & Weaver (1995) and Woosley et al. (1995); LC - Limongi & Chieffi (2003). Cond. Effic. refers to the condensation efficiency of Kepler if the progenitor star had the corresponding initial mass for an average dust mass of 1 $M_\odot$ and average yield from WW.

The dust mass loss rate in Marchenko et al. (2002) then implies that the maximum amount of dust produced in the WR wind would be ~ 0.01 $M_\odot$. Therefore we reject dust swept up from the prior WR wind only, but recognise that the swept up RSG phase may account for some of the dust seen in the remnants.

Another argument used against the sub-mm emission being due from supernova dust is that the explosions would not have produced enough heavy elements to provide the building blocks to create the dust from (Dwek 2004a). However, the maximum heavy elements ejected from massive stars during their lifetimes is $2 - 10$ $M_\odot$ with $2 - 6$ $M_\odot$ ejected (Table 6.1) during the SNe phase (Maeder 1992; Woosley & Weaver 1995; Limongi & Chieffi, 2003). Table 6.1 shows there are sufficient metals for dust to condense from using the available hydrodynamical explosion codes, particularly in Kepler's case.

6.2.3 Interaction of Blast Wave and Wind Material.

Previous work has suggested that supernova shocks could themelves provide a catalyst to form dust in the shell material, which is also seen in the wind collisions of WC binaries (Usov 1991; Tuthill et al. 1999; Marchenko et al. 2002). In Pozzo et al. (2004), this has been suggested to explain the IR luminosity of SN1998S (a Type II SN). In this scenario dust forms in the cool, dense region between the interaction of the ejecta and the wind. The heavy elements are provided by the wind but the SN blast wave is needed to start the condensation process. The maximum amount of heavy elements expected to be ejected during the stellar wind phases of a star with progenitor mass M $<$ 40 $M_{\odot}$ is $\sim$ 6 $M_{\odot}$ (Maeder 1992). If the SN blast wave is 100% efficient at forming dust, it could explain all of the dust mass in both remnants. More detailed hydrodynamical modelling of such environments would be required to explore whether or not this scenario is valid.

So assuming a large amount of condensable elements exist in the previous wind, the interaction of the blast wave causing these elements to condense could explain the dust seen in the SNRs. Also the sweeping up of the WR and RSG phase could be a possibility. In order to investigate this latter hypothesis, we looked at the available archival sub-mm observations on massive stars (Section 6.3.1).

6.3 Dust Formation in Massive Stars

6.3.1 η Carinae

η Carinae is one of the most luminous objects in our Galaxy (10^6 $L_{\odot}$) and is well known for dramatic outbursts in which material is ejected outwards from the star. Its most famous mass ejection (known as the Great Eruption) is thought to have

occurred in the early 19th Century, where a few solar masses of gas was expelled in a few decades. This feature is clearly seen in observations as a bipolar nebula, known as the Homunculus (Figure 6.1). The origin of the shape of the Homnculus is unknown, but could occur due to ejection in a non-uniform interstellar medium i.e. if the ambient medium was denser in the equatorial plane, the nebula would preferentially expand along the poles. The central star is hidden from view by this structure but is thought to be a Luminous Blue Variable (LBV) star with mass 100 $M_{\odot}$ (Pittard 1999; Smith et al. 2003). LBV stars are well known for large luminosities, violent instabilities and periods of large mass loss. LBVs are massive with initial mass > 40 $M_{\odot}$, and are probably in a pre-supernova (post red supergiant?) phase. Humphreys (1988) classified the sequence as

$$O \rightarrow LBV \rightarrow WN \rightarrow WR \rightarrow SN.$$

Recent X-Ray observations have suggested that there is a strong periodicity in the mass loss rates and fluxes with a period of 5.5 years (e.g. Pittard 2003). These observations suggest a binary companion is affecting the evolution of η Car. The presence of a binary companion would provide an explanation for the catastrophic mass ejections and the strong variabilities seen in the radio (Cox et al. 1995; Duncan & White 2003). In such a scenario, the binary disturbs η Car, a star close to the Eddington Limit (where the gravitational force balances the radiation pressure pushing gas outwards) and causes the star to release mass and energy which in turn stabilises it. The variations in the radio fluxes are quite extreme. Observations with the ATCA presented in Duncan & White (2003) show an unresolved point source at 3 cm with flux 0.6 Jy in 1992 growing to a 4 arcsec source with flux 3 Jy. By 1998. the flux had decreased back to 1 Jy. This decrease in radio flux occurred

simultaneously with a decrease in X-Ray and an increase in the near Infra-Red brightness by a factor of 2. These observations suggest that an increased mass loss event (i.e. a shell-event) took place. The ejected gas and dust in the shell obscures the radio and X-ray emission from the ionised central stellar wind. The cycle of periodicity suggests that any exisiting binary would have to have a highly eccentric orbit, leading to strong wind-wind collisions such as those seen in WR binaries (Marchenko et al. 2002; Pittard 1999). X-ray modelling of colliding wind binaries fit the observations of η Car with an O star binary and parameters (Humphreys 1988; Pittard 1999):- M(η Car) $\sim$ 70 $M_\odot$, M(Ostar) $\sim$ 70 $M_\odot$, $T_{\rm eff} \sim 20,000$ K, mass loss rate $\dot{M} \sim 9 \times 10^{-5}$ $M_\odot$ yr^{-1}, $v_\infty \sim 9300$ km s^{-1} and distance 2.6 kpc. If η Car is a single star, the mass loss rate needs to increase to 3×10^{-4} $M_\odot$ yr^{-1} to fit the observed X-ray spectra with initial mass, M $\sim$ 100 $M_\odot$. An LBV phase can last up to 10^5 yrs (Pittard 2003) in which a single star could lose of order 1 $M_\odot$ of gas.

The structure of η Car is revealed in the many multiwavelength observations, yet there are issues surrounding the origin of the Homunculus and its mass and the question of the origin of the IR emission. IR observations with ISO at 2 - 200 μm revealed a smaller structure within the Homunculus with IR luminosity $\sim 10^6$ $L_\odot$ (Morris et al. 1999). They found a small bright core a few arcsecs across which they interpreted as a disk/torus of dust with two components - T $\sim$ 190K and T $\sim$ 110K (the first indication of the presence of colder dust). They suggest that the disk lies in the midplane of the lobes. Using ordinary dust absorption properties for the ISM, they estimate that there is $\sim 0.15 \pm 0.05$ $M_\odot$ of dust in the torus (Figure 6.4(a))[1]. This would suggest (with a normal gas-to-dust ratio of 100) that the gas within this torus would be $\sim$ 15 $M_\odot$.

[1]Robinson et al. (1987) were the first to show IR excess at 8-13 μm with dust distributed preferentially in the plane of the sky in a region $\sim 8''$ in radius. By fitting the SED they found that the dust has temperature 240K and dust mass 0.008 $M_\odot$.

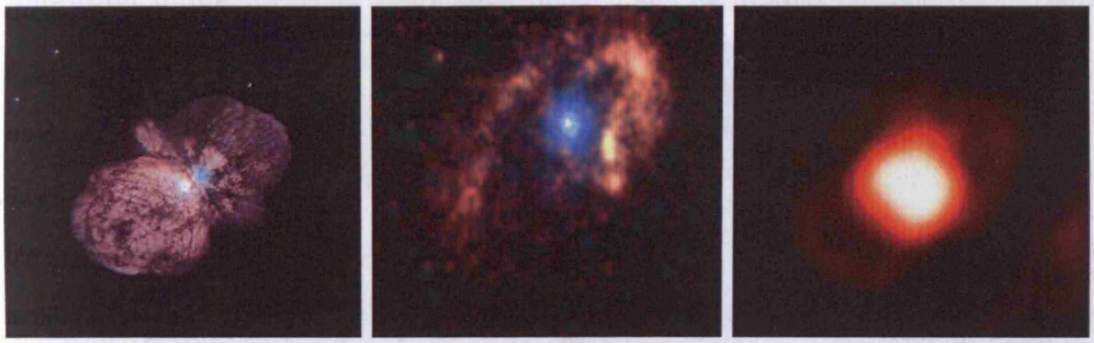

Figure 6.1: Images of η Carinae at different wavelengths. (a) HST image courtesy of http://www.hubblesite.org; credit: Jon Morse (University of Colorado) and NASA. The polar diameter of the nebula is $\sim 18''$. (b) X-Ray image taken with CHANDRA publicly available on the website, courtesy of NASA/CXC/SAO. The X-ray image reveals a hot inner core with three distinct structures: the outer, horseshoe shaped ring, a hot inner core ($\sim 8''$) and a hot central source which probably contains the bright LBV. The X-rays are produced by shocked material as the wind material flows outwards. The optical image fits inside the horseshoe structure i.e. in the blue region in the X-Ray. (c) The radio image is taken at 15GHz by the Australian Telescope. This image was taken from the CHANDRA webpage. These images are not to scale.

However, the origin of the IR emission has always been highly debated. Morris et al. used the ISO images to predict that the size of the dust emitting region was a few arcsecs across in a compact circumstellar region, yet Davidson & Smith (2000) proposed that this was too small to account for the large luminosities radiated at 100 μm. With a flux of 22,000 Jy at 100 μm and dust temperature 110K at 2.3 kpc, the luminosity constrains the area of the emitting region to be $\sim$ 38 arcsec^2. Thus the area of the IR region must be far bigger (by ten times) than Morris et al. thought. They also suggest that the dust region is even further out as there is no evidence of an opaque torus in the visual wavelength image. Hony et al. (2001) used high resolution images at 8 - 20 μm to suggest that the observed IR dust is not warm dust at 110K, but actually hot dust at 200K with a strange overlapping ring structure in the middle of the nebula. They argue that these rings are similar to those seen in SN1987A and are at different polar axes to each other. If this scenario

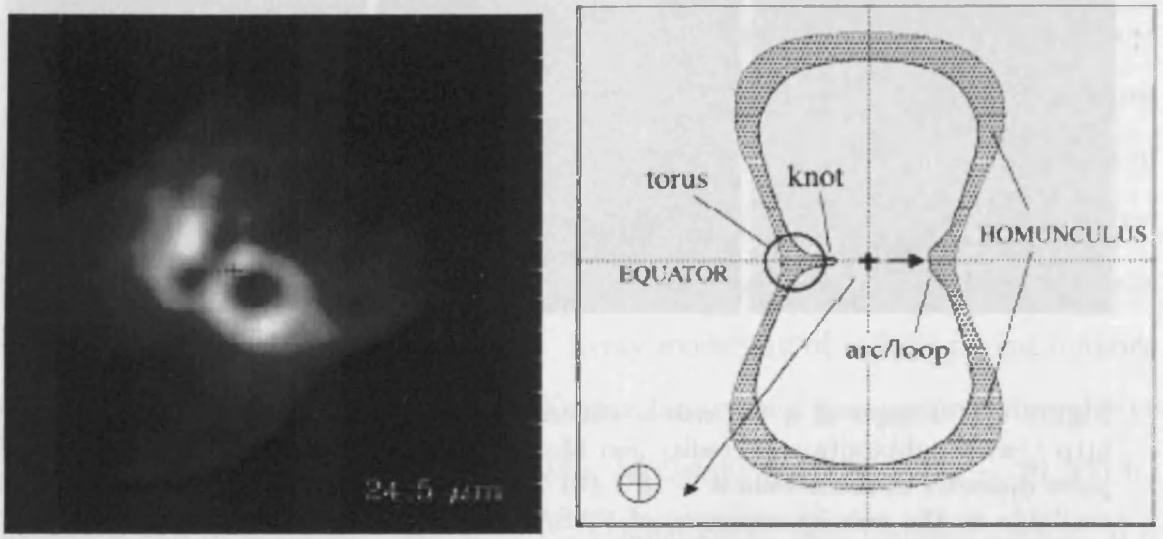

Figure 6.2: (a) 24.5 μm image from Smith et al. (2002) taken using the Baade 6.5m telescope. The arcs and hotspots are clearly seen. (b) Schematic from Smith et al. (2002) showing the cross section of the Homunculus. The dust torus is in the midplane of the lobes. The short arrow shows the arcs which are thought to be swept back by the wind.

is correct, the dust mass in η Car is only $\sim 10^{-4}$ $M_{\odot}$ due to the dependence on T.

Smith et al. (2002, 2003) dispute this claim, suggesting lots of reasons for the Hony et al. model to be discounted (see papers for detailed discussion). With higher resolution observations, Smith et al. propose that the strange smooth loop like structure seen in the Hony et al. observations is simply due to a disrupted torus (Figure 6.2 (a)) with compact knots and hotspots in the IR. This could be due to a toroidal distribution of dust which has been disrupted by subsequent mass loss (Figure 6.2 (b)). In their 2003 work, they also suggest that colder 'hidden' dust is distributed in the polar lobes and not in a compact circumstellar torus.

It has been argued that there is missing mass which should have been ejected that has never been accounted for by the observations (e.g. Morris et al. 1999; Davidson & Smith 2000; Smith et al. 2002). This missing ejected mass will have

important implications for the energy budget and estimated parameters of the star as well as its future evolution. Morris et al. (1999) have used the IR observations from dust thermal emission to indirectly estimate the amount of gas ejected from the star to be 15 $M_{\odot}$. The temperature maps of the 18/2 μm images from ISO suggest colder dust could reside in the polar lobes (Smith et al. 2002, 2003) which cannot be constrained without long wavelength measurements beyond the mid IR regime. We therefore decided to look at the sub-mm observations to determine if any colder dust (and hence missing mass) is present.

Submillimetre Observations

The sub-mm observations of η Carinae were originally observed by Henry Matthews with SCUBA in January 1998 in Grade II weather. The data was taken from the JCMT archive and consisted of a single Jiggle map observation. This was reduced using the method outlined in Chapter 3 with sky opacities obtained from CSO-FITS and skydips to give relatively stable optical depths (Table 6.2). The remsky option was used with the outer ring of bolometers flagged as sky bolometers (as η Car is almost a central point source in the maps) and the option for addback was turned off. The central part is not resolved by the SCUBA fov but we see an interesting feature in the eastern part of the remnant which appears to be extended in the x direction, along the midplane of the nebula (Figure 6.3). Subtracting the beam shape from the image (by fitting a 2-D Gaussian to the beam with FHWM = 14.7 arcsecs and peak 0.058 Jy/beam) shows emission characteristic of an extended source but it is difficult to determine the significance of this since it is at such a high airmass. The sub-mm emission does not appear to be orientated in the same way as the IR and this may be due to contamination from the free-free emission of the stellar wind, which is seen in the similarity between the sub-mm and the mm

Name	Run	λ	τ	θ_A	Jy/b/V	Jy/p/V	E
η Car	91	450	0.88				
		850	0.18				
mars	17	450	0.93	8.8	890.9	5.7	78%
		850	0.19	15.9	280.0	0.89	22%
crl618	77	450	0.84	8.0	968.7	7.6	76%
		850	0.18	16.0	360.0	0.90	35%

Table 6.2: The data and calibration observations used to obtain FCFs for η Car. τ represents the optical depth estimated at each wavelength; θ_A is the estimated beam size. Jy/b/V and Jy/p/V are the Flux Conversion Factors (FCFs) estimated by placing an aperture of diameter 90″ on the data map and the calibrator. E is the error lobe of the beam.

images (Cox et al. 1995). The image is calibrated using two calibrators (Mars and crl618) observed on the same night with similar atmopsheric properties (although lower air mass). These were reduced in the same way as the data without removing spikes. Calibrating with Mars produces Flux Conversion Factors (FCFs) of 280 and 890 Jy/b/V at 850 and 450 μm respectively (Table 6.2). Although these are higher than the nominal values given in Section 3.4, the observations were taken in 1998 before the filters on the telescope were changed, so the average FCF for SCUBA in this period was a lot higher. This is therefore consistent with the value estimated here. Multiplying the map by the FCF gives a 1σ noise level of $\sim$ 50 mJy/beam with peak signal-to-noise of $\sim$ 22 at 850 μm.

The integrated flux was measured by placing the same aperture over both η Car and the calibrators and measuring the total flux in Volts on both. Multiplying this fraction by the true flux of the object (as given by the SURF routine FLUXES) gives the object flux in Jy. The fluxes of η Car at 850 and 450 μm were found to be 16.7 and 90.5 Jy respectively as measured in an aperture of diameter 40″. The total errors, including large calibration errors due to the high airmass, were estimated to be $\pm$3.4 Jy (20%) at 850 and 26.0 Jy (30%) at 450 μm repectively.

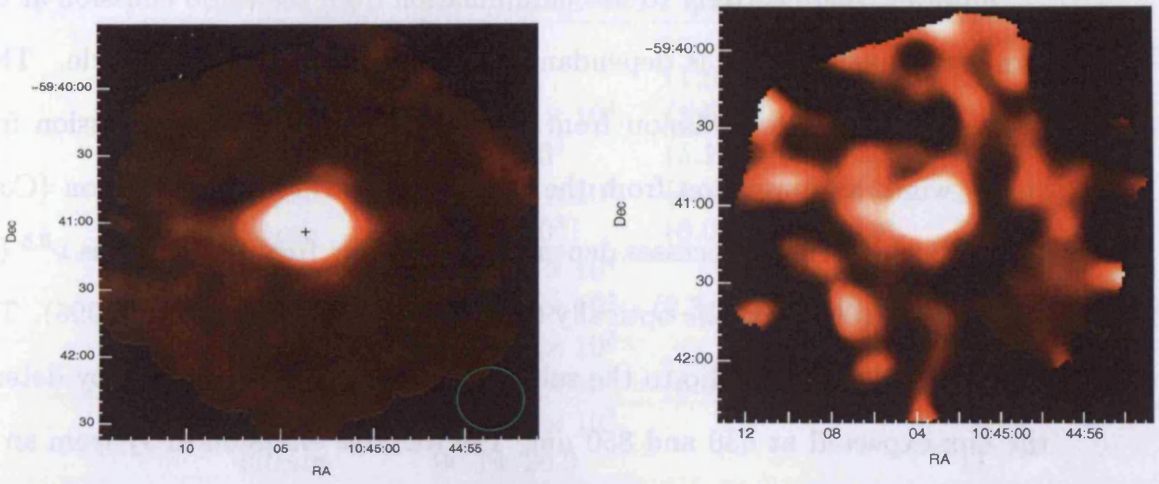

Figure 6.3: (a) 850 and (b) 450 μm image of η Car. Both images have been smoothed to the same resolution (850 μm by a 6″ Gaussian and the 450 μm by 12″). The cross marks the position of the central star and the circle represents the SCUBA FWHM 14″. The structure seems elongated along the x axis, particularly at 850 μm.

Dust Mass Estimation

Due to the high variability in the X-ray, Radio, mm and IR and as the sub-mm observations of η Car were taken during a shell-event in 1998, the literature fluxes used were chosen for comparison in two epochs, 1992 (where the star is radio loud) and 1998 corresponding to a radio quiet epoch (Table 6.3). This allows a direct comparison of the sub-mm with any variability in the radio contamination, as well as determining the evolution of the SED during this time. The 1.3 and 3.4 mm fluxes were observed in 1992 - 1994 (Cox et al. 1995) and the 7 mm flux corresponds to the same epoch of the SCUBA observations and were taken in January 1998 (Abraham & Damineli 1999).

We fitted the Spectral Energy Distribution (Figure 6.4 (b)) with a modified blackbody using a χ^2 test. The best fit parameters for the two epochs are listed in Table 6.4 with a two temperature component required to fit the SED from 12 - 850 μm. The SED is compared to the Morris et al. (1999) result (Figure 6.4 (a)).

However, there is likely to be contamination from the radio emission at the sub-mm wavelengths which is dependant on the epoch of the radio cycle. There are two sources of radio emission from the star: free free ionised emission from the stellar wind, and emission from the optically thin Homunculus region (Cox et al. 1995). Both thermal processes depend on frequency; free-free varies as $\nu^{0.6}$ (Lamers & Cassinelli 1999) and the optically thin region as $\nu^{-0.1}$ (Cox et al. 1995). The contamination from the radio to the sub-mm emission can be removed by determining the flux expected at 450 and 850 μm. The free-free emission in Jy from an ionised stellar wind is given by (Lamers & Cassinelli 1999 - Appendix B):

$$F_\nu = \left[\frac{1}{0.095} \left(\frac{Z^2 \gamma_e}{\mu^2} \right)^{1/2} \frac{\dot{M}}{v_\infty} \frac{(\nu g_\nu)^{1/2}}{d^{3/2}} \right]^{4/3} \tag{6.2}$$

g_ν is the Gaunt factor, d is the distance to the star in kpc, $\dot{M}$ is the mass loss rate in $M_\odot$ yr^{-1}, v_∞ is the terminal velocity in km s^{-1} and γ_e is the number of free electrons per ion. Z is the rms charge of the ions (i.e. $Z = 1$ for singly ionised gas) and μ_i is the mean atomic mass of the ions. The power law expected given the parameters of η Car and assuming a doubly ionised wind is shown in Figure 6.4 (b) (dashed line). The power law is significantly below the sub-mm fluxes but it underpredicts the observed 1.2 and 3mm fluxes. Cox et al. (1995) suggest that the power law slope from the free-free emission is actually $\nu^{1.0}$ in the mm regime due to hydrogen recombination changing the electron and proton densities in the wind. The emission then turns over at $\lambda \sim 1.2$ mm to the normal slope of 0.6 as we would expect by inspection of the mm - IR fluxes in Figure 6.4 (b). If the $\nu^{1.0}$ spectral slope continued through to the sub-mm regime, the contamination at 450 and 850 μm from the radio emission would be 70 Jy and 20 Jy respectively i.e. most of the sub-mm emission would be free-free and not dust. However, with the turnover to the classical slope of $\nu^{0.6}$, we estimate the contamination to be ~18 and

Wavelength	Integrated Flux (Jy)		Refs
2μm		2.0×10^2	8
8μm		$(1.6 \pm 0.3) \times 10^4$	6
10μm	$(7.0 \pm 1.4) \times 10^4$	$(1.6 \pm 0.3) \times 10^4$	1, 6
12μm	7.2×10^3	$(5.2 \pm 1.0) \times 10^4$	7, 9
20μm	$(8.0 \pm 1.6) \times 10^4$	$(5.2 \pm 1.0) \times 10^4$	1,6
25μm	2.4×10^3	$(6.0 \pm 1.2) \times 10^4$	7,9
35μm	$(3.8 \pm 0.8) \times 10^4$		5
50μm	$(1.9 \pm 0.2) \times 10^4$	$(2.3 \pm 0.3) \times 10^{4**}$	5, 9
80μm	$(7.7 \pm 1.1) \times 10^3$		5
100μm	$(5.2 \pm 1.0) \times 10^3$	$(6.9 \pm 1.6) \times 10^3$	5, 9
175μm	$(1.0 \pm 0.2) \times 10^3$		5
450μm	90.7± 26.0		11
850μm	16.7± 3.4		11
1mm	15.8±1.9		1
3mm	9.2±1.0	..	1
7mm	11.0±1.0	3.0±1.0	10
3cm	0.7±0.1	1.0±0.1	2, 4
21cm	0.9 ± 0.3		3
35cm	1.1 ± 0.1		2

Table 6.3: Observed flux of η Car at IR - radio wavelengths during past epochs. References - (1) Cox et al. 1995; (2) White 1994; (3) Retallack 1983; (4) Duncan & White 2003; (5) Harvey 1978; (6) Hony et al. 2001; (7) Robinson et al. 1987; (8) van Boekal et al. 2003; (9) Morris et al. 1999; (10) Abraham & Damineli 1997; (11) This work. ** - 60 μm.

12 Jy respectively. Therefore the contribution from free-free emission at the sub-mm wavelengths using the 1992 mm data is $\sim$ 18% at 450 μm and 75% at 850 μm. The sub-mm flux is still in excess of the free-free emission after subtraction.

The coldest component from the best fit to the SED is $\sim$ 110 K (c.f. previous work where the temperatures ranged between $200 - 300$ K), so unlike the SNe, there appears to be no cold dust, just as would be expected due to the close proximity to the hot, central star. The dust is heated by the luminosity of the star and cools as a greybody. This can be roughly approximated by

$$T_d = \left(\frac{R_*}{2D}\right)^{2/4+\beta} T_*$$

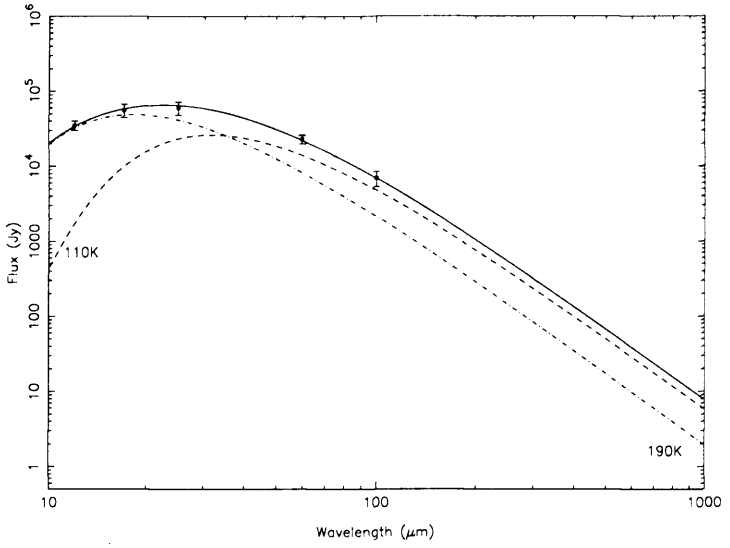

(a)

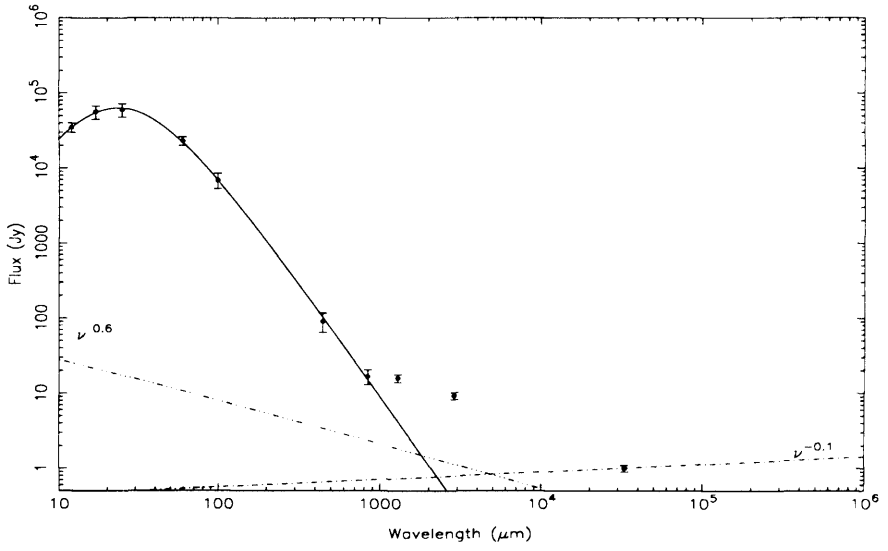

(b)

Figure 6.4: The SED of η Car. (a) The IR-submm SED reproduced from the Morris et al. (1999) observations. The solid line is a two temperature component fit with T_h = 190 K and T_w = 110 K. (b) The solid line is the two temperature component fit to the IR - sub-mm fluxes with best fit parameters in Table 6.4 with T_h = 196K and T_w = 98K. The dashed line shows the power law of the expected free-free emission from the stellar wind of a star with parameters similar to η Car and spectral index $\alpha = 0.6$. The dot-dashed line represents the emission from the optically thin, ionised Homunculus with spectral slope $\alpha = -0.1$ normalised to the 3 cm flux. The regime with free-free emission with spectral slope = 1.0 proposed by Cox et al. (1995) fits the observed 1992 mm fluxes but turns over at 1.2 mm. The IR and radio fluxes are given in Table 6.3. The IR-submm luminosity is $\sim L_{fir} = 10^{6.3}\ L_{\odot}$ which is in good agreement with the values quoted in Cox et al. (1995); Morris et al. (1999).

where T_* is the temperature of the central star, ($\sim$ 20,000K for η Car) and D is the distance of the dust shell from the star. If the dust is situated in a shell $\sim 10''$ from the star, then with a stellar radius of 40 $R_\odot$, the dust reaches an equilibrium temperature of $\sim$ 120 K. This is actually likely to be higher, since the dust is distributed in a disk with its own local heating effects i.e. friction. The dust would probably reside in the polar lobes which extend out in a $10''$ nebula from the central star rather than the compact torus which only has diameter $5''$, where the dust would simply be too hot to be radiating at <120K.

Once the free-free contanimation has been subtracted from the sub-mm fluxes, the best fit to the 1998 SED gives different parameters (Table 6.4). The dust temperature is colder with a similar dust mass of $\sim$ 1 $M_\odot$ for normal interstellar dust due to the increased power law slope (β) required to fit the data. With an interstellar gas-to-dust ratio of 100, this suggests that $\sim$ 100 $M_\odot$ has been expelled in the wind. This is clearly too much, which may indicate that the gas-to-dust ratio in the atmospheres of massive stars could be lower than predicted e.g. as seen in the LBV AG Car (Voors et al. 2000). Alternatively, the dust could be more efficient at emitting than normal ISM dust. Previous modelling of the SED of η Car has shown that the dust does not follow an opacity law of $\kappa \propto \lambda^{-\beta}$ (Robinson et al 1987). If we use the high absorption coefficient estimated from Chapter 4 to represent pristine, newly formed dust, we obtain 0.1 $M_\odot$ which would require $\sim$ 10 $M_\odot$ of gas to be expelled which is in good agreement with the original hypothesis of Morris et al. (1999) and the suggestion that colder dust exists in the polar lobes (Smith et al. 2002).

As noted in Smith et al. (2003), the fit to the energy distribution is not unique, a range of values of temperature could achieve a satisfactory fit to the spectrum within the errors on the fluxes. Indeed in their work, they re-produce an adequate

Epoch	Parameters			Dust Mass ($M_\odot$)			χ^2
	β	T_{warm} (K)	T_{cold} (K)	κ_3	κ_2	κ_1	
1998	1.2 ± 0.1	203^{+25}_{-23}	107^{+23}_{-29}	$1.2^{+0.2}_{-0.3}$	0.35 ± 0.1	0.21 ± 0.1	0.69
bestfit	$1.5^{+0.2}_{-0.1}$	196^{+40}_{-16}	98^{+11}_{-13}	$0.9^{+0.2}_{-0.1}$	0.27 ± 0.1	0.14 ± 0.1	0.60

Table 6.4: The parameters obtained from the SED fitting for η Car. The best fit case repesents the best fit to the 1998 SED with the free-free contamination subtracted from the sub-mm fluxes. Dust masses are shown for 450 μm with different absorption properties (κ). The values of κ are (as in Dunne et al. 2003): $\kappa_1(450) = 1.5$ m^2 kg^{-1}(laboratory studies). $\kappa_2(450) = 0.88$ m^2 kg^{-1} (observations of evolved stars). $\kappa_3(450) = 0.26$ m^2 kg^{-1} (observations of the diffuse ISM). The bootstrap technique was used to fit 1000 SEDs to the perturbed IR-sub-mm fluxes (Figure 6.5) and the quoted value is the median (which is similar to the best fit values). The errors represent a 68% confidence interval from the distribution.

fit to the Morris et al. (1999) data with dust temperatures of 140 K and 200 K. However, these two previous fits do not produce the observed 450/850 ratio as we have estimated from the SCUBA data. Including the extra fluxes at the long wavelength tail provides another constraint, which forces the fit to have a colder temperature than the previous two models with T $\sim$ 100K. In order to account for the degeneracy in these models, we have used the bootstrap technique to fit 1000 SEDs to the perturbed fluxes (Figure 6.5). The wide range of SEDs is due to the wide range in errors particularly on the sub-mm fluxes. The 68% confidence intervals from the distribution of the parameters obtained via this method are quoted as errors from the median value (Table 6.4).

It is extremely important to separate the dust emission from the free-free, indeed if the wind is optically thin, most of the IR emission would be due to dust and not contaminated by free-free processes. A future proposal has been submitted to observe at 450/850 μm and 1.3 mm with SCUBA and the heterodyne reciever at JCMT later this year. These observations should allow us to determine the

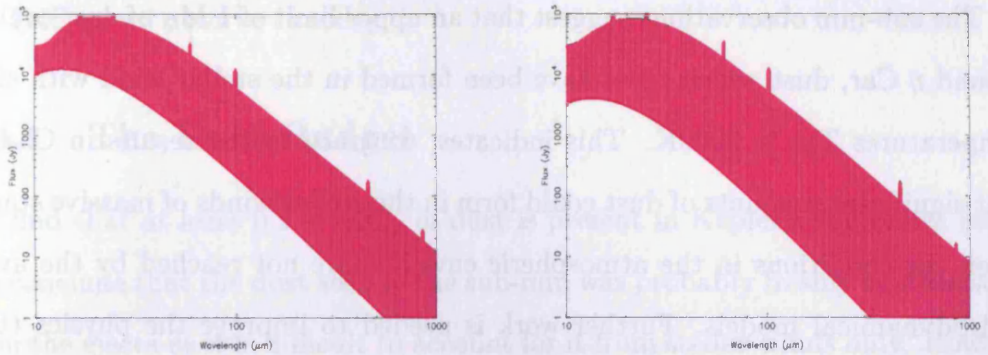

(a) (b)

Figure 6.5: Modelling η Car's SED using the bootstrap technique. 1000 fits were made to the range of fluxes obtained from perturbing the original data set within gaussian errors for (a) the 1998 original sub-mm fluxes and (b) 1998 free-free subtracted sub-mm fluxes. The distribution of parameters from this method are used to estimate errors as the 68% confidence interval for each case.

variability of the sub-mm and mm fluxes during a minimum in the radio cycle.

6.3.2 The Implications of the Dust in η Car

If we assume that the dust around η Car is similar to dust in the ISM, the the central LBV star has ejected 1 $M_\odot$ in the last 10^5 yrs. The dust mass loss rate is then $\sim 10^{-5}$ $M_\odot$ yr^{-1}. This is an order of magnitude greater than the dust mass loss rate estimated from observations of Wolf-Rayet binaries (Marchencko et al 2002) and more than suggested by previous IR observations of η Car. If the dust is located in the polar lobes of the nebula then it must have been ejected during the same event - the great eruption. This is thought to have last for a few decades which gives a time-averaged gas mass loss rate of ~ 3 $M_\odot$ yr^{-1} (for normal ISM dust) and ~ 0.5 $M_\odot$ yr^{-1} (for more efficient dust emitters). Such a high mass loss rate was first postulated in Smith et al. (2003) and suggests that the pulsational mass loss

in η Car is far more extraordinary than imagined.

The sub-mm observations suggest that an upper limit of 1 $M_{\odot}$ of dust could exist around η Car, dust which must have been formed in the stellar wind with effective temperatures $T_{eff} \geq 2000K$. This indicates, contrary to the results in Chapter 2, that significant amounts of dust could form in the stellar winds of massive stars even when the conditions in the atmospheric envelope are not reached by the available hydrodynamical models. Further work is needed to improve the physics that are put into these models to simulate a real wind more realistically.

These observations provide some evidence that a comparable amount of dust could be formed in a massive star to that observed in Kepler and Cas A. However, in this case η Car is extremely massive ($\sim$ 100 $M_{\odot}$) and highly unstable, so the huge dust mass loss rate is not unexpected. It is very unlikely that the lower mass stars which were responsible for the supernova events of Kepler and Cas A would ever have enough mass ejection to form such a large quantity of dust.

6.4 Implications for Dust Evolution

If supernovae are responsible for polluting the high redshift Universe, this will have important consequences for the first episodes of star formation. The presence of dust is believed to be important in determining the mass of stars condensing out of gas clouds (i.e. the distribution of the IMF). The first stars are likely to be massive since the lack of cooling processes leads to higher Jeans mass (Ferrara 2003; Schneider et al. 2004). Once there are significant amounts of metals, the Jeans mass is effectively reduced due to the extra cooling allowing for further fragmentation of the gas clouds. Dust will be crucial to this process since it not only acts as a coolant but it facilitates the formation of molecular hydrogen which is also a coolant. The

presence of dust may therefore cause the transition from massive star formation to the IMF as we observe it today.

6.4.1 The Dust Budget

We find that at least $0.2 - 3$ $M_{\odot}$ of dust is present in Kepler's supernova remnant. We conclude that the dust seen in the sub-mm was probably freshly synthesised dust from the ejecta as it is difficult to account for it from stellar winds only. However we note that if it was the prior stellar wind then this is still significant in explaining the origin of dust seen in high redshift galaxies since this is still a rapid mechanism. The work presented in this Chapter therefore shows that supernovae or their massive star progenitors are important contributors to the interstellar dust budget and are likely to be net contributors and not destructors as previously thought. This not only explains the observations of extremely dusty high redshift galaxies but also furthers our understanding of the current discrepancy between dust injection and destruction rates. Quantitatively, if each supernova injects about 2 $M_{\odot}$ of dust into the ISM at a rate of 1 every 30 years (Panagaia 2000), then the dust replenishing/production timescale is 8×10^8 yrs instead of the 10^{10} yrs calculated for stellar winds. This is in better agreement with the dust destruction timescales from Jones et al. (1994) and hence supernova dust could well solve this problem.

Alternatively, comparing with the models in TF01, for a 30 $M_{\odot}$ star, they predict a dust mass of 3 $M_{\odot}$ which corresponds to a condensation efficiency of 0.8. If we assume that Cas A (and Kepler's) progenitor stars were 30 $M_{\odot}$ which produced 2 - 4 (0.3 - 3) $M_{\odot}$ of dust then the observational condensation efficiency is 0.5 - 1.0 (0.2 - 0.8). Scaling the dust mass per SN progenitor mass in TF01 to this amount and summing over the stellar mass spectrum, we find that the condensation efficiency of all Type II like SNe is $\sim 0.6 - 0.8$ $(0.2 - 0.6)$. Incorporating this into

Stellar Type	$\dot{M}_G$	$10^{-3}[\dot{M}_G]_d$	%
M giants	2.0	3	10.8 - 16.7
OH -IR stars	2.0	3	10.8 - 16.7
Carbon stars	1.0	0.2	0.7 - 1.0
M supergiants	0.2	0.1	0.4 - 0.6
Planetary Nebulae	0.3	0.1	0.4 - 0.6
WC stars	0.01	0.06	0.3 - 0.4
Total stars	5.5	6.3	22.7 - 35.4
Novae	0.003	0.02	0.05
Supernovae	0.1	5 - 15	28.1 - 54.0

Table 6.5: Taken from Whittet 2003 and revised with the supernovae results from this work. The table shows estimates of integrated mass loss rates in $M_\odot$ yr^{-1} for stars injecting dust into the ISM. Columns are (1) stellar type (2) total mass loss rate (3) dust mass loss rate for stars calculated by $[\dot{M}_G]_d = Z_d[\dot{M}_G]$ where Z_d is the dust-gas ratio in the outflow (=0.007 here except for planetary nebulae which has observed values of 4×10^{-4}). For supernovae the results from this analysis replace the estimates in Whittet. Percentage contribution to total interstellar dust budget for supernovae for $5 - 15$ ($\times 10^{-3}$) $M_\odot$ yr^{-1} is $28 - 50\%$.

the simple model we find that SNe produce $\sim 5 \times 10^7 - 2 \times 10^8$ $M_\odot$ of dust after 10 Gyrs in our Galaxy (with no destruction). This suggests that SNe can inject $\sim 11 - 24$ ($\times 10^{-3}$) $M_\odot$ yr^{-1} or $\sim 5 - 15$ ($\times 10^{-3}$) $M_\odot$ yr^{-1} of dust into the ISM. From Chapter 2, we find that stellar winds inject 6 ($\times 10^{-3}$) $M_\odot$ yr^{-1}. So if we use the dust mass observed in Kepler and Cas A as the condensation efficiency of SNe, we infer that SNe can inject up to 3 - 5 times more than stellar winds. This suggests that SNe are the most important contributors to dust and not the stellar winds from the RG/AGB phases of intermediate mass stars. The dust budget table for our Galaxy at 10^{10} yrs first shown in Chapter 1.5 is revised to incorporate the SNe results in Table 6.5.

The dust mass evolution with time (as originally presented in Chapter 2), with the revised condensation efficiency of dust in SNe is shown in Figure 6.6. This implies that the dust mass from SNe is now the dominant source of dust in the past and at the present.

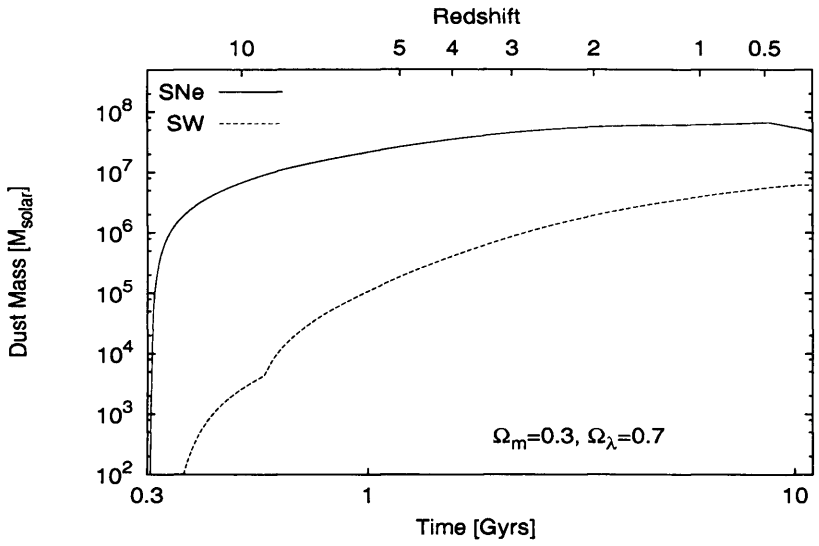

Figure 6.6: The dust evolution for a galaxy with the revised SNe condensation efficiency from this work of $\chi_1 = 0.6$. This is the revised version of Figure 2.15 (b) with $g = 2 \times 10^{10}$ $M_\odot$ and k=0.24. Redshift is estimated for Ω_m=0.3, Ω_Λ=0.7 with star formation 'turned on' at $t = 3 \times 10^8$ yrs. 'SW' represents the dust production in stellar winds with values of $\chi_2 = 0.45$.

6.4.2 Destruction

By adding SNe to the dust sources in the models in Chapter 2, we can constrain the dust destruction parameter δ. If we follow the evolution of our Galaxy which after 10 Gyrs has an observed Galactic dust mass of 1% of the gas mass (i.e. $\sim 5 \times 10^7$ $M_\odot$), then the rate of dust production in SNe and stellar winds as estimated here must be able to reproduce this amount to be compatible with observations. Figure 2.15 shows that stellar winds produce about 10^7 $M_\odot$ at 10 Gyr with a condensation efficiency of 0.45. The work in Chapter 4 suggests that the revised stellar mass weighted condensation efficiency of SNe is ~ 0.6 which will increase the interstellar dust mass even more. Adding the contribution from SNe as shown in Figure 6.6, adds another $\sim 6 \times 10^7$ $M_\odot$ giving a total injection dust mass of $\sim (0.6-1) \times 10^8$ $M_\odot$. We can then ask ourselves what value of δ (i.e. how much destruction) is needed to reconcile the model with the observed galactic dust mass? Figure 6.7 (a) shows the evolution of

the dust mass (from supernovae *and* stellar winds) with different δ values, including the revised condensation efficiency of SNe from the sub-mm observations.

As noted in E01, small values of the destruction parameter makes little difference in the qualitative behaviour of the dust evolution. However, Figure 6.7 (a) suggests that if SNe are significant contributors to the ISM dust budget, the destruction constant should be $0.5 < \delta < 3.0$ to reproduce the galactic dust mass. For this amount of destruction, the ratio of the grain core mass-to-metallicity η is shown in Figure 6.7 (b). For $\delta = 0.0$, and including the condensation efficiency of dust, $\eta \sim 0.6$ at low gas masses c.f. 0.16 for the equal χ model in E01. With the range of δ values from (a) this is decreased to $\eta \sim 0.2$ at galactic gas masses, $g \sim 0.1$. The value of the destruction parameter is not so important at high redshifts since the timescale for it to become important is 1 Gyr (although for higher star formation rates, this timescale will be shorter). The fact that we see SNe dust in such abundance also suggests that the destruction rates predicted by the models of Jones et al. (1994) are overestimated. Their models conclude that in shocks with velocity > 200 km s^{-1}, more than half of any dust encountered by the shock is destroyed. However recent work has shown that SNe shocks may be a lot less efficient at destroying dust than previously thought (Gray & Edmunds 2003).

6.5 Summary

- The observations of dust in massive stars are reviewed as an alternative explanation for the dust in the supernova remnants. We propose that the sub-mm dust seen in the SNRs is due to a combination of freshly synthesised dust in the ejecta and the interaction of the blast wave with the enriched pre-SNe wind material.

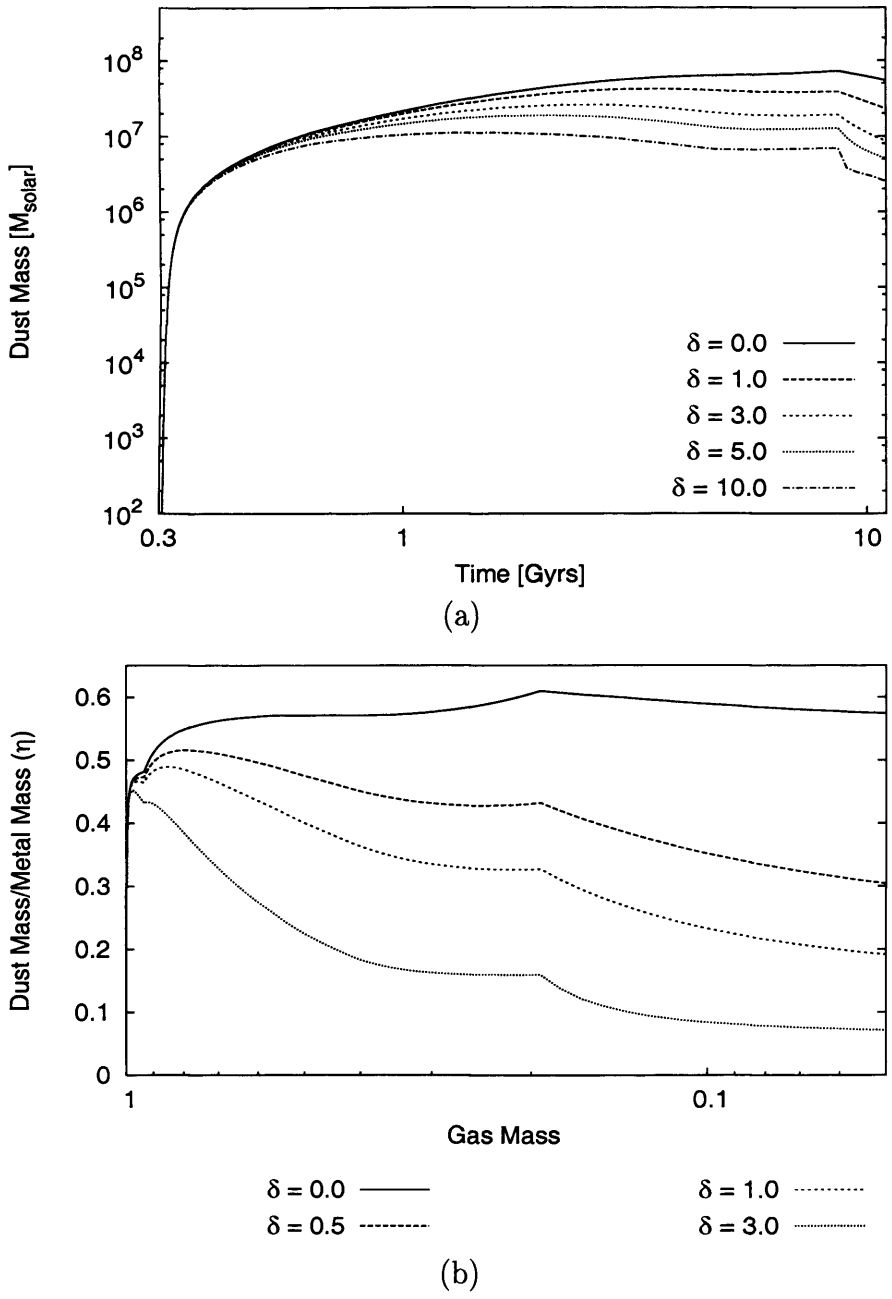

Figure 6.7: (a) The dust mass evolution with time for our galaxy with SNe condensation efficiency of 0.6 and destruction parameter ranging from $\delta = 0.0 - 10.0$. (b) The dust core mass-heavy element mass ratio $\eta = y/Z$ with $\chi_1 = 0.6$ and destruction parameter $0.5 < \delta < 3.0$. The bumps in the curves are due to the finite step size of mass ranges used in the model with different condensation efficiencies.

- We present the sub-mm observations of the massive star η Car which has a dust mass of $\sim$ 1 $M_{\odot}$ for normal interstellar grain opacity. This suggests massive stars could be prolific producers of dust but cannot explain the higher limit of the dust seen in Kepler's remnant.

- We show that destruction may be significant at later times to reproduce the dust mass observed in our Galaxy. We estimate that δ ranges from 0.5 - 3.0 for $\chi_2 = 0.45$, $\chi_1 = 0.6$. If $\chi_2 = 0.45$, $\chi_2 = 0.2$ as in Chapter 2, then δ is likely to be lower.

- We show that SNe, or their massive star progenitors, are injecting comparable amounts of dust to stellar winds.

Chapter 7

Conclusions and Future Work

"..for dust thou [art], and unto dust shalt thou return"

Genesis 3:19

7.1 Conclusions

The contributions of this thesis to our understanding of the issues discussed in Chapter 1 can be summarised as follows:

Dust Formation In Stars

One of the largest unknowns for any dust model is the origin of the dust, i.e. the relative contribution of supernovae and stellar winds to the ISM. By considering current evolution tracks and atmosphere models we can predict a condensation efficiency of dust formation in stellar winds. We estimated this amount by determining the amount of time the star spends in the right conditions and how much mass is lost in metals during that time.

We found that the TP-AGB phase appears to be very efficient for dust nucleation, due to the low temperatures and high mass loss rates during this phase of stellar evolution. Freshly synthesised carbon is dredged-up from the core and could produce more carbon dust. We suggest that a dichotomy in the stellar wind condensation efficiency could be identified - (1) dust from recycled elements in stellar winds and (2) dust from freshly synthesised elements. The normalised dust condensation efficiency in stellar winds can be set to a maximum of 0.45 and is likely to be much lower (~ 0.16) with very little variation with metallicity.

Although massive stars were ignored as a significant dust source since their atmospheres are not conducive to dust formation, analysis of sub-mm observations of the massive star η Carinae showed that this view may need to be revised, with around 1 $M_{\odot}$ of dust detected in the wind region. However, very massive stars are rare and it is difficult to separate the emission from dust from free-free emission in the hot, ionised wind. A complete observational study of evolved stars in the sub-mm regime is required to determine the dust mass formed in different stages, since the theoretical models are hampered by difficulties with hydrodynamic simulations.

The large mass of dust observed in two young remnants (see below) is not likely to have originated from condensation in the pre-Supernova stellar wind phase.

This work suggests that stellar winds inject $\sim 5 \times 10^{-3}$ $M_{\odot}$ yr^{-1} of dust into the interstellar medium, in agreement with present day observations. However, we find this injection rate is not enough to produce the dusty galaxies observed in the early Universe, or to replenish the interstellar dust mass if significant destruction by supernova shocks occur. The lower dust yields in this work places a greater burden for producing dust in the early Universe and even in our own galaxy.

Dust Formation In Supernovae

Although young supernova remnants have been shown to be sources of mid IR radiation, the masses of dust inferred from such observations suggest they are not significant contributors to the interstellar dust budget. Using chemical evolution models we showed that supernova are required to be more efficient at condensing their heavy element yield into dust grains. Our submillimetre observations of two young, Type II like supernova remnants (Kepler and Cassiopeia A) found high levels of emission well in excess of the level of synchrotron expected at these wavelengths. We have attributed the sub-mm observations to thermal emission from dust grains at around 20K, missed by the previous IR observations since these were biased towards grains radiating at > 35K. The dust mass in Kepler ranges from between $0.3 - 3$ $M_{\odot}$ depending on the value of the absorption coefficient (κ). For Cas A, the dust mass ranges from $2 - 27$ $M_{\odot}$. This embarrassingly high value implies that the absorption properties of the dust in the supernovae may be different to interstellar dust (i.e. are $\sim 10\times$ more efficient at emitting radiation), perhaps due to the SN dust grains having undergone less processing. The reduced sub-mm observations of the young Type Ia galactic remnant Tycho obtained so far, suggest that the dust mass in Tycho is < 8 $M_{\odot}$ for 'normal' interstellar values of κ.

Multiwavelength images of both remnants were used to determine the distribution of the sub-mm emission w.r.t the emission at other wavelengths and to obtain some understanding of the processes which led to dust formation. The sub-mm emission is found to be anti-correlated with the emission at every other wavelength. The dust in Cas A is located within the forward and reverse shocks of the remnant whereas in Kepler, the sub-mm emission is further out than the bright X-ray ring. Using radial profiles of the intensity evolution over different parts of the remnant, we propose that Kepler's forward shock wave is further out than previously

believed. With this new position most of the dust exists within this radius and can be associated with the ejecta.

The supernova dust is colder than one might expect for dust residing in a hot X-ray plasma. We find that spherical grains can remain cold in the hot X-ray gas if the grains are large (remain at a lower equilibrium temperature) or more efficient at radiating energy. Alternatively, the dust grains can be colder if they exist in a more diffuse phase of the gas than the hot X-ray.

The origin of the sub-mm emission has been attributed to thermal emission from elongated iron needles (by Dwek 2004a) which are highly conductive and have absorption coefficients up to 10^6 times greater than normal interstellar dust. The IR - sub-mm SED of Kepler can only be reproduced by iron needles with resistivities of $\sim (3-40) \times 10^{-5}$ Ω cm ($10-100$ times greater than those required to fit Cas A's SED). The iron needle mass in both remnants would be only $10^{-3}-10^{-2}$ $M_{\odot}$. If this hypothesis is true, the dust contribution from SNe is no longer significant in terms of mass, although the sub-mm emission from high redshift galaxies would also be attributed to less dust. The assumptions on which the approximation for the high absorption of the needles is valid are only satisfied with extremely small needles. It is unclear how such tiny needles could exist in astrophysical environments.

We conclude that supernovae, or their massive star progenitors are important contributors to the dust budget. Although it is unlikely that most of the dust in the remnants formed in the pre-SN stellar wind phase, it could originate from a combination of freshly synthesised dust in the ejecta and condensation from the interaction of the blast wave with the enriched pre-SN wind material. Either way, we have found that the major dust source in a galaxy is (i) injected on short timescales (Myrs) and (ii) from freshly synthesised metals and does not need to wait for the interstellar metallicity to build up. Adding this extra source of dust goes a long

way towards solving the current problems on the dust in the early Universe *and* the current dust budget crisis.

Evolution of Galactic Dust Mass

Chemical evolution models can be used to follow the evolution of the gas and metal history of a galaxy. If a fixed fraction of metals condenses into dust grains, the different parameters included in this model will determine the global dust mass and improve our understanding of galactic dust evolution. We have addressed a number of these parameters and updated the current models to include time delays, recent new tables of stellar yields and improved destruction rates. The parameter which determines the fixed fraction of the ejected metals from stars which condense into dust, was relatively unknown and the global dust mass history is highly dependent on this factor. This work is the first attempt to determine the condensation efficiencies for stars of different masses, in different phases of their evolution. Although highly simplified, the condensation efficiencies estimated for the TP-AGB, AGB, RSG and SNe with the full chemical evolution model allows a more realistic model of the evolution of dust in galaxies.

7.2 Future Work

The work in this thesis has helped our understanding of the origin of dust but there are many issues which are still unresolved. The advent of better instruments and, of course, more observations will allow us to determine the relative contribution of stars and supernovae with more confidence than could be done here. The modelling of dust in galaxies also requires more work - better observational constraints on the parameters are needed as well as the development of a model which follows evolution

in elliptical galaxies. The key scientific goals which lead on from this thesis are:

- Are the dust shells seen around the supernova remnants from pre-existing circumstellar dust or newly synthesised supernova dust?
- If the dust is made in the supernova ejecta then is it composed of carbon/silicon grains or iron needles? Is supernova dust different to interstellar grains and those formed in stellar winds?
- Are dust shells seen in other galactic supernovae or are Cas A and Kepler a special case?
- Do Type Ia supernova remnants also have dust shells?
- Are massive stars a significant source of interstellar dust?
- What evolutionary stage is responsible for dust shells seen around massive stars - are they produced during the Red Supergiant, Luminous Blue Variable or Wolf-Rayet phase?

In order to attempt to answer these questions, we have a number of observations planned for the near future:

Dust Mass in Supernovae

The Cardiff team will be submitting proposals to increase the sample size of supernova remnants with SCUBA. Only 20% of the time allocated for Tycho's SNR has been used due to bad weather so as yet, no conclusions can be reached about dust formation in Type Ia SNe. However, this proposal is still 'owed' time and any extra data obtained in better weather will increase the signal.

Object	Co-ords (J2000)		Size	Scan	Repeats
	RA	Dec	Map	Box	
Cas A	23 23 25.4	58 48 52.3	8.5 x 8.5	459.130 480 35.0 45	9
Kepler	17 30 41.25	-21 29 29.0	4.5 x 4.5	345.600 360 30.0 45	29
G54.1+0.3	19 30 30.13	18 52 14.1	4 x 4	228.571 240 20.0 45	10
G41.1-0.3	19 07 34	07 08	4 x 4	228.571 240 20.0 45	10
G43.3-0.2	19 11 08	09 06	4 x 4	228.571 240 20.0 45	10
G79.29+0.46	20 31 50.71	+40 22 01	4 x 4	228.571 240 20.0 45	5

Table 7.1: List of sources to observe at 350 μm with SHARCII. Box stands for type of boxscan needed to cover area of remnant with the correct sensitivity. Sens. represents the sensitivity needed to obtain a high enough SN.

Observing time was also granted on the SHARC-II bolometer array at Caltech Submillimetre Observatory in November 2003. SHARC-II observes at 350 μm which is around the peak of the second bump in the SED. These will provide an alternative estimate of the sub-mm fluxes to compare with those already obtained with SCUBA. Due to bad weather, the observations were re-allocated to April 2004. The objects which have already been observed are listed in Table 7.1 along with other objects we wish to observe further. We currently have 29 integrations of Kepler and 9 integrations of Cas A but due to problems with the reduction pipeline when observing extended sources (Attila Kovac - priv. communication), we have not been able to obtain any results as yet.

Spitzer is a new Infra-red space telescope which has three modes - MIPS (imaging) at 24, 70 and 160 μm, IRAC (spectroscopy) and IRS in the near-mid IR. The resolution is far better than the previous space infra-red detectors IRAS and ISO (e.g. 40″ at 160 μm instead of 2′ at 100 μm for IRAS) with unprecedented sensitivity. I am part of two recently accepted science cases to observe supernovae. The observations will allow a complete multiwavelength analysis of the remnants.

- Cas A (P.I. Larry Rudnick et al)

  High resolution IRAC and IRS spectral mapping combined with existing MIPS and sub-mm data will provide a census of the ejecta and pre-supernova circumstellar medium over a wide range of temperatures. These observations will probe (i) dust formation, heating and destruction and the thermal history of the shocked ejecta; (ii) variations in abundances and composition (iii) synchrotron fluxes in the infra-red and (iv) the missing iron problem. In this scenario, cold iron is thought to radiate in the IR and not the X-ray where the hot iron exists.

- Young Supernova Remnants (P.I. Jeonghee Rho et al)

  The observations consist of MIPS imaging of six young supernova remnants (Tycho, Kepler, W49B, N132D, IE102-72.3, SC397) at all three wavelengths combined with IRAC spectroscopy at 3–6 μm and 8 μm to observe synchrotron contribution and dust emission respectively. The remnants were chosen as they are believed to be either young and/or ejecta dominated. These observations will investigate (i) the fraction of young remnants with dust shells; (ii) whether or not Type Ia form dust (Tycho, W49B) and if so, the differences in composition/structure to the Type II observations; (iii) the iron needle hypothesis (the 160 μm flux will constrain the spectral energy distribution of the remnants and determine if the emission is from iron needles or 'normal dust') and (iv) the missing iron problem in different types of remnants.

Iron Needles

Polarimetry observations of Cas A are required to determine if the dust seen in the sub-mm is due to emission from iron whiskers. We have been awarded time to

observe the polarisation of grains in Cas A with the polarimetry mode on SCUBA and optical polarisation towards Kepler using the VLT. If the dust is iron needles, the strong magnetic fields in the remnant will align the grains which will result in polarisation of the stars behind the remnants. The direction of the polarisation signal will distinguish between the timescales of alignment and hence the polarisation signal (Loretta Dunne, priv.comm.). If the iron needles have had enough time to align, the polarisation signal could be as high as 100%.

Dust in Massive Stars

There are a number of observations which are needed to determine if the dust around the supernovae could have been created in the pre-SN stellar wind. The archival observations of η Car reduced in this thesis have shown that quite a large amount of dust can form in the outflows of a massive Luminous Blue Variable but this environment is so hostile to dust formation it is difficult to see how this occurs. The list of unknowns when considering dust formation in massive stars is endless - for example we do not know the correct dust masses as this has only been determined so far by IR observations which are sensitive to dust at temperatures > 35 K. Longer wavelength observations are required to estimate the 450/850 ratio properly as this is crucial to determine the cold dust mass. If more dust is present in the disks of these stars, it suggests that the dust mass injection rate has been severely underestimated for many years. Obtaining the dust mass in these atmospheres will provide the first observational determination of the condensation efficiency in massive stars and their dust to gas ratios.

SCUBA observations of the IR dust shells seen around massive stars would be an important step towards beginning this survey. The SCUBA archive is limited in the amount of stars it has observed so far, with most being observed in Pho-

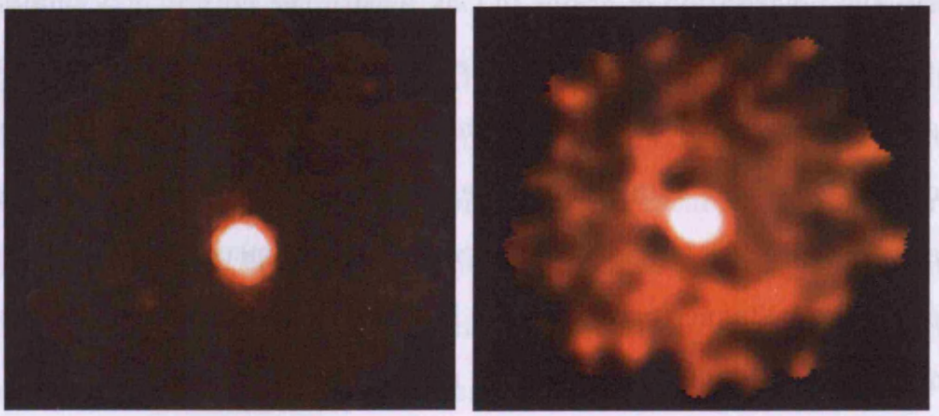

(a) (b)

Figure 7.1: (a) 850μm unsmoothed image of the pre-LBV star MWC349*. (b) 450 μm image smoothed by a 10″ Gaussian and is comparable to the beam size of the 850 μm image.

tometry Mode. This uses the central pixel to observe a point like star, but we require observations further out to detect colder dust in ejected shells (some of which have been detected in the IR out to a few arcmins (e.g. WR112; G79.29+0.46)). The stars available in the SCUBA archive include MWC349 (see below), PCygni, G79.29+0.46, WR104, WR112, all of which have IR detections. A proposal will be submitted to observe these stars (and a selection of the sample below) with SCUBA in jiggle map mode. I have already begun to reduce the data of the archival stars to obtain an estimate of the dust masses. As an illustration, I have reduced the submm observations of MWC349 (a binary system thought to be in pre-LBV phase, Gordon et al. 2001) shown in Figure 7.1 . IR studies and extinction Effects towards the more evolved star of the binary system suggest an edge on circumstellar disk is present with mass loss rates of 10^{-5} $M_{\odot}$ yr^{-1} (Cohen et al. 1985). The submm fluxes of MWC349 are 2.3 Jy and 6.7 Jy at 850 and 450 μm respectively. The radio contamination can be estimated by extrapolating from the radio wavelengths

with power law slope $\alpha = 0.69$ (Olnon 1975). The fluxes at 1.3mm and 3.4mm are 1.7 ± 0.2 and 0.9 ± 0.1 Jy (Downes et al. 1999) which gives an estimate of the free-free contamination in the sub-mm regime of 2.3 ± 0.2 Jy at 850 and 3.2 ± 0.2 Jy at 450 μm.

It would be ideal to obtain observations of massive stars with SPITZER and Herschel. A proposal will be submitted to observe a small sample of massive stars in their latest stages of evolution. I have chosen a sample of stars ideally suited to this problem, many of which are unresolved with IRAS which has a fov of $\sim 2'$ at 100 μm. Unfortunately due to the sensitIvity of SPITZER, most of the sources originally chosen to look at are far too bright and will saturate the detector at the longer wavelengths. The stars in Table 7.2 were chosen so that (i) dust shell diameters seen in the infra-red are at a distance <5 pc from the central star to ensure they are young and have swept up less interstellar mass than ejected; (ii) low radio fluxes to ensure little contamination from free-free or synchrotron emission; (iii) binary WRs are included to test the hypothesis that dust formation is enhanced in the region behind the shockfront formed in colliding wind binaries; (iv) Wolf-Rayets surrounded by genuine planetary nebulae which arise from low-intermediate mass stars are excluded and (v) luminous blue variables are included to compare the dust shells seen in the two different phases of stellar evolution. The sample is listed in Table 7.2. We include some stars not included in the sample due to high IR fluxes/high backgrounds (identified by N/A) which we hope to observe with SCUBA/SCUBA-2/Blast where possible. Once the saturation limits of the detectors have been more effectively characterised after the initial observing run, we will resubmit this proposal including IRS spectroscopy to obtain dust compositions in the different stars. This is an unique opportunity to study dust formation and evolution in massive stars and compare the dust formed in different phases.

Table 7.2: The observational parameters with known and predicted IR fluxes. Columns are:-(1) Name of source. (2) Type of star. (3) Co-ordinates. (4) Distance to source in kpc. (5) Mass loss rate of wind. (6) Angular radius of shell in arcmins. * refers to size in IR, $^{+}$ refers to size in near-IR. (7) IR fluxes in Jy at 12, 25, 60 and 100 μm. (8) Predicted fluxes in Jy from the SPITZER tool EX-PET using the 70 or 100 μm flux for a modified blackbody with $\beta = 1.0$ and $T_d < 100K$ for 24, 60 and 160 μm. N/A refers to wavelengths not observed with Spitzer due to high backgrounds causing a saturation warning or due to high brightness of source. (9) BG is the level of background at each wavelength determined using SPOT. (10) Dust mass estimated using the ratio of 60/100 μm fluxes as given in Mathis et al (1995) calculated by $M_d = 4.84 \times 10^{-4} D^2(kpc) F(100)^{2.5} F(60)^{-1.5}$. The dust masses obtained by fitting the IR SED from the various authors are in parenthesis.

Name	Type	Position J2000.0 α (h m s)	δ (° ′ ″)	D (kpc)	$\dot{M} \times 10^{-5}$ ($M_\odot yr^{-1}$)	θ (′)	F_{obs} (Jy)	F_{pr} (Jy)	BG	M_d ($M_\odot$)
HR Car	LBV	10 22 53.8	-59 37 38.4	2.5	??	2*	??	..	..	0.06
							11	5	M	
							54	35	H	
							37	34	H	
WRA 751	LBV	11 08 40.4	-60 42 51.0	4.5	0.3	$> 0.1^{+}$	15	..	..	0.05 (0.02)
							200	4	H	
							100	28	H	
							30	27	H	
RCW 58	WN8	11 06 17.2	-65 30 35.0	2.6	6.3	4*	< 1.4	..	..	0.02
							8	3	L	
							43	21	M	
							22	20	H	
WR 11	WC8+O	08 09 33.0	-47 19 21.0	??	??	??	19.4	..	..	
							8.5	0.1	M	
							4.2	1.5	M	
							3.1	1.5	H	
WR 48	WC6+O	13 08 07.17	-65 18 22.9			10*	0.5	..	..	
							0.33	0.8	M	
							< 0.9	5.6	M	
							< 5.9	5.3	H	
WR 92	WC9	17 25 23.28	-43 29 31.6	3.8	< 2.5	??	0.1	..	..	0.41

Table 7.2: (Continued.)

Name	Type	Position J2000.0 α (h m s)	δ (° ′ ″)	D (kpc)	$\dot{M} \times 10^{-5}$ ($M_\odot yr^{-1}$)	θ (′)	F_{obs} (Jy)	F_{pr} (Jy)	BG	M_d ($M_\odot$)
							0.2	0.6	M	
							< 1.0	0.2	M	
							< 5.1	0.4	H	
WR 103	WC9	18 01 43.14	-32 42 55.2	2.2	1.2	??	1.0	..	..	0.57
							0.3	0.5	H	
							< 0.9	1.2	H	
							< 9.0	0.5	HH	
WR 112	WC9+O	18 16 33.49	-18 58 42.5	4.2	6.2	$> 0.2^+$	153.6	..	..	0.01 (0.03)
							73.4	??	H	
							19.3	??	H	
							7.33	??	H	
WR136	WN6	20 12 06.5	+38 21 17.8	1.8	13	12*	7	..	..	0.30
							76	??	M	
							400	??	H	
							390	??	H	
AG CAR	LBV	10 56 11.6	-60 27 12.8	6.0	3.0	$> 0.3^+$	12	..	..	9.6 (0.25)
							200	N/A	N/A	
							200	N/A	N/A	
							100	N/A	N/A	
MWC 349	LBV	20 23 45.44	+40 39 36.8					..	..	
								N/A	N/A	
								N/A	N/A	
								N/A	N/A	
G79.29+0.46	LBV			1.8	0.8	1*	2	..	..	0.30 (0.14)
							140	N/A	N/A	
							680	N/A	N/A	
							410	N/A	N/A	
AFGL 4106	LBV	10 23 19.47	-59 32 04.8	3.3	90.0	> 0.1	201	..	..	0.09 (0.04)
							1755	N/A	N/A	
							852	N/A	N/A	

And Finally...

The work in this thesis has encouraged further investigation into a number of dusty issues, including: the iron needles debate (Dwek 2004a; 2004b), the source of the Infra-Red luminoisty in SNe (Pozzo et al. 2004), the dilution of crystalline silicates from stars (Kemper et al. 2004), supporting theoretical models for dust formation in primordial supernovae (Schneider et al. 2004) and the role of dust in different star formation environments (Hirashita & Hunt 2004). This work has also been referenced in a review of the dredge up phase in intermediate mass stars (Herwig 2004) since we found that this phase may be an important contributor to dust.

The future observations outlined in this Chapter should provide more information on the origin of dust in the supernova remnants, the dynamics of supernovae and the relative contributions from stellar winds and supernovae in the interstellar medium which we have only just begun to investigate. These issues are important, not only for the study of dust and galactic evolution in the high redshift Universe, but also because it suggests that the building blocks for life and planet formation were available when the Universe was only 1/10th of its present age. If we do not understand even the most basic property of dust i.e. where it comes from, we cannot understand how the Universe and our planet came to be the way it is today.

Appendix A

Radial Profiles

A.1 Cassiopeia A

The radial profiles of Cas A averaged over the entire remnant are shown in Figure A.1. The main peak in all the wavelengths is in the same place (a) but it is clear that the sub-mm emission extends further out than the bright X-ray and radio ring. The outer bump at 270″ is not seen in either the X-ray or the radio as these images only extend to $r < 230''$.

The radial profiles comparing the continuum and the ejecta emission in the X-ray are plotted in Figure A.2 for the southern and western regions.

A.2 Kepler

In Figure A.3, the flux density profiles for the X-ray emission, radio (2″ bins, smoothed to 7″) and noise weighted 850 μm (7″ bins) are compared over the whole remnant. In (a), the radio, sub-mm and broadband X-ray trace each other quite well with the first peak in the emission at $\sim 85''$. The radio emission appears to be slightly extended at $\sim 110'' - 120''$. This agrees with the position of the second peak

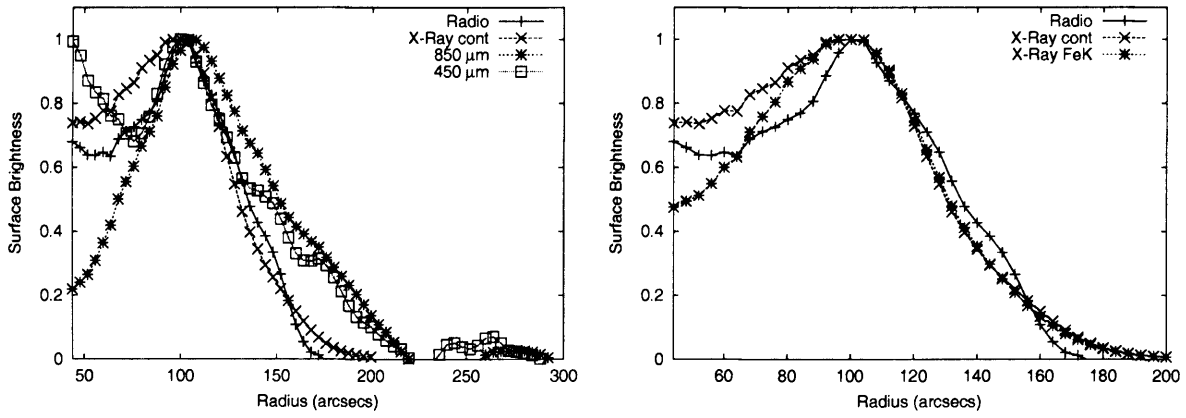

Figure A.1: Radial profiles of Cas A averaged over the whole remnant for (a) X-Ray continuum vs radio and sub-mm and (b) FeK line with the X-Ray continuum and radio emission. The images were smoothed at 450 μm by 7″ gaussian and at 850 μm by a 6″ gaussian per 3arcsec pixel, resulting in a final resolution of $\sim$ 22″. A 1σ error bar is shown. The X-Ray and radio profiles are smoothed by a gaussian of 21″. The profiles are normalised to the maximum value and by area. The centre was chosen to be the centre of the outer shock in Gotthelf et al. (2001) at $\alpha_{2000} = 23^h\ 23^m\ 26.98^s$, $\delta_{2000} = -58°\ 48'\ 45.9''$.

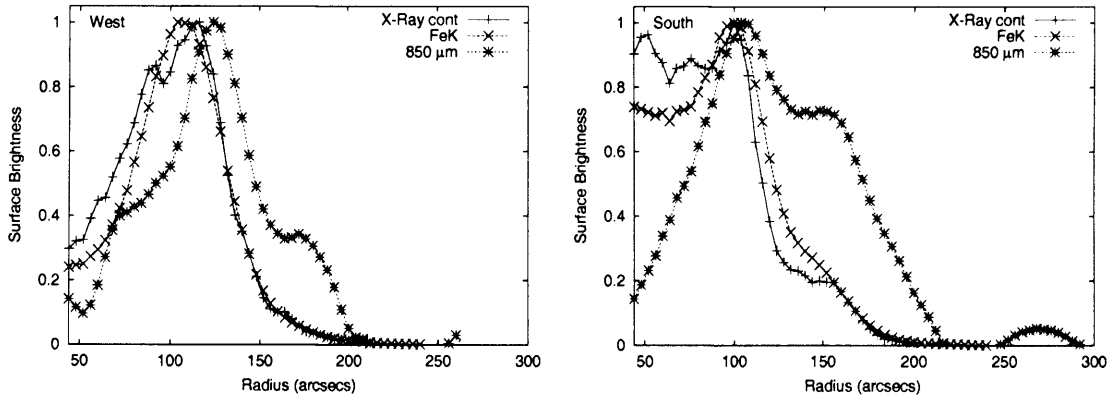

Figure A.2: The X-Ray profiles of Cas A separated into FeK and Continuum emission and the sub-mm in the West and South regions of the remnant.

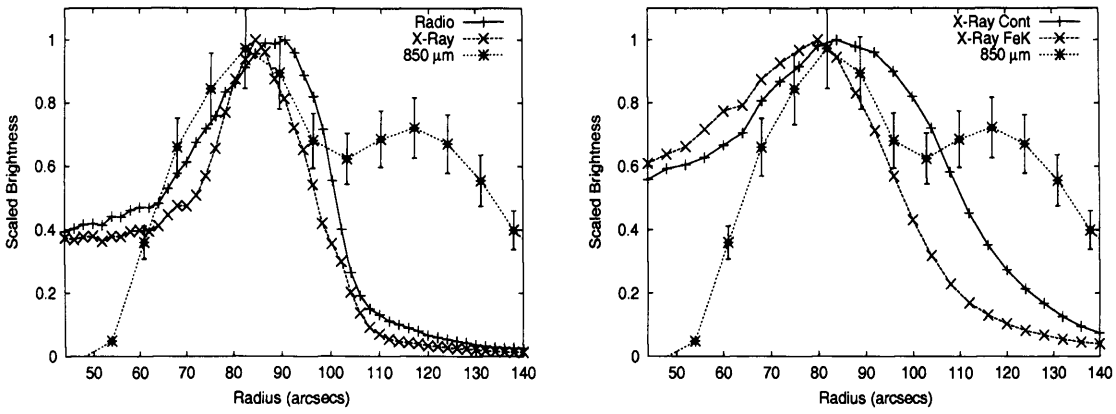

(a) (b)

Figure A.3: The intensity profiles averaged over the whole remnant for the broadband CHANDRA X-ray (ejecta dominated) and radio emission (binned over 2″) and the noise weighted, synchrotron subtracted 850 μm emission (binned over 7″). In (b) we compare the XMM-Newton smoothed (14″) image separated into line (ejecta) and continuum (outer shock) emission with the 850 μm. The profiles in (b) are binned over 4″. The continuum emission is associated with the outer shock (as it sweeps up neutral medium) and the line FeK emission is from shocked ejecta (where it has hit the reverse shock). The profiles are normalised by area.

seen in the 850 μm but is smaller than the radius of the ring which encompasses all the wisps in Figure 5.9 ($\sim$ 133″). In (b) we show the profiles from the smoothed X-ray emission. Over the whole remnant, the line emission peaks at 80″ and is due to shocked iron in the ejecta. Thus the outer shock peaks at 92″ over the whole remnant. This figure shows that the broadband X-Ray is line (ejecta) dominated and that the 850 μm emission seems to peak outside the outer shock.

In the above profiles, three regions were chosen to follow the emission in the remnant. These were chosen to incorporate the X-Ray and Radio features so we could compare the sub-mm emission with the profiles calculated by other authors. Unfortunately, this may not include all of the dust features (as shown in Figure 5.11, particularly in the northwest). We have therefore chosen two other regions, a new South (90° – 145°) and a new northwest (0 – −90°) to incorporate the dust features

seen on the sub-mm. In this newly defined south region, we are looking at the emission from the region near the eastern ear and out to where the 850 μm seems to extend outside the bright ring.

In these profiles we see very small bumps in the X-ray outside the bright ring at 117″ (NW) and in the Radio at 120″ (NW, S) both corresponding to bumps in the 850μm profiles. Therefore there is clearly evidence for dust outside the main peak when we look at the regions where dust dominates.

The X-Ray and Radio Properties of Kepler

In the previous section and Section 5.3.2 we have shown that the X-ray and radio emission trace each other well which suggests something about the magnetic field distribution and density properties in the ejecta.

The time delay required for the amplification for the magnetic field from the shock to turn on the synchrotron radiation usually means that the X-ray outer shock is further out than the radio (e.g. in Cas A). This can be interpreted as the outer shock not being responsible for the magnetic field amplification so that the synchrotron occurs behind it due to shear amplification of clumps and turbulence in the post shock medium. As, unlike Cas A, the radio and X-ray in Kepler do seem to trace each other well, we can propose that: (i) the synchrotron has caught up with the X-ray (Kepler is slightly older than Cas A); (ii) the outer shock in Kepler is efficient enough to amplify the magnetic field and cause synchrotron emission at the outer shock position; (iii) the outer shock is much further out than the peaks we see in the intensity profiles and is actually at a radius of 130″ as suggested by the sub-mm (Figure 5.9). In this scenario, the radio is lagging behind as seen in Cas A. This is only true if the wisps and the ears seen in the X-ray are tracing the true position of the outer shock.

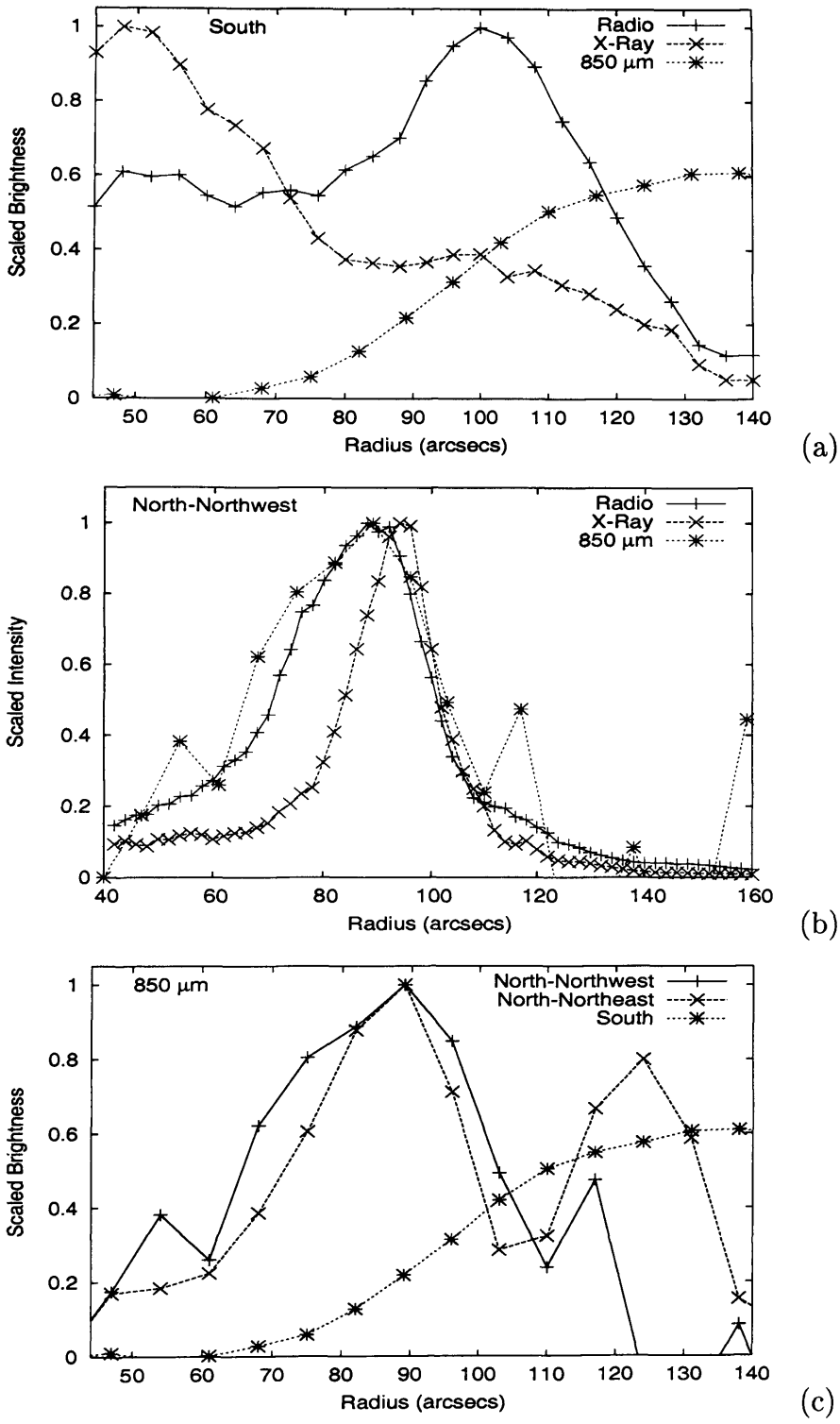

Figure A.4: Comparison of the surface brightness with radius for the X-Ray, Radio and the noise weighted 850μm emission averaged over newly defined regions chosen to incorporate the main dust features of the remnant. (a) North-Northwest (0 - $-90°$) and (b) South (90° - 145°). In (c) we show the profiles for the 850μm emission over the three regions with Northeast defined previously as in Figure 5.12.

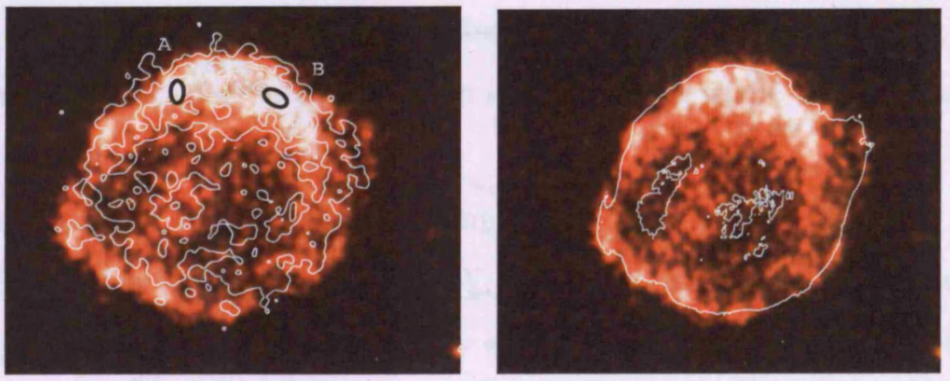

Figure A.5: The XMM-Newton smoothed (9″) X-ray images of Kepler compared with the radio. Left: the continuum image is shown (4 - 6keV) overlaid with FeK contours. A and B show the densest regions in FeK. Right: the continuum image overlaid with the outer contour of the radio (6cm). The reduced X-ray data was kindly provided by Tim Waskett.

The irregular outer shell in the continuum suggests that the ambient material was not homogeneous. Bright knots are seen in the X-ray line and continuum emission in the north (well within the outer edge of the emission) which are also co-incident with peaks on the radio map, suggesting that they are shocked ejecta. The FeK emission extends further out in the north than the continuum, whereas the continuum extends further out in the south, which suggests that there are variations in the heavy element distribution and temperatures across the X-ray emitting plasma. The only place in the remnant where the radio and continuum boundaries overlap is in the western ear. The radio overlaps with the FeK emission in the northern part where the emission is the brightest but there is very little emission in both wavelengths in the south. After the work in this Appendix was completed, a full analysis of the XMM-Newton observations of Kepler was published by Cassam-Chenai et al. (2004). In their analysis (which included the SiK emission attributed to 'soft' ejecta), they came to similar conclusions as presented here. They found, using radial profiles, that the FeK emission peaks at a smaller radius than the continuum (see our Figure 5.14) as well as the SiK emission (their Figure 3(a)). Comparing the SiK with the FeK

(which could not be done here due to unavailable data), they show that the hottest part of the remnant is inwards, towards the centre, which is consistent with emission from the inward moving reverse shock. Their radial profiles show no evidence of peaks in the emission at radii $> 130''$ yet they only show flux scaled from 0.1 to 1.0 which cannot detect the low level peaks seen in our Kepler profiles as they are slightly less than 0.1.

Appendix B

Free-Free Emission

Stars have an Infra-red and submillimetre-mm excess from their ionised stellar wind. This is due to free-free emission[1] which depends on the density and temperature of the wind. Without this excess, the stars photospheric flux would decrease with wavelength as it is in the Rayleigh-Jeans tail of the Planck function, i.e. $F_\nu \propto \lambda^{-2}$. The excess flux however decreases at longer wavelengths with a flatter slope. $F_\nu \propto \lambda^{-0.6}$ which can be derived from the simple argument given in Lamers & Cassinelli (1999):

The luminosity from a star without a stellar wind is given by

$$L_\nu^* = 4\pi R_*^2 \pi B_\nu(T_{eff})$$

where L_ν^* is the photospheric luminosity and B is the Planck function at a frequency ν for a given effective temperature, T_{eff}. With a stellar wind, the luminosity is

$$L_\nu \sim 4\pi r^2(\tau_\nu = \tau_{eff})\pi B_{\nu,w}(T(\tau_\nu = \tau_{eff}))$$

[1] free-free emission occurs when a thermal electron is accelerated by Coulomb attraction of nearby proton and emits radiation. The name free-free occurs as both the electron/proton pair are in a free state before and after the interaction.

so the excess is given by the ratio of these two luminosities (Equation B.1).

$$\frac{L_\nu}{L_\nu^*} = \frac{r^2(\tau_\nu = \tau_{eff})}{R_*^2} \times \frac{B_{\nu,w}(T(\tau_\nu = \tau_{eff}))}{B_\nu(T_{eff})} \tag{B.1}$$

The effective optical depth in an extended stellar wind is about 1/3. The free-free opacity follows a ν^{-2} power law so the optical depth along the line of sight varies as $\tau = \int \kappa_\nu \rho dr \rightarrow \nu^{-2}$. The radius where $\tau = \tau_{\rm eff}$ is therefore larger at larger wavelengths such that a radio image presents a larger radius than an optical image. If $T_w \sim T_{\rm eff}$, the excess (Equation B.1) is given by the larger effective radius of the star as we go out to longer wavelengths.

The absorption coefficient per cm^3 in an ionised gas at long wavelengths where $\rho = \dot{M}/4\pi r^2 v$, is (for a full derivation see Lamers & Cassinelli (1999)):

$$\kappa_\nu \rho \sim \left(\frac{Z^2 \gamma_e}{\mu_i^2}\right) \nu^{-2} \, g_\nu \, T^{-3/2} \, R_*^{-4} \left(\frac{\dot{M}}{v_\infty}\right)^2 \frac{R_*^4 \, v_\infty^2}{r^4 \, v(r)^2}$$

where γ_e is the number of free electrons per ion (where electron density, $n_e = \gamma_e n_i$), Z is the rms charge of the electrons (i.e $Z = 1$ for singly ionised gas) and μ_i is the mean atomic mass of the ions such that $n_i = \rho/(\mu_i m_H)$. g_ν is the Gaunt factor which for $h\nu < KT$ is approximated by

$$g_\nu = 10.6 + 1.90 \log T - 1.26 \log \nu Z$$

The free-free emission originates from the constant velocity region of the stellar wind i.e. where $v \rightarrow v_\infty$ and $v(r)/v_\infty = 1$, the terminal velocity. At this distance from the star, r, T is assumed to be constant $= T_w$. The optical depth is calculated from

$$\tau_\nu = \int_r^\infty \kappa_\nu \rho dr \sim \left(\frac{Z^2 \gamma_e}{\mu_i^2}\right) \nu^{-2} \, g_\nu \, T_w^{-3/2} \, R_*^{-3} \left(\frac{\dot{M}}{v_\infty}\right)^2 \frac{R_*^3}{r^3}$$

The effective optical depth is reached when $\tau = 1/3$ at a distance from the wind

$$r/R_* \sim \left(\frac{Z^2\gamma_e}{\mu_i^2}\right)^{1/3} \nu^{-2/3}\, g_\nu^{1/3}\, T_w^{-1/2}\, R_*^{-1} \left(\frac{\dot{M}}{v_\infty}\right)^{2/3}$$

and as the emission from the wind is at the RJ tail such that $B_\nu \rightarrow \nu^2 T$, the luminosity is given by

$$L_\nu = 4\pi R_*^2 (r/R_*^2)(\tau \sim \tau_{eff})\pi B_\nu(\tau \sim \tau_{eff})$$

$$L_\nu \sim \left(\frac{Z^2\gamma_e}{\mu_i^2}\right)^{2/3} \left(\frac{\dot{M}}{v_\infty}\right)^{4/3} \nu^{2/3} g_\nu^{2/3}$$

Rewriting this in terms of flux in Jy (1Jy = 10^{-26} $\mathrm{Wm^{-2}}$) with distance to the star d in kpc, $\dot{M}$ in $\mathrm{M_\odot\ yr^{-1}}$ and v_∞ in units of km $\mathrm{s^{-1}}$ gives

$$F_\nu = \left[\frac{1}{0.095}\left(\frac{Z^2\gamma_e}{\mu^2}\right)^{1/2} \frac{\dot{M}}{v_\infty} \frac{(\nu g_\nu)^{1/2}}{d^{3/2}}\right]^{4/3}$$

therefore, taking into account the weak dependence of the gaunt factor on frequency, the flux from the free-free emission is $\propto \nu^{0.6}$.

At radio wavelengths, there is also free-free emission with a $\nu^{-0.1}$ dependancy, thought to arise from extended regions of optically thin ionised gas.

Appendix C

Iron Whiskers

Whiskers have been postulated for many years to account for large dust masses at high redshifts (e.g. Edmunds & Wickramsinghe 1975) and to explain the Cosmic Microwave Background (CMB; Li 2003). If the dust seen in high redshift Quasars and Galaxies is due to the thermal emission from normal dust grains, we require dust masses of up to 10^{10} $M_{\odot}$ (Bertoldi et al. 2003; Eales et al. 2003) which are thought by some to be unfeasibly large (Hoyle & Wickramsinghe 1988). If we invoke grains which are not similar to 'normal' interstellar dust but have emission efficiencies $10 - 10^{6}$ times greater, the dust mass is decreased by the same factor and is no longer large (Edmunds & Wickramsinghe 1975). Antennae or conducting needles are ideally suited for this purpose. Made out of iron, these type of grains also provide an alternative scenario to the origin of the CMB. Hoyle & Wickramsinghe (1988) postulated that dust could be responsible for the shape of the CMB spectrum at Infra-Red wavelengths. Recent work by Li (2003) has shown that only iron whiskers with axial ratios $l/a > 10^{4}$ can provide sufficient opacity to thermalize the CMB.

However, there is not enough work on the absorption properties of iron needles. There are many different parameters involved in modelling the emission from iron

whiskers so in Chapter 5, we have tried to constrain the parameters to explain the supernovae observations (following Dwek 2004a). Here I reproduce the derivation of the absorption coefficient used in Edmunds & Wickramsinghe (1975), Hoyle & Wickrmasinghe (1988), Wright (1982), Li (2003), Dwek (2004a) and Morgan et al. (2004).

Following Wright (1992), the average absorbed power of needle-like grains is given by $P = VI/2 = V^2/2R$ with resistance, $R = \rho L/D^2$, cross sectional area D^2, length L, and resistivity ρ. The increment in potential difference is equal to the work done per unit charge in dL such that (Duffin, 1998)

$$V = \int -E.dL = \int -Ecos\theta dL \tag{C.1}$$

where θ is the angle between the E-field and the needle. Over a needle of length, L, the power absorbed is therefore

$$P = E^2 cos^2\theta LD^2/\rho.$$

The absorption cross section of the needle is given by the ratio of the power absorbed to the energy flux $\sigma = P/S$ where $S = cE^2/8\pi$ is the Poynting vector (Wright 1992; Duffin 1998). If we take an averaged-direction of the cross section i.e. $< cos^2\theta >= 1/3$ then

$$\sigma = \frac{4\pi LD^2}{3\rho c} \tag{C.2}$$

and for volume, V_L:

$$\sigma = \frac{4\pi V_L}{3\rho c}. \tag{C.3}$$

The mass absorption coefficient, κ_{abs} is given by σ/m_d where m_d is the mass of the dust grain. If ρ_m is the density of the grain, we obtain the result presented in Wright (1982), Li (2003) and Dwek (2004a).

$$\sigma = \frac{4\pi}{3}\frac{1}{\rho_m \rho c}. \tag{C.4}$$

There will be a long wavelength cutoff when the capacitive reactance $C = Q/V$ of the needle equals its resistance (Wright 1992) i.e at the the RC time constant. If we assume the charge density in the needle is linear with charge (l) at either end of needle length and zero in the middle, we obtain an enclosed charge distribution of $Q = lL/3$. The voltage distribution between two points at radii A and B in the cylinder using Equation C.1 is $2l\ln(\mathrm{A/B})$. Wright (1992) sets $A = L/2$ and $B = D/2$ and $V = 4l\ln(\mathrm{L/D})$. Therefore the capacitance is

$$C = \frac{L}{12\ln(\mathrm{L/D})}.$$

At the RC time constant $2\pi f = 1/\tau$ and $\tau = RC$. The wavelength cutoff when the capacitor reactance equals the resistance is then

$$\lambda_0 = 2\pi c(RC)$$

and

$$\lambda_0 \sim \frac{0.5\rho c\ (L^2/D^2)}{\ln(\mathrm{L/D})}. \tag{C.5}$$

Equations C.5 & C.3 have been used widely in the literature to obtain the dust opacities. However, recently Li (2003) showed this may not be appropriate under the conditions required for the grains to absorb efficiently. Under these circumstances in

the IR where the particles are smaller than the wavelength of the incoming photons, the Rayleigh approximation is applicable where

$$\frac{2\pi l}{\lambda} \ll 1 \quad ; \qquad |m|\frac{2\pi l}{\lambda} \ll 1 \tag{C.6}$$

and $m(\lambda) = n+ik$ is the complex refractive index (e.g. Krugel 2002). The imaginary part allows for the *absorptive* index of the material which is high for iron since it is an electrical conductor. For metals, m is purely imaginary and $n \to k \approx (\sigma\lambda/c)^{1/2}$ where σ is the electrical conductivity (ρ^{-1}) (Li 2003; Krugel 2002). This criterion must be satisfied for the cross section in Equation C.3 to be applicable, otherwise we are overestimating the efficiency. As Li (2003) points out, the high absorption efficiencies are only obtained when all the elements radiate in phase with each other. Equation C.6 therefore places a limit on the particle length, l such that Equation C.7 must be satisfied;

$$l \ll \frac{1}{2\pi}\left(\frac{\lambda c}{\sigma}\right)^{1/2} = \frac{1}{2\pi}\left(\lambda c\rho\right)^{1/2}. \tag{C.7}$$

Bibliography

[1] Abraham, Z., Damineli, A., 1999, in *Eta Carinae at the Millenium*, ASP No. 179, eds. J.A.Morse, R.M.Humphreys, A.Damineli, p.263

[2] Almaini, O., Lawrence, A., Boyle, B.J., 1999, MNRAS, 305, L59

[3] Agladze, N. I., Sievers, A. J., Jones, S. A., Burlitch, J. M., Beckwith, S. W., 1996, ApJ, 462, 1026

[4] Alton, P., Bianchi, S., Rand, R.J., Xilouris, E.M., Davies, J.I., Trewhella, M., 1998, ApJ, 507, L125

[5] Amure, M., 2003, PhD Thesis, University of Wales, Cardiff

[6] Anderson, M.C., Rudnick, L., 1996, ApJ, 456, 234

[7] Archibald et al., 2002, MNRAS, 336, 1

[8] Arendt, R.G., 1989, ApJS, 70, 189

[9] Arendt, R.G., Dwek, E., Moseley, S.H., 1999, ApJ, 521, 234

[10] Bandiera, R., 1987, ApJ, 319, 885

[11] Barnard, V.E., Vielva, P., Pierce-Price, D.P.I., Blain, A.W., Barreiro, R.B., Richer, J.S. Qualtrough, C., 2004, MNRAS, 352, 961

[12] Bhatnagar, S., 2001, PhD Thesis, National Centre for Radio Astrophysics, Tata Institute for Fundamental Research

[13] Bertoldi, F., Carilli,C., Cox, P., Fan, X., Strauss, M.A., Beelen, A., Omont, A., Zylka, R., 2003, A & A, 406, L55

[14] Bianchi, S. , Goncalves, J., Albrecht, M., Caselli, P., Chini, R., Galli, D., Walmsley, M., 2003, A&A, 399, L43

[15] Blair, W.P., Long, K.S., Vancura, O., 1991, ApJ, 366, 484

[16] Blöcker, T., 1995a, A & A, 297, 727

[17] Blöcker, T., 1995b, A & A, 299, 755

[18] Blocker, T., Osterbat, R., Weigelt, G., Balegon, Y., Meishchikov, A., 2001, in *Post AGB Objects as a Phase of Stellar Evolution*, eds. R. Szczerba & S.K. Gornysk, Astrophysics and Space Science Library, Vol. 265, 241, Kluwer Academic Publishers, Netherlands

[19] Bode, M.F., 1988, in *Dust in the Universe*, eds. M.E.Bailey & D.A. Williams, P73, Cambridge University Press, Great Britian

[20] Borkowski, K.J., Blondin, J.M., Sarazin, C.L., 1992, ApJ, 400, 222

[21] Boulanger, F. et al., 1996, A & A, 312, 256

[22] Braun, R., 1987, A & A, 171, 233

[23] Brown, J.A., Johnson, H.R., Alexander, D.R., Cutright, L.C., Sharp, C.M., 1993, A & A, 277, 578

[24] Cadwell, B.J., Wang, H.A.I., Feigelson, E.D., Frenklach, M., 1994, ApJ, 429, 285

[25] Cassam-Chenai, G., Decourchelle, A., Ballet, J., Hwang, U., Hughes, J.P., Petre, R., 2004, A & A, 414, 545

[26] Chevalier, R.A., 1977, Ann. Rev. Astron. Astrophs. 15, 175

[27] Chevalier, R. A., Oishi, J., 2003, ApJ, 593, L23

[28] Cohen, M., Beiging, J.H., Dreher, J.W., Welch, W.J., 1985, ApJ, 292, 249

[29] Clayton, D.D., Deneault, E.A-N., Meyer, B.S., 2001, ApJ, 562, 480

[30] Cox, P., Mezger, P.G., Sievers, A., Najarro, F., Bronfman, L., Kreysa, E., Haslam, G., 1995, A & A, 297, 168

[31] Crowther, P.A., 2001, in *The Influence of Binaries on Stellar Population Studies*, ASSL, 264, p.215, Kluwer Academic Publishers

[32] Dale, D.A., Helon, G., Neugebauer, G., Soifer, B.T., 2001 Frayer, D.T., Condon, J.J., AJ, 122, 1736

[33] Davidson, K., Smith, N., 2000, Nature, Vol 405, P.532

[34] Decourchelle, A., Sauvageot, J.L., Audard, M., Aschenbach, B., Sembay, S., Rothenflug, R., Ballet, J., Stadlbauer, T., Wets, R.G., 2001, A & A, 365, 218

[35] Delaney, T., Koralesky, B., Rudnick, L., Dickel, J.R., 2002, ApJ, 580, 914 [DKRD02]

[36] Delaney T., Rudnick L., 2003, ApJ, 589, 818

[37] Dickel, J.R., Sault, R., Arendt, R.G., Matsui, Y., Korista, K.T., 1987, ApJ, 330, 254

[38] Dominik, C., Sedlmayr, E., Gail, H.P., 1993, A & A, 277, 578

[39] Douvion, T., Lagage, P.O., Cesarsky, C.J., Dwek, E., 2001a, A & A, 373, 281

[40] Douvion, T., Lagage, P.O., Pantin, E., 2001b, A & A, 369, 589

[41] Downes, D., et al., 1999, A & A, 347, 809

[42] Draine, B.T., & Lee, H.M., 1984, ApJ, 285, 89

[43] Draine, B.T., 2003, in *The Cold Universe: Saas-Fee Advanced Course 32*, eds. D.Pfenniger, Springer-Verlag, in press, also available on astro-ph/0304488

[44] Duffin, W.J., 1998, *Electricity and Magnetism*, McGraw-Hill International Ltd., UK

[45] Duncan, R.A., & White, S.M., 2003, MNRAS, 338, 425

[46] Dunne, L., 2000, Phd Thesis, University of Wales, Cardiff.

[47] Dunne L., Eales S., Edmunds M.G., Ivison R., Alexander P., Clements D.L., 2000, MNRAS, 315, 115

[48] Dunne L., Eales S., 2001, MNRAS, 327, 697

[49] Dunne, L., Morgan, H.L., Eales, S., Ivison, R., Edmunds, M.G., 2003, Nature, 424, 285.

[50] Dunne, L., Eales, S., Edmunds, M.G., Ivison, R., Alexander, P., Clements, D.L., 2000, MNRAS, 315, 115

[51] Dwek E., 1987, ApJ, 332, 812

[52] Dwek, E., 1998, ApJ, 501, 643 [D98]

[53] Dwek, E., 1999, ApJ, 521, 234

[54] Dwek, E., 2004a, ApJ, 607, 848

[55] Dwek, E., 2004b, submitted, ApJ, also available on astro-ph/0407005

[56] Dwek, E., & Scalo, J.M., 1980, ApJ, 239, 193

[57] Dwek, E., Dinerstein, H.L., Gillet, F.C., Hauser, M.G., Rice, W.L., 1987, ApJ, 315, 571

[58] Dwek, E., & Arendt, R.G., 1992, ARA & A, 30, 11

[59] Dwek, E., Mosely, S.H., Glaccum, W., Graham, J.R., Loewenstein, R.F., Silverberg, R.F., Smith, R.K., 1992, ApJ, 389, L21

[60] Dwek, E., et al., 1998, ApJ, 508, 106

[61] Edmunds, M.G., 2001, MNRAS, 328, 223 [E01]

[62] Edmunds, M.G. & Wickramasinghe, N.C., 1975, Nature, 256, 713

[63] Edmunds, M.G., & Eales, S.E., 1998, MNRAS, 299, L29.

[64] Eales, S., Lilly, S., Webb, T., Dunne, L., Gear, W., Clements, D., Yun, M., 2000, AJ, 120, 2244

[65] Eales, S., Bertoldi, F., Ivison, R., Carilli, C.L., Dunne, L., Owen F., 2003, MNRAS, 344, 169

[66] Ferrara, A., 2003, in *Atrophysics of Dust*, eds. A.N. Witt, G.C. Clayton, B.T.Draine, ASP No. 309, 15

[67] Frisch, P.C., & Slavin, J.D., A & A, 201, 112, 2002

[68] Fujii, T., Nakada, Y., Pathasarath, M., 2001, in *Post AGB Objects as a Phase of Stellar Evolution*, eds. R. Szczerba & S.K. Gornysk, Astrophysics and Space Science Library, No. 265, 111

[69] Gail, H.-P., Sedlmayr, E., 1999, A & A, 347, 594

[70] García-Lario, P., & Pera Calderon, J.V., 2001, in *Post AGB Objects as a Phase of Stellar Evolution*, eds. R. Szczerba & S.K. Gornysk, Astrophysics and Space Science Library, Vol. 265, 339, Kluwer Academic Publishers, Netherlands

[71] García-Segura, G., Langer, N., MacLow, M.-M., 1996, A & A, 316, 133

[72] Gear, W.K, Lilly, S.J., Stevens, J.A., Clements, D.L., Webb, T.M., Eales, S.A., Dunne, L., 2000, MNRAS, 316, 51

[73] Gehrz, R., 1989, in *Interstellar Dust*, IAU Symp. 135 eds. L.J. Allomandola & A.G.G.M. Tielens, P445

[74] Gerardy, C.L., Fesan, R.A., Höflich, P., Wheeler, J.C., 2000, AJ, 119, 2968

[75] Glushak, A.P., 1985, Sov.Astr.Lett., 11, 350

[76] Gordon, M. A.; Holder, B. P.; Jisonna, L. J., Jr.; Jorgenson, R. A.; Strelnitski, V. S., 2001, ApJ, 559, 402

[77] Gomez, E.L., PhD Thesis, University of Wales, Cardiff

[78] Gotthelf, E.V., Koralesky, B., Rudnick, L., Jones, T.W., Hwang, U., Petre, R., 2001, ApJ, 552, L39

[79] Gray, M.D., & Edmunds, M.G., 2004, MNRAS, 349, 491

[80] Greaves, J., 1998, ApJ, 506, L133

[81] Green, D.A., 2001, A Catalogue of Galactic Supernova R nants (2001, December version), Mullard Radio Astronomy Observatory, Cavendish Laboratory, Cambridge, U.K. (also available at http://www.mrao.cam.ac.uk/surveys/snrs/)

[82] Groenewegen, M.A.T., 1999, in *Asymptotic Giant Branch Stars,*, IAU 191, eds. T. Le Bertre, A. Lebre, C. Waelkens, 535

[83] Harper, G.M., Brown, A., Lim, J., 2001, ApJ, 551, 1073

[84] Harvey, P.M., Hoffman, W.F., Campbell, M.F., 1978, A & A, 70, 165

[85] Hauschildt, P.H., Allard, F., Baron, E., 1999a, ApJ, 512, 377

[86] Hauschildt, P.H., Allard, F., Ferguson, J., Baron, E., Alexander, D.R., 1999b, ApJ, 525, 871

[87] Henry, R.B.C., Edmunds, M.G., Köppen, J., 2000, ApJ, 541, 660

[88] Herwig, F., 2004, ApJ, 605, 425

[89] Herwig, F., Blöcker, T., Dreibe, T., 1999, A & A, L349, 5

[90] Hildebrand, 1983, Quart.J.Roy.Astron.Soc., 24, 267

[91] Hirashita, H., Ferrara, A., 2002, MNRAS, 337, 921

[92] Hirashita, H., Hunt, L.K., Ferrara, A., 2003, in *Galaxy Evolution: Theory and Observations*, eds. V.Avila-Reese, C.Firmani, C.S.Frenk & C.Allen, Revista Mexicana de Astronomia y Astrofisica (Serie de Conferencias), Vol. 17, 97

[93] Hirashita, H., Hunt, L.K., 2004, A & A, 421, 555

[94] Holland, W., et al., 1999, MNRAS, 303, 659

[95] Hony, S., Dominik, C., Waters, L.B.F.M., Icke, V., Mellema, G., van Boekal, R., de Koter, A., Morris, P.M., Barlow, M., Cox, P., Kaufl, H.U., 2001, A & A, 377, L1

[96] Hoyle, F. & Wickramsinghe, N.C., 1988, Astro. & Sp. Sci., 147, 245

[97] Hughes, D.H., et al., 1998, Nature, 394, 241

[98] Hughes, J.H., 1999, ApJ, 527, 298

[99] Hughes, J.H., 2000, ApJ, 545, 53

[100] Humphreys, R.W., 1988, in *Physics of Luminous Blue Variables*, eds K. Davidson, A.F.J.Moffat, H.J.G.L.M.Lamers, P.3., IAU Symposium 113, Kluwer Academic Publishers, Netherlands

[101] Hwang, U., Decourchelle, A., Holt, S.S., Petre, R., 2002, ApJ, 581, 1101

[102] Inoue, A.K., 2003, PASJ, 55, 901

[103] Ivison et al, 2002, MNRAS, 337, 1

[104] Isaak, K., Priddey, R.S., McMahon, R.G., Omont, A., Peroux, C., Sharp, R.G., Witthington, S., 2002, MNRAS, 329, 149

[105] James A., Dunne L., Eales S., Edmunds M.G., MNRAS, 2002, 335, 753

[106] Jones, A.P., Tielens, A.G.G.M., Hollenbach, D.J., McKee, C.F., 1994, ApJ, 433, 797

[107] Jones, A.P., Tielens, A.G.G.M., Hollenbach, D.J., McKee, C.F., 1997, in *Astrophysical Implications of the Laboratory Study of Presolar Materials*, AIP Conference Proceedings, eds. T.J. Bernatowicz & E. Zinner,

[108] Jørgensen,U.G., Johnson, H.R., Nordlund, Å., 1992 A & A, 261, 263

[109] Katz-Stone, D.M., Kassim, N.E., Lazio, T., Joseph, W., O'Doneel, R., 2000, ApJ, 529, 453

[110] Kemper, F.; Vriend, W. J.; Tielens, A. G. G. M., 2004, ApJ, 609, 826

[111] Kinugasa, K., Tsunemi, H., 1991, PASJ, 51, 239

[112] Klien, U., Emerson, D.T., Haslam, C.G.T., Salpeter, C.., 1979, A & A, 76, 120

[113] Knapp G.R., 1985, ApJ, 293, 273

[114] Köppen, J., & Edmunds, M.G., 1999, MNRAS, 306, 317

[115] Kosaza, T., Hasegawa, H., Nomoto, K., 1989, *Paper I*, ApJ, 344, 325

[116] Kosaza, T., Hasegawa, H., Nomoto, K., 1991, *Paper II*, ApJ, 249, 474

[117] Krugel, E., 2002, *The Physics of Interstellar Dust*, Institute of Physics, Great Britian

[118] Lamers, H.J.G.L.M., & Cassinelli, J.P., 1999, *An Introduction to Stellar Winds*, Cambridge University Press, Great Britian

[119] Lawrence, A., 2001, MNRAS, 323, 147

[120] Li, A., 2003, ApJ, 584, 593

[121] Limongi, M., & Chieffi, A., 2003, ApJ, 592, 404

[122] Longair, M., *High energy astrophysics. Volume 2: Stars, the galaxy and the interstellar medium*, 1994, Cambridge Univeristy Press, UK

[123] Lorenz-Martins, S., de Arainjo, F.X., Codina Landaberry, S.J., de Almeda, W.G., de Nader, 2001, A & A, 367, 189,

[124] Lucy, L.B., Danziger, I.J., Gouiffes, C., Bouchet, P., 1991, in *Supernovae, The Tenth Santa Cruz Workshop in Astronomy and Astrophysics*, ed S.E.Woosley, p.82, Springer-Verlag, New York

[125] Mackey, J., Bromm, V., & Hernquist, L., 2003, ApJ, 586, 1

[126] Maeder, A., 1992, A & A, 264, 105

[127] Marchenko, S.V., Moffat, A.F.J., Vacca, W.D., Côté, S., Doyon, R., 2002, ApJ, 565, L59

[128] Mathis, J.S., Cassinelli, J.P., van der Hucht, K.A., Prusti, T., Wesselius, P.R., Williams, P.M., 1992, ApJ, 384, 197

[129] Marigo, P., 1998, A & A, 338, 209

[130] Marigo, P., 2000, in *The Evolution of the Milky Way: stars versus clusters*, eds. F.Matteucci and F.Giovannelli, p481, Kluwer Academic Publishers, Netherlands

[131] Marigo, P., Bressan, A., Chiosi, C., 1996, A & A, 313, 545

[132] Marigo, P., Girardi, L., Bressan, A., 1999, A & A, 344, 123

[133] Martin, P.G., 2003, in *Atrophysics of Dust*, eds. A.N. Witt, G.C. Clayton, B.T.Draine, ASP, 309, 15, San Francisco, USA

[134] Matsui, Y., Long, K.S., Dickel, J.R., Greisen, E.W., 1984, ApJ, 287, 298

[135] Mckee, 1989, in *Interstellar Dust*, IAU Symposium No. 135, eds by L.J.Allamandola and A.G.G.M. Tielens, p.431

[136] Molster, F.J., Yamamura, I., Wates, L.B.F.M., Nyman, L.A., Kaufl, H.U., de Jong, T., Loup, C., A & A, 366, 923, 2001.

[137] Morgan, H.L., Edmunds, M.G.E, 2003, MNRAS, 343, 427

[138] Morgan, H.L., Dunne, L., Eales, S., Ivison, R., Edmunds, M.G., 2003, ApJ, 597, L33

[139] Morris, P.W. et al., 1999, Nature, 402, 502

[140] Motte, F., André, P., Ward-Thompson, D., Bontemps, S., 2001, A& A., 372, L41

[141] Nozawa T., Kozasa T., Umeda H., Maeda K., Nomoto K., 2003, ApJ, 598, 785

[142] Olnon, F.M., 1975, A & A, 39, 217

[143] Pagel, B.E.J., 1997, *Nucleosynthesis & the Chemical Evolution of Galaxies*, Cambridge University Press, Great Britian

[144] Pagel, B.E.J., 2002, in *Vulcano Workshop: Chemical Enrichment of Intracluster and Intergalactic Medium*, eds. F.Matteucci and F.Giovannelli, ASP Conference Series, p.489

[145] Panagia, N., 2000, in *Proceedings of the International Summer School on Experimental Physics of Gravitational Waves*, eds. M.Barone, G.Calamai, M.Mazzoni, R.Stanga and F.Vetrano, World Scientific Publishing Co. Pte. Ltd., p107, Singapore

[146] Pittard, J., PhD Thesis, 1999, Birmingham University, U.K

[147] Pittard, J., 2003, Astronomy and Geophysics, Vol 44, P.1.17

[148] Plez, B., Brett, J.M., Nordlund, A., 1992a, A & A, 256, 551

[149] Plez, B., 1992b, A & AS, 4, 527

[150] Pols, O.R., Tout, C.A., Eggleton, P.P., Han, Z., 1995, MNRAS, 274, 964

[151] Pozzo M., Meikle W.P.S., Fassia A., Geballe T., Lundqvist P., Chugai N.N., Sollerman J., 2004, MNRAS, 342, 457

[152] Renzini, A., & Voli, M, 1981, A & A, 94, 175

[153] Reynoso, E.M., Moffett, D.A., Goss, W.M., Dubner, G.M., Dickel, J.R., Reynolds, S.P., Giacani, E.B., 1997, ApJ, 491, 816

[154] Reynoso, E.M., Goss, W.M., 1999, AJ, 118, 926

[155] Renzini, A., & Voli, M, 1981, A & A, 94, 175

[156] Retallack, D.S., 1983, MNRAS, 204, 669

[157] Robinson. G., Mitchell, R.M., Aitken, D.K., Briggs, G.P., Roche, P.F., 1987, MNRAS, 227, 535

[158] Rowan-Robinson, M., Lock, T. D., Walker, D. W., Harris, S., 1986, MNRAS, 222, 273

[159] Saken J.M., Fesen R.A., Shull J.M., 1992, ApJS, 81, 715

[160] Salasnich B., Bressan A., Chiosi C., 1999, A & A, 342, 131

[161] Salpeter, E.E., ApJ, 193, 579, 1974.

[162] Sandell G., Jessop N., Jenness T., 2001, SCUBA Map Reduction Cookbook, starlink cookbook 11.2

[163] Serjeant, S., et al., 2003, MNRAS, 344, 887

[164] Schaerer, D., Meynet, G., Maeder, A., 1993, Paper II, A & AS, 98, 523

[165] Schaller, G., Schaerer, D., Meynet, G., Maeder, A., 1992 Paper I, A & AS, 96, 269

[166] Schaller, G., Schaerer, D., Meynet, G., Maeder, A., Charbonnel, C., 1993, Paper IV, A & AS, 102, 329

[167] Schneider R., Ferrara A., Salvaterra R., 2004, MNRAS, 351, 1379

[168] Schönberner, D., & Steffan, M., 2001, in *Post AGB Objects as a Phase of Stellar Evolution*, eds. R. Szczerba & S.K. Gornysk, Astrophysics and Space Science Library, Vol. 265, p85, p113, Kluwer Academic Publishers, Netherlands

[169] Scott, S.E. et al., 2002, MNRAS, 331, 817

[170] Smail I., Ivison R.J., Blain A.W., 1997, ApJ, 490, L5

[171] Smith, N., Gehrz, R.D., Hinz, P.M., Hoffman, W.F., Mamajek, E.E., Meyer, M.R., Hora, J.L., 2002, ApJ, 567, L77

[172] Smith N., Gehrz R.D., Hinz P.M., Hoffmann W.F., Hora, J.L., Mamajek E.E., Meyer M.R., 2003, ApJ, 125, 1458

[173] Sodroski T. J. et al., 1997, ApJ, 480, 173

[174] Sopka R. J et al., 1985, ApJ, 294, 242

[175] Talbot, R.J.Jr., Arnett, W.D., 1973, ApJ, 186, 51

[176] Tielens, A.G.G.M., 1998, ApJ, 499, 267

[177] Tielens, A.G.G.M., Allamandola, L.J., 1987, in *Interstellar processes*, Proceedings of the Symposium, Grand Teton National Park, WY, p.397

[178] Tinsley, B.M., 1980, Fund. Cosmic. Phys., 5, 287

[179] Thomas, R.C., Kantowski, R., 2000, Physical Review D, *Particles, Fields, Gravitation, and Cosmology*, No. 62, 10

[180] Todini, P., & Ferrara, A., 2001, MNRAS, 325, 726

[181] Trams, N.R., Th. van Loon, J., 1999, et al, A & A, 344, L17

[182] Tuffs, R.J., et al., 1999, in *The Universe as seen by ISO*, eds. Cox P., Kessler M.F., p241

[183] Tuthill P.G., Monnier J.D., Danchi W.C., 1999, Nature, vol 398, 487

[184] Usov V.V., 1991, MNRAS, 252, 49

[185] van Boekal, R., Kervella, P., Schöller, M., Herbst, T., Bradner, W., de Koter, A., Waters, L.B.F.M., Hillier, D.J., Paresce, F., Lenzen, R., Lagrange, A.-M., 2003, A & A, 410, l27

[186] van den Bergh, S., 1993, ApJ, 413, 67

[187] van den Hoek, L.B., & Groenewegen, M.A.T., 1997, A & A Supp, 123, 305

[188] van Loon, J., 2000, A & A, 354, 125

[189] van Zadelhoff, G.J., van Dishoeck, E.F., Thi, W.F., Blake, G.A., 2001, A & A, 377, 566

[190] Voors R.H.M., et al., 2000, A & A., 356, 501

[191] Waskett, T.J., et al., 2003, MNRAS, 341, 1217

[192] Waters, L.B.F.M., 2003, in *Atrophysics of Dust*, eds. A.N. Witt, G.C. Clayton, B.T.Draine, ASP, 309, 15, San Francisco, USA